Effect of Variation of Degree of Saturation with depth on Soil–Concrete Pile Interface in Clayey Soil

Zainal, Abdul Kareem Esmat
Assistant Professor
College of Engineering-University of Baghdad
Email: kareem_esmat@yahoo.com

Abbas, Mohammed Fadhil
Department of Civil Engineering
College of Engineering-University of Baghdad
Email:mhfa1984@yahoo.com

ABSTRACT

Bearing capacity of a concrete pile in fine grained cohesive soils is affected by the degree of saturation of the surrounding soil through the contribution of the matric suction. In addition, the embedded depth and the roughness of the concrete pile surface (expressed as **B**ritish **P**endulum **N**umber **BPN**) also have their contribution to the shear strength of the concrete pile, consequently its bearing capacity. Herein, relationships among degree of saturation, pile depth, and surface roughness, were proposed as a mathematical model expressed as an equation where the shear strength of a pile can be predicted in terms of degree of saturation, depth, and BPN. Relationship among undrained shear strength of the soil, depth and degree of saturation also found and expressed as mathematical equation that represents a 3D- surface; where the value of c_u can be predicted by knowing the other aforementioned factors. Relationship between shear strength and the concrete surface roughness was also shown reflecting that the shear strength increases with the increase of surface roughness.

Keywords: unsaturated soil, shear strength, concrete piles, deep foundation.

تأثير تغير درجة التشبع مع العمق على التماسك بين التربة والركيزة الكونكريتية في التربة الطينية

م.م. محمد فاضل عباس
قسم الهندسة المدنية
كلية الهندسة / جامعة بغداد

ا. م. د. عبد الكريم عصمت زينل
قسم الهندسة المدنية
كلية الهندسة / جامعة بغداد

الخلاصة

سعة التحمل للركائز الخرسانية المستخدمة في الترب ذات الحبيبات الناعمة والتي لها خاصية التماسك تتأثر بشكل كبير بدرجة التشبع لتلك التربة من خلال مساهمة قوى المص الجزيئي. إضافة إلى تأثير كل من عمق الركيزة، ودرجة خشونة سطح الكونكريت معبَّراً عنه بالرقم البندول البريطاني BPN ، من خلال التأثير على قوى تحمل القص. في هذا البحث، تم إيجاد علاقات تجمع بين العوامل المؤثرة وهي درجة التشبع، العمق، والرقم البندول البريطاني من خلال نموذج رياضي على شكل معادلة يمكن من خلالها التنبؤ بإجهاد تحمل القص للركيزة من خلال معرفة العوامل أعلاه.

و تم إيجاد علاقة بين إجهاد التماسك غير المبزول ودرجة التشبع والعمق على شكل معادلة رياضية تمثل سطح ثلاثي الإبعاد يمكن من خلالها التنبؤ بإجهاد التماسك من خلال معرفة باقي العوامل المذكورة. كما تم إيجاد علاقة تربط بين خشونة سطح الكونكريت المستخدم في الركيزة وتحمل إجهاد القص يبين زيادة اجهاد التحمل مع زيادة خشونة سطح الكرنكريت.

كلمات مفتاح: تربة غير مشبعة, مقاومة القص ,الركائز الكونكريتية , الأسس العميقة

1. INTRODUCTION

In geotechnical engineering, classical soil mechanics design are used for the precast concrete pile foundations assuming that the soil is in saturated state. However, in several situations, the soils in natural state are found in an unsaturated state as the water under earth's surface is at a low depth level. This is especially true for soils in barren and semi–barren zones. Almost 40 percent of the natural soils on the earth's surface are in a partially saturated state **Kholghifard, et al., 2012**. Most of the structures and building foundations including piles are constructed in this zone or a mixed zone of saturated / unsaturated conditions, where the shear strength of the unsaturated soil vary significantly and is important to be known.

Shear strength in unsaturated soils based on the suction pressure that varies with the degree of saturation for soil; consequently, that makes the shear strength of the soil varies with degree of saturation. **Fredlund, et al., 1978**.

Interfaces between soil and structure could experience relative motions under static and dynamic loadings. These relative motions include translational, rotational, and rocking motions. The ultimate shaft resistance of pile in unsaturated soil (coarse and fine-grained soils) can be estimated by the modified α and λ methods **Vanapalli,** and **Mohammed, 2007**. The methods listed can be used for determining the change of the friction capacity of the precast concrete pile with respect to suction using the properties of soil in saturated state and Soil Water Characteristic Curve (SWCC).

Vanapalli, and **Taylan, 2012** studied the contribution of matric suction effect on the shaft capacity of single piles. Based on the experimental results, the traditional (λ, α, and β) methods were modified to determine the total shaft resistance of piles in unsaturated soils by including the effect of suction.

Uchaipichat, 2012 showed simulations performed on a pile with diameter of 0.40 m and it length ranges from 5 to 20 m. installed in clay layer (unsaturated state) with matric suction that ranges from 10 to 10,000 kPa. The results show a decrease in matric suction with decreasing pile capacity and factor of safety.

The interface shear strength between concrete and soil is an important design parameter for estimating the bearing capacity of concrete pile. General concept for interface between soil and pile was discussed by many investigators; **Taha, 2010** explored the interface characteristics between a marine clay, steel and concrete investigating the effects of several parameters such as interface roughness, degree of saturation, OCR, dry density and clay salt content. The critical controlling parameter of interface strength was found to be the relative steel surface roughness.

These tests described the minimum residual strength acquired in each test and provided a basis for a arbitrage with other published research. It is demonstrated that the residual strength depends mainly on the material and its roughness, soil properties, and the clay fraction.

2. THEORETICAL BACKGROUND

The reliable determination of soil-structure interaction parameters requires cumbersome laboratory or field tests. Alleviating the need of such cumbersome tests; empirical methods are proposed to estimate the skin friction, *fs* based on the conventional shear strength parameters and the information related to the variation of effective stresses along the length of the piles.

$$fs=f\,(\sigma'_v\,,\varphi',\,c_u) \qquad (1)$$

where, σ'_v = vertical effective stress, φ'= effective friction angle, and c_u = undrained shear strength. Eq. (1) suggests that the skin friction, *fs* can be analyzed in terms of either total or

effective stress approach considering the loading and drainage conditions (i.e., *TSA* or *ESA*), respectively.
Experimental programs were planned to determine the contribution of matric suction on the shaft resistance and not the end bearing resistance.

The λ-method is an empirical method, based on effective stresses induced in the soil and total soil strength (calculated from undrained shear strength). This method may be used to relate the unit skin friction to the passive earth pressure. The value of λ was empirically-determined by examining the results obtained from various load tests conducted on piles in cohesive soils. Therefore, this method is more accurate, if used for the same soil and pile conditions.

The λ - method combines the total (i.e., undrained) and effective (i.e., drained) stress approaches for determining the shaft capacity of driven piles into cohesive soils **(Vijayvergiya and Focht, 1972)**. This technique is useful in reducing the sensitivity of the shear strength parameters measured using the total stress and effective stress approaches. Eq. (3.10) was used to calculate the skin friction for saturated condition:

$$Q_f = \lambda(\sigma_v' + 2cu)\pi dl \qquad (2)$$

λ = frictional capacity coefficient which is a function of entire embedded depth of pile.
Only one method (α-method will be considered in this work to demonstrated the effect of depth of pile and degree of saturation on the soil-concrete pile interface), for other methods refer to Abbas, Mohammed F., 2015).

2.1 The α Method

The α-method is a semi-empirical approach of calculating the pile skin friction, based on the total stresses induced in the soil and calculated using the soil's undrained shear strength (c_u). This method was mainly developed for cohesive soils. It has been used for many years and has proven to provide reasonable design capacities for piles.
This method depends on the alpha factor (α), which is indirectly related to the soil's undrained shear strength (c_u). The factor was back calculated from several pile load tests. The ultimate shaft capacity of a pile, Q_f is dependent on the undrained shear strength, c_u in soil adjacent to the foundation. The unit skin resistance, f_s can be expressed as in Eq. (2) using undrained shear strength, c_u.

$$f_s = \alpha c_u \qquad (2)$$

The adhesion factor, α is not constant but decreases with increasing undrained shear strength, c_u of the soil and varies from close to unity for low strength soft clays and reach almost to a value of 0.4 for stiff clays **Tomlinson, 1957** and **Skempton, 1959**. The ultimate shaft capacity, Q_f for cylindrical piles using the α method can be estimated as in Eq. (3).

$$Q_f = f_s \times A_s = \alpha c_u \pi dl \qquad (3)$$

where, d = pile diameter, and l = length of pile.
The adhesion factor, α can be computed from API (1984). Eq. (4) can be used for estimating the α value.

$$\alpha = 1.0 \qquad \text{for } cu < 25kPa$$
$$\alpha = 1.0 - 0.5\left(\frac{cu - 25}{50}\right) \qquad \text{for } 25kPa < cu < 75kPa \qquad (4)$$
$$\alpha = 0.5 \qquad \text{for } cu > 75kPa$$

2.2 Modified α Method

Several investigators related the load bearing capacity of a single pile to the undrained shear strength, c_u of the cohesive soils **Tomlinson, 1957, Dennis,** and **Olsen , 1983**. Eq. (5) given by **Oh** and **Vanapalli, 2009** can be used to estimate the variation of undrained shear strength with respect to matric using the *SWCC* and undrained shear strength for saturated condition, $cu_{(sat)}$.

$$c_{u(unsat)} = c_{u(sat)}\left[1 + \frac{(u_a - u_w)}{(P_a/101.3)}\left(s^v\right)\Big/\mu\right] \qquad (5)$$

where, $c_{u(sat)}$ and $c_{u(unsat)}$ = undrained shear strength under saturated and unsaturated conditions, respectively, P_a = atmospheric pressure (i.e. 101.3 kPa), and v and μ are fitting parameters.
The fitting parameter v depends on the soil type (i.e., coarse or fine-grained soils) and is equal to 1 for coarse-grained soils and 2 for fine-grained soils. The fitting parameter μ however is a function of plasticity index, *PI.*

$$\mu = 9 \qquad (8 \le PI(\%) \le 15.5) \qquad (6)$$

$$\mu = 2.1088\, e^{0.0903PI} \qquad (15.5 \le PI(\%) \le 60) \qquad (7)$$

The ultimate shaft capacity of piles in unsaturated soils as given below.

$$Qf_{(unsat)} = \alpha c_{u(sat)}\left[1 + \frac{(u_a - u_w)}{(Pa/101.3)}\left(s^v\right)\Big/\mu\right]\pi dl \qquad (8)$$

The undrained shear strength under saturated condition, $cu_{(sat)}$ and the *SWCC* are required to estimate the variation of ultimate shaft capacity of pile, $Qf_{(unsat)}$ with respect to matric suction.

3. SOIL PROPERTIES

Soil samples were collected from one site within AL–Muthanna governorate from Samawah city region. The physical properties of this soil was studied by conducting series of tests in the laboratory, these tests included: Specific gravity, Grain size distribution, Atterberg limits, Direct shear test, and Interface between clayey soil and concrete pile surface by modified direct shear box test. For each sample, the matric suction was measured using the filter paper technique (Whatman No.42) at different degrees of saturation. Atterberg limits and other soil properties values are summarized in Table (1) and grain size distribution is shown in **Fig.1**.

4. Experimental Program

Soil samples were collected from one site within AL–Samawah city region from depth (3.7 m – 4.5 m). These samples were subjected to testing program that included the following tests:

4.1 Direct Shear Box Test

Direct shear tests were carried out after remolding the samples in accordance with ASTM D3080. Different loading was used to find the shear strength of the sample soil at failure according to the following assumption:

1- A typical pile of 6m depth is assumed for this study.
2- Three places through the pile depth were examined to identify the strength of the soil-pile interface; these places are at the depths of 2m, 4m, and 6m from soil surface.
3- Normal stresses to the pile surface were computed at these three places regarding different unit weight conditions of the soil; low, natural, and high representing low unit weight, normal unit weight (as in situ), and high unit weight, this reflects low, natural and high value. K_o value was computed according to **Das, 2002**, where he suggested that for fine grained, normally consolidated soils, the following Eq.(9) for K_o can be used :

$$K_o = 0.44 + 0.42(PI\%/100) \quad (9)$$

where:
K_o = the coefficient of lateral earth pressure at rest,
PI = plasticity index
PI value for the soil is, PI = 20%
$\therefore K_0 = 0.525$
Normal stress for direct shear test = $\gamma \times h \times K_o$ (10)

So each sample was sheared till reaching failure for three normal stresses: 17 kPa, 22 kPa, and 24 kPa for the depth of 2m and 34KPa, 44KPa, 48 kPa for the depth of 4 m and 50.5 kPa, 66KPa, 72.5 kPa for the depth of 6m depth respectively.

4- The undrained shear strength (c_u) of each sample was measured by carrying out direct shear test through remolding the sample at different degrees of saturation (100%, 90%, 80%, 70%, and 60%) (Smaller values of degree of saturation gave insignificant contribution to the results).

4.2Matric Suction of soil by filter paper method

The filter paper method has long been used in soil science and engineering practice and it has recently been accepted as an adaptable test method for soil suction measurements because of its advantages over other suction measurement devices. Basically, the filter paper comes to equilibrium with the soil either through vapor (total suction measurement) or liquid (matric suction measurement) flow. At equilibrium, the suction value of the filter paper and the soil will be equal. After equilibrium is established between the filter paper and the soil, the water content of the filter paper disc is measured. Then, by using filter paper water content versus suction calibration curve, the corresponding suction value is found from the curve. This is the basic approach suggested by ASTM Standard Test Method for Measurement of Soil Potential (Suction) Using Filter Paper (ASTM D 5298), the results are shown in **Fig.2**.

4.3Pile Interfaces

The interface roughness between the soil and pile material plays an important role in determining the frictional strength capacity along the shaft of the concrete pile. In this study, three concrete materials pile interface were taken into consideration with roughness for each one.

The effect of the roughness is studied in order to establish a relationship between the shear strength property for the clayey soil and the concrete pile surface roughness. Micro roughness is relevant at the scale of the particle size of the soil being sheared against the surface.

Surface roughness was measured using **The British Pendulum Number (BPN),** the British pendulum tester is one of the simplest and cheapest instruments used in the measurement of friction characteristics of pavement surfaces. The British Pendulum Number (BPN) values for the three concrete materials are shown in Table 2.

The CBPN65 interface was taken from the precast concrete pile's body by cutter with dimensions (5.8×5.8) cm which placed in lower half of the shear box. The other two concrete samples were prepared by using a pre-mixed cement-fine sand grout with a 1:3 ratio of sand to cement, and 40% water cement ratio by weight. The samples were cast in the lower portion of a shear box device with different face roughness, and allowed to cure for 14 days prior to initial testing. **Fig. 3** and **Fig. 4** show the concrete–soil interface before and after the test respectively.

4.4Experimental Procedure

The interface characterization program was carried out using a direct shear test apparatus (ASTM D3080/D3080M, 2012). The direct shear test apparatus consists of a displacement controlled testing apparatus used to apply a fixed displacement rate to the shear box device through a series of gearing mechanisms. The shear box has inside specimen dimensions of 60×60 mm, outside dimensions of 90×90 mm and a specimen height of 25.4 mm. schematic drawing of the shear box is shown in **Fig. 5** and the device is shown in **Fig. 6**.

The normal pressure is applied by a steel bearing arm using weights to apply vertical stresses to the specimen. The shearing stresses are measured through a digital load cell connected horizontally to the top section of the shear box.

Horizontal and vertical displacements are measured through linear variable differential transducer (LVDT) connected to a digital logging station using Lab View software. The shear box device was slightly modified by replacing the lower half of the standard direct shear box with the interface material for interface tests.

4.5Testing Procedure

Interface testing was carried out in accordance with ASTM D3080/D3080M (2012). The modified shear box device was placed within a metal container which was laid upon a set of linear ball bearings allowing unrestricted horizontal displacements. The normal loading was applied through a steel bearing arm connected to the top section of the shear box.

Three different normal pressures of (17, 22 and 24) kPa for 2m depth, (34, 44, and 48) kPa for the 4m depth, and (50.5, 66, and 72.5) kPa for the 6m depth were applied to simulate typical lateral earth pressures along the pile shaft at a moderate driving depth.

The shearing rates applied were achieved through the use of a precise screw type actuators calibrated to 2.5 mm/min in order to simulate undrained condition.

5. Results of the Experimental Tests

The undrained shear strength (c_u) of soil was measured by carrying out direct shear test through remolding the samples at different degree of saturation (100%, 90%, 80%, 70%, and 60%). The results demonstrate that the undrained shear strength (c_u) increases with the decrease of the degree of saturation (S), while the angle of internal friction (Ø) is found to be very small and had very small effect especially with clayey soils; this was also noticed by **Fredlund and Rahardjo, (1993).** The results of direct shear test (undrained and unconsolidated) are shown in table 3 and graphically in **Fig. 7**.

5.1 Direct Shear Test for (Clay–Concrete) Samples

Direct shear tests were conducted on the three concrete materials. Through these tests, it is required to determine the shear strength of the clay–concrete interface and to determine the location of failure from direct observations.

Split samples are prepared having one half filled with concrete and the other half is filled with soil. The direct shear test results (undrained condition) are shown in **Fig.8 to Fig. 10.**

5.2 Estimation of the Ultimate Shaft Capacity of Concrete Pile in unsaturated Fine soil by α Method.

The modified α method was used to estimate the ultimate shaft capacity of a single pile in unsaturated undrained condition, implementing modified direct shear test for concrete pile's surface, and three different depths. The modified α is proposed in a functional form such that it can be used to predict the variation of shaft capacity of the pile with respect to matric suction under undrained loading conditions.

Similar to the approach used for saturated soils, the ultimate shaft capacity of a pile is related to the undrained shear strength, c_u by introducing a dimensionless parameter which is the adhesion factor, α. In other words, the method is based on the total stress approach based on Eq. (8) for estimate shaft capacity of concrete pile. Results are show in table 4 to table 6 for CBPN49, from table 7 to table 9 for CBPN52, and from table 10 to table 12 for CBPN56 respectively. Graphical representations of these tables are shown in figure 11 to 19 respectively with the tables.

6. DISCUSSION

Regarding the experimental data results obtained from the tests conducted on the samples of soil and soil–concrete combinations that describe the interaction between the soil and the pile surface material it can be noted that:

6.1 Variation of the Undrained Shear Strength with Depth and Degree of Saturation.

From Table (3) and **Fig.7** it can be noted that there is a variation in the undrained shear strength of the soil with depth and the degree of saturation. This relationship can be described as a surface represented in **Fig.20**. This surface may describe the variation of the undrained shear strength of the soil with depth and degree of saturation. The increase of the undrained shear strength with decreasing degree of saturation was noticed by many investigators **Nishimura** and **Vanapalli, 2004, and Fattah, et al., 2012** and is explained due to the contribution of the matric suction to the shear strength. The increase of undrained shear strength with increasing depth may be explained as the contribution of overburden pressure that may increase the effect of adhesion factor due to increasing the confining pressure with depth, hence affecting the angle of friction δ' and increasing the factor tan δ'. However, since the soil used is a cohesive fine grained soil, the contribution of (tan δ') is observed to be very small compared to the contribution of the degree of saturation S. A proposed relationship was found through curve fitting computer programs, as in Eq. (11), with R^2=0.989, and shown in **Fig.21.**

$$c_u = \frac{S - 159.3}{0.002758D^2 - 1.07} - \frac{2850}{S} \qquad (11)$$

where S = Degree of Saturation in percent, D = Depth in meters.

6.2 Failure Location

To determine the failure location that may occur under loading, it is necessary to determine the weaker shear stress resistance between the soil itself (c_u) and the adhesive bonds at

the interface between the soil and the concrete. Since these stresses vary with the degree of saturation, the study of these variations are important to determine the failure location (i.e. soil failure or interface failure). Results for three depths of (e.g. CBPN65) are shown in **Tables (13, 14, and 15)** and represented graphically in **Fig.13, 14 and 15**.

It can be observed generally that the value of (c_u) is low at lower degrees of saturation and high at higher degrees of saturation, in opposite to the value of τ where it could be observed to be low at higher degrees of saturation and high at lower degrees of saturation for all of the three depths shown (i.e. 2m, 4m, and 6m). A transient range can be observed between about S=75% to 85% that the lower values between c_u and τ change places.

The failure usually occurs when the weaker value of the shear resistance is reached, and since the weaker value changes with the degree of saturation then it is worth to note that the correct value of the shear resistance should be used during design depending on the degree of saturation. Varying degree of saturation during seasons makes it unavoidable for the designer to establish a relationship between the weaker shear resistance and the degree of saturation for the soil type, and pile surface roughness used for the pile foundation design.

7. Conclusions

Trying to predict relationships among many factors that may affect the carrying capacity of a concrete pile foundation could help in adding a more clear vision of pile use (design or analysis) from economical or strength points of view in unsaturated soils.

Factors like the degree of saturation (S), length of a pile (D), and roughness of the pile surface expressed as **B**ritish **P**endulum **N**umber (BPN) were found to have good contribution in affecting the shear strength of a frictional pile, these contributions were expressed mathematically and many conclusions may be expressed herein.

1. Undrained shear strength of soil related to the depth and degree of saturation was obtained as a surface, and expressed as a mathematical model shown by Eq. (11).
2. Equations describing the shear strength of pile foundations were found to be very helpful in predicting the shear strength for unsaturated soils regarding the contribution of the matric suction. These equations can be used to express the shear strength for cohesive soils that may exhibit adhesive bonds between pile surface and fine grained soils like clayey soils.
3. The concrete of the pile surface gave greater shear strength for the rougher surface (BPN49) and became lesser for the softer surface (BPN65). This observation proves the contribution of the surface roughness to the shear strength of the pile.
4. Failure location (where the failure occurs either in the soil material or in the interface part between the soil and the pile surface) was found to be affected by the degree of saturation. Failure location was noticed to occur in the soil material for the degree of saturation less than about 75% and the failure was noticed to occur at the soil–material interface for the degree of saturation greater than about 85%. Degree of saturation between about 75% – 85% was found to be a transient range where the failure type changes from failure type to another.
5. Since CBPN49 and CBPN52 were molded concrete and CBPN65 was already taken from precast pile, it can be roughly concluded that precast piles are smoother than the cast in place piles. This may increase the contribution of the adhesive bonds (and also frictional part in c–ϕ and ϕ soils) and consequently the shear strength and bearing capacity of the pile.

REFRENCES

- Abbas, Mohammed F., 2015, "Effect of Variation of Degree of Saturation with depth on Soil – Concrete Pile Interface in Clayey soil", Thesis submitted to the college of Engineering / Baghdad University / Civil Engineering Dept.
- API (1984). Recommended Practice for Planning Designing and Construction Fixed Offshore Platforms, 14th Edt. APIRP2A, American Petroleum Institute, Dallas, TX.
- Das, B.M., (2002), *Principles of Geotechnical Engineering*, fifth edition, wadsworth group,pp.340.
- Dennis, N.D.; Olsen, R.E.,(1983), "Axial capacity of steel pipe piles in clay," in Proc. Geotechnical Practice in Offshore Engineering. ASCE, pp. 370-388.
- Fredlund, D.G., Morgenstern, and Wider, R.A.,(1978), *The Shear Strength of Unsaturated Soil*, Canadian Geotechnical Journal,Vol.15,pp.313-321.
- Kholghifard, M. A., Kamarudin A., and Nima, L., 2012, *The Influence of Suction Changes on Collapsibility and Volume Change Behavior of Unsaturated Clay Soil***,** Electronic Journal of Geotechnical Engineering, Vol. 17, pp 2623-2631.
- Oh, W.T.; Vanapalli, S.K.,(2009), "A simple method to estimate the bearing capacity of unsaturated fine-grained soils," in Proc. 62nd Canadian Geotechnical Conf & 10thJoint CGS/IAH-CNC Groundwater Conf., pp. 234-241.
- Skempton, A.W., (1959), "Cast-in-situ bored piles in London clay," Geotechnique, vol. 9, pp. 153-173.
- Taha, A. M.,(2010), *Interface Shear Behaviour of Sensitive Marine Clay - Leda Clay*, M.Sc. Thesis, University of Ottawa, Ottawa, Ontario, Canada.
- Tomlinson, M.J.,(1957), "The adhesion of piles driven in clay soils," in Proc. 4th Int. Conf. on Soil Mech. and Foundation Eng., vol. 2, pp. 66-71.
- Uchaipichat, A. (2012). *Variation of Pile Capacity in Unsaturated Clay Layer with Suction*, Electronic Journal of Geotechnical Engineering,Vol.17,pp.2425-2433.
- Vanapalli, S.K. and Mohamed, F. M. O.,(2007), *Bearing Capacity of Model Footing in Unsaturated Soils*, In Experimental Unsaturated Soil Mechanics, Springer Proceeding in physics, Springer- Verlag Berlin Geidelberg, Vol. 112, pp.483-493.
- Vanapalli, S.K. ,(2009), *Shear strength of unsaturated soils and its applications in geotechnical engineering practice*, Proceedings of the 4th Asia-Pacific Conference on Unsaturated Soils. New Castle, Australia. Nov. 23-25, 2009,pp.579-598.
- Vanapalli S.K. and Taylan Z.N.,(2012), *Design of Single Piles Using the Mechanics of Unsaturated Soils*, Int. J. of GEOMATE, Vol. 2, No. 1 (Sl. No. 3), pp. 197-204.
- Vijayvergiya, V.N.; Focht, J.A.,(1972), "A new way to predict capacity of piles in clay," in Proc. Offshore technology Conf., pp. 865-871.

SYMBOLES

μ= fitting parameter, dimensionless.
A= area , m^2
BNP= british pendulum number, dimensionless.
C_a= adhesion component of cohesion, kPa.
c_u= undrined shear strength ,kN/m^2.
D= depth of pile, m^2
e= void ratio, dimensionless.

Gs= specific gravity, dimensionless.
k_o= the coefficient of lateral earth pressure at rest, dimensionless.
L.L= liquid limit, dimensionless.
P.I= plasticity index, dimensionless.
P.L= plastic limit, dimensionless.
p_a = atmospheric pressure, kPa.
Q_f = carrying load capacity, kPa.
S= degree of saturation, dimensionless.
u_a-u_w =matric suction, kPa .
USCS= unified soil classification system.
v= fitting parameter, dimensionless.
α = adhesion factor, dimensionless.
γ= unit weight, kN/m^3
τ= shear stress ,kN/m^2.
τ_f = shear stress at failure, kPa.
ϕ = internal friction angle ,degree.
δ'= internal friction angle between pile and soil, degree.
h = height, m.
d= pile diameter, m.

Table 1. Properties of used soil.

PROPERTY	***VALUE***
Liquid limit % (L.L)	39
Plastic limit % (P.L.)	19
Plasticity index % (P.I.)	20
Specific gravity(Gs)	2.79
Natural degree of saturation (S%)	100
Clay %	67.5
Void ratio,(e_o)	0.644
Total Unit weight (kN/m^3)	20.93
Natural moisture content %	23.3
Classification according to (USCS)	CL

Table 2. Values of Pile interface British Pendulum Number, average roughness, and name used.

Interface Surface	BPN	**Ra(µm)**	Name Used in This Research
Concrete (1)	49	25	CBPN49
Concrete (2)	52	23.7	CBPN52
Concrete (3)	65	21.2	CBPN65

Table 3 Results of direct shear test on remolded samples at different degrees of saturation.

Depth(m)	**S (%)**	**c_u(kPa)**
2	100%	10.3
	90%	35.24
	80%	45.74
	70%	53.61
	60%	60.42
4	100%	13.11
	90%	39.9
	80%	48.77
	70%	61.17
	60%	66.5
6	100%	15.9
	90%	48.31
	80%	52.57
	70%	70.6
	60%	73.29

Table 4 . Estimated and measured ultimate shaft capacity for CBPN49 surface using the modified α method at depth (2) m.

S	***u_a-u_w***	***$C_{u(sat)}/_{unsat.}$ Meas.***	***µ***	***v***	***α***	***Back Cal. α value***	***$\tau_{f(us)}$ Est.***	***$\tau_{f(us)}$ Meas.***
%	**kPa**	**kPa**	**----**	**-----**	**-----**		**kPa**	**kPa**
100	0	10.3	13	2	1	1.05	10.3	10.81
90	49.2	35.24	13	2	0.83	0.76	35.28	31.9
80	107.7	45.74	13	2	0.61	0.69	39	45.2
70	221	53.61	13	2	0.5	0.64	48.1	61.9
60	319	60.42	13	2	0.5	0.66	50.64	67.42

Table 5. Estimated and measured ultimate shaft capacity for CBPN49 surface using the modified α method at depth (4) m.

S	u_a-u_w	C_u meas.	μ	ν	α	Back Cal. α value	$\tau_{f(us)}$ Est.	$\tau_{f(us)}$ Meas.
%	kPa	kPa	----	-----	-----		kPa	kPa
100	0	13.11	13	2	1	1.1	13.11	14.5
90	49.2	39.9	13	2	0.71	0.69	38.3	37.1
80	107.7	48.77	13	2	0.5	0.6	41.3	49.8
70	221	61.17	13	2	0.5	0.605	61.16	73.9
60	319	66.5	13	2	0.5	0.61	64.4	78.38

Table 6. Estimated and measured ultimate shaft capacity for CBPN49 surface using the modified α method at depth (6) m.

S	u_a-u_w	C_u meas.	μ	ν	α	Back Cal. α value	$\tau_{f(us)}$ Est.	$\tau_{f(us)}$ Meas.
%	kPa	kPa	----	-----	-----		kPa	kPa
100	0	15.9	13	2	1	0.92	15.9	17.3
90	49.2	48.31	13	2	0.6	0.66	39.4	42.8
80	107.7	52.57	13	2	0.5	0.55	50.1	55.22
70	221	70.6	13	2	0.5	0.54	74.17	81.19
60	319	73.29	13	2	0.5	0.548	78.18	85.79

Table 7. Comparison between the measured and estimated ultimate shaft capacities for CBPN52 surface using the modified α method at depth 2 m.

S	u_a-u_w	$C_{u(sat)}/_{unsat.}$ Meas.	μ	ν	α	*Back Cal. α Value*	$\tau_{f(us)}$ Est.	$\tau_{f(us)}$ Meas.
%	kPa	kPa	----	-----	-----		kPa	kPa
100	0	10.3	13	2	1	0.98	10.3	10.1
90	49.2	35.24	13	2	0.83	0.73	35.28	30.71
80	107.7	45.74	13	2	0.61	0.65	39	42.63
70	221	53.61	13	2	0.5	0.62	48.1	60.28
60	319	60.42	13	2	0.5	0.63	50.64	63.91

Table 8. Comparison between the measured and estimated ultimate shaft capacities for CBPN52 surface using the modified α method at depth (4)m.

S	u_a-u_w	C_u meas.	μ	ν	α	*Back Cal. α Value*	$\tau_{f(us)}$ Est.	$\tau_{f(us)}$ Meas.
%	kPa	kPa	----	-----	-----		kPa	kPa
100	0	13.11	13	2	1	1.06	13.11	14.01
90	49.2	39.9	13	2	0.71	0.69	38.3	36.7
80	107.7	48.77	13	2	0.5	0.55	41.3	46.22
70	221	61.17	13	2	0.5	0.56	61.16	69.09
60	319	66.5	13	2	0.5	0.55	64.4	71.94

Table 9. Comparison between the measured and estimated ultimate shaft capacities for CBPN52 surface using the modified α method at depth (6) m.

S	u_a-u_w	C_u meas.	μ	ν	α	*Back Cal. α Value*	$\tau_{f(us)}$ Est.	$\tau_{f(us)}$ Meas.
%	kPa	kPa	----	-----	-----		kPa	kPa
100	0	15.9	13	2	1	1.03	15.9	16.46
90	49.2	48.31	13	2	0.6	0.62	39.4	40.1
80	107.7	52.57	13	2	0.5	0.48	50.1	47.9
70	221	70.6	13	2	0.5	0.5	74.17	75.13
60	319	73.29	13	2	0.5	0.52	78.18	82.39

Table 10. Comparison between the measured and estimated ultimate shaft capacities for CBPN56surface using the modified α method at depth 2 m.

S	u_a-u_w	$c_{u(sat)}/_{unsat}$ meas.	μ	ν	α	*Back Cal. α Value*	$\tau_{f(us)}$ Est.	$\tau_{f(us)}$ Meas.
%	kPa	kPa	----	-----	-----		kPa	kPa
100	0	10.3	13	2	1	0.96	10.3	9.98
90	49.2	35.24	13	2	0.83	0.72	35.28	30.1
80	107.7	45.74	13	2	0.61	0.87	39	40.86
70	221	53.61	13	2	0.5	0.6	48.1	58.33
60	319	60.42	13	2	0.5	0.62	50.64	63.29

Table 11. Comparison between the measured and estimated ultimate shaft capacities for CBPN56 surface using the modified α method at depth (4) m.

S	u_a-u_w	C_u meas.	μ	ν	α	*Back Cal. α Value*	$\tau_{f(us)}$ Est.	$\tau_{f(us)}$ Meas.
%	kPa	kPa	----	-----	-----		kPa	kPa
100	0	13.11	13	2	1	0.97	13.11	12.74
90	49.2	39.9	13	2	0.71	0.67	38.3	36.16
80	107.7	48.77	13	2	0.5	0.54	41.3	44.97
70	221	61.17	13	2	0.5	0.55	61.16	67.32
60	319	66.5	13	2	0.5	0.549	64.4	70.78

Table 12. Comparison between the measured and estimated ultimate shaft capacities for CBPN56 surface using the modified α method at depth (6)m.

S	u_a-u_w	c_u meas.	μ	ν	α	*Back Cal. α Value*	$_{f(us)}$ Est.	$_{f(us)}$ Meas.
%	kPa	kPa	----	-----	-----		kPa	kPa
100	0	15.9	13	2	1	0.88	15.9	14.11
90	49.2	48.31	13	2	0.6	0.58	39.4	37.96
80	107.7	52.57	13	2	0.5	0.57	50.1	57.26
70	221	70.6	13	2	0.5	0.504	74.17	74.77
60	319	73.29	13	2	0.5	0.507	78.18	79.34

Table 13.Comparison between values (c_u and measured τ) at 2 m depth CBPN65.

Depth m	**S**	**$c_{u(sat)}/_{unsat.}$ Meas.**	**$\tau_{f(us)}$ Meas.**
	%	kPa	kPa
2	100	10.3	9.98
	90	35.24	30.1
	80	45.74	40.86
	70	53.61	58.33
	60	60.42	63.29

Table 14.Comparison between values (c_u and measured τ) at 4 m depth CBPN65.

Depth m	S	c_u meas.	$\tau_{f(us)}$ Meas.
	%	kPa	kPa
4	100	13.11	12.74
	90	39.9	36.16
	80	48.77	44.97
	70	61.17	67.32
	60	66.5	70.78

Table 15.Comparison between values (c_u and measured τ) at 6 m depth CBPN65.

Depth m	**S**	**c_u meas.**	**$\tau_{f(us)}$ Meas.**
	%	kPa	kPa
6	100	15.9	14.11
	90	48.31	37.96
	80	52.57	57.26
	70	70.6	74.77
	60	73.29	79.34

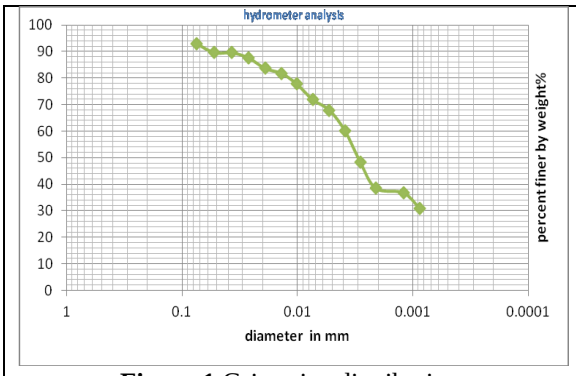

Figure 1. Grian size distribution.

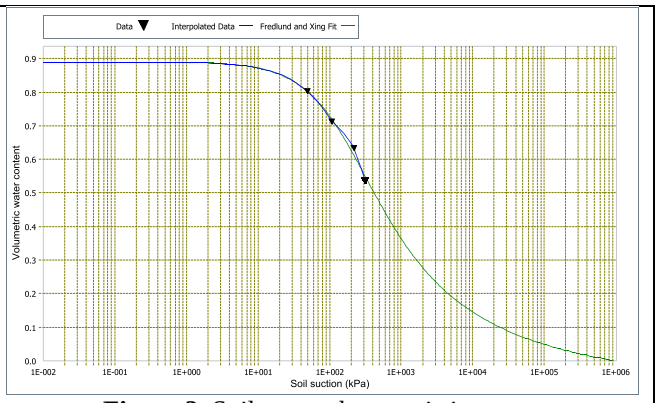

Figure 2. Soil water characteristic curve.

Figure 3. Concrete Interface surface

Figure 4. Concrete–Soil Interface after Failure

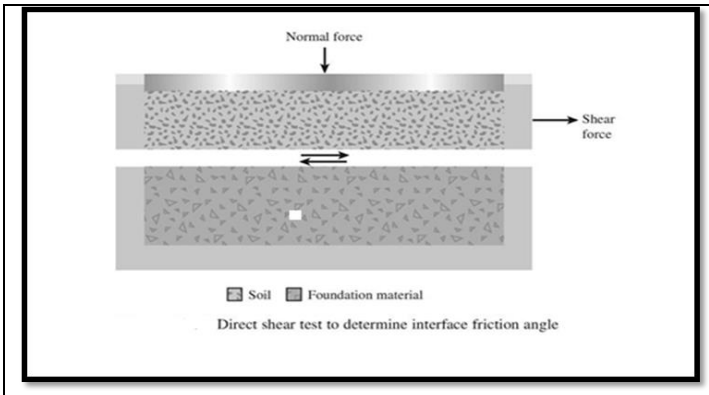

Figure 5. Modified shear box schematic

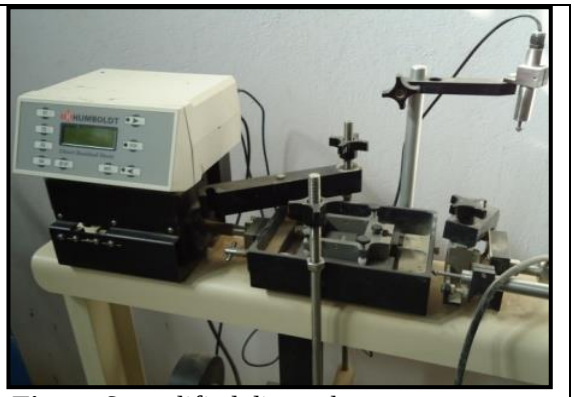

Figure 6. modified direct shear test apparatus

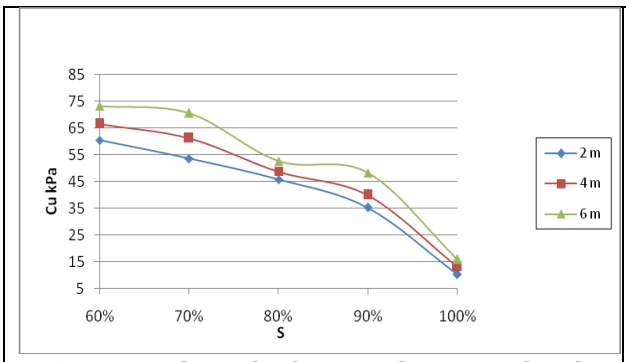

Figure 7. Relationship between shear strength and degree of saturation with different depths.

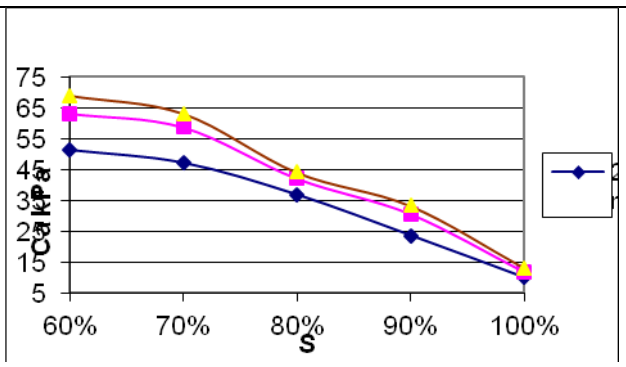

Figure 8. Relationship between adhesion and degree of saturation at different depths for CBPN49 surface.

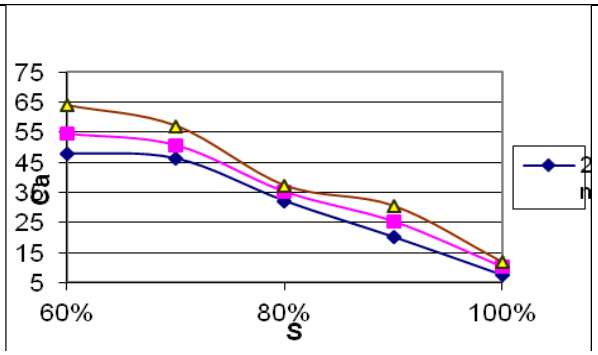

Figure 9. Relationship between adhesion and degree of saturation at different depths for CBPN52surface.

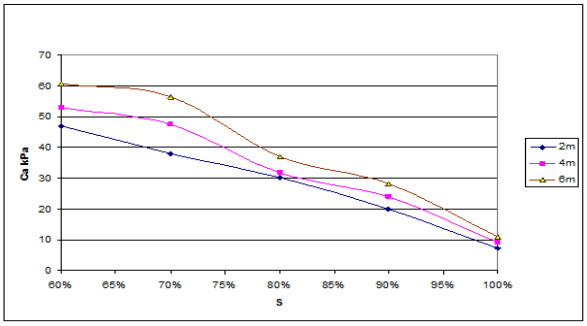

Figure 10. Relationship between adhesion and degree of saturation at different depths for CBPN56surface.

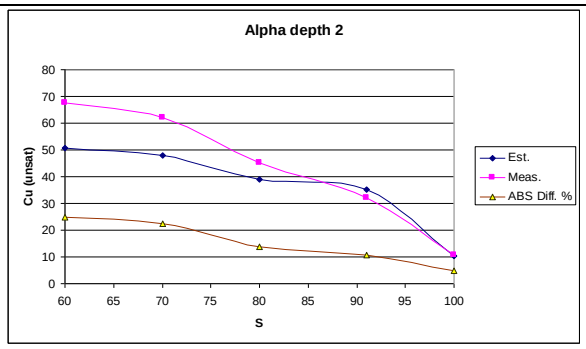

Figure11. Relationship between shear stress(Est. and Meas.) and degree of saturation for CBPN49by using the modified α method with depth (2)m.

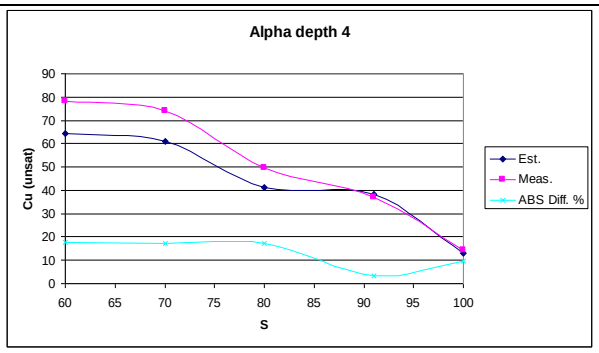

Figure12. Relationship between shear stress(Est. and Meas.) and degree of saturation for CBPN49by using the modified α method with depth (4)m.

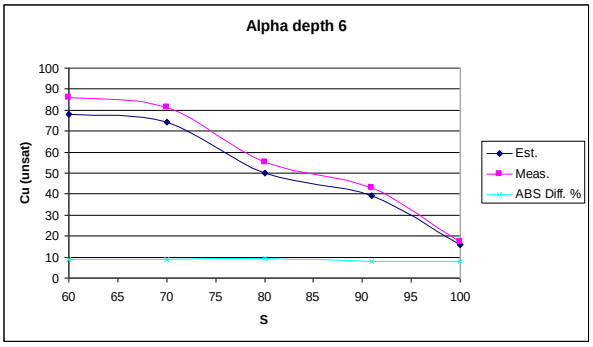

Figure 13. Relationship between shear stress(Est. and Meas.) and degree of saturation for CBPN49by using the modified α method with depth (6)m.

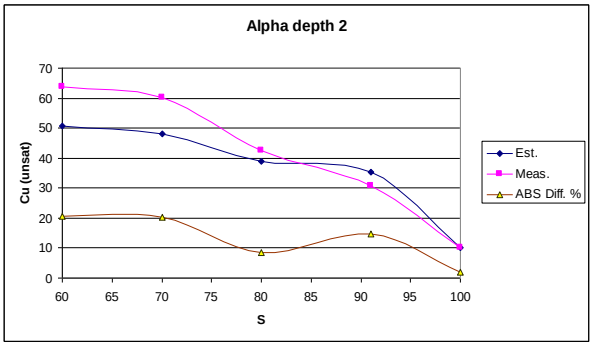

Figure 14. Relationship between shear stress (Est. and Meas.) and degree of saturation for CBPN52 surface

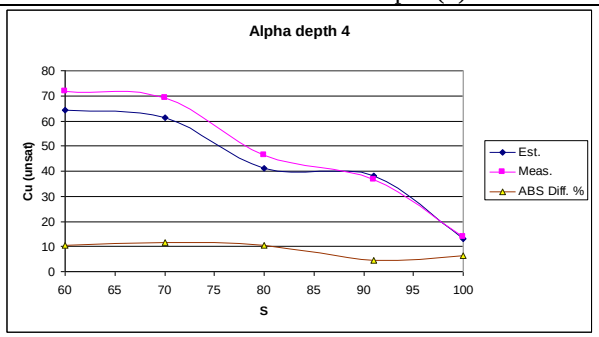

Figure 15.Relationship between shear stress (Est. and Meas.) and degree of saturation for CBPN52 surface

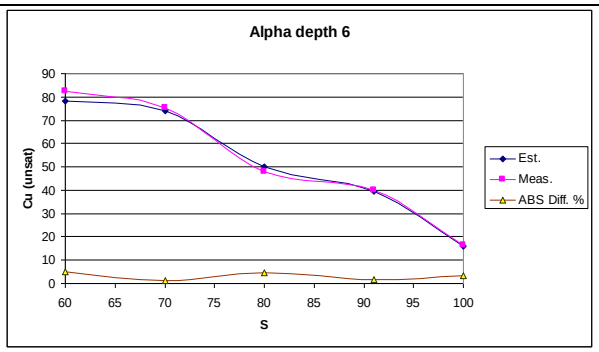

Figure16. Relationship between shear stress (Est. and Meas.) and degree of saturation for CBPN52 surface

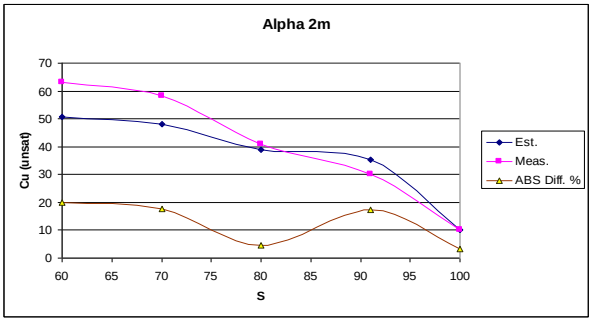

Figure 17. Comparison between estimated and measured shear stress values with different degree of saturation by α method at 2 m depth CBPN56.

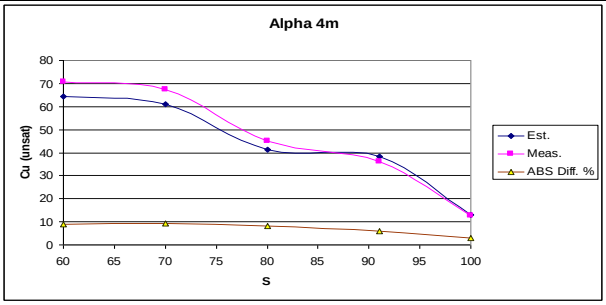

Figure 18. Comparison between estimated and measured shear stress values with different degree of saturation by α method at 4 m depth CBPN56.

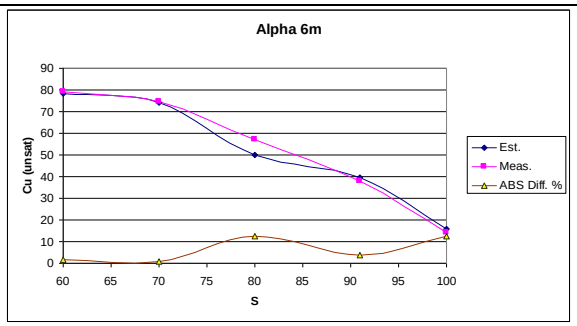

Figure 19. Comparison between estimated and measured shear stress values with different degree of saturation by α method at 6 m depth CBPN56.

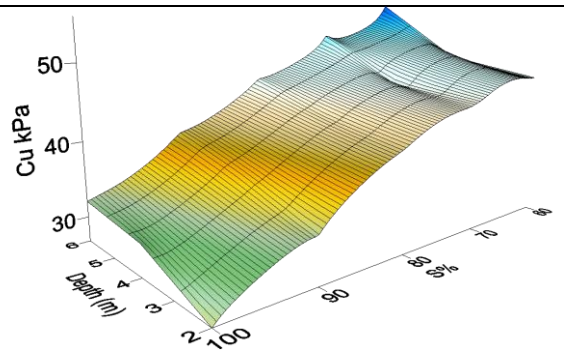

Figure 20. Surface among shear strength, depth and degree of saturation.

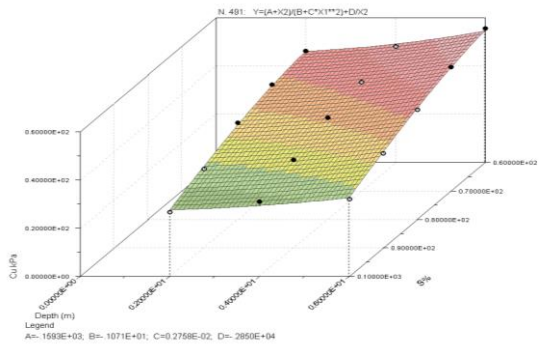

Figure 21. 3D-Surface among shear strength, depth and degree of saturation.

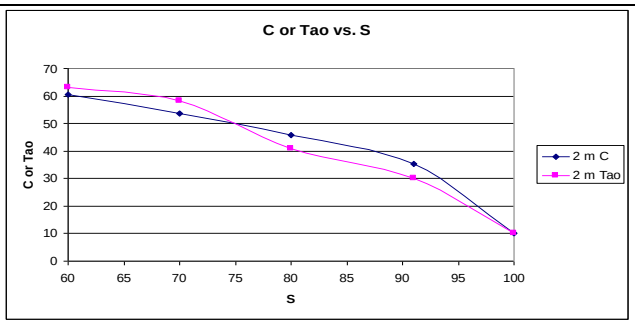

Figure 13. Relationship between (undrained shear strength, undrained shear stress) and degree of saturation at 2 m depth CBPN65.

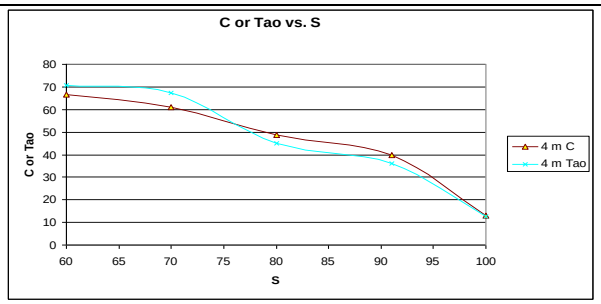

Figure 14. Relationship between (undrained shear strength, undrained shear stress) and degree of saturation at 4 m depth CBPN65.

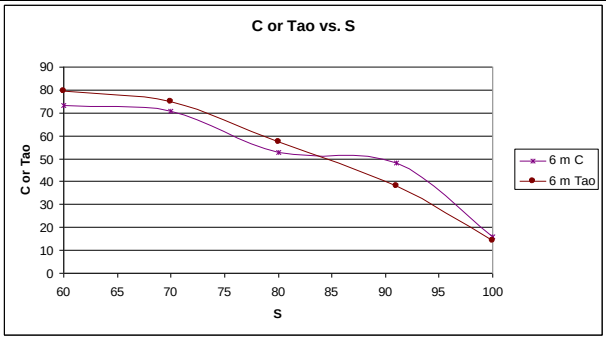

Figure 15. Relationship between (undrained shear strength, undrained shear stress) and degree of saturation at 6 m depth CBPN65.

Experimental Behavior of Steel-Concrete-Steel Sandwich Beams with Truss Configuration of Shear Connectors

Dr.Thaar Saud Salman Al-Gasham
Lecturer
College of Engineering - University of Wasit
E-mail:dr.thaaralgasham@yahoo.com

ABSTRACT

This paper presents experimentally a new configuration of shear connector for Steel-Concrete-Steel (SCS) sandwich beams that is derived from truss configuration. It consists of vertical and inclined shear connectors welded together and to cover steel plates infilled with concrete. Nine simply supported SCS beams were tested until the failure under a concentrated central load (three-point bending). The beams were similar in length (1100mm), width (100mm), and the top plate thickness (4mm). The test parameters were; beam thickness (150, 200, 250, and 300mm), the bottom plate thickness (4, and 6mm), the diameter of the shear connectors (10, 12, and 16mm), and the connector spacing (100, 200, and 250mm). The test results showed that the stiffness of SCS beam augmented with the increase in beam thickness, lower plate thickness, and connector diameter while it decreased with increasing the connector spacing. The ultimate load capacity of the SCS beams increased to 72.2% and 42.1% by enlarging the beam thickness and connector diameter to 100% and 60%, respectively. Increasing the connector spacing of 150% led to a considerable reduction in the ultimate load reached to 68.4%. Finally, the ultimate strength was not affected by augmenting the bottom plate thickness up to 50%.

Keywords; sandwich beam, SCS beam, shear connectors, steel plate, concrete core, truss configuration

السلوك التجريبي للعتبـات السندوجية حديد-خرسانة-حديد مع روابط قصية بهيئة مسنم

د. ثائر سعود سلمان الغشام
كلية الهندسة / جامعة واسط

الخلاصة

في هذا البحث تم تقديم هيئة جديدة(هيئة المسنم) للروابط القصية في العتبات السندوجية بشكل تجريبي . هذه الهيئة تتكون من روابط قصيه عمودية ومائلة مرتبطة مع بعضها ومع الصفائح الحديدية بواسطه اللحام مملوءه بالخرسانة. تم فحص تسع عتبات بسيطة الاسناد الى حد الفشل تحت تأثير حمل مركز مسلط في منتصف العتبة. هذه العتبات متشابهة في الطول (1100 ملم) و العرض (100ملم) وسمك الصفيحة العلوية (4ملم) . متغيرات الفحص تضمنت سمك العتبات (150 و 200 و 250 و 300 ملم) وسمك الصفيحة السفلية (4 و 6 ملم) وقطر الروابط القصية (10 و 12و 16 ملم) ومسافات الروابط القصية (100 و 200 و 250 ملم) . نتائج الفحص بينت , أن صلابة العتبات تزداد مع زيادة كلاً من سمك العتبة وسمك الصفيحة السفلية وقطر الروابط القصية في حين أنها تقل مع إزدياد المسافات بين الروابط القصية . أن الحمل الاقصى للعتبات قد أزداد بحدود 72.2 % و 42.1% عند ازدياد سمك العتبة وقطر الرابط القصي الى 100% و 60% على التوالي. زيادة مسافات الروابط القصية الى 150% أدى الى نقصان كبير في الحمل الاقصى وصل الى 68.4% . اخيراً الحمل الاقصى لم يتأثير بزيادة سمك الصفيحة السفلية بحدود 50%.

الكلمات المفتاحية: العتبة السندوجية , الروابط القصية, الصفيحة الحديدية, اللب الخرساني, هيئة المسنم.

1. INTRODUCTION

Steel-Concrete-Steel (SCS) beams are a comparatively modern system of construction composed of two relatively thin cover plates and a core of plain concrete sandwiched between them. The forces between the concrete core and the cover plates are transferred by shear connectors. Thus, the structural behavior of SCS sandwich beams to be influenced significantly by shear connectors' efficiency, **Anandavalli, et al., 2013**. The first use of SCS construction was in a submerged tube tunnel for Conway River in Cardiff, UK. The SCS system sometimes is known as Double skin Composite (DSC) construction.

The SCS sandwich beams are considered more economical than the beams with ordinary reinforcement due to the replacement of both conventional reinforcement and permanent formwork by external plates and second, the exterior plates and shear connectors are easy to fabricate at the site. Therefore, their cost is relatively low compared with the high cost for detailing, bending and fixing of the conventional bar reinforcement. The cover plates improve the water tightness of SCS sandwich constructions. The SCS beams have an ability to endure large deformations without cracking because of their ductility and energy absorption are relatively high, **Shanmugam and Kumar, 2005**.

Various forms of shear connectors are used in the SCS sandwich constructions. The common forms are through-through connectors and headed stud connectors. In conventional headed stud connectors, the pullout strength of studs influences the resistance of cover plates against tensile separation, **Wright, et al., 1991**.

In Bi-Steel SCS system, an array of transverse bars welded into surface plates is used as shear connectors. Bars have regular patterns with close spacing. **Roberts et al., 1996**, tested a series of SCS sandwich beams under two or four-point loads with a range of the span to depth ratios. The tests showed that the yield and slip in tension plates caused the primary failure modes. **Xie, et al., 2007**, tested eighteen SCS beams with Bi-steel connectors. The tests showed four types of failure mode; concrete shear failure, bar tension failure, bar shear failure, and tension plate yielding.

In **2008, Foundoukos, et al**., presented experimental and analytical studies to evaluate the static and fatigue responses of Bi-Steel SCS beams. A truss model with tapering web compression was developed to determine the forces inside the beams. The predictions of the model were conservative comparing with the test results. J-hook connectors were used by **Liew and Sohel, 2009**, to fix the cover plates on their position with the light weight concrete core. Push-out tests observed that the abilities of J-hook connectors to transfer the shear force were larger than that of the conventional headed stud connector. **Chu, et al., 2013**, tested eight SCS beams with channel steel connectors. Angle steel was used to connect the surface plates with channel steel. Most of the beams experienced ductile failure where the tension steel plates yielded. Numerical simulation using the finite-element approach was presented in 2013 by **Anandavalli, et al.,** to study the static behavior of SCS beams. In this study, two new configurations of Bi-directionally connectors were introduced. The results indicated that Bi-directionally inclined connectors were more ductile than through-through connectors while the ultimate load remained same.

In this paper, a new shape of shear connectors (truss configuration) was proposed. The static behavior of SCS sandwich beams with truss configuration connectors under three-point loads was studied experimentally. The tests focused on the influences of beam thickness, tensile plate thickness, diameter and spacing of shear connectors.

2. SPECIMENS DESIGN

A total of nine SCS sandwich beams with truss configuration of shear connectors were fabricated to exhibit different failure modes. All beams were conformable in length and width that were 1100mm and 100mm, respectively. The thickness of top cover plates was 4mm and kept constant for all specimens. The other geometric properties were varied to study their effect on the static behavior of SCS sandwich beams. They included; beam thickness (150, 200, 250, and 300mm), bottom plate thickness (4 and 6 mm), connector diameter (10, 12, and 16mm) and connector spacing (100, 200, and 250mm).

The reference beam (R) was constructed with thickness of 200mm, lower plate (tensile plate) thickness of 4mm, and shear connectors' diameter and spacing of 10 mm and 100mm, respectively. The remaining eight specimens are named by codes composed of three capital letters followed by a number. The first two letters are (RE); they mean that specimens are geometrically similar to the reference beam except for one property. The third letter refers to this property as follows (H=beam thickness, P=bottom plate thickness, D=connector diameter, and S=connector spacing). Finally, the number refers to the value of property in mm. The details of test specimens are listed in **Table 1**.

The truss shear connectors consisted of vertical and inclined members equally spaced over the length of SCS sandwich beams, as shown in **Figs. 1 and 2**. They were deformed bars and welded to the cover plates using a welding gun. All beams contained two rows of shear connectors spaced at 60mm center to center in the width direction. **Table 2** shows the properties of the shear connectors and the cover plates.

A normal-weight concrete was used as a core sandwiched between the two external plates. The core composed of normal Portland cement, well-graded crushed aggregates of 10 mm maximum size, and washed sand. The mix design proportions by weight were 1 (cement): 1.77 (sand): 2.22 (gravel) with 0.52 water cement ratio. All three specimens were cast in one batch. The compressive concrete strength of each batch was determined by taking the average strength of three cubes with the side length of 150mm as summarized in **Table 1**.

A mechanical mixer was used to produce the concrete. The mixing operations were performed according to the procedure of ASTM C192-1995, where the course and fine aggregates with two-thirds of required water were blended first for one minute, then the cement with the rest water was added and mixed for three minutes followed by three minutes rest period. The specimens were placed inside the plywood molds; these molds were lightly oiled. After mixing, the concrete was poured into molds by three layers. For each layer, well compacting was ensured using vibrator tables, especially in the regions of shear connectors and corners. After removing the molds, the specimens were covered with nylon sheets and kept wet for twenty-eight days.

3. TEST SET UP

The specimens were simply supported and tested under a centrally concentrated load (three-point bending) as shown in **Fig. 3**. The supported length for all beams was 1000mm. A universal machine of 150-ton capacity was employed to apply the load gradually until the failure of the specimen. At each load increment, the initiation and propagation of cracks were carefully examined and marked, and the central deflection of the beams was recorded using a digital dial gauge of 0.01mm accuracy. At the end of the test, both the ultimate strength and the failure mode were determined. The tests were performed at the concrete laboratory at the Engineering College of Wasit University.

4. TEST RESULTS

4.1 Failure Modes

The nine specimens displayed various failure modes depending on their geometric properties as illustrated in **Fig.4**. For all beams, the first flexural cracks were initiated at loads of 25-50kN in the middle third of the beams as listed in **Table 3**.

In the reference specimen R with 200mm thick, the flexural cracks were little and did not cause the failure. The failure mode was characterized by the shear connector failure at the left end.

The specimen REH150 of 150mm thickness failed in the flexural mode. In which, the first flexural crack was initiated at the mid-span. As the applied load increased, this crack widened and moved up towards the top of the beam as well as the formation of other flexural cracks in the middle third of the beam. At failure load, the concrete crushing and the buckling in the upper steel plate were noticed at the top of the beam.

The flexural-shear failure was observed in the specimen REH250 (250 mm thick), where a large number of flexural and diagonal shear cracks developed and spread throughout the length of the beam.

In the beam REH300 with the largest thickness of 300mm, two inclined shear cracks occurred in the right third of the beam and extended to the compression face resulting in shear failure of the specimen.

The shear connector diameter has a great effect on the failure modes, where the specimen RED12 (connector diameter=12mm) showed the similar failure mode to the reference beam R (connector diameter=10mm). However, increasing the connector diameter to 16mm as in the beam RED16, changed the failure mode from connector failure to the flexural failure.

Furthermore, the Shear connector failure was observed in the specimens RES200 and RES250, in which the connectors were spaced at 200 and 250mm, respectively. Finally, the failure mode was not influenced by enlarging the tensile plate thickness where specimen REP6 with the thicker plate (6mm) failed in the same mode of the reference beam R with the thinner plate (4mm).

4.2 Ultimate Strength

The ultimate loads for all specimens are summarized in **Table 3**. In order to investigate the effect of the beam thickness on the load carrying capacity, the test results of specimens REH150, R, REH250, and REH300 are compared in **Fig. 5**. They were constructed with the thickness of 150, 200, 250, and 300mm, respectively. The other properties of them were kept constant. The test results showed that a marginal decrease in the failure load of specimen REH150, about 5.3%, compared with the reference specimen R due to change the mode of failure from flexural to the shear connector failure. Beyond this, the failure load increased rapidly to about 57.9% and 63.2% for specimens of thickness 250 and 300mm with respect to the reference beam R, respectively, because they did not experience the connector failure. However, the shear failure of the beam REH300 caused a little increase in the ultimate strength about 3.3% compared with the specimen REH250 that failed in combined flexural-shear.

Increasing the diameter of connectors enlarged the contact area between the shear connectors and the cover plates and enhanced the bonding between these plates and the concrete core, this reflected at the failure load as plotted in **Fig.6**. The ultimate loads of specimens RED12 and RED16 were 31.6% and 42.1% greater than that of the reference specimen R, respectively.

Fig.7 shows the inverse relationship between the connectors spacing and the failure load. The ultimate loads dropped by about 31.6% and 68.4% when the spacing of connectors increased from 100 mm to 200 and 250mm, respectively.

Finally, enlarging the thickness of tensile steel plate (bottom plate) from 4 to 6mm did not influence the failure load, where both specimens R and REP6 collapsed at the load of 95kN since they showed the connector failure.

4.3 Load-Deflection Response

Since the deflection is a one term of the serviceability measurements, the deflections for all specimens are compared at a service load of the reference specimen R that is 66.5 kN representing 70% of its ultimate load.

Fig.8 shows the effect of the beam thickness on the load-deflection responses of SCS sandwich beams. It is clear that the stiffness of the beam raised with increasing the beam thickness due to the increment in the moment of inertia of the beams. At the load of 66.5 kN, the recorded deflection for the smallest specimen REH150 was 30.8% larger than that of the specimen R. Whereas the larger specimens REH250 and REH300 displayed major reductions in deflection relative to the reference beam at the service load, which were 60.6% and 63.6%, respectively.

The load-deflection behaviors for specimens, constructed with connector diameters of; 10mm (R), 12mm (RED12), and 16mm (RED16), are plotted in **Fig.9**. The three specimens showed an extremely identical response until occurring the yielding in the tensile steel plate (second point of deviation the curve of load-deflection). The flexural plateau is observed clearly in the response of specimen RED16 because it failed in flexure. However, small reductions of 10.1% and 15.7% were recorded in the deflections of specimens RED12 and RDE16 with regard of specimen R at the service load, respectively.

Since the connection between the steel plates and the shear connector, and the bonding between the plates and the concrete core were weakened significantly by increasing the spacing of the shear connectors more than 100mm, specimens RES200 and RES250 behaved like an unreinforced beam where their responses were approximately linear as shown in **Fig.10**. Both specimens failed at loads less than the service load of the specimen R.

Increase the tensile steel plate thickness enhanced the stiffness of the SCS sandwiched beam, especially after initiating of the first crack as illustrated in **Fig.11**. At the service load, the measured deflection of the specimen REP6 (plate thickness= 6mm) was 66.7% smaller than that of specimen R with the plate thickness of 4mm.

5. CONCLUSIONS

The main conclusions of the presented experimental program are summarized as follows:

1. All specimens with 200mm thick, except for specimen RED16 (connector diameter=16mm), experienced the connector failure. The specimen RED16 failed in the flexure. Also, the flexural failure was observed at specimen REH150 with thickness of 150mm .The specimen REH250 of beam thickness 250 mm displayed flexural-shear failure. Finally, the shear failure was exhibited by specimen REH300 (beam thickness=300mm).
2. The ultimate strength and the stiffness of the SCS sandwich beams improved by increasing their thickness. A considerable increase in the failure load, about 72.2%, was observed when the thickness of the beam increased to double.

3. Augmenting the diameter of the shear connector had a negligible effect on the beam stiffness before yielding of the tensile steel plate. After that, the stiffness enhanced with raising the connector diameter. However, increasing the connector diameter to 60% caused an increment in the ultimate load about 42.1%.
4. Increase the connector spacing influences adversely the ultimate capacity and stiffness of the SCS beams. A great reduction in the failure load reached to 68.4% was noticed as spacing increased by 150%.
5. Enlarging the thickness of the tensile plate thickness by 50% increased only the stiffness of the SCS beams, especially after occurring the first crack. The load carrying capacity did not affect.

REFERNCES

- American Specification for Test and Materials, *Making and Curing Concrete Test Specimens in the Laboratory*, C192-1995.

- Anandavalli, N., Rajasankkar, J., Parkash, A., and Sivaprasad, B., 2013, *Static Response of Steel-Concrete-Steel Sandwich Beam with Bi-Directionally Inclined Connections*, American Journal of Civil Engineering and Architecture, Vol.1, No.1, PP.15-20.

- Chu, M., Song, X., and Ge, H., 2013, *Structural Performance of Steel-Concrete-Steel Sandwich Composite Beams with Channel Steel Connectors*, 22nd Conference on Structural Mechanics in Reactor Technology, San Francisco, California, USA-August 18-23, Division X.

- Foundoukos, N., Xie, M., and Chapman, J.C., 2008, *Behavior and Design of Steel-Concrete-Steel Sandwich Construction, Advanced Steel Construction*, Vol.4, No.2, PP. 123-133.

- Liew, J. Y. R., and Sohel, K. M. A., 2009, *Lightweight Steel-Concrete-Steel Sandwich System with J-hook Connectors*, Engineering Structures, Vol.31, No.9, PP.1166-1178.

- Roberts, T. M., Edwards, D. N., and Narayanan, R., 1996, *Testing and Analysis of Steel-Concrete-Steel Sandwich Beams*, Journal of Construction Steel Research, Vol.38, No.3, PP.257-279.

- Shanmugam, N. E., and Kumar, G., 2005, *Behavior of Double Skin Composite Slab-an Experimental Study,Steel Structures*,Vol.5, No.5, PP.431-440.

- Wright, H. D., Oduyemi, T. O., and Evans, H. R., 1991, *The Design of Double Skin Composite Elements*, Journal of Constructional Steel Research, Vol.19, No.2, PP.111-132.

- Xie, M., Foundoukos, N., and Chapman, J.C., 2007, *Static Test on Steel-Concrete-Steel Sandwich Beams*, Journal of Construction Steel Research, Vol.63, No.5, PP.735-750.

Table 1. Details of test specimens.

Specimen designation	Beam thickness (mm)	Bottom plate thickness (mm)	Connectors' diameter (mm)	Connectors' spacing (mm)	Concrete compressive strength (MPa)
R	200	4	10	100	34.37
REH150	150	4	10	100	34.37
REH250	250	4	10	100	34.37
REH300	300	4	10	100	33.96
REP6	200	6	10	100	33.96
RED12	200	4	12	100	33.96
RED16	200	4	16	100	33.88
RES200	200	4	10	200	33.88
RES250	200	4	10	250	33.88

Table 2. Properties of steel bars and cover plates.

	Nominal diameter (mm)	Yield stress (MPa)	Ultimate stress (MPa)
Shear connectors	10	436	556
	12	482	571
	16	520	618
Cover plates	Plate thickness (mm)	Yield stress (MPa)	Ultimate stress (MPa)
	4	245	369
	6	251	384

Table 3. First cracking and ultimate loads of tested specimens.

Specimen designation	First cracking load (kN)	Ultimate load (kN)	Failure mode
R	30	95	Shear connector
REH150	25	90	Flexural
REH250	40	150	Flexural-shear
REH300	50	155	Shear
REP6	40	95	Shear connector
RED12	30	125	Shear connector
RED16	30	135	Flexural
RES200	25	65	Shear connector
RES250	25	30	Shear connector

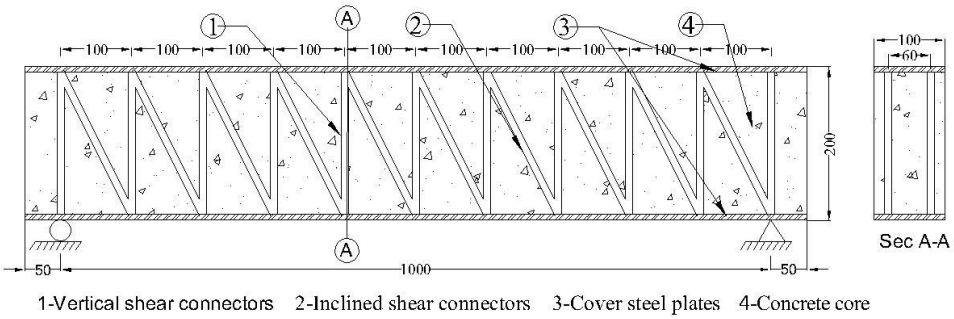

All dimensions are in mm

Figure 1. Experimental details of reference specimen (R).

Figure 2. Typical cover plates welded with shear connectors.

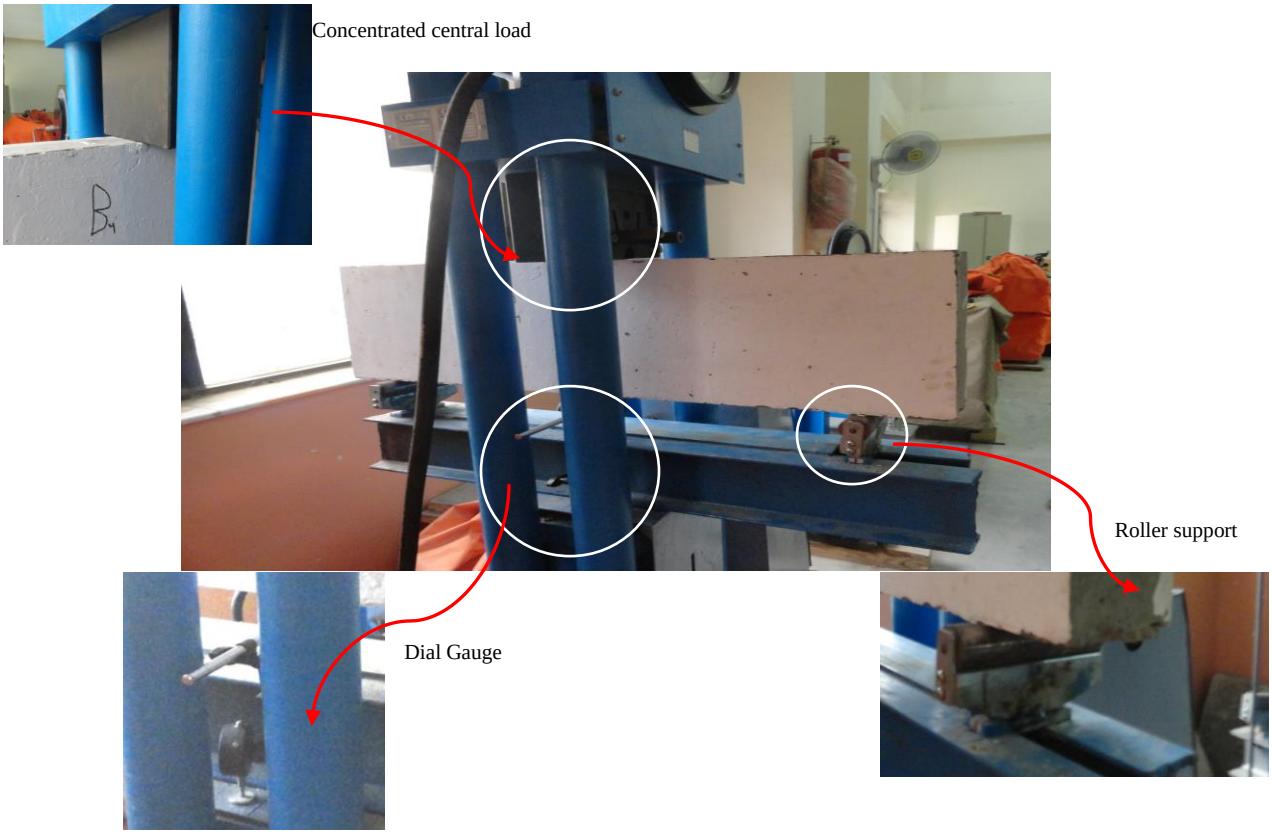

Figure 3. Photograph of the testing setup.

(a) Specimen REH150

(b) Specimen R

(c) Specimen REH250

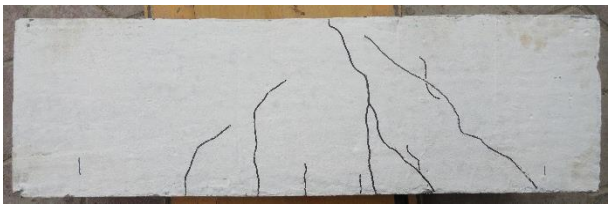

(d) Specimen REH300

(e) Specimen RED12

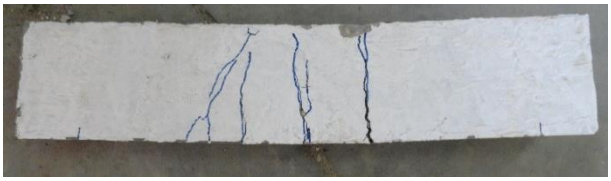

(f) Specimen RED16

(g) Specimen RES200

(h) Specimen RES250

(i) Specimen REP6

Figure 4. Crack patterns for nine tested specimens.

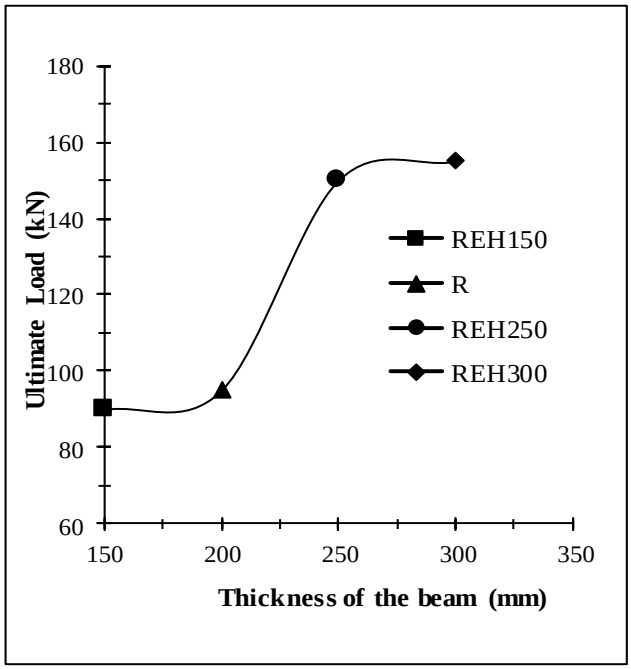

Figure 5. Ultimate load versus thickness of the beam.

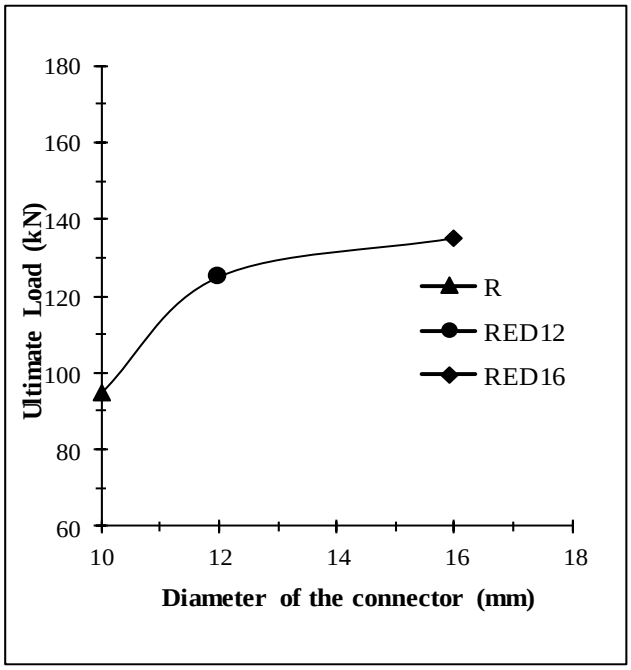

Figure 6. Ultimate load versus diameter of the connector.

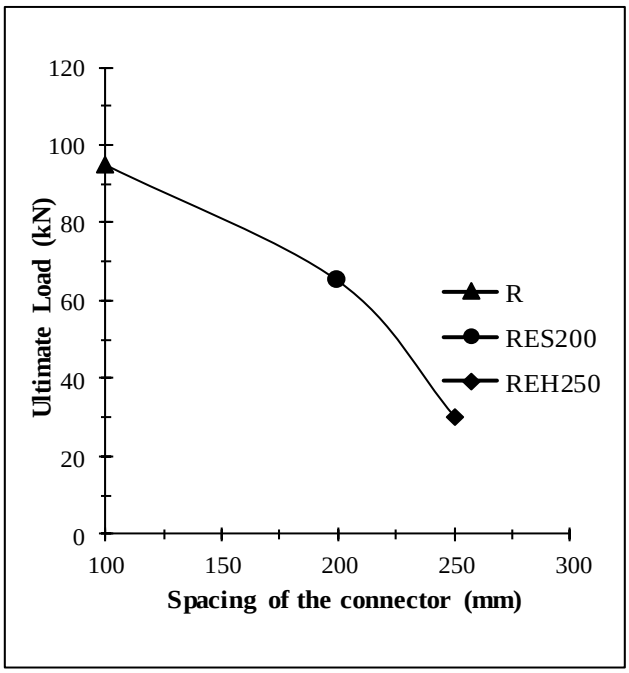

Figure 7. Ultimate load versus spacing of the connector.

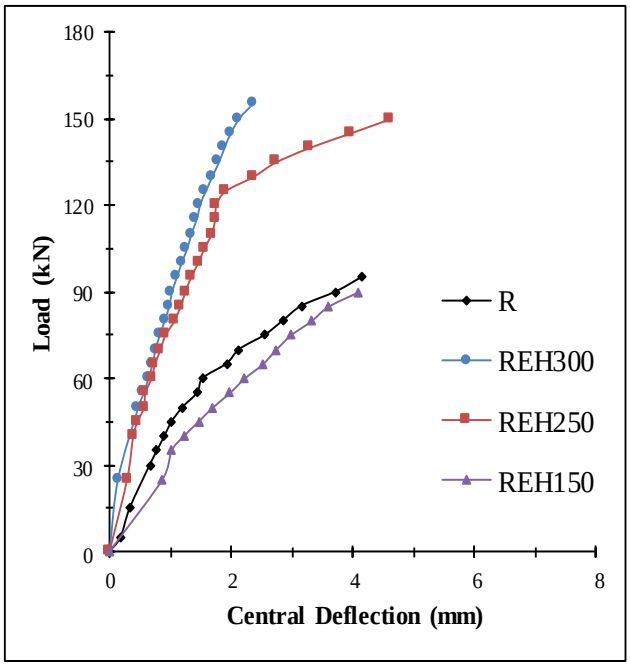

Figure 8. Load-deflection response of specimens with different beam thickness.

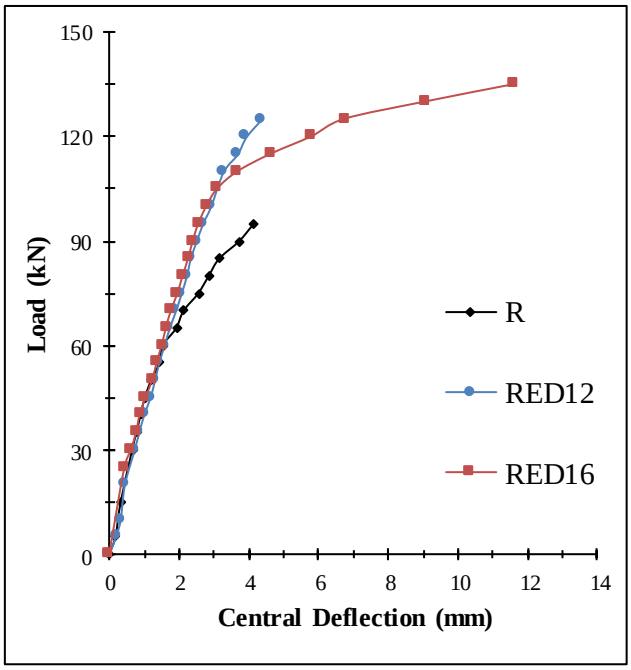

Figure 9. Load-deflection response of specimens with different connector diameter.

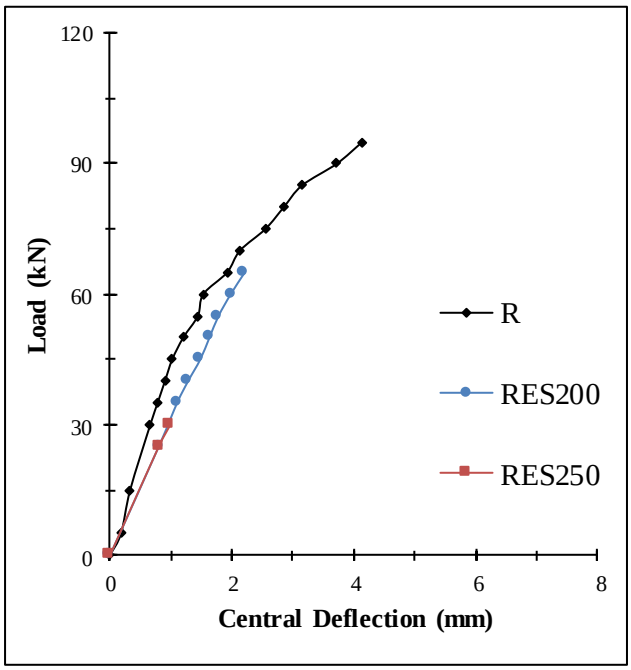

Figure 10. Load-deflection response of specimens with different connector spacing.

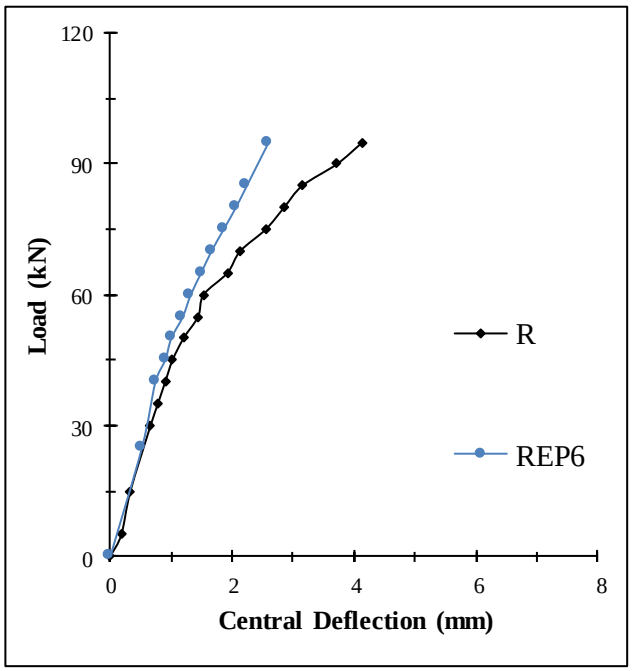

Figure 11. Load-deflection response of specimens with different tensile steel plate thickness.

The Use of the Artificial Damped Outrigger Systems in Tall R.C Buildings Under Seismic Loading

Dr. Abbas Abd Elmajeed Allawi
Assistant Professor
College of Engineering - University of Baghdad
E-mail: abbasallawi2004@yahoo.com

Amneh Hamid Al Mukhtar
M. Sc. Student
College of Engineering - University of Baghdad
E-mail: amena1981eng@gmail.com

ABSTRACT

This paper studies the combination of fluid viscous dampers in the outrigger system to add supplementary damping into the structure, which purpose to remove the dependability of the structure to lower variable intrinsic damping. This optimizes the accuracy of the dynamic response and by providing higher level of damping, basically minimizes the wanted stiffness of the structure while at the same time optimizing the achievement.

The modal considered is a **36** storey square high rise reinforced concrete building. By constructing a discrete lumped mass model and using frequency-based response function, two systems of dampers, parallel and series systems are studied. The maximum lateral load at the top of the building is calculated, and this load will be applied at every floor of the building, giving a conservative solution. For dynamic study **Response Spectrum Analysis** was conducted and the behavior of the building was determined considering response parameters. **MATLAB** software, has been used in the dynamic analysis for three modes.

For all modes, it is observed that the parallel system of dampers result in lower amplitude of vibration and achieved more efficiently compared to the damper is in series, until the parallel system arrives **100%** damping for mode three.

Key words: outrigger system, fluid viscous damper, discrete model.

استخدام أنظمة دعامة الإخماد الاصطناعي في المباني الخرسانية المسلحة العالية تحت تأثير الأحمال الزلزالية

د. عباس عبد المجيد علاوي
استاذ مساعد
كلية الهندسة-جامعة بغداد

آمنة حامد المختار
طالبة ماجستير
كلية الهندسة-جامعة بغداد

الخلاصة

تمت دراسة عملية دمج مخمدات السائل اللزج في نظام الدعامة لإضافة إخماد تكميلي للمنشأ ، والذي يهدف إلى إزالة اعتماد المنشأ على القيمة المنخفضة للإخماد الجوهري. هذا يحسن من دقة الاستجابة الديناميكية ومن خلال توفير مستوى أعلى من التخميد، بشكل أساسي يتم تقليل الصلابة المطلوبة للمنشأ في الوقت نفسه يتم تحسن الأداء.

النموذج الذي اخذ بنظر الاعتبار لهذه الدراسة هو 36 طابق مربع المقطع للمباني الخرسانية المسلحة الشاهقة. من خلال انشاء نموذج من كتل متجمعة منفصلة, واستعمال دالة الاستجابة المعتمدة على التردد, لنظامين من المخمدات، وهما نظاما التوازي والتوالي ويتم دراستها. يتم احتساب الحد الأقصى للحمل الجانبي في الجزء العلوي من المبنى، وسيتم تطبيق هذا الحمل في كل طابق من المبنى، معطيا حلا محافظا. للحالة الديناميكية يتم استعمال طريقة استجابة تحليل الطيف ويتم تحديد سلوك المبنى بالاخذ بنظر الاعتبار لمتغيرات الاستجابة. برنامج MATLAB, استعمل في التحليل الديناميكي لثلاثة انماط.

لكل الانماط، لوحظ أن المخمد السائل اللزج بوضعية التوازي ينتج ذبذبات ذات قيم اقل ويحقق كفاءة أكثر مقارنة عندما المخمد بوضعية التوالي. حتى يصل لنظام التوازي الى الاخماد بنسبة 100٪ للنمط الثالث.

الكلمات الرئيسية: نظام الدعامة, مخمد السائل اللزج, نموذج منفصل.

1. INTRODUCTION

Outrigger are a common system of strengthening and stiffening tall buildings. They work by connecting the central core, comprising either braced frames or shear walls, to the outer perimeter columns. The explication of building outrigger behavior is easy because outriggers represent as firm arms engaging external columns, at the point when a core have a tries to incline, its rotation at the outrigger level generates a tension- compression couple in the external column moving contrary to that movement. As the outcome, the outrigger restrict the bending of the core by introducing a point of inflection in the deflection profile, as shown in **Fig.1**. Thus decreasing the lateral motion at the top when the reversal in curvature**, Nanduri, et al., 2013** and **Melek, et al., 2012.**

Besides at the outrigger intersection lowering the core moment, the system equals the differential shortening of exterior columns coming from axial load imponderables and temperature. Another influence of using outriggers is the considerable lowering of net tension and uplift force at the foundation level**, Choi, et al., 2012.**

The damped outrigger system works by the insertion of viscous dampers between the external columns and the outriggers. When it done, there was a considerable rise in damping**, Willford,** and **Simith, 2008.** Therefore, the outrigger system is used as one of the structural system to control the excessive drift during lateral load due to earthquake load.

2. STRUCTURAL DESCRIPTION AND MODELING

2.1 Structural Parameters

The modal considered for this study is 36 stories square high rise reinforced concrete building with a base dimension of 30 m by 30 m will be analyzed. The floor to floor height is 4 m contributing to a total building height of 144 m. The building will have a 14 m by 14 m central concrete core with a thickness of 45 cm. The building will have two outrigger arms cantilevering from the core to the perimeter columns from each of the side of the core. W14**X**398 sections with an approximate cross-section area of 0.15 m^2 will be utilized as the perimeter columns**, Gamaliel, 2008** and **Smith** and **Willford, 2007.**

The gravity system used in conjunction with central concrete core consists of 25 cm thick reinforced concrete slabs, with beams section of 45 cm **X** 70 cm, and square reinforced concrete columns (45 cm **X** 45 cm). Fig. 2 summarizes the building dimensions described.

2.2 Structural Model

To create a realistic modal of the proposed building described in section 2.1, each floor of the building will be modeled as a series of masses lumped at the center of the core. Each mass will have three degrees of freedom and the vertical translation degree of freedom has been neglected to simplify the modal, as shown in **Fig. 3**.

The general discrete equation of motion written in matrix form as

$$\boldsymbol{M\,\ddot{U} + C\,\dot{U} + K\,U = P} \tag{1}$$

To obtain the global stiffness matrix, the direct stiffness approach is used. A standard two-node member element with two degrees of freedom for each node is considered in this study. The element stiffness matrix are given by

$$\boldsymbol{k(n)_{AA}} = \begin{bmatrix} \left(\frac{AE}{L}\,(\sin a)^2 + \frac{12EI}{L^3}\,(\cos a)^2\right) & \frac{6EI}{L^2}\cos a \\ \frac{6EI}{L^2}\cos a & \frac{4EI}{L} \end{bmatrix} \tag{2}$$

$$\boldsymbol{k(n)_{AB}} = \begin{bmatrix} \left(-\frac{AE}{L}(\sin a)^2 + \frac{12EI}{L^3}(\cos a)^2\right) & \frac{6EI}{L^2}\cos a \\ -\frac{6EI}{L^2}\cos a & \frac{2EI}{L} \end{bmatrix} \tag{3}$$

$$\boldsymbol{k(n)_{BA}} = \begin{bmatrix} \left(-\frac{AE}{L}(\sin a)^2 + \frac{12EI}{L^3}(\cos a)^2\right) & -\frac{6EI}{L^2}\cos a \\ \frac{6EI}{L^2}\cos a & \frac{2EI}{L} \end{bmatrix} \tag{4}$$

$$\boldsymbol{k(n)_{BB}} = \begin{bmatrix} \left(\frac{AE}{L}(\sin a)^2 + \frac{12EI}{L^3}(\cos a)^2\right) & -\frac{6EI}{L^2}\cos a \\ -\frac{6EI}{L^2}\cos a & \frac{4EI}{L} \end{bmatrix} \tag{5}$$

Where, A = area of the lumped mass = 53.19 m^2, E = elastic modulus of the core, I = moment of inertia of the lumped mass with respect to the bending axis $= 3184.406\ m^4$, L = floor height = 4 m, a = angle of reference with respect to the global coordinate = 0, b = core length = 14 m, and t = core thickness = 0.45 m.

The mass matrix $\boldsymbol{M}$ is a diagonal matrix containing the floor mass as well as the rotational inertia of the following form

$$\boldsymbol{M} = \begin{bmatrix} \boldsymbol{M_1} & & & \boldsymbol{0} \\ & \boldsymbol{J_1} & & \\ & & \ddots & \\ & & & \boldsymbol{M_{36}} \\ \boldsymbol{0} & & & \boldsymbol{J_{36}} \end{bmatrix} \tag{6}$$

Since the floor layout is the same throughout the building height, $M_1 = M_2 = \cdots = M_{36} = M$. Similarly, the rotational inertia entries are equal throughout the height, thus $J_1 = J_2 = \cdots = J_{36} = J$. Rotational inertia is assumed to be provided by the concrete core system only, and the gravity system have negligible effect on rotation because it is not rigidly attached to the core**, Gamaliel, 2008**.

Where, M = nodal mass = gravity system mass (m_f) + core mass (m_c) = 1,100,093 Kg;
J= nodal rotational inertia = 7,895,042.64 Kg m^2.

The intrinsic damping in a high-rise building is a key design parameter. Although the effect of damping is less important for seismic response than for wind response, the values assigned to structural damping should be selected with care. The intrinsic damping ratio of between 1% and 2% appears reasonable for buildings more than 50 m and less than 250 m in height, **Willford, et al., 2008**. While some studies using the intrinsic damping ratio of **2.5%** for **50** stories high rise reinforced concrete building**, Melek, et al., 2012.**

2.3 The Damped Outrigger Concept

The concept of the damped outrigger is shown in **Figs. 4,5, and 6**. **Fig. 4** appears how the outrigger systems activate in easy conditions while incorporated inside a usual core-to-perimeter columns outrigger systems. As a structure subjects dynamic sway motion, there is proportional vertical motion between the ends of stiff outrigger element that cantilevering from the core and the perimeter column. There are needful for the outriggers to shift vertically proportional to the floor at these levels, while the floors bend in double curvature to stay attached to the outer columns and the central core. The dampers are incorporated across this building discontinuity, dissipating energy through the cyclic motion, and producing the raise in the total damping for the structure. **Fig. 5** shows in terms of a conceptually the form of detail commonly wanted at the level where the damper is incorporated. The arranging can be as shown in **Fig. 6** at the outriggers level in this situation, **Smith** and **Willford, 2007**.

2.4 The Damped Outrigger Model

While the concept given by **Willford** and **Smith** implies that the perimeter columns is in series configuration with the dampers. Parallel configuration of columns and dampers studied by **Gamaliel, 2008** provided a good comparative study, as shown in **Fig. 7.**

The approach to drive typical damper characteristic is based on macroscopic point of view. Where in this point of view, the stiffness is defined based on the slope of the diagonal line of the hysteresis loop and the damping is derived from the hysteresis loop of tested damper**, Al Mallah, 2011**. Then, the equivalent complex stiffness for both parallel and series configuration were obtain.

2.4.1 **Hysteresis loop and characteristics of tested damper**

Considering a simple single degree of freedom (**SDF**) system with a viscous damper is subjected to a harmonic load, under steady- state response, the damping force equals to:

$$\boldsymbol{P(t) = C_o \frac{du}{dt} = C_o\, \omega\, u_o\, cos(\omega t - \delta) = C_o\, \omega \sqrt{u_o^2 - u_o^2\, sin^2(\omega t - \delta)}}$$

$$\boldsymbol{= C_o\, \omega \sqrt{u_o^2 - [u(t)]^2}} \qquad (7)$$

$$\boldsymbol{\left(\frac{u}{u_o}\right)^2 + \left(\frac{P(t)}{C_o\, \omega\, u_o}\right)^2 = 1} \qquad (8)$$

Which is the equation of the ellipse shown in **Fig. 8.** The area enclosed by the ellipse is $\boldsymbol{\pi\,(u_o)(C_o\, \omega\, u_o) = \pi\, C_o\, \omega\, u_o^2}$, which is equal to the dissipated energy

$$\boldsymbol{E_D = 2\pi\, \zeta\, \frac{\omega}{\omega_n}\, K\, u_o^2} \qquad (9)$$

Due to harmonic force with $\omega = \omega_n$, and based on macroscopic point of view, the loose stiffness, K_2 is defined based on the slope of the diagonal line of the hysteresis loop. The damping coefficient, C_o, is equal to the loose stiffness divided by ω, and is also calculated from above as:

$$\boldsymbol{C_o = \frac{E_D}{\pi \omega\, u_o^2}} \qquad (10)$$

The equivalent damping ratio $\boldsymbol{\zeta_{eq}}$ calculated from a test at $\boldsymbol{\omega = \omega_n}$ would not be right at any exciting frequency, but it would be a satisfying approximation.

$$\boldsymbol{\zeta_{eq}} = \frac{\mathbf{1}}{\mathbf{4\pi}} \frac{\boldsymbol{E_D}}{\boldsymbol{E_{SO}}} \tag{11}$$

Where the strain energy, $E_{SO} = K\, u_o^2\, /2$ *is calculated from the stiffness K resolved by experience,* **Chopra, 2008**. Based on the above, C_o and ζ_{eq} can be calculated from hysteresis loop of the tested dampers.

The model considered for this study is based on the material behavior in linear elastic range. However, it must be mentioned that most dampers classified as viscous dampers do not behave fully linear over the range of the entire velocity. This due to nonlinear material behavior and sealing friction which ends up in a nonlinear viscous behavior at low velocities.

2.4.2 Derivation of equivalent complex stiffness

Damping introduces complexity to the solution by adding a term involving velocity. In order to define the complex frequency-response function, the steady-state motion of a **SDOF** system is applied for both parallel and series configuration, which the equivalent complex stiffness can be derived as:

- Parallel configuration, The harmonic motion at the forcing frequency, $\boldsymbol{\omega}$, can be expressed as

$$\boldsymbol{u(t) = H_u(\omega)\, e^{i\omega t}} \tag{12}$$

$$\boldsymbol{\dot{u}(t) = i\omega\, H_u(\omega)\, e^{i\omega t}} \tag{13}$$

The equation of motion for the parallel configuration of damper and column is

$$\boldsymbol{p(t) = k_{col}\, u(t) + C\, \dot{u}(t) = (k_{col} + i\omega C)\, H_u(\omega) = k_{eq}\, H_u(\omega)} \tag{14}$$

$$\boldsymbol{\therefore k_{eq} = k_{col} + i\omega C} \tag{15}$$

, Chopra, 2008 and **Gamaliel, 2008**, see **Fig**. **9**.

-Series configuration and the harmonic motion at the forcing frequency, $\boldsymbol{\omega}$, can be expressed as:-

$$\boldsymbol{u(t) = H_u(\omega)\, e^{i\omega t}\text{, and } u(t)_1 = H_{u1}(\omega)\, e^{i\omega t}} \tag{16}$$

$$\boldsymbol{\dot{u}(t) = H_u(\omega)\, e^{i\omega t}\text{, and } \dot{u}(t)_1 = i\omega\, H_{u1}(\omega)\, e^{i\omega t}} \tag{17}$$

Then, the equation for the series configuration of damper and column is

$$\boldsymbol{p(t) = k_{col}\, u(t)_1 = C\, (\dot{u}(t) - \dot{u}(t)_1)} \tag{18}$$

$$\boldsymbol{(i\omega C)\, H_u(\omega) = (k_{col} + i\omega C)\, H_{u1}(\omega)} \tag{19}$$

$$\boldsymbol{H_{u1}(\omega) = \frac{i\omega C}{k_{col} + i\omega C}\, H_u(\omega)} \tag{20}$$

$$\boldsymbol{p(t)} = \frac{\boldsymbol{k_{col}\, i\omega C}}{\boldsymbol{k_{col} + i\omega C}}\ \boldsymbol{H_u(\omega)} = \boldsymbol{k_{eq}\ H_u(\omega)} \tag{21}$$

$$\therefore\ \boldsymbol{k_{eq}} = \frac{\boldsymbol{k_{col}\, i\omega C}}{\boldsymbol{k_{col} + i\omega C}} \tag{22}$$

Chopra, 2008 and **Gamaliel, 2008**, see **Fig**. **10**. The above procedure has been derived by the equivalent complex stiffness for both parallel and series damper configuration. The next step is to obtain the rotational stiffness at the outrigger level.

2.4.3 Derivation of the rotational stiffness

The column-restrained outriggers oppose the rotation of the core, when subjected to lateral loads, causing the moments and the lateral deflections in the core to be minimal than if the freestanding core alone resisted the loading. The exterior moment is now resisted not by bending of the core alone, but also by the axial compression and tension of the exterior column connected to the outrigger**, Taranath, 2010**.

The axial shortening and elongation of column is clearly equal to the rotation of the core multiplied by their particular distances from the exterior column to the center of the core. If the distance of the equivalent columns is d/2 from the central core, the axial distortion of the columns is then equal to βd/2, where β is the core rotation. Then the stiffness of the equivalent spring is studied for unit rotation of the core (i.e., β = 1), therefore the axial deformation of the equivalent columns is equalize to 1 × d/2 = d/2 units, **Taranath, 2010**. The next step was the derivation of the rotational stiffness.

The corresponding axial load is as following

$$\boldsymbol{p(t)\ = A\ E\ d/2\ (aH)} \tag{23}$$

$p(t)$ is the column axial load; A is the column area; E is the modulus of elasticity; d is the distance from the center of core to the exterior column; aH is the height at the outrigger level, see **Fig. 11**. Using the notion K_R for the rotational stiffness, and noticing that there are two equivalent columns, each situated at a distance from the core, we obtain

$$\boldsymbol{K_R = p(t)\ \times\ d/2\ \times 2} \tag{24}$$

$$\boldsymbol{K_R} = \frac{\boldsymbol{A\ E\ d^2}}{\boldsymbol{2\ aH}} \tag{25}$$

The addition of rotational stiffness to the core at the outrigger level can be obtained as follows

$$\boldsymbol{M = p(t)\ \times\ d/2} \tag{26}$$

Where, $\boldsymbol{p(t) = k_{eq}\ H_u(\omega)}$, $\boldsymbol{H_u(\omega) = \frac{d}{2}\ \beta}$ **,** and $\boldsymbol{M = K_R\ \beta}$

$$\therefore\ \boldsymbol{K_R = k_{eq}\ \left(\frac{d}{2}\right)^2} \tag{27}$$

2.5 Applying Outrigger Effect to Discrete Model

The effect of the outrigger can be modeled by introducing a minor change in the stiffness matrix. A rotational spring is to be added to the nodal point where the outrigger is located. Hence, the outrigger nodal point will have a modified rotational stiffness comprised of the existing rotational stiffness from the core (cantilever beam) and the rotational stiffness, K_R, from the outrigger. From previous section, the value of K_R has been derived. Because the Damping introduces complexity to the solution by adding a term involving velocity, the equivalent complex stiffness has been derived for both parallel and series damper configuration, and has been incorporated this effect into the stiffness matrix of the core**, Gamaliel, 2008** and **Taranath, 2010**.

In the case of a damped outrigger, the damping matrix, $\boldsymbol{C}$, is required to solve the full differential equation of motion. The conventional approach is to work in the real domain by constructing the damping matrix and introducing the damping coefficient $\boldsymbol{C_o}$ at the location corresponding to the rotation of the outrigger node. However, it is algebraically more convenient to work in the complex domain, by collapsing the $\boldsymbol{C}$ matrix altogether and lumping the effect of damping into the stiffness matrix, forming an equivalent complex stiffness matrix**, Gamaliel, 2008**, which had been obtained in section 2.4.1.

3. DYNAMIC ANALYSIS

3.1 Modal Analysis

In order to analyze the dynamic response of the structure due to seismic effect, the first step of the procedure is to perform Eigen-value analysis of the building with an offered elastic stiffness and mass in order that coincide its modal characteristics. The characteristics of special importance are the natural period of vibration of the buildings and modal shapes. Consequently, the Eigen-value problem can be solved from the relationship

$$\boldsymbol{k\,\phi = \omega^2\, M\,\phi} \tag{28}$$

Where ϕ, the eigenvectors, represent the mode shape and the Eigen-values correspond to ω^2; M, the mass matrix(see Sec. 2.2); k, the element stiffness matrix(see Sec. 2.2) plus the rotational stiffness, K_R which has been derived in Sec. 2.4.3. The modal period of vibration of the building can then be obtained by the following equation

$$\boldsymbol{T = \frac{2\pi}{\omega}} \tag{29}$$

Using **MATLAB** software for each series and parallel configuration, the frequencies, natural periods, and mode shapes of the first three modes will be obtained. For modal analysis the frequency and damper coefficient are set to zero, therefore the equivalent complex stiffness for parallel configuration equal to k_{col}(see Eq. 15) and for series configuration close to zero(see Eq. 22). **Table 1** summarizes the frequency and natural periods of the first three modes for series and parallel configuration, and **Fig. 12** shows mode shapes of series and parallel systems. The fundamental period for series and parallel configurations equal to 2.246 and 2.202, respectively.

3.2 Modal Response Spectrum Analysis

The ground motion risks that rely on the regional seismicity depending upon a list of basics. Then considered to be ingrained in building designed to **ASCE 7-05** the design ground motions are depend on the margin of a minimal bound evaluation versus collapse. Depend on

experiment this minimal bound has been believed in ground motion to be almost a factor of 1.5, **Taranath, 2005**. Subsequently, the design earthquake ground motion has been selected at a ground motion shaking level that is 1/1.5, which is equal to the 2/3 of the MCE ground motion.

ASCE 7-05 explains the **MCE** ground motion at short periods, *Ss*, in terms of the mapped values of the spectral response acceleration and also at 1 second, *S*1, for site class *B* for soft rock. these values may be gained from the map developed by **USGS**. The maps developed by **USGS** define sites of fault using both the probabilistic and deterministic proceedings, and contours of random horizontal acceleration values**, Taranath, 2005.**

In this study, the parameters ***Ss*** and ***S*1** determine from the major map developed by **USGS**, in Irvine, California for site class D, using an importance factor, I_E , is equal to 1 for the Occupancy Category II, and the effective seismic weight, Wx at each node is equal to 12,000 KN.

For service-level estimates, the **response spectrum analyses** which uses modal analyses to obtain building response will generally be used for linear dynamic analysis**, Willford, et al., 2008.**

The effective masses are multiplied by the acceleration coefficient, CS_m, to afford individual modal base shears by the following equations

$$\boldsymbol{V_m = CS_m\ W_m} \tag{30}$$

$$\boldsymbol{W_m = \frac{\left(\sum_{i=1}^{n} W_i\ \ \phi_{im}\right)^2}{\sum_{i=1}^{n} W_i\ \ \phi_{im}{}^2}} \tag{31}$$

Where, CS_m, is the coefficient of the modal seismic design; W_m, is the loads of the effective modal gravity; W_i, the portion of the total gravity load of the structure at level i; ϕ_{im}, displacement amplitude while shaking at ith level.

The distributing the base shear for each mode up the height of the structure as a set of equivalent lateral forces (proportional to the mode shape and mass distribution), by the following equations

$$\boldsymbol{F_m = Cx_m\ V_m} \tag{32}$$

$$\boldsymbol{Cx_m = \frac{W_x\ \phi_{xm}}{\sum_{i=1}^{n} W_i\ \ \phi_{im}}} \tag{33}$$

Where, Cx_m, is the vertical distribution factor at the mth mode in the xth level.

The values of, V_m and F_m, for series and parallel configurations are shown in **Table 2**.

3.3 Dynamic Analysis Using Software Program

To get the response function of the structure to seismic dynamic excitation, a complex periodic loading function will be applied in which

$$\boldsymbol{P_t = p(t)\ \sin wt,} \text{ or } \boldsymbol{P_t = p(t)\ \cos wt} \tag{34}$$

The term $\boldsymbol{P_t}$ can therefore be expressed as

$$\boldsymbol{P_t = p(t)\ e^{i\omega t}} \tag{35}$$

In order to determine the amplitude of vibration, the general equation of motion as following

$$\boldsymbol{M\,\ddot{u}(t) + k_{eq}\,u(t) = p(t)\;\; e^{i\omega t}} \tag{36}$$

The resulting displacement is then the real or imaginary part of the complex displacement, which it mentioned in sec. 2.4.2, $u(t) = H_u(\omega)\, e^{i\omega t}$.
Taking the time derivative of equation, we obtain

$$\boldsymbol{\dot{u}(t) = H_u(\omega)\, e^{i\omega t}}, \text{ and } \boldsymbol{\ddot{u}(t) = -\,\omega^2\, H_u(\omega)\, e^{i\omega t}} \tag{37}$$

Substituting Eq. (37) into the differential Eq. (36**)**, we get

$$\boldsymbol{(k_{eq} - \omega^2 M) H_u(\omega) = p(t)} \tag{38}$$

For simplifying, the quantity $\boldsymbol{\widehat{k_{eq}}}$ is defined as following

$$\boldsymbol{\widehat{k_{eq}} = (k_{eq} - \omega^2 M)} \tag{39}$$

The matrix equation is run in **MATLAB** to be solved is

$$\boldsymbol{\widehat{k_{eq}}\;\; H_u(\omega) = p(t)} \tag{40}$$

Therefore, the displacement matrix is defined as following

$$\boldsymbol{H_u(\omega) = \widehat{u(t)} = \widehat{k_{eq}}^{\,-1}\;\; p(t)} \tag{41}$$

For analysis purpose, the maximum drift at the top is used $\widehat{u(t)}_{36}$. The value k_{eq} is a complex quantity due to contribution from damping, see **Sec. 2.4.2** for series and parallel configuration. Therefore the resulting displacement contains the real and imaginary parts. Taking the sum of the squares of the real and imaginary parts to obtained the amplitude value, then taking the square root as following

$$\boldsymbol{\left|\widehat{u(t)}_{36}\right| = \sqrt{(\widehat{u(t)}_{36})^2_{real} + (\widehat{u(t)}_{36})^2_{imaginary}}} \tag{42}$$

The range of $\boldsymbol{\omega}$ is set to be from 0-55 rad⁄sec to cover the first three modes. The maximum equivalent lateral forces, which calculated in **Sec. 3.2**, applied at nodes at each modes.

Response function for series and parallel configuration at different values of damping coefficient at fundamental mode are shown in **Fig. 13**, it is observed that the parallel system of dampers result in lower amplitude of vibration compared to when the damper is in series and with increase of damping coefficient the fundamental frequencies of the building was raised for parallel system. Also, **Figs. 14, 15,** and **16**, show Frequency-based response function for the second and third modes, it is observed that the parallel placement of viscous damper result in lower amplitude of vibration compared to when the damper is in series, and see **Figs. 17** and **18** at constant frequency and natural periods of the first and second modes for difference values of damper coefficient.

3.4 Half Power Bandwidth Method

The half power bandwidth method employs the transfer function plot to get the damping. The method consists of deciding the frequencies at which the amplitude of the transfer function is $\mathbf{A_2}$ where

$$A_2 = \frac{A_{max}}{\sqrt{2}} \tag{43}$$

Where A_{max}, is the amplitude at the peak. The frequencies ω_1 and ω_2 associated with the half power points are obtained on either side of the peak, as shown in **Fig. 19**. Then the damping ratio ξ is getting employs the formula

$$\xi = \frac{\omega_2 - \omega_1}{2\omega_n} \tag{44}$$

The damping ratio associated with each natural frequency can be obtained using the half power bandwidth method.

To investigate the relationship between the amount of damping, response function were generated with different values of damping coefficient, **C**, and the corresponding fraction of critical damping, ξ, is obtained by the half power bandwidth method in **MATLAB**.

The result of the relationship between the damping coefficient, **C**, and the critical damping, ξ, is shown in **Table 3**.

4. CONCLUSIONS

- The use of complex stiffness matrix in dynamic analysis leading to a more efficient solution scheme and lumping the effect of damping into the stiffness matrix, forming an equivalent complex stiffness matrix, and has been incorporated this effect into the stiffness matrix of the core.
- For Eigen-value analysis, for the fundamental mode, the frequencies between the two configurations show a very slightly difference between series and parallel systems. Therefore, this slightly difference not appears in the plot. The frequencies to the higher modes (second and third) in both systems are obviously close to each other.
- For Frequency-based response function for mode one, it is observed that the parallel system of dampers result in lower amplitude of vibration compared to when the damper is in series. For series system, the critical damping reaches its peak at around ***C*** = **300,000** ***(KN.s/m)***, and beyond this point the critical damping loses its effectiveness gradually. While the parallel system increase of critical damping with increase of damping coefficient, and raising the fundamental frequencies of the building and has caused an increase in stiffness of the system and a decrease in fundamental period and become more narrow band of frequency as shown in **Fig. 13**.
- For Frequency-based response function for mode two, it is observed that resonant response occur over a very narrow band of frequency, which is very difficult to excite these modes continuously. But from analysis data, the parallel placement of viscous damper result in lower amplitude of vibration compared to when the damper is in series as shown in **Figs. 14 and 15**.
- For Frequency-based response function for mode three, it is observed that the critical damping is equal to **1.00**, which is **100%** damping for parallel system at any value of damping coefficient as shown in **Fig. 16(b)**.
- Both series and parallel systems will allow the reduction of member sizes and material due to the reduction of dynamic stiffness required. Viscous dampers can be made highly reliable

and redundant, eliminating the need to provide space for devices such as the tuned mass dampers. Damping applies to all frequency range. The structure as well as economic benefits of damped outrigger systems.

- The result of analysis suggests that viscous dampers should be installed in parallel with the perimeter column where the outrigger connects. However, to achieve this type of parallel connection takes more of a construction challenge than connecting it in line with column as proposed by **Smith** and **Willford,2007**. Two columns side by side will be required to connect the damper in parallel.

REFERENCES

- Al Mallah, N. M., 2011, *The Use of Bracing Dampers in Steel Building Under Seismic Loading*, Ms. D. Thesis : College of Engineering, University of Baghdad.

- ASCE, 2006, *ASCE Standard 7-05:Minimum Design Loads for Buildings and Other Structures* , American Society of Civil Engineers.

- Choi, H., Ho, G., Joseph, L., Mathias, N., 2012, *Outrigger Design for High Rise Buildings*, Chicago,USA : CTBUH Technical Guides.

- Chopra, A., 2008, *Dynamics of Structures:Theory and Applications to Earthquake Engineering*, New Delhi : Prentice-Hall of India.

- Gamaliel, R., 2008, *Frequency- Based Response of Damped Outrigger System for Tall Buildings*, Civil and Environmental Engineering, University of California.

- Melek, M., Darama, H., Gogus, A., and Kang, T., 2012, *Effects of Modeling of RC Flat Slabs on Nonlinear Response of High Rise Building Systems*, 15 WCEE.

- Nanduri, R., Suresh, B., and Hussain, I., 2013, *Optimum Position of Outrigger System for High- Rise Reinforced Concrete Buildings Under Wind and Earthquake Loadings*, American Journal of Engineering Research,Vol. 2, pp. 76- 89.

- Sathyanarayanan, K., Vijay, A., and Balachandar, S., 2012, *Feasibility Studies on the Use of Outrigger System for RC Core Frames*, India : Department of Civil Engineering, SRM University.

- Smith, R. J., and Willford, M. R., 2007, *The Damped Outrigger Concept for Tall Building*, Arup, London, UK : John Wiley & Sons, Inc.

- Taranath, B., 2010, *Reinforced Concrete Design of Tall Buildings*, US : Taylor and Francis Group.

- Taranath, B. S., 2005, *Wind and Earthquake Resistant Buildings: Structural Analysis and Design*, California : Marcel Dekken.

- Willford, M., and Simith, R., 2008, *Performance Based Seismic and Wind Engineering for 60 Story Twin Towers in Manila*, Beijing, China : The 14th World Conference on Earthquake Engineering.

➢ Willford, M., Whittaker, A., and Klemencic, R., 2008, *Recommendations for the Seismic Design of High- Rise Buildings*, Chicago : Council on Tall Buildings and Urban Habitat.

NOMENCLATURE

A = area of the lumped mass, m^2.
A_2=area of control valves, m^2.
A_{max}= amplitude at the peak, m.
aH=height at the outrigger level, m.
b = core length, m.
C_0= damping coefficient, N.s/m,
CS_m=modal seismic design coefficient, dimensionless.
Cx_m=vertical distribution factor at the *x*th level in the *m*th mode, dimensionless.
E =elastic modulus of the core, Pa.
E_D = energy dissipation, N.m.
E_{SO}= strain energy, N.m.
F_m= equivalent lateral forces in the *m*th mode, KN.
$H_u(\omega)$ =complex frequency-response function, dimensionless.
I = moment of inertia of the lumped mass, m^4.
J= nodal rotational inertia, Kg m^2.
K= stiffness matrix, N/m.
K_2=loss stiffness, N/m.
K_R=rotational stiffness, N/m.
k_{col}=stiffness of column, N/m.
k_{eq}=equivalent complex stiffness, N/m.
L =floor height, m.
M=mass matrix, Kg.
P_t=complex periodic loading function, KN.
*S*1=mapped MCE, 5 percent damped, spectral response acceleration parameter at a period of 1, %g.
Ss=mapped MCE, 5 percent damped, spectral response acceleration parameter at short periods, %g.
t =core thickness, m.
u= displacement of the system and the damper, m.
$\dot{u}$=velocity of the piston, m/s.
u_o=amplitude of the displacement, m.
V_m=modal base shears, KN.
W_i=the portion of the total gravity load of the structure at level i, KN.
W_m=effective modal gravity load, KN.
Wx=effective seismic weight at each node, KN.
ω=frequency of motion, rad/s.
ω_n =vibration Natural Frequency, rad/s.
δ=phase angle, rad.
ζ =damping ratio, dimensionless.
ζ_{eq} =equivalent damping ratio, dimensionless.
β=rotation of the core, rad.
ϕ=eigenvectors represent the mode shape and the Eigen-values, dimensionless.

ϕ_{im}=displacement amplitude at the *i*th level of the structure when vibrating in its *m*th mode, m.

ϕ_{xm}=displacement amplitude at the *xth* level of the structure when vibrating in its *m*th mode, m.

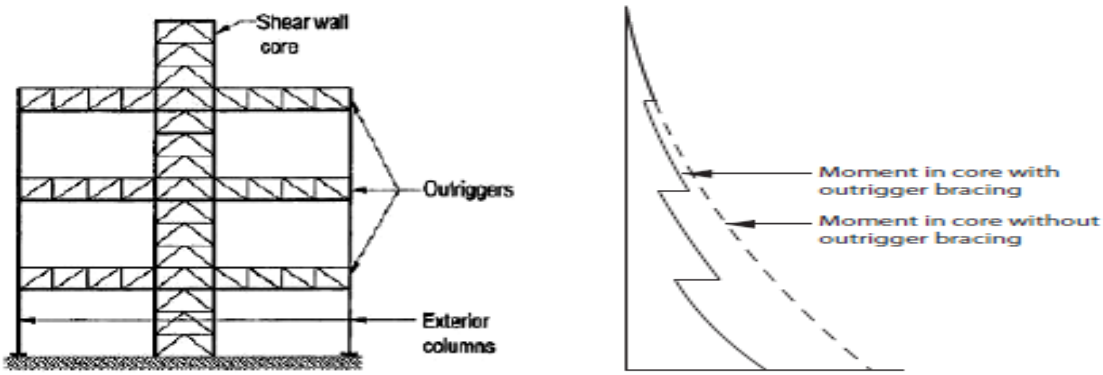

Figure 1. Core – Supported outrigger structures**, Sathyanarayanan, et al., 2012.**

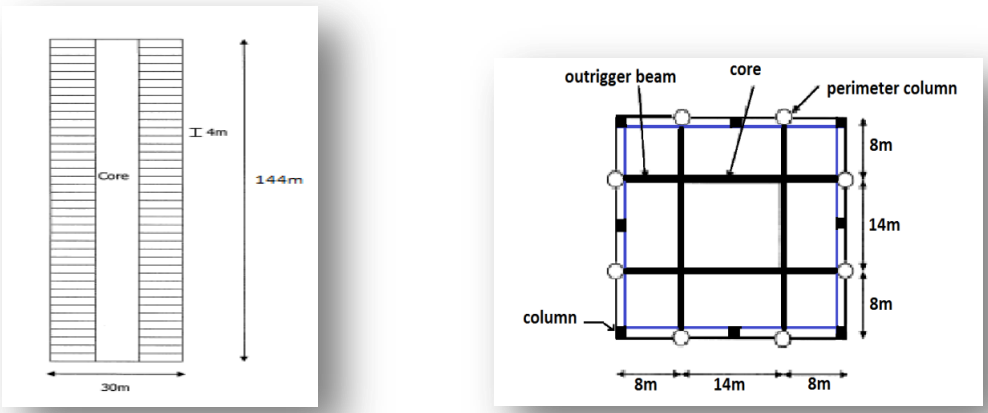

(a) **(b)**

Figure 2. Buildings dimensions (a) in elevation, (b) in plan (some details and beams for gravity system omitted for clarity).

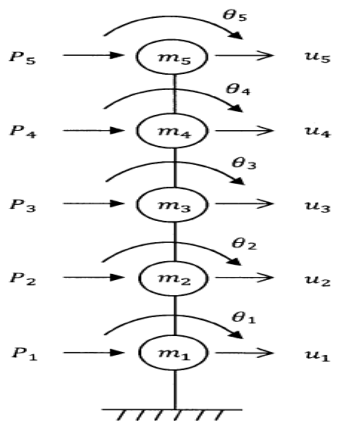

Figure 3. Discrete lumped mass modal for a 5- story building.

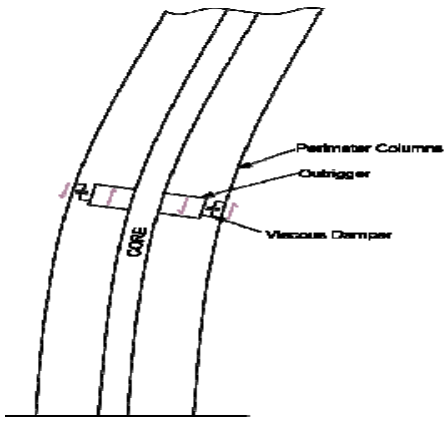

Figure 4. Patent pending (damped outrigger), **Smith, and Willford, 2007.**

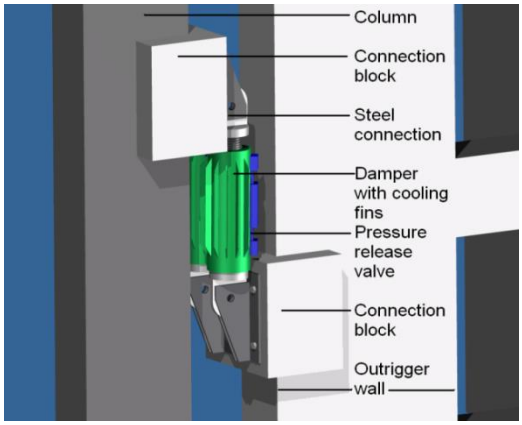

Figure 5. Conceptual detail at outrigger level, **Smith, and Willford, 2007.**

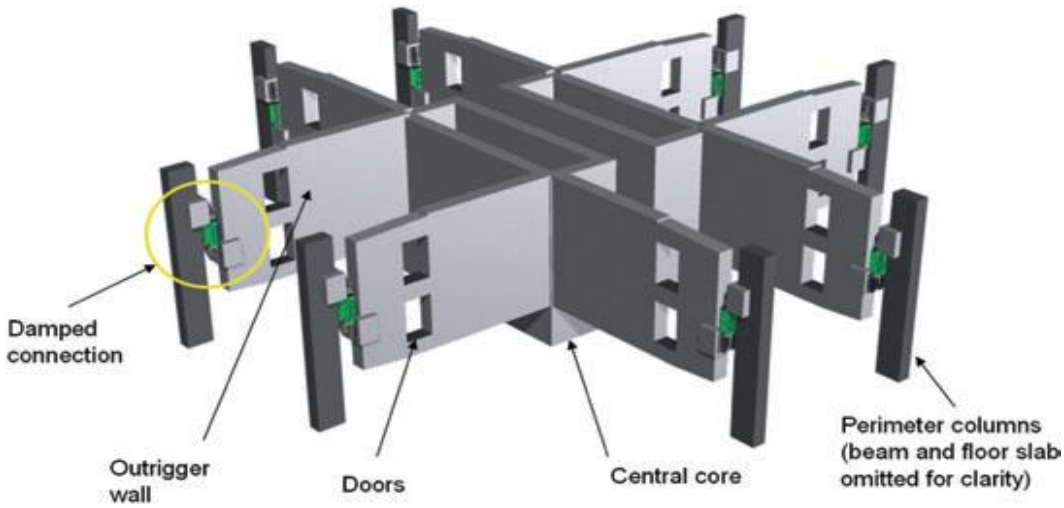

Figure 6. General arrangement of outrigger levels**, Smith and Willford, 2007.**

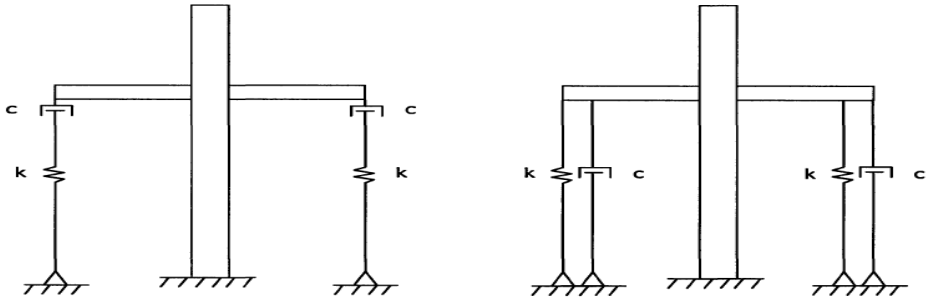

(a) **(b)**

Figure 7. Simplified models of the damped outrigger systems in (a) series (b) parallel**, Gamaliel, 2008.**

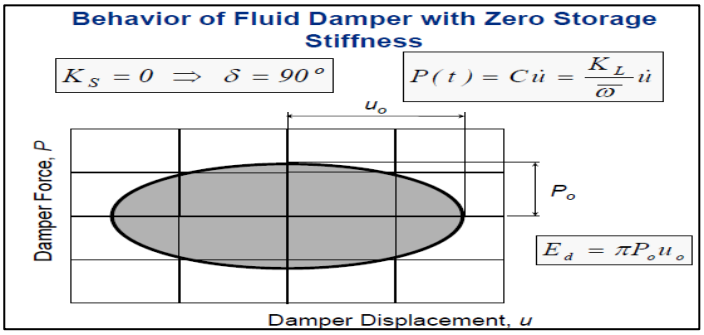

Figure 8. Hysteretic loop for viscous damper.

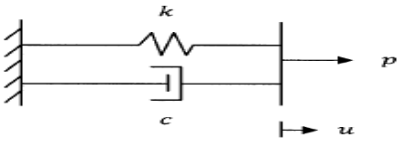

Figure 9. Damper in parallel.

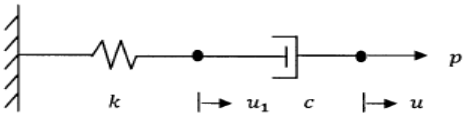

Figure 10. Damper in series.

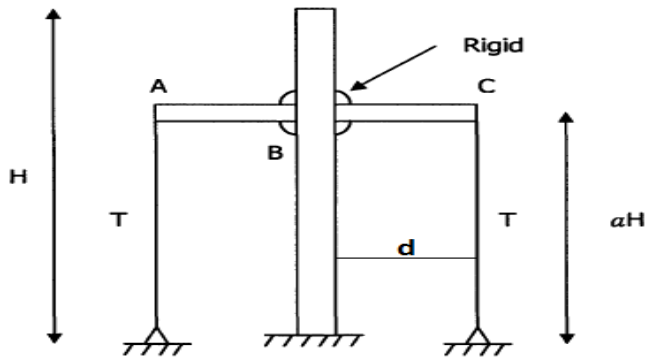

Figure 11. Simplified single outrigger model.

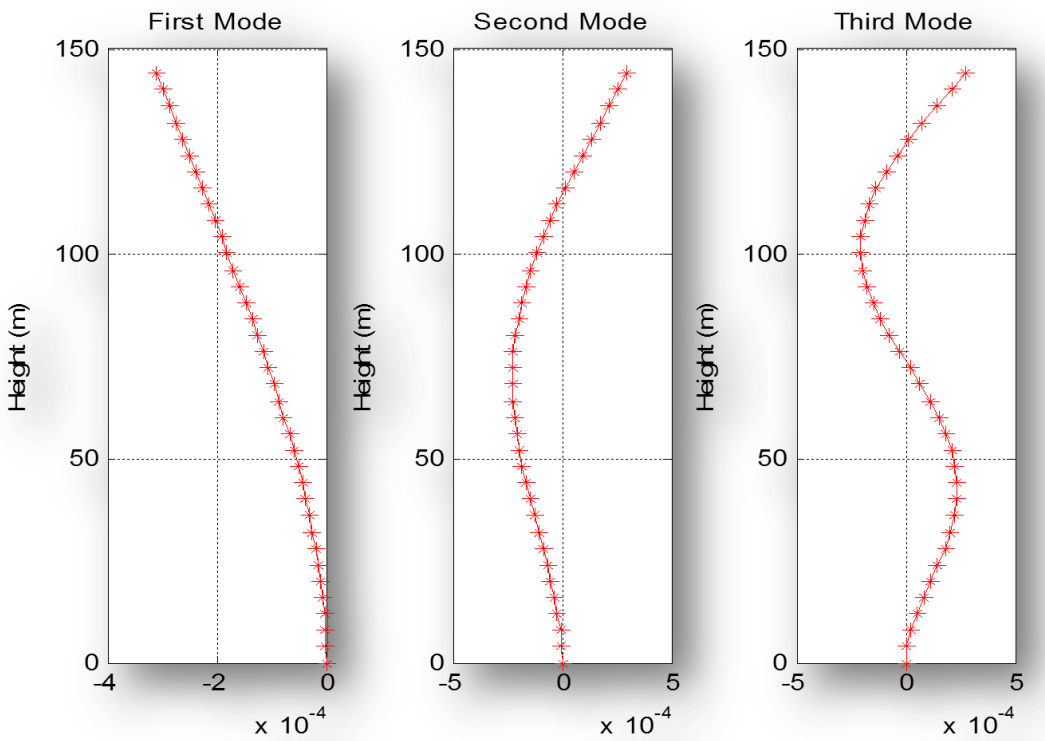

Figure 12. Mode shapes of first three modes for series and parallel system.

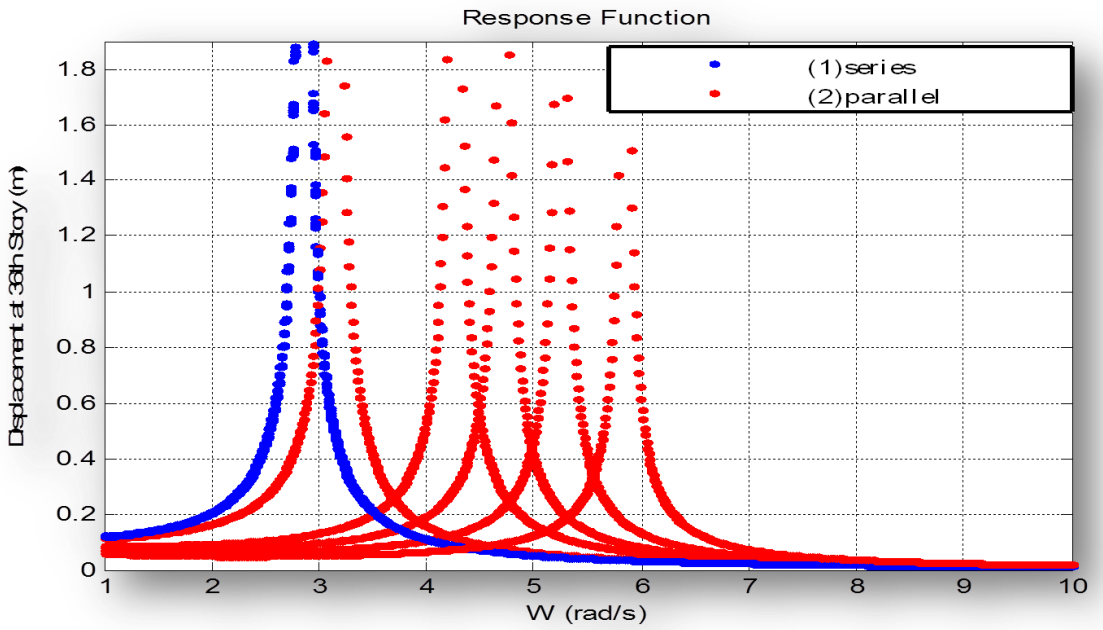

Figure 13. Response function at fundamental mode with different values of damping coefficient, C= 50; 100; 150; 200; 300($MN.S/m$), (horizontal displacement at 36th story **vs** w (rad/seconds)).

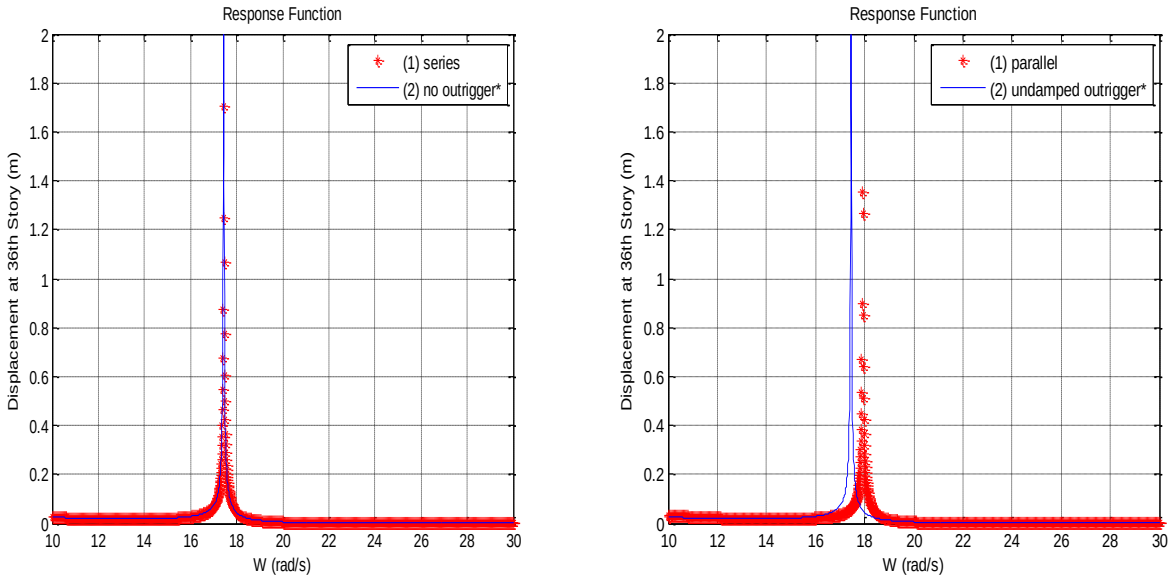

(a)series system (b)parallel system

Figure 14. Frequency-based response function for mode two at C = 100,000 $(KN.S/m)$ (horizontal displacement at 36th story **vs** w (rad⁄seconds)).

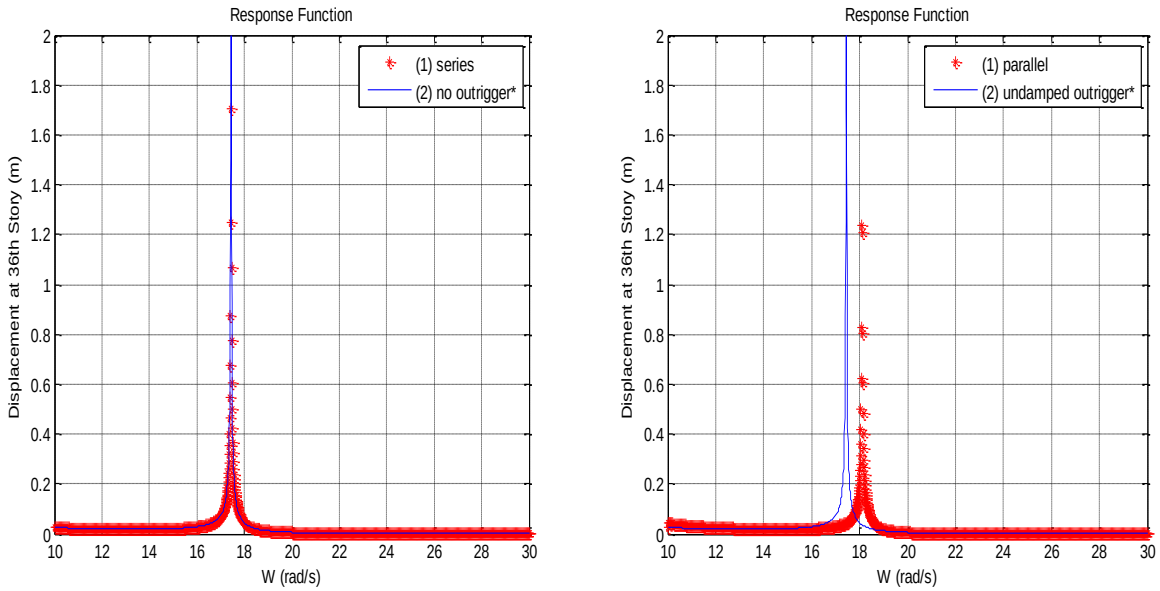

(a)series system (b)parallel system

Figure 15. Frequency-based response function for mode two at C = 200,000 $(KN.S/m)$ (horizontal displacement at 36th story **vs** w (rad⁄seconds)).

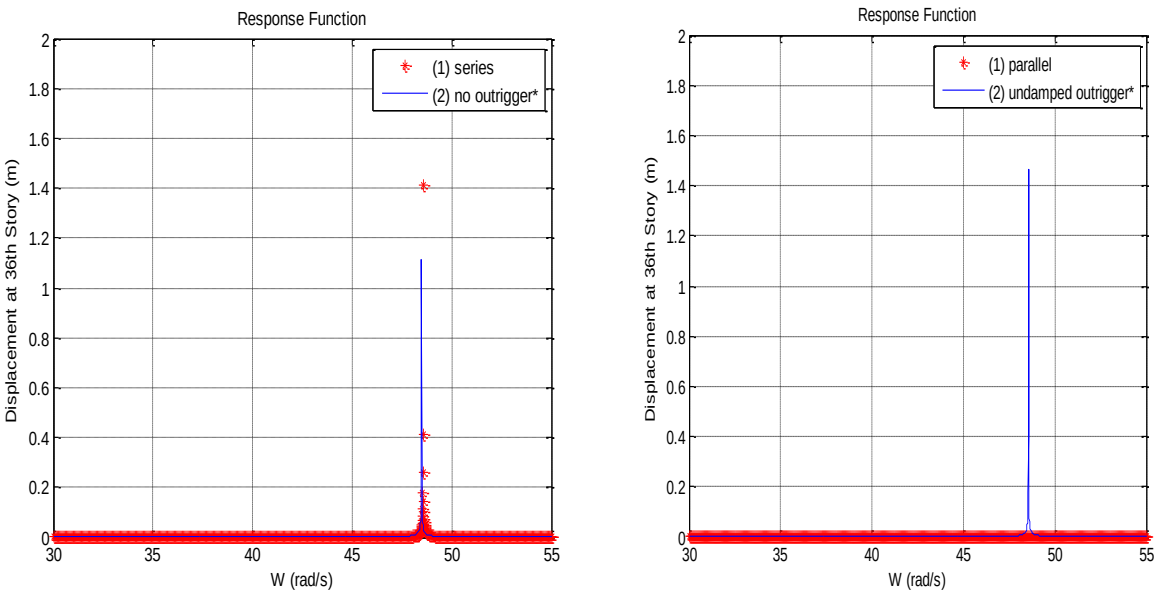

(a)series system (b)parallel system

Figure 16. Frequency-based response function for mode three at C = 100,000 ($KN.S/m$) (horizontal displacement at 36th story **vs** w (rad⁄seconds)).

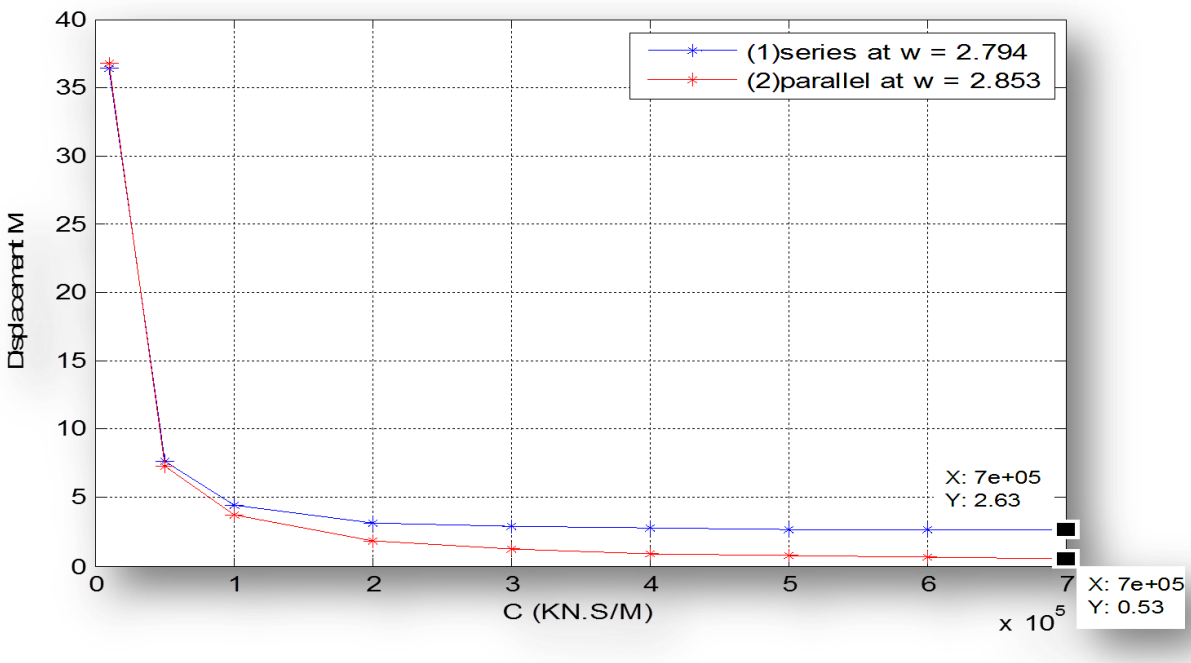

Figure 17. Plot damping coefficient vs displacement at mode one.

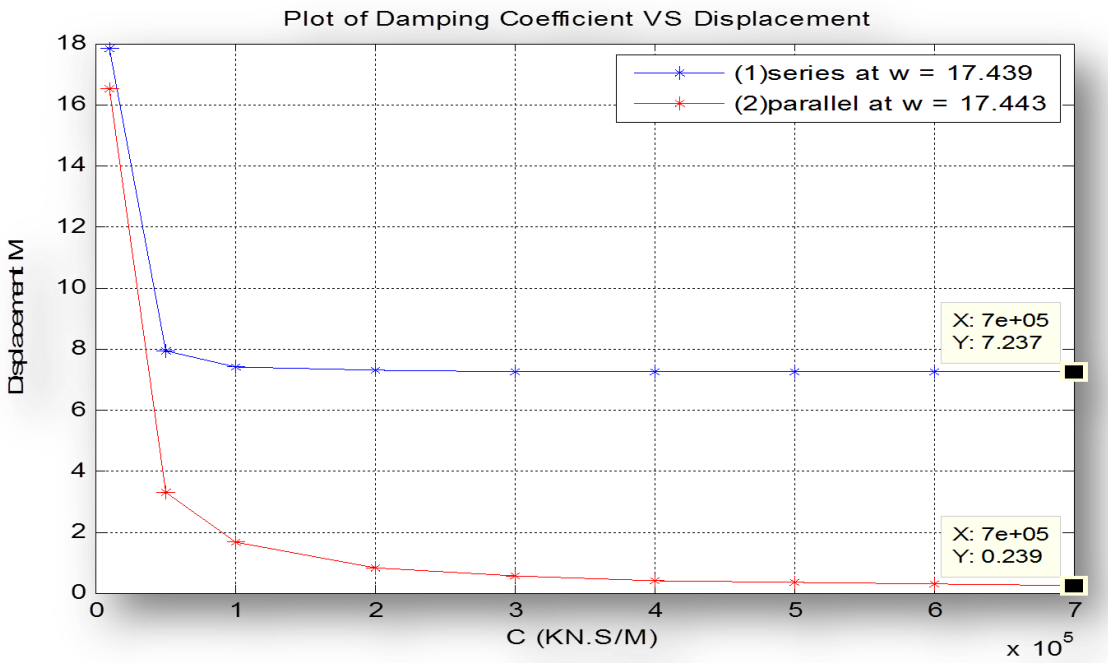

Figure 18. Plot damping coefficient vs displacement at mode two.

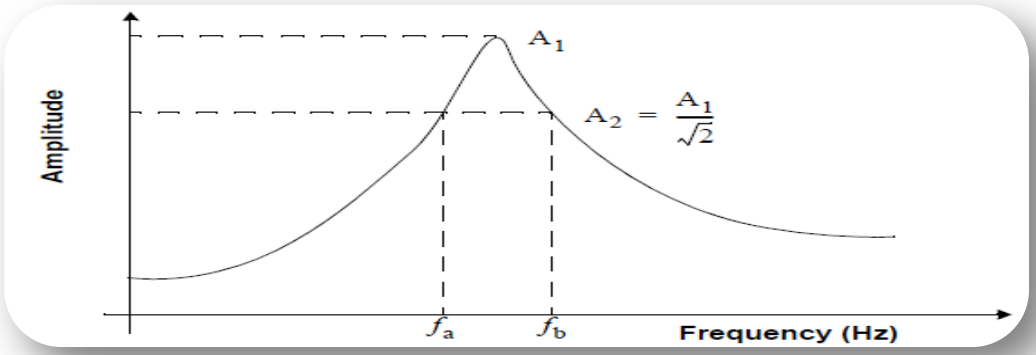

Figure 19. Half power bandwidth method.

Table 1. Frequency and natural periods for series and parallel configuration.

	Mode No.	Frequency (rad / sec)	Period (seconds)
Series configuration	1	**2.794**	**2.246**
	2	**17.439**	**0.3603**
	3	**48.487**	**0.1296**
Parallel configuration	1	**2.853**	**2.2023**
	2	**17.443**	**0.3602**
	3	**48.557**	**0.1294**

Table 2. Modal base shears and equivalent lateral forces for series and parallel configuration.

Mode No.	T_m (seconds)	Sa_m spectral acceleration	CS_m modal coefficient	V_m (*KN*)	Cx_m distribution factor	F_m (*KN*)
1*	2.248	0.2322	0.033	8907	0.0687	611.666
2*	0.3603	0.9840	0.141	11686	0.1175	1373.200
3*	0.1296	0.9840	0.141	4048	0.1903	770.316
1**	2.2023	0.2370	0.034	9104	0.0686	624.735
2**	0.3602	0.9840	0.141	11650	0.1178	1372.700
3**	0.1294	0.9840	0.141	4042	0.1903	768.945

* series configuration

** parallel configuration

Table 3. For mode one (relationship between the C and ξ).

C (KN.s/m)	ξ		% damping	
	series	parallel	series	parallel
10,000	**0.037**	**0.032**	**3.7**	**3.2**
50,000	**0.041**	**0.036**	**4.1**	**3.6**
100,000	**0.044**	**0.042**	**4.4**	**4.2**
150,000	**0.046**	**0.049**	**4.6**	**4.9**
200,000	**0.051**	**0.058**	**5.1**	**5.8**
300,000	**0.054**	**0.066**	**5.4**	**6.6**
400,000	**0.052**	**0.085**	**5.2**	**8.5**
500,000	**0.047**	**0.123**	**4.7**	**12.3**

Separation of Lead (Pb^{2+}) and Cadmium (Cd^{2+}) from Single and Binary Salt Aqueous Solutions Using Nanofiltration Membranes

Ahmed Abed Mohammed
Assistant Professor
College of Engineering, University of Baghdad
email: Ahmed.abedm@yahoo.com

Qusay Fadhil Alsalhy
Professor
Chemical Engineering, University of Technology
email: qusay_alsalhy@yahoo.com

Salwa Hadi Ahmed
Instructor
College of Engineering, University of Baghdad
email: env.salwa99@gmail.com

ABSTRACT

The present work reports on the performance of three types of nanofiltration membranes in the removal of highly polluting and toxic lead (Pb^{2+}) and cadmium (Cd^{2+}) from single and binary salt aqueous solutions simulating real wastewaters. The effect of the operating variables (pH (5.5-6.5), types of NF membrane and initial ions concentration (10-250 ppm)) on the separation process and water flux was investigated. It was observed that the rejection efficiency increased with increasing pH of solution and decreasing the initial metal ions concentrations. While the flux decreased with increasing pH of solution and increasing initial metal ions concentrations. The maximum rejection of lead and cadmium ions in single salt solution was 99%, 97.5 % and 98 % at pH 6, 6.5 and 6.2 and 78%, 49.2% and 44% at pH 6.5, 6.2 and 6.5 for NF1, NF2 and NF3 respectively. On the other hand, maximum permeate flux for single NF2 (32.2)> NF3 (16.1)>NF1 (14.2) ($l/m^2.h$) for 100 ppm, higher than binary salt solution was NF2 (23.7) > NF3 (13) > NF1 (8) ($l/m^2.h$) for (10 Pb^{2+}/50 Cd^{2+}) ppm. The NF membranes proved able to achieve high separation efficiency of both lead and cadmium ions in very suitable conditions, leaving wastewaters in a condition suitable prior discharged into the environment.

Keywords: Hollow fiber membrane; Nanofiltration; Wastewater; Heavy metals

فصل ايونات الرصاص والكادميوم من المحاليل الملحية المفردة والثنائية باستخدام الاغشية النانوية

سلوى هادي احمد
مدرس
كلية الهندسة- جامعة بغداد

قصي الصالحي
استاذ
قسم الهندسة الكيمياوية- الجامعة التكنولوجية

احمد عبد محمد
استاذ مساعد
كلية الهندسة- جامعة بغداد

الخلاصة

تقدم الدراسة الحالية إداء ثلاث انواع من الاغشية النانوية في ازالة ايونات الرصاص والكادميوم العالية التلوث والسمية من المحاليل الملحية المفردة والثنائية المماثلة لمياه الفضلات الحقيقية. تحديد تاثير المتغيرات التشغيلية (- 6.5) pH (5.5, نوع الغشاء النانوي وتركيز الايون الابتدائي (10-250) جزء بالمليون) على عملية الفصل وتدفق الماء. لاحظ زيادة الرفض مع زيادة pH المحلول ونقصان التركيز الابتدائي للايون. بينما يتناقص الجريان مع زيادة pH وزيادة التركيز الابتدائي للايون. اعلى رفض للرصاص والكادميوم في المحلول المنفرد كان 99% ,97.5 ,98 عند pH 6.2, 6.5, 6 و78% ,49.2 ,44 عند pH 6.5, 6.2, 6.5 للاغشية NF1, NF2,NF3 على التوالي. من جهة اخرى, اعلى جريان راشح للمحلول المنفرد كان ($l/m^2.h$) NF1 (14.2)>NF3 (16.1)> NF2 (32.2) عند تركيز ابتدائي

100(جزء بالمليون), اعلى من المحاليل الثنائية (l/m^2.h) NF1 (8) < NF3 (13) < NF2 (23.7) لتركيز ابتدائي ($10\ Pb^{2+}$/ $50\ Cd^{2+}$) (جزء بالمليون). الاغشية النانوية اثبتت قابليتها لتحقيق اعلى كفاءة فصل لايوني الرصاص والكادميوم في ظروف مستقرة جدا, لطرح مياه الفضلات بشكل مناسب الى البيئة.

1. INTRODUCTION

During the last years, attention has been concentrate on the removal heavy metal ions from the wastewater due to its toxicity and thus its impact on human health. Therefore, according to the environmental regulations it is important to remove all of the heavy metals from the wastewater of various industries so that the wastewater requires total control prior discharge to the environment, **Al-Rashdi et al., 2011**.Various traditional processes have been used to remove heavy metals from effluents such as sorptive flotation, **Muhaisn, 2014**. Phytoremediation processes, **Ziarati, and Alaedini, 2014**, **Paz-Ferreiro et al., 2014**. Electrochemical process, **Moosavi, et al., 2014**, adsorption, ion exchange and electrocoagulation, most of these processes suffer from economic limitations and other disadvantages. For example, in adsorption process most of adsorbents do not have adsorption capacities, need long adsorption contact times, slow adsorption kinetics, low of selectivity and still most of adsorbents especially nanoparticles are expensive. Also, solvent extraction and chemical precipitation have considered as polluting processes themselves, **Moore, and Ramamoorthy, 1985, Sarvi, et al., 2014**. The membrane separation processes were found to be efficient, economic, and green (non-polluting) separation processes compare with those traditional and polluting methods mentioned above and gained wide salability in treatment of various industrial wastewaters. There are several membrane separation processes were used for the removal of heavy metals from wastewaters such as Microfiltration (MF), Ultrafiltration (UF), Reverse osmosis (RO) and Nanofiltration (NF), **Kozlowski, and Walkowiak, 2005, Soares, et al., 2005, Ortega, et al., 2008, Evina, et al., 2011**. Nanofiltration membranes (NF) has been used mainly in various industries for removal of heavy metals compare with UF and RO processes due to the high removal efficiency and works under moderate pressure, **Peeters, 1998, Evina, et al., 2011**. Despite the efficient of the use of NF membrane for removal of heavy metals, but the researchers have found that there are several factors affected the performance of NF membranes such as pH, metal ions, type of membrane and metal concentration, **Perkin-Elmer, 1996, Tanninen, et al., 2006**. From the literature it was found that the preparation of hollow fiber NF membranes for heavy metal removal is still rare and few studies have been reported on high concentrated multicomponent solutions using NF membranes. Therefore, in this work effective removals of two heavy metals such as Cd^{2+} and Pb^{2+} from simulated aqueous solutions were investigated using three different NF membranes prepared for this purpose. These two heavy metals are selected due to its severe side effects to human health. The effect of the operating conditions such as pressure, initial feed concentration and pH solution on membrane separation performance and water flux were studied.

2. EXPERIMENTAL WORK

2.1 Materials and Method

Simulated wastewater was prepared by adding the cadmium nitrate $Cd(NO_3)_2.4H_2O$ and lead nitrate $Pb(NO_3)_2$ to the distilled water. Stock solutions

(1000 ppm) of Cd^{2+} and Pb^{2+} were prepared by dissolving the appropriate weight of cadmium nitrate and lead nitrate in distilled water and kept in polyethylene container at room temperature. The desired concentrations were prepared by diluting the stock solution in accurate proportions to different initial concentrations. Several solutions were prepared with different concentrations of (10 - 250 ppm) and pH values of (5- 7). Three different types of polyethersulfone (PES) NF membranes (PES type Radel, was provided by Solvay Advanced Polymers (Belgium)) prepared by using dry/wet phase inversion method coded as NF1, NF2, and NF3 for the purpose of heavy metals removal. The surface morphology and all the specifications of NF membranes are summarized in Table 1. The pH value was measured using a calibrated pH meter (HQ411d, pH /mv, HACH Company) whereas concentrations of metal ion in simulated and treated solutions were examined using (AAS-6200) Atomic absorption flam emission spectrophotometer (Shimadzu company, Japan). The instrument was calibrated regularly and calibration curve was verified before each sample set. The surface charge of the membrane surface depends on the value of the pH, negative charge for solution pH value higher than 5 and positive membrane surface charge when pH value of the solution is less than 4, **Tanninen, et al., 2004, Al-Rashdi et al., 2011.**

2.2 Membrane Filtration Experiments

The permeate flux of distilled water and heavy metals solutions as well as rejection of heavy metals experiments using NF1, NF2, and NF3 hollow fibers were achieved by module cross-flow pattern filtration as shown in **Fig. 1**. NF membranes experiments were carried out at a transmembrane pressure of 1 bar, solution temperature of 25 ± 3 ˚C , different initial metals concentration (10 -250 ppm) and pH (5 -7). Permeate flux (*J*) and heavy metals rejection (R %) was obtained from the following Eq. (1), **Xu, 2002,** and (2), respectively:

$$J = \frac{V}{A \times t} \quad (1) \qquad \text{and} \qquad R(\%) = \left[1 - \frac{Cp}{Cf}\right] \times 100 \quad (2)$$

where *V* is the volume of the permeate (l), *t* is the collected permeate time (h), *A* is the membrane surface area (m^2), C_f and C_p are the heavy metal concentrations in bulk feed and permeate solution, respectively. After each set of experiments, for a given feed concentration, the setup is rinsed with distilled water for 60 min at 4 bars to clean the NF membrane experimental system, followed by measurement of pure water permeation flux with distilled water to ensure that the initial membrane flux is restored. Moreover, pH value was adjusted using 1 M NaOH or 1 M HCl.

3. RESULTS and DISCUSSION

Permeability of NF Membrane

Pure water permeability (PWP) measurements as a function of (TMP) for three types nanofiltration membranes were carred out by using Eq. (1) as shown in **Fig. 2**. It can be seen that PWP increased linearly when (TMP) increased from 1 to 4 bar, which may be explained that the performance of the membrane was not significantly affected by the fouling. The membrane pearmeability were found to be 37.9 > 16.6 > 16.4 (l/m^2.h.bar), at 1 bar transmembrane pressure

for NF2, NF3 and NF1, respectively. The reason of this behavior is due to that of the porosity of NF2 is higher than the others as the following squence:

NF2 67.6 > NF3 58.1 > NF1 52.5 %

PWP considered to be a reference to the fouling of the membrane, concentration polarization and to evaluate cleaning procedure.

3.2 Lead and Cadmium Ions Removal from Single Salt Solutions

3.2.1 Effect of feed pH on NF membranes performance

At the beginning of the work, carried out all the experiments at pH values of (1.5- 11) to determine the effect of pH on the permeate flux and rejection of heavy metal ions, Where noticed that at acidic pH lower 5.5 not happened any rejection for metal ions therefore, the results not dependent. on the other hand, the rejection of heavy metal ions at alkaline pH (7-11) nearly 100 percent and appeared white sediments , this mean the rejection of heavy metal ions because of deposition and not NF membranes, therefore, the results not dependent. Therefore, the effect of pH values on permeates flux and rejection was studied at pH (5.5-6.5).

Fig. 3 to 5 show the effect of the pH feed solution on the permeate flux of the three types of NF membranes for 100 ppm initial Pb^{2+} and Cd^{2+} concentrations at different times, generally, it can be noticed that the permeate flux of all solutions decreases with increase of feed pH from 5.5 to 6.5. Using NF1, permeate flux decreased from 14.2 to 11.7 ($l/m^2.h$) and 10.5 to 9.8 ($l/m^2.h$) with increase of feed pH from 5.5 to 6.5 for Pb^{2+} and Cd^{2+}, respectively.

Using NF2, it can be seen that the same behavior is observed as in NF1, permeate flux decreased from 32.3 to 29 ($l/m^2.h$) and 28.4 to 27.3 ($l/m^2.h$). While for the third type membrane NF3, permeate flux decreased from 16.1 to 14 ($l/m^2.h$) and 14.9 to 12.8 ($l/m^2.h$) with increase of feed pH from 5.5 to 6.5 for Pb^{2+} and Cd^{2+}, respectively.

This phenomenon is mainly attributed to the charge of the membrane surface, with increasing pH from 5.5 to 6.5 the charge of the membrane becomes more negatively due to the increase of OH^-, therefore, adsorption of heavy metal ions occurs at the surface of the hollow fiber membrane because of the electrostatic attraction, which in turn lead to decrease pore size of membrane thus, decrease the permeation flux. The explanation is due to shrinkage of the membrane layer as a result of differences in the hydration of membrane ionized groups, **Ballet, et al., 2004**.In addition, **Wang, et al., 2007;** explain the change due to concentration polarization and membrane fouling**.** Similar behavior was found in the literature, **Tanninen, et al., 2004.**

Fig. 6 to 8 present the effects of pH feed solution on the rejection of the three types of NF membranes for 100 ppm initial concentration of Pb^{2+} and Cd^{2+} at different times. Using NF1, rejection of Pb^{2+} increases from 63.5 to 83.4% with increased pH from 5.5 to 6 while the rejection of Pb^{2+}decreased significantly to 65.5 % at pH value 6.5. Regarding the rejection of Cd^{2+} , it can be seen that the rejection increases from 22 to 68% with an incease of pH value from 5.5 to 6.5. The same behavior of NF2 membrane is observed as in NF1, the rejection of Pb^{2+} increases from 61.4 to 66.5 % with increase pH from 5.5 to 6.5. The rejection of Cd^{2+} increases from 18 to 45% with increase pH from 5.5 to 6.2 while the rejection of Cd^{2+} decreased significantly to 33% at pH value 6.5. Moreover, using NF3 membrane, rejection of Pb^{2+} increased from 36.6 to 67.6% with increase pH from 5.5 to 6.2 while the rejection of Pb^{2+} decreased significantly to 63 % at pH value 6.5. Regarding the rejection of Cd^{2+} increased from 11 to 32% with increase pH from 5.5 to 6.5. From the results mentioned above it can be

said that the heavy metals rejection increases with increase of pH value mainly due to increase the negative charge on the membrane surface and then result to increase the attraction between the lead and cadmium ions and the membrane surface, which leads to enhance the membrane separation performance . Similar behavior was found in the literature, **, Tanninen, et al., 2004, Al-Rashdi et al., 2011.**

3.2.2 Effect of initial metal concentration on NF performance

Fig. 9 to 11 show the effect of the initial concentration of Pb^{2+} and Cd^{2+} on the permeate flux for the three types of NF membranes at the best initial pH value obtained from the study of the effect of pH at different times. Using NF1, it can be observed that the permeate flux significantly decreased from 13 to 10.3 ($l/m^2.h$) and 10 to 9.3 ($l/m^2.h$) with increase initial Pb^{2+} and Cd^{2+} concentration from (10-250 ppm), respectively. Using NF2, noticed decrease permeate flux with increase initial metal ions concentration where permeate flux decreased from 32.3 to 28.6 ($l/m^2.h$) and 28.8 to 20.8 ($l/m^2.h$) with increase initial Pb^{2+} and Cd^{2+} concentration from (10- 250 ppm), respectively. While permeate flux for NF3 decreased from 16 to 14.3 ($l/m^2.h$) and 13.9 to 12.4 ($l/m^2.h$) for Pb^{2+} and Cd^{2+} solution, respectively, with increased initial ions concentration from (10-250 ppm).

This decline in permeate flux may be due to the increase of deposition of the metals on the membrane surface with increase of initial metal ions concentration, which leads to clogged pores of the membrane and decrease the pore size and also the exit portion of the solutes with permeate water, leading to a decrease permeate flux. Also from the results above it is worthy to mention here that the Cd^{2+} were more fouled on the membrane surface compared with Pb^{2+}, where permeate flux of NF2 (32.3)> NF3 (16) > NF1(13) ($l/m^2.h$) for Pb^{2+}, NF2 (28.8) > NF3 (13.9) > NF1 (10) ($l/m^2.h$) for Cd^{2+} at initial ions concentrations 10 ppm, while permeate flux of NF2 (28.6) > NF3 (14.3) > NF1 (10.3) ($l/m^2.h$) for Pb^{2+}, NF2 (20.8) > NF3 (12.4) > NF1 (9.3) ($l/m^2.h$) for Cd^{2+} at initial ions concentrations 250 ppm. The same behavior was noticed by **Al-Rashdi, et al., 2013.**

The effect of initial metal ions concentrations on rejection of the three different NF membranes are depicted in **Fig. 12 to 14**. Using NF1 membrane, the rejection was decreased from 99 to 43% and 78 to 41.6% with increased initial ions concentration from (10-250 ppm) for Pb^{2+} and Cd^{2+}, respectively. While the rejection by using NF2 was decreased from 97.5 to 43% and 50.2 to 26% with increased initial ions concentration from (10- 250 ppm) for Pb^{2+} and Cd^{2+}, respectively, and also the rejection by using NF3 was decreased from 98 to 49% and 44 to 25% for Pb^{2+} and Cd^{2+}, respectively. Rejection decreases with increasing the initial concentration of metal ions at the best initial values of pH which be obtained from the single component experiments and at different times, which depends on the type of metal removed by membranes, **Murthy, and Gupta, 1997**, **Peeters, 1998, Bouranene, et al., 2008**. It is a characteristic nature of the NF membranes and interpreted by screen phenomena. The increase in initial ions concentrations leads to screen such formation of cations above the membrane in high pressure side. This cations screen formations neutralizes the negative charge of the membrane. The total charge of the membrane decreases and the repulsion between the membrane and the cations will decrease, **Farares, et al., 2005.**

3.3 Lead and Cadmium Removal From binary aqueous solutions

3.3.1 Effect of initial metal concentration on permeate flux

Data in **Fig. 15**, show the effect of different initial metal ions concentrations in binary model on the permeate flux of NF membranes at optimum pH and 1 bar pressure. It can be noticed that the permeate flux decreases with increasing initial ions concentrations. For binary aqueous solution (Pb^{+2}/ Cd^{+2}) experiments for (10/50 ppm), (50/10 ppm) and (50/50 ppm) initial ions concentrations, the permeate flux of NF1 were 8, 7.7 and 7.6 (l/m^2.h), of NF2 were 23.7, 23.3 and 23 (l/m^2.h) and of NF3 were 13, 12.7and 12.5 (l/m^2.h), respectively. Compared with PWP 16.4, 37.9 and 16.6 (l/m^2.h) for NF1, NF2 and NF3, respectively, the permeate flux was in the following sequence: NF2 23.7 > NF3 13 > NF1 8 (l/m^2.h) for initial ions concentrations (10/50 ppm), because of that porosity of NF2 67.6 > NF3 58.1 > NF1 52.5%, allow the exit of the largest amount of permeate flux. Also, the decline in permeate flux happen due to several reasons, including, adsorption of soluble hydroxide of the metal on the surface of the membrane, the composition of the cake layer deposited metal hydroxide and concentration polarization, **Al-Rashdi et al., 2011.** In other word,the largest atomic wight has low permeate flux (Pb^{2+} = 207.2 and Cd^{2+} = 112.4 gm/mol), **Bouranene, et al., 2008, Gherasim, et al., 2013.**

3.3.2 Effect of initial metal concentration on rejection

The rejection of two metal ions in the aqueous solution is studied and the results are depicted in Figures 16. For binary aqueous solution model (Pb^{2+}/ Cd^{2+}), using NF1, the rejection of Cd^{2+}47.4 > Pb^{2+} 34%, Cd^{2+} 49 > Pb^{2+} 45.4% and Cd^{2+} 54 > Pb^{2+} 40.4 % at initial concentration (50/50 ppm), (10/50 ppm) and (50/10 ppm), respectively. Moreover, using NF2, the rejection of Cd^{2+} 52.6 > Pb^{2+} 51.3, Cd^{2+} 55.8% > Pb^{2+} 55.4 and Cd^{2+} 61.3 % > Pb^{2+} 52.4% at initial concentration (50/50 ppm), (10/50 ppm) and (50/10 ppm), respectively. While, using NF3, the rejection of Cd^{2+} 42.1 > Pb^{2+} 40.2%, Pb^{2+} 49.3 > Cd^{2+} 45.5% and Cd^{2+} 56 > Pb^{2+} 44.6% at initial concentration (50/50 ppm), (10/50 ppm) and (50/10 ppm), respectively. The explanation of that, the cadmium ions rejection is higher than lead ions rejection, and this higher rejection of cadmium salt is determined by the higher hydration energy of cadmium cation (-1755 kJ/mol of Cd^{2+}) > (-1425 Kj/mol of Pb^{2+}), **Marcus, 1997**. Similar results which highlight the increase in the cation retention with increasing hydration energy were obtained by **Gherasim, et al., 2013**.

4. CONCLUSIONS

In the present study, concluded the maximum rejection of Pb^{2+} in single salt solution were 99, 97.5 and 98%, and of Cd^{2+} were 78, 49.2 and 44 % for NF1, NF2 and NF3, respectively. While the maximum rejection of Pb^{2+} in binary aqueous solution were 45.4, 55.4, 49.3 % , and of Cd^{2+} rejection were 49,55.8 and 45.5 % for NF1, NF2 and NF3, respectively. It can be concluded that the permeation flux and rejection of Pb^{2+}were higher than that of Cd^{2+} at different pH values and initial ions concentration and NF2 was very efficient hollow fiber NF membrane for removal of Pb^{2+} and $Cd^{2+}$and also for binary aqueous solution. Finally, the separation performance of hollow fiber NF membranes is strongly depending on the membrane properties such as mean pore size, pore size distribution, and thickness.

REFERENCE

- Al-Rashdi, B., Somerfield, C., and Hilal, N., 2011, *Heavy Metals Removal Using Adsorption and Nanofiltration Techniques*, Separation and Purification Reviews Journal, Vol. 40, No. 3, PP. 209 -259.
- Al-Rashdi, B.A.M., Johnson, D.J., and Hilal N., 2013, *Removal of Heavy Metal Ions by Nanofiltratio*, Desalination Vol.315, PP.2–17.
- Ballet, G.T., Gzara, L., Hafiane, A., and Dhahbi, M., 2004, *Transport Coefficients and Cadmium Salt Rejection in Nanofiltration Membrane*, Desalination Vol.167, PP.369 – 376.
- Bouranene, S., Fievet, P., Szymczyk, A., El-Hadi, S. M., and Vidonne, A., 2008, *Influence of Operating Conditions on the Rejection of Cobalt and Lead Ions in Aqueous Solutions by a Nanofiltration Polyamide Membrane*, Journal of Membrane Science Vol.325, PP.150–157.
- Childress, A.E., and Elimelech, M., 2000, *Relating Nanofilb'ation Membrane Performance to Membrane Charge (Electrokinetic) Characteristics*, Environmental Science Technology, Vol. 34, PP. 3710-3716.
- Evina, K. , Simos, M., Katherine, J. H., and Maria, L., 2010, *Use of Ultrafiltration Membranes and Aluminosilicate Minerals for Nickel Removal from Industrial Wastewater*, Journal Membrane Science, Vol.360, PP. 234–249.
- Farares, N.B., Taha, S.,and Dorange G., 2005, *Influence of the Operating Conditions on the Elimination of Zinc Ions by Nanofiltration*, Desalination Vol.185, PP. 245–253.
- Gherasim, C., Cuhorka, J., and Mikulasek, P., 2013, 2013, *Analysis of Lead (II) Retention from Single Salt and Binary Aqueous Solutions by a Polyamide Nanofiltration Membrane: Experimental Results and Modeling*, Journal Membrane Science, Vol. 436, PP.132-144.
- Kozlowski, C. A., and Walkowiak, W., 2005, *Applicability of Liquid Membranes in Chromium (VI) Transport with Amines as Ion Carriers*, Journal Membrane Science Vol. 266, PP.143-150. C.A.
- Marcus, Y., 1997, *Ion Properties, Marcel Dekker Inc*., New York, PP. 122–123.
- Moore, M., and Ramamoorthy, S., 1985, *Heavy Metals in Natural Waters, Springer-Verlag*, New York, PP. 112–11.
- Moosavi, Gh. , Mostafaii, Gh., Roozitalab, N., Rabbani, D. , and Iranshahi, L., 2014, *Application of Electrochemical Process in Removal of Heavy Metals from Landfill Leachate*, Quarterly of International Archives of Health Sciences, Vol. 1, No.1,PP.31-35.
- Muhaisn, L.F., 2014, *Competitive Removal of Heavy Metal Ions from Simulated Wastewater by Sorptive Flotation using Punica Granatum*, Thesis master, Env. Eng. Dep. College of Eng., University of Baghdad, (2014).
- Murthy, Z.V.P., and Gupta, S.K., 1997, *Estimation of Mass Transfer Coefficient Using a Combined Nonlinear Membrane Transport and Film Theory Model*, Desalination Vol.109, PP.39–49.
- Ortega, L. M., Lebrun, R., Blais, J. F., Hausler, R., and Droguit, P., 2008, *Effectiveness of Soil Washing, Nanofiltration and Electrochemical Treatment for the Recovery of Metal Ions Coming from a Contaminated Soil*, Water Research, Vol. 42 PP. 1943-1952.
- Paz-Ferreiro, j., Lu, H., Fu, S., Méndez, A., and Gascó, G., 2014, *Use of Phytoremediation and Biochar to Remediate Heavy Metal Polluted Soils: a review*, Solid Earth, Vol. 5, PP. 65–75, www.solid-earth.net/5/65/2014/.

- Peeters, T. A., 1998, *Purification of Landfill Leachate with Reverse Osmosis and Nanofiltration*, Desalination, Vol.119, PP. 289–293.
- Perkin-Elmer, 1996, *Analytical Methods for Atomic Absorption Spectroscopy*, The Perkin-Elmer Corporation, USA.
- Sarvi, M. S., Bee, T. B., Gooi, C. K., Woonton, B. W., Gee, M.L., and O'Connor, A. J., 2014, *Development of Functionalized Mesoporous Silica for Adsorption and Separation of Dairy Proteins*, Chemical Engineering Journal Vol. 235, PP. 244–251.
- Semiao, A. J. C., and Schafer, A. I., 2001, Estrogenic Micro-pollutant Adsorption Dynamics onto Nanofiltration Membranes, Journal Membrane Science, Vol.381, PP. 132 – 141.
- Soares, M. C. V., Bertrans, M. A., Lemos, F.A., and Masson, I. O. C., 2005, *Removal of Lead, Cadmium and Zinc from Industrial Effluents using Nanofiltration and Reverse Osmosis Membranes*, In: XIII International Conference on Heavy Metals in the Environment, Rio de Janeiro, Brazil.
- Tanninen, J., Mänttäri, M.,and Nyström, M., 2006, *Effect of Salt Mixture Concentration on Fractionation with NF Membranes*, Journal Membrane Science,Vol. 283, PP. 57-64.
- Tanninen, J., Platt, S., Weis, A., and Nystrom, M., 2004, *Long-term Acid Resistance and Selectivity of NF Membranes in very Acidic Conditions*, Journal Membrane Science, Vol. 240, PP.11–18.
- Wang, Z., Liu, G., Fan, Z., Yang, X., Wang, J., and Wang, S., 2007, *Experimental Study on Treatment of Electroplating Wastewater by Nanofiltration*, Journal Membrane Science, Vol. 305, PP.185 – 195.
- Xu J., Xu Z-L., 2002, *Poly (vinyl chloride) (PVC) hollow fiber ultrafiltration membranes prepared from PVC/additives/solvent*, Journal of Membrane Science, Vol. 208, pp. 203-211.
- Ziarati, P., and Alaedini, S., 2014, *The Phytoremediation Technique for Cleaning up Contaminated Soil By Amaranthus sp*.,Journal of Environmental & Analytical Toxicology, Vol. 4, No. 208, http://dx.doi.org/10.4172/2161-0525.1000208.

NOMENCLATURE

A = area, m^2.
C_P = concentrations in permeate solution, ppm.
C_b = concentrations in bulk feed, ppm.
J = permeate flux, l/m^2.hr.
ppm = part per million.
PWP = pure water permeability.
R = rejection, %.
t = time, h.
V = volume, l.

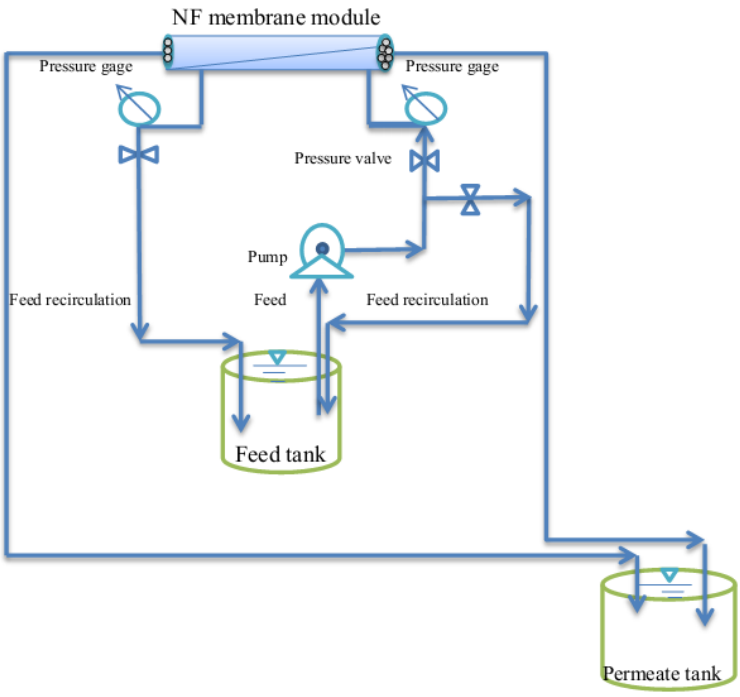

Figure1. A Schematic diagram of the membrane filtration test system.

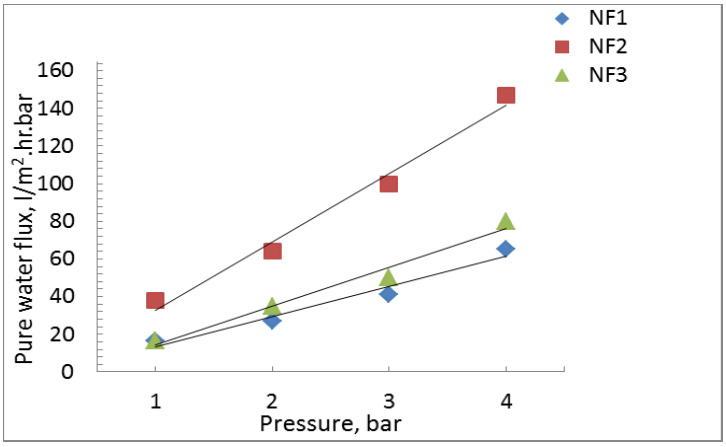

Figure2. Pure water permeability as a function of trans-membrane pressure.

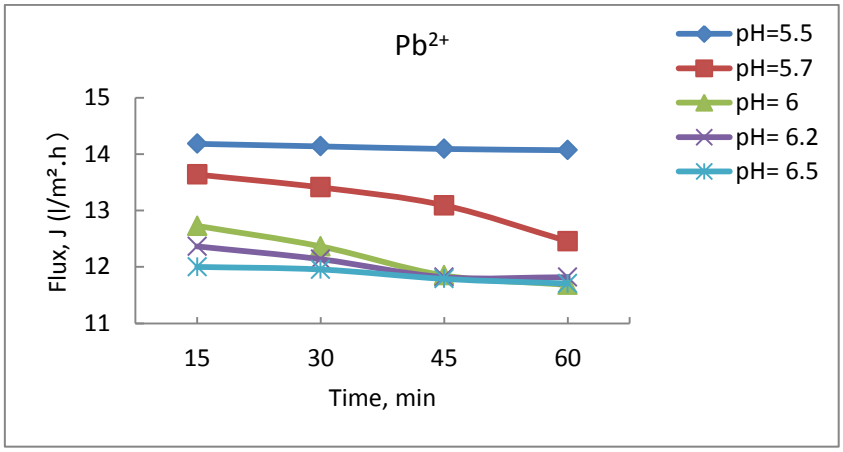

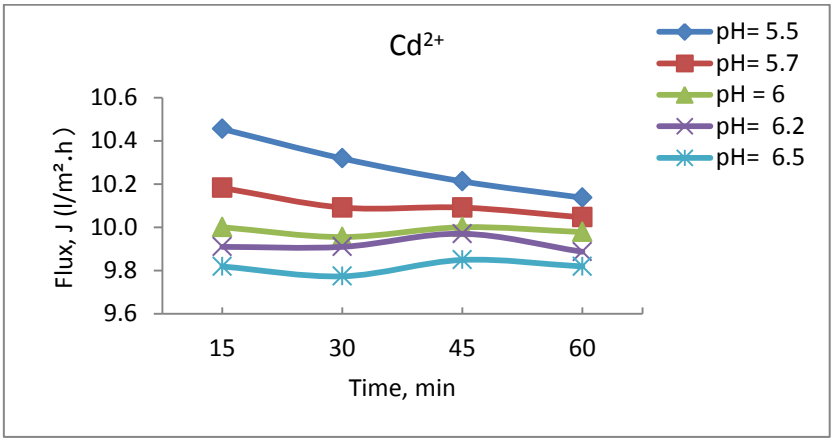

Figure3. Effect feed pH solution on permeate flux of NF1 membrane at different times.

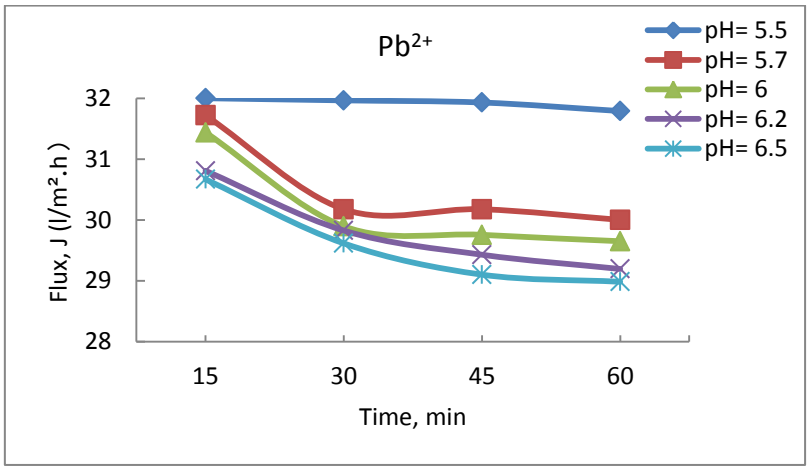

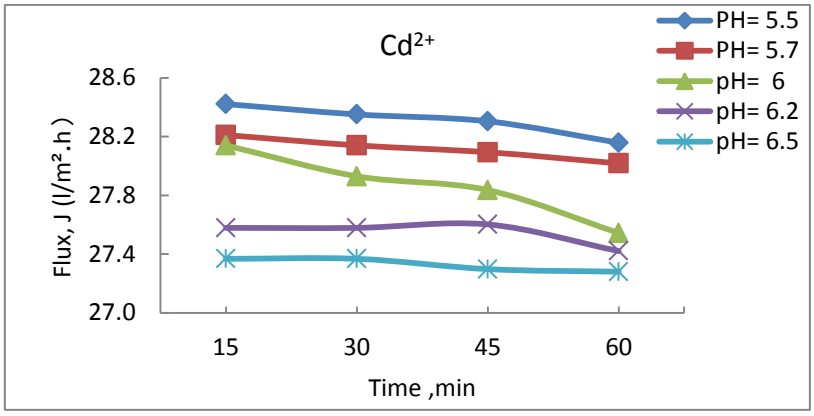

Figure4. Effect feed pH solution on permeate flux of NF2 membrane at different times

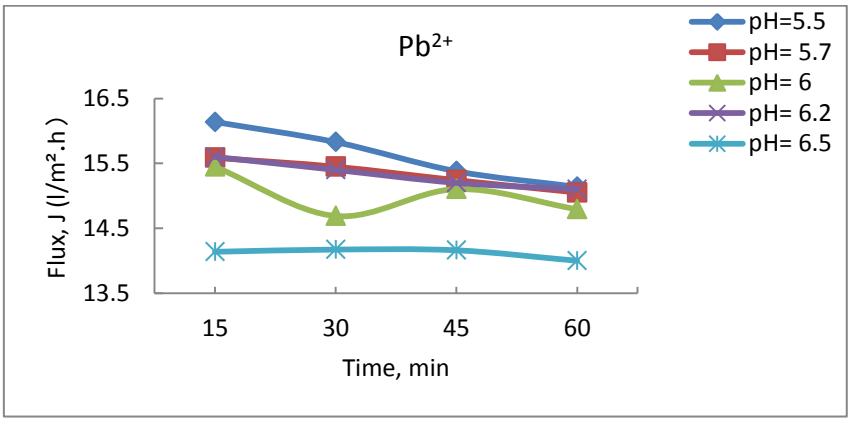

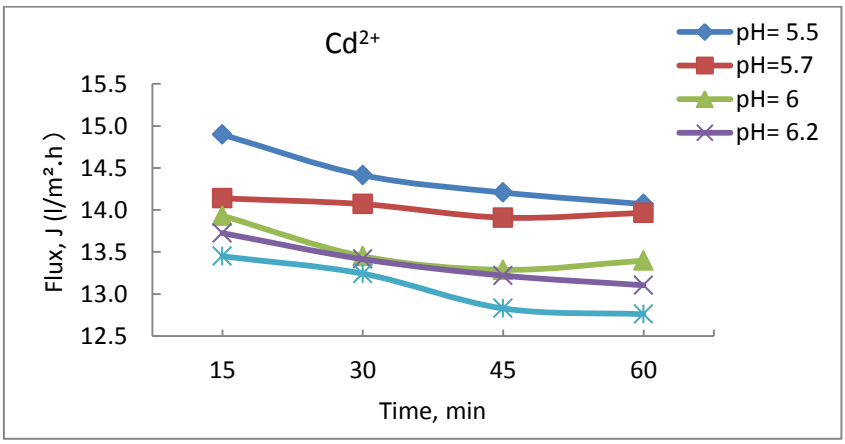

Figure5. Effect feed pH solution on permeates flux of NF3 membrane at different times

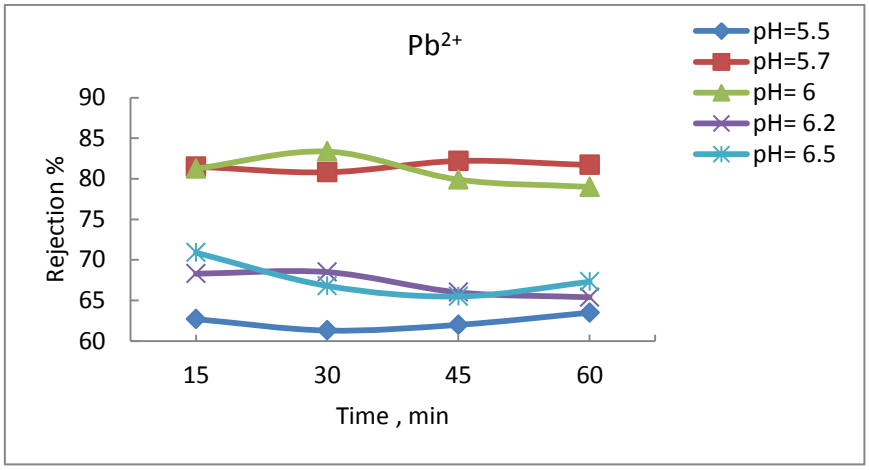

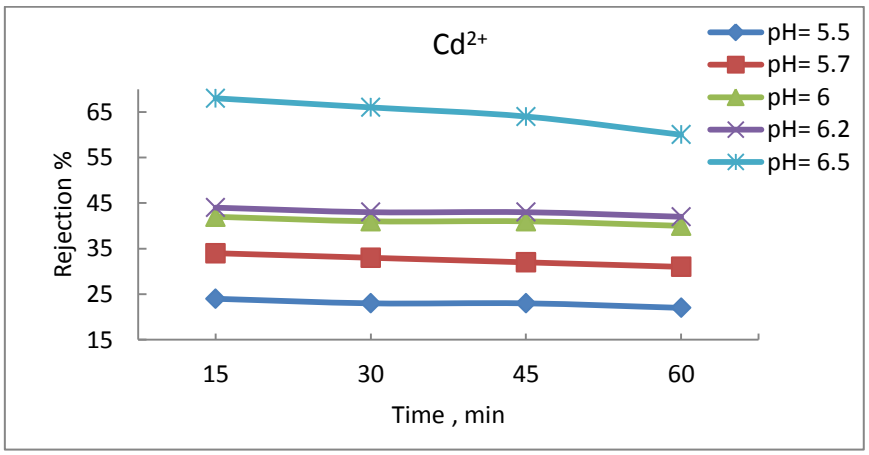

Figure 6 . Effect feed pH solution on rejection of NF1 membrane at (initial con.100 ppm and different times)

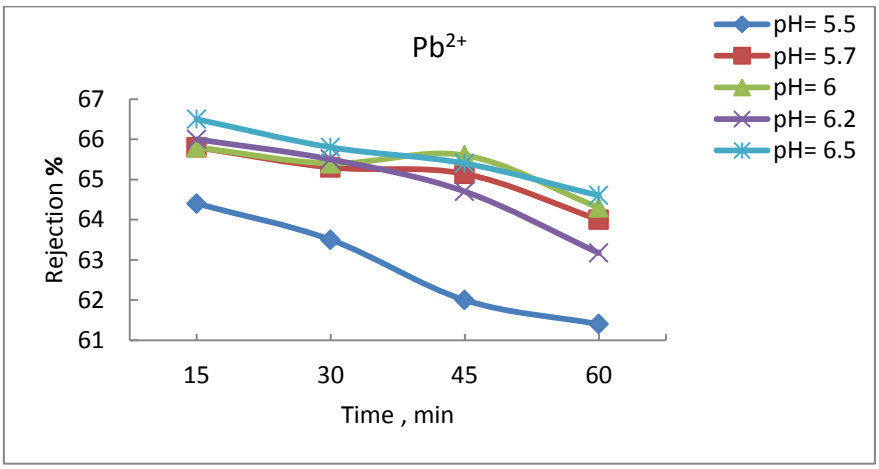

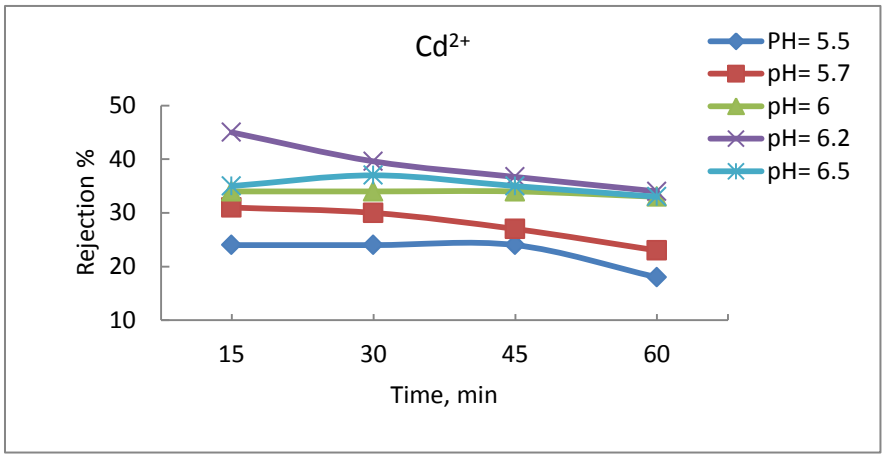

Figure 7. Effect feed pH solution on rejection of NF2 membrane at (initial con.100 ppm and different times)

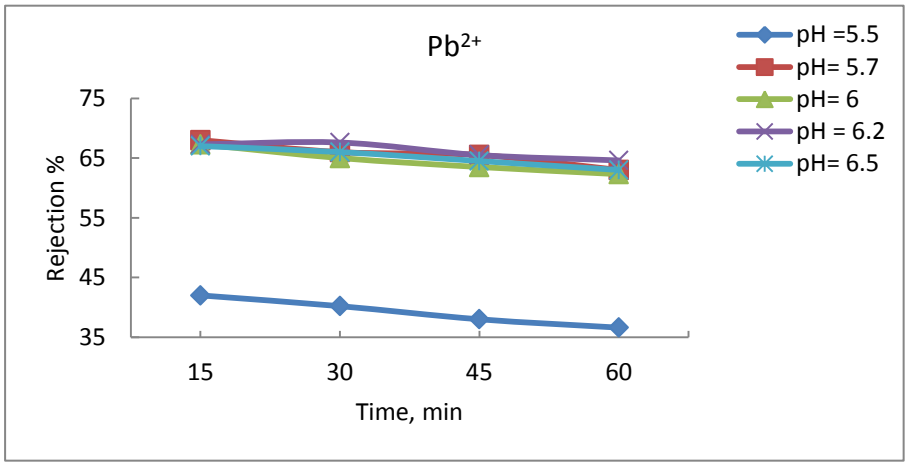

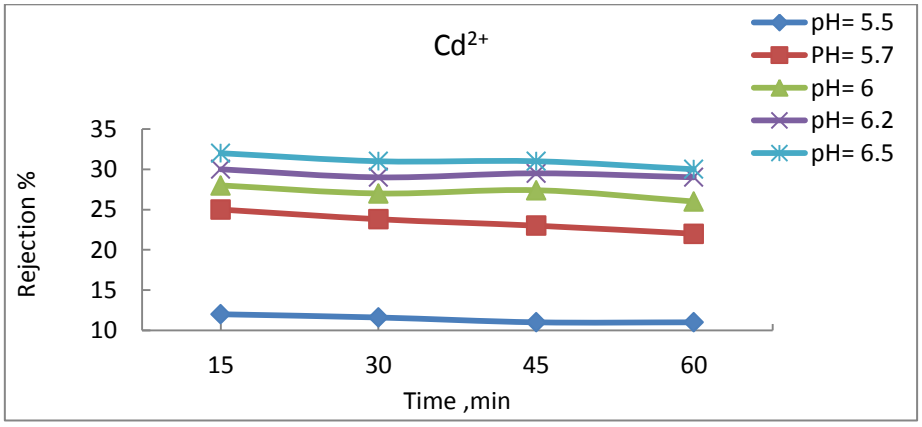

Figure 8. Effect feed pH solution on rejection of NF3 membrane at (initial con.100 ppm and different times)

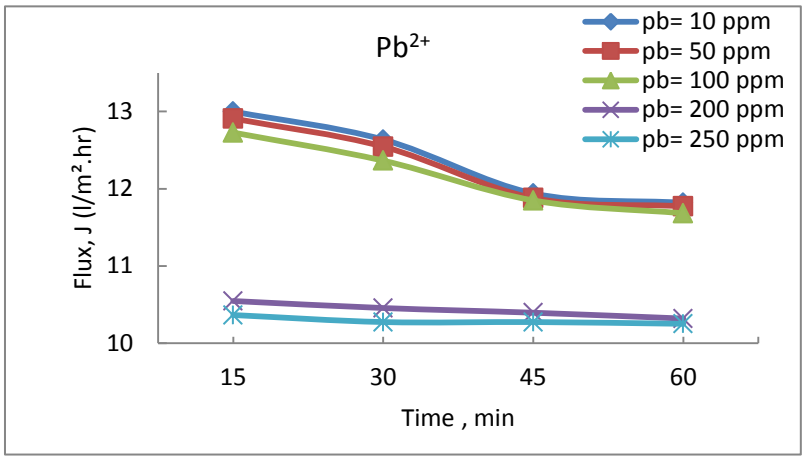

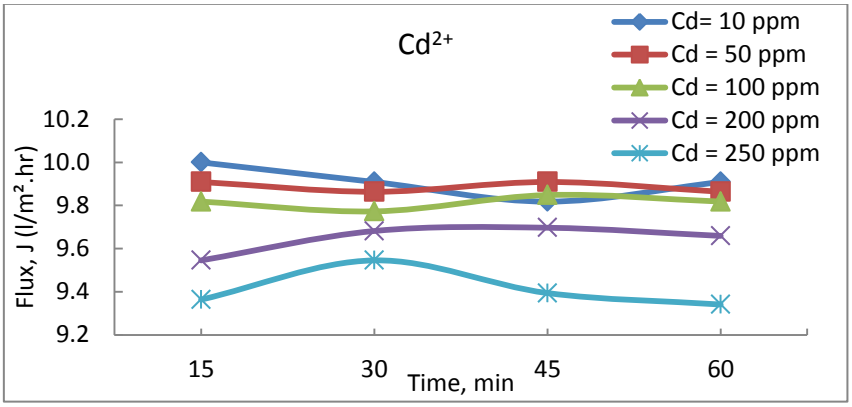

Figure 9. Effect of initial concentration on flux of NF1 membrane at different times

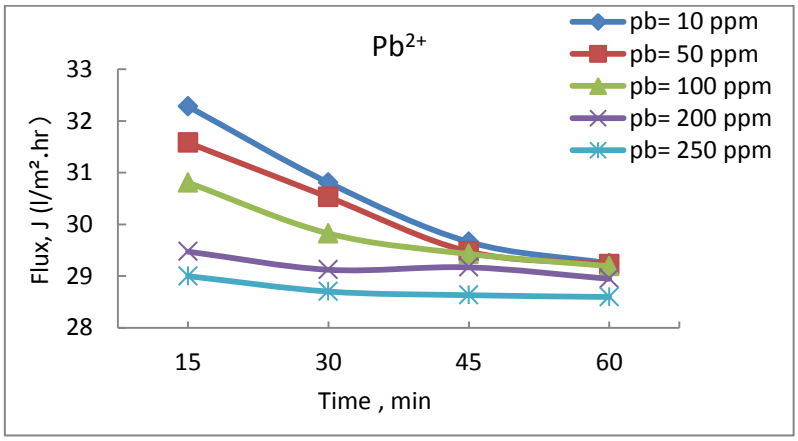

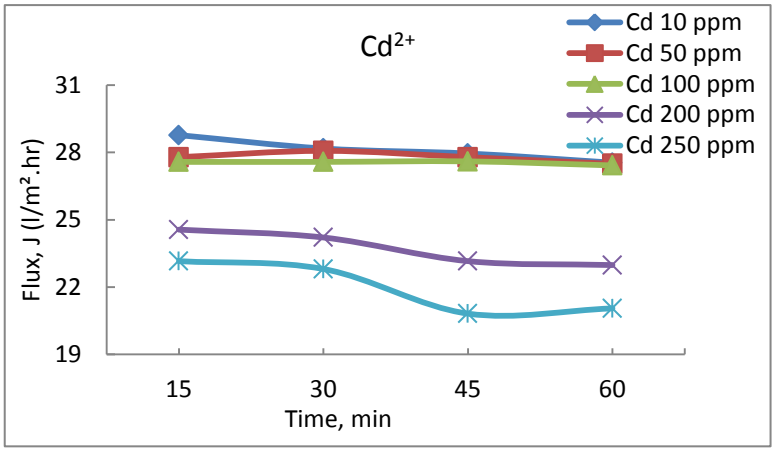

Figure 10. Effect of initial ion concentration on flux of NF2 membrane at different times.

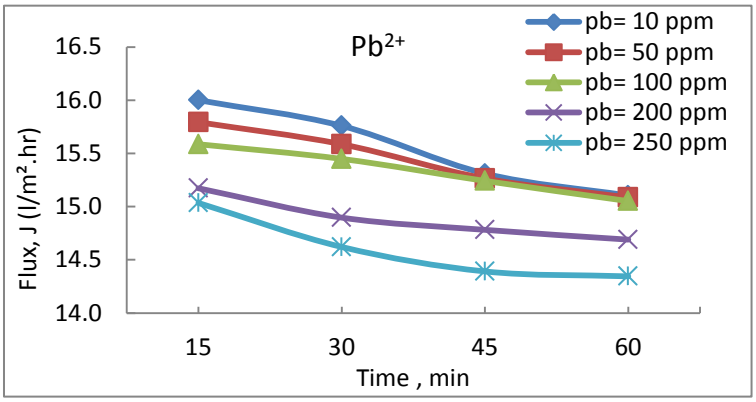

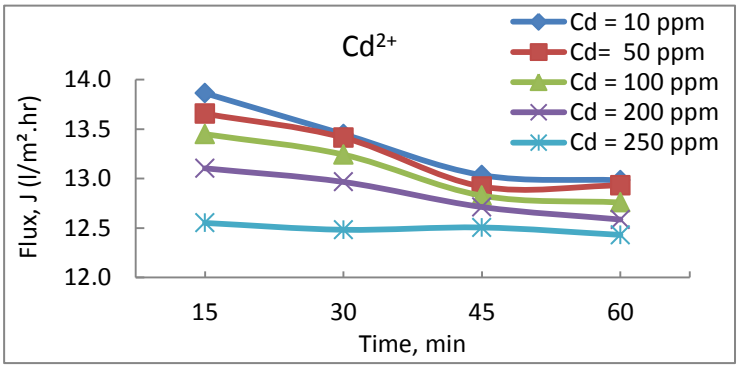

Figure 11. Effect of initial ion concentration on flux of NF3 membrane at different times

.

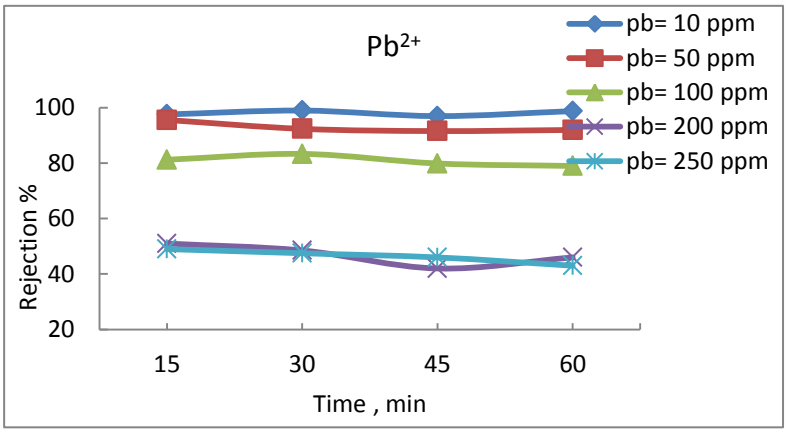

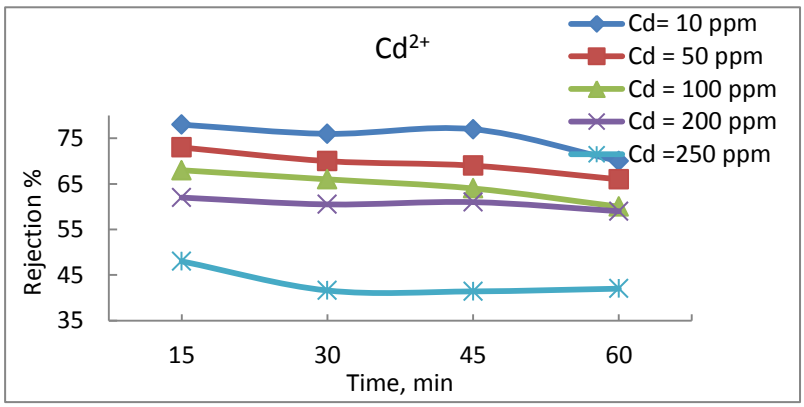

Figure 12. Effect of initial metal concentration on rejection of NF1 membrane at different times

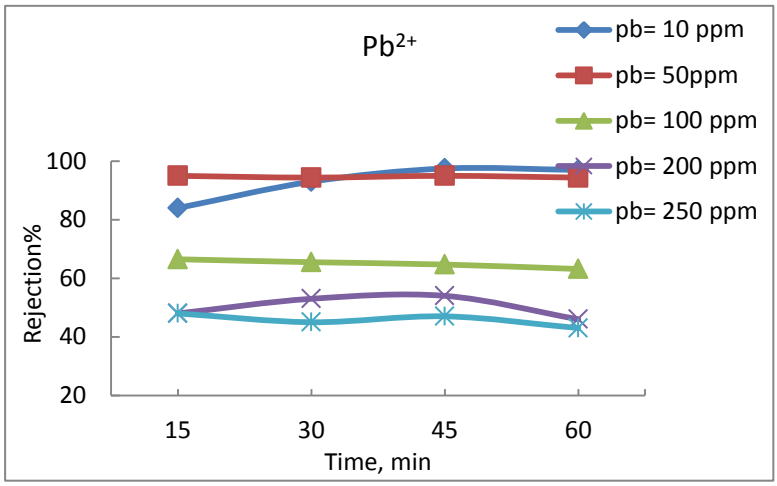

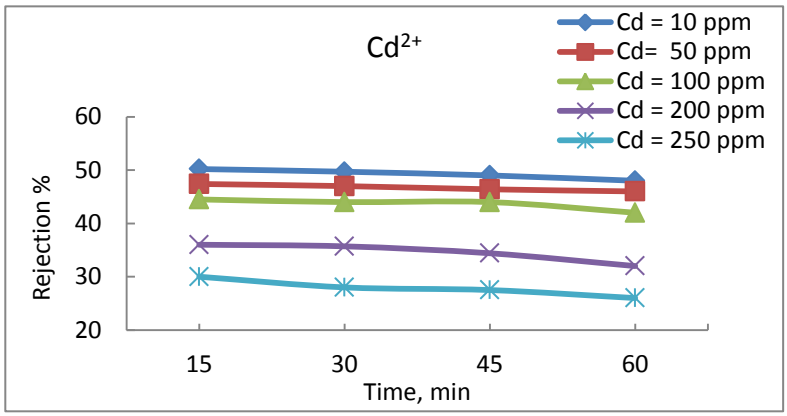

Figure 13. Effect of initial metal concentration on rejection of NF2 membrane at different time

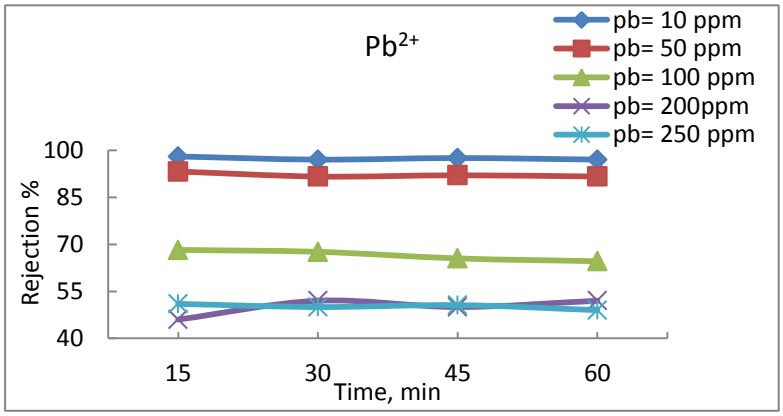

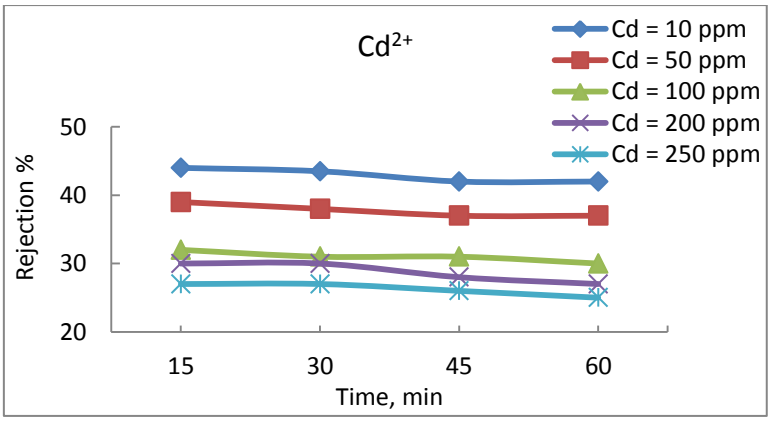

Figure 14. Effect of initial metal concentration on rejection of NF3 membrane at different times

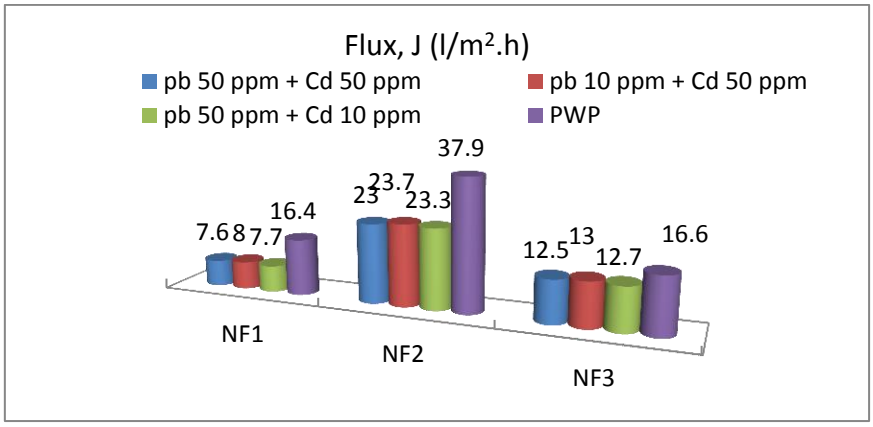

Figure 15 . Effect of initial feed concentration of (Pb^{2+} / Cd^{2+}) on permeate flux for three types of NF membrane (pH 6±0.2 and time 30 min)

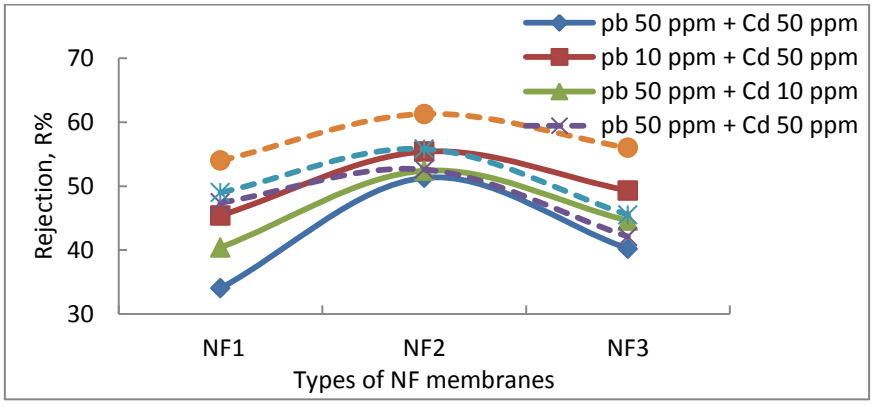

Figure 16. Effect of initial feed concentration of (Pb^{2+} (solid line) and Cd^{2+} (the dotted line)) on rejection for three types of NF membrane (pH 6±0.2 and time 30 min)

Table 1. Characteristics of the NF membranes

Type of membrane	NF1	NF2	NF3
Material	PES (29%)	PES (27%)	PES (27%)
Module	Hollow fiber	Hollow fiber	Hollow fiber
Length (cm)	22.2	22.7	23.1
Active Area (m^2)	4.4×10^{-3}	5.7×10^{-3}	5.8×10^{-3}
Max operating temp (°C)	45	45	45
Average pore size (nm)	52.04	58.11	47.75
pore size distribution (nm)	25 - 100	35 - 130	20 - 115
Porosity (%)	52.5	67.6	58.1
Outer diameter (µm)	1012	958.4	1005
Inner diameter (µm)	620	576	603.6

Aerobic biodegradation of phenol by Immobilized *Pseudomonas sp.* cells in two different bio-carrier matrices

Prof. Zainab Ziad Ismail
Department of Environmental Engineering
College of Engineering
Baghdad University
Email: zismail9@gmail.com

Asst. Lect. Haneen Ahmed Khudhair
Department of Environmental Engineering
College of Engineering
Tikrit University
Email: ayacherry_2008@yahoo.com

ABSTRACT

Biotreatment using immobilized cells (IC) technology has proved to be the most promising and most economical approach for the removal of many toxic organic pollutants found in petroleum-refinery wastewater (PRW) such as phenol. This study was undertaken to evaluate the degradation of phenol by *Pseudomonas* cells individually immobilized in two different bio-carrier matrices including polyvinyl alcohol-guar gum (PVA-GG) and polyvinyl alcohol-agar agar (PVA-AA). Results of batch experiments revealed that complete removal of phenol was attained in the first cycle after 150 min using immobilized cells (IC) in both PVA-GG and PVA-AA. Additional cycles were confirmed to evaluate the validity of recycling beads of immobilized cells for phenol biodegradation. Results revealed that the phenol percentage removals were 95, 92, 86, and 84 % for second, third, fourth, and fifth cycles, respectively using *Pseudomonas* immobilized in PVA-GG beads. Whereby they were 96, 92, 90, and 84 % using *Pseudomonas* immobilized in PVA-AA beads for the same sequence of cycles.

Key words: Immobilized cells, *Pseudomonas*, bio-carrier, wastewater, and phenol

التحلل الهوائي للفينول باستخدام خلايا البكتريا الزائفة المقيدة في نوعين من الحوامل الاحيائية

أ. زينب زياد اسماعيل
قسم الهندسة البيئية
كلية الهندسة / جامعة بغداد

م.م. حنين أحمد خضير
قسم هندسة البيئة
كلية الهندسة / جامعة تكريت

الخلاصة

ان المعالجة الاحيائية باستخدام تقنية الخلايا المقيدة من اهم الاساليب الحديثة والمجدية اقتصاديا لازالة معظم المواد العضوية المثبطة والمقاومة للتحلل البايولوجي والتي تتواجد ضمن مخلفات المصافي النفطية ومن ضمنها الفينول. اذ تم اجراء هذا البحث لغرض دراسة تحلل الفينول بتركيز ابتدائي 20 ملغم/لتر باستخدام خلايا البكتريا الزائفة والمقيدة ضمن نوعين من الحوامل الاحيائية وهما البولي فينيل الكحول- صمغ البازلاء والبولي فينيل الكحول- المادة الطحلبية الهلامية. بينت النتائج التجريبية عملية ازالة كلية للفينول بعد 150 دقيقة في الدورة الاولى باستخدام الخلايا المقيدة. تم استخدام خرز الخلايا المقيدة في دورات اعادة استخدام اضافية لتقييم اعادة استخدام تلك الخرز في عملية التحلل البايولوجي للفينول. وقد كانت النسب المئوية لازالة الفينول كالتالي: 95، 92، 86 و 84 % للدورات الثانية، الثالثة، الرابعة والخامسة على التوالي بعد مرور 150 دقيقة باستخدام الخلايا المقيدة في خرز PVA-GG، في حين كانت نسب الازالة: 96، 92، 90 و 84 % لنفس تسلسل الدورات على التوالي باستخدام الخلايا المقيدة في خرز PVA-AA.

الكلمات الرئيسيه: الخلايا المقيدة، *Pseudomonas*، الحامل الاحيائي ، مياه الصرف الصحي، والفينول .

1. INTRODUCTION

Phenol is the first compound inscribed into the list of priority pollutants by the US Environmental Protection Agency (US EPA). Phenol irritates skin and causes its necrosis; it damages kidneys, liver, muscle and eyes, Phenolic compounds are carcinogenic to human and lethal to aquatic life at relatively low concentration levels (5-25) mg/L, **Michalowicz, and Duda, 2007; Al-Khalid, and El-Naas, 2012**. The maximum allowable concentration of phenol is 0.5 mg/L according to the Iraqi legislation. Thus; the removal of phenol from industrial aqueous effluents is of great practical significance for environmental protection, **Al Zarooni, and Elshorbagy, 2006; El-Naas et al., 2010**. The physical and chemical treatment methods have limited success when applied to the treatment of refractory organic pollutants because these processes led to secondary effluent problems due to formation of toxic materials. Therefore, intensive attention has been paid to the degradation of these pollutants by microorganisms and their transformation into compounds inoffensively with formation of new cellular mass, **Karigar, et al., 2006; Cozma, et al., 2012**. Biotreatment of phenol has attracted great attention due to its environmentally friendly approach and its ability to mineralize toxic organic compounds completely. However, phenol degradation by bacterial cells generally limited by substrate inhibition and low conversion rates. These drawbacks can be overcome by immobilization technology. Immobilized cells (IC) technology utilizes the colonization of specialized bacterial cells into beads made from natural and synthetic polymers. Bacteria of the genus *Pseudomonas* are a group of increasing both fundamental and biotechnological interest that exhibit a diverse range of metabolic activities and play an important role in the degradation of aromatic hydrocarbon in the PRW, **Kuyukina et al, 2009**. However, toxicity of organic pollutants may prevent or slow metabolic reactions in biological treatment. So, the introduction of new and improved biotechnologies that enable engineers and scientists to tackle the more contemporary environmental problems such as detoxification of hazardous compounds through the use of living microorganisms would be necessity, **Loh, et al., 2000; Martins, et al., 2013**. It has been shown that the biodegradation rate can be improved by immobilizing the cells by using solid support particles such as polyvinyl alcohol (PVA) to obtain the maximum degradation capability, **Al-Khalid, and El-Naas, 2012**. There were a little previous works that dealt with relatively low initial phenol concentration. However, **El-Naas, et al., 2009** evaluated phenol biodegradation by *Pseudomonas Putida* immobilized in PVA gel pellets at initial phenol concentration of 75 mg/L. In the study done by **Chung, et al., 2003** that compared between free and immobilized cells of *Pseudomonas putida*, free cells (FC) could degrade phenol up to about 600 mg/L in batch reactor whereas this level becomes up to 1000 mg/L for immobilized cells (IC) in Ca-alginate beads. **Wang, et al., 2007** used PVA carrier for immobilization and reported that the immobilized cells of *Acinetobacter sp.* could tolerate higher phenol levels and the immobilized cells possessed better storage stability, which demonstrated that PVA carrier cubes had good flexibility and retained a high mechanical strength. **Zhiguo, et al., 2012** isolated a bacterial strain *Pseudomonas sp*. that was capable of degrading nitrobenzene, phenol, aniline, and other aromatics and then immobilized its cells in the mixed carrier of polyvinyl alcohol and sodium alginate to improve its degrading efficiency. In the study of **El-Gendy, and Nassar, 2015** was isolated the marine diesel-oil degrading bacterium, *Pseudomonas aeruginosa* NH1 and examined its ability to degrade diesel oil contaminating seawater as immobilized cells by entrapment in Ca-alginate. The biodegradation rate of different components of diesel oil was enhanced by immobilization, indicating the improved

tolerance of the immobilized cells towards different toxic components of diesel oil and environmental conditions.

The aim of this study is to evaluate the phenol biodegradation by immobilized cells of the bacterium of genus *Pseudomonas*. Two natural bio-carrier polymers; guar gum (GG) and agar-agar (AA) reinforced by Polyvinyl alcohol (PVA), were used to immobilize the bacterium of genus *Pseudomonas* for investigating the performance of the suggested system in enhancement phenol removal efficiency.

2. MATERIALS AND METHODS

The materials which were used as bio-carriers in this study were natural polysaccharide polymers including Agar-Agar (AA) and Guar Gum (GG) as given in **Table 1**. These biopolymers were individually cross-linked with polyvinyl alcohol (PVA) to improve the strength and mechanical stability of beads since the natural polysaccharides are abundantly available but they are less stable in the wastewater than synthetic polymers, **Stolarzewicz, et al., 2011**.

2.1 Isolation of inoculum for use in the preparation of immobilized cells

A phenol-degrading bacterial strain was isolated from the activated sludge freshly collected from Baiji Oil Refinery, (Iraq), and identified as *Pseudomonas* sp. via enrichment culture technique which included streaking the bacterial strain on Petri dishes. Three-3-day-old colonies that incubated at 25 °C on Inoculum Production Medium (IPM) agar were transferred into 5 ml of IPM and incubated statically for 48 h at 25 °C. Subsequently, this culture was transferred into 250 ml screw-capped Erlenmeyer flask containing 45 ml of IPM. The loosely capped flask was incubated for 24 h in an orbital shaker at 25 °C and 150 rpm, **Safont, et al., 2012**.

2.2 Immobilization Protocol

2.2.1 Polyvinyl alcohol-guar gum matrix

PVA-GG matrix was prepared as follows: 6 g PVA and 2 g GG were dissolved in 100 ml distilled water and blended by a magnetic stirrer at 70 °C for 30 min. After cooling the mixture to room temperature, it was inoculated with 5 ml of inoculum culture prepared from previous step and was stirred by a magnetic stirrer for 15 min. The obtained solution was poured into sterile micro-plates to form beads of 3 mm diameter contained immobilized cells, kept in the freezer for 12 hours, and then thawing them. The freezing-thawing procedure was repeated for 3 times to improve the stability of beads, **Bai, et al., 2010**.

2.2.2 Polyvinyl alcohol-agar agar matrix

A 2% solution of Agar-Agar was prepared with 0.9 % PVA powder. A 5ml volume of biomass inoculum was added to the PVA-agar mixture, shaken well for few seconds (without

forming entrapped bubbles), poured into 2 sterile micro-plates and allowed to solidity in the freezer and then thawed. The beads were washed with distilled water 3 to 4 times, **Kumer, et al., 2014**. **Fig. 1** presents samples of the prepared beads with 3 mm in diameter.

2.3 Culture Medium

1 L of the mineral salt medium (MSM) for inoculum cultivation consisted of (g L^{-1}): NaCl, 1; Na_2HPO_4, 1.5; KH_2PO_4, 0.5; $MgSO_4.7H_2O$, 0.2; and yeast extract, 0.5, in distilled water (DW). The pH of MSM was adjusted to 7. To prepare the culture medium containing carbon and energy sources, an appropriate amount of phenol from a stock solution of 20 mg/L (stored in a dark bottle at 4°C) was firstly dispended into 250 ml flasks. MS medium was then added to the 500 ml flasks and finally the resulted aqueous solution was added to spouted bed bioreactor (SBBR).

2.4 Experimental System Configuration and Setup

The experimental system consisted of a specially designed fluidized bed bioreactor, known as spouted bed bioreactor (SBBR) made of Perspex column (inner diameter 50 mm, height 70 cm) with 45° conical base. The SBBR could be operated in batch and continuous mode operation as well. The SBBR was outfitted with a Perspex jacket (inner diameter 80 mm) for temperature control. A water bath was designed to continuously circulate the water at a desired temperature of 30°C. The water bath consisted of 6 Liter-cylindrical Perspex tank, occupied with heater (Aquarium immiscible heater rod, China) and water pump (RS Electrical, RS-80, Q_{max} = 1000 L/h & H_{max} = 1m) to circulate the water into the reactor jacket. The aqueous solutions were fed to the SBBR via a peristaltic pump (Thomas 3386). In order to provide an intense mixing and maintain aerobic environment into the spouted bed bioreactor, air was injected from the bottom of the reactor by an air pump (HAILEA, ACO-308, China) through a 6 mm-orifice. A flow meter and controller (GENTEK, GNT604) was provided to control the air flow into the system. The experimental setup is given in **Fig. 2**. The spouted bed bioreactor reactor was operated in an up flow co-current air/water mode with 4 L/min and 20 ml/min for air and liquid flowrates, respectively.

2.5 Analytical Analysis and Methodologies

Phenol concentration in aqueous samples was determined by T80 UV-VIS Spectrophotometer at 270 nm wavelength. The cells counting in each experiment with immobilized microorganisms involves removal of the cells from the immobilization matrix by dissolving the beads by immersing them in 4 % $NaHCO_3$ solution for 30 min. Samples of microorganisms residing in the wastewater were used without additional treatment. Routine counts of biomass cells in wastewater or within the beads were counted by the Plate Count Method (CFU/mL) in a series of dilutions (in 0.85 % saline) and traditional approach of volatile suspended solids (VSS, g/L), **Cruz, et al., 2013**.

3. RESULTS AND DISCUSION

3.1 Effect of Beads Concentration on Biodegradation Rate

The amount of immobilized cells beads in the bioreactor plays an important role in the biodegradation process. The performance of immobilized cells was examined at initial concentration of 500 mg/L equivalent to free cells system by using 10 and 25 % (v/v) of beads. In order to make a reasonable comparison between biodegradation rates at the two bead densities (10 and 25 % (v/v)) examined in this study, the initial bacterial cells concentration was kept in the beads and increasing the number of beads at lower cell density inside them. This can be explained by the fact that the higher cell concentration inside the beads limits the nutrients availability inside beads. This could have in turn contributed to the enhancement and improvement of biodegradation process, **Safont, et al., 2012**. **Fig. 3** shows the effect of beads concentration (as volume percentage) on the biodegradation of phenol. The degradation rates of phenol using 10 % (v/v) of immobilized cells in PVA-GG and PVA-AA beads were 5.298 and 6.240 mg/L.h, respectively. Whereby, they were 7.50 and 7.53 mg/L.h, respectively using 25 % (v/v). Hence, the biodegradation rate using 25 % (v/v) of beads was higher than the biodegradation rate using 10 % (v/v). It is well expected since the concentration of the beads in the bioreactor can be related directly to the amount of the bacterial biomass immobilized in these beads. The results which performed by **Loh, et al., 2000,** who used an immobilized-cell membrane bioreactor to investigate phenol degradation at high concentrations using Pseudomonas Putida, showed that 25 % (v/v) of immobilized cells were effective in rapid degradation of 100 mg phenol/L.

3.2 Time Course of Phenol Biodegradation

Time course of phenol biodegradation was examined at initial phenol concentration of 20 mg/L by taking a sample periodically every 30 min. Results given in **Fig. 4** and **Fig. 5** showed that the bacterium of *Pseudomonas sp.* was capable to complete removal of 20 mg/L of phenol after 150 min for the bacterial cells immobilized in both PVA-GG and PVA-AA beads at the 1st degradation cycle without any further acclimation to the phenol initial concentration. These results were compared to results that performed by **El-Naas, et al., 2009,** which indicated that the bacterium of *Pseudomonas Putida* was capable to complete removal of 25 mg/L of phenol after 48 min for the bacterial cells immobilized in PVA gel pellets due to previous acclimation process to the phenol which the microorganism used as a source of carbon and energy. According to **Karigar, et al., 2006**, there was a decline in the growth rate of immobilized cell of *Arthrobacter citreus* due to the inhibitory effects of phenol at 22mM.

3.3 The Potential of Using Immobilized Cells for Phenol Degradation

Results demonstrated complete degradation of phenol can be obtained using Pseudomonas immobilized in PVA-GG and PVA-AA beads in the first cycle after 150 min. In addition, to determine the validity of recycling immobilized cells of *Pseudomonas* was determined by carrying out consecutively excessive batch experiments using recycled beads. Results revealed that immobilized cells can be efficiently reused without decline in their biodegradation capability. The results of the phenol percentage removals for the last four excessive cycles were as following: 95, 92, 86, and 84 % for second, third, fourth, and fifth cycles, respectively using Pseudomonas immobilized in PVA-GG beads at degradation

period of 150 min. Whereby they were 96, 92, 90, and 84 % using Pseudomonas immobilized in PVA-AA beads for the same sequence of cycles. According to the results noted by, **Wang, et al., 2007,** the immobilized cells of *Acinetobacter sp.* degraded 69% of 100 mg phenol/L after two reuse cycles.

In this study as shown in **Fig. 4** and **Fig. 5**, this phenomenon could reduce expenses during operational periods, **Cai, et al., 2011**. However, the biodegradation rates of phenol were decreased slightly and gradually with the consecutive cycles due to the mechanical instability of beads and gradual leakage from their porous.

4. CONCLUSION

The physical freezing-thawing method of immobilization proposed in this study was shown to be a successful with natural polymers in phenol biodegradation. The biodegradation rate of phenol using *Pseudomonas* cells individually immobilized in PVA-GG and PVA-AA matrices was evaluated in a spouted bed bioreactor (SBBR). Experimental results demonstrated that complete removal of phenol can be obtained after 150 min using immobilized cells in both PVA-GG and PVA-AA beads. Also, the use of immobilized cells (IC) allowed to increase the number of biodegradation process cycles, but relatively reduced the degradation rate. However, excessive degradation cycles up to 5 cycles were carried out and results revealed that the potential recycling of immobilized cells for complete removal of phenol at different time periods. Results indicated that increasing the beads concentration resulted in the increasing the biodegradation rate of phenol since the increasing of beads resulted in increasing the biocatalyst cells concentration in these beads and therefore the degradation rate would be higher.

REFRENCES

- AL-Khalid, T., and EL-Nass, M., 2012, *Aerobic Biodegradation of Phenols: A Comprehensive Review. Critical Reviews*, Journal of Environmental Science and Technology, Vol.42, PP. 1631–1690.

- Al Zarooni, M., and Elshorbagy, W., 2006, *Characteristics and Assessment of Al Ruwais Refinery Wastewater*, Journal of Hazardous Materials, Vol.136, No.3, PP. 398-405.

- Bai, X., Ye, Z., Li, Y., Yang, L., Qua, Y., and Yang, X., 2010, *Preparation and Characterization of a Novel Macroporous Immobilized Microorganism Carrier*, Journal of Biochemical Engineering, Vol.49, PP. 264–270.

- Cai, T., Chen, L., Ren, Q., Cai, S., and Zhang, J., 2011, *The Biodegradation Pathway of Triethylamine and Its Biodegradation by Immobilized Arthrobacter protophormiae Cells*, Journal of Hazardous Materials, Vol.186, PP. 59-66.

- Chung, T.P., Tseng, H.Y., and Juang, R.S., 2003, *Mass transfer effect and intermediate detection for phenol degradation in immobilized Pseudomonas putida Systems*, Vol.38, No.10, PP. 1494-1507.

- Cozma, P., Hlihor, R., Apostol, L.C., Diaconu, M, Pogancean, M.O., and Gavrilescu, M., 2012, *Aerobic Biodegradation of Phenol by Activated Sludge in a Batch Reactor,* Journal of Environmental Engineering and Management, Vol.11, PP. 2053-2058.

- Cruz, I., Bashan, Y., Carmona, G., and Bashan, L., 2013, *Biological Deterioration of Alginate Beads Containing Immobilized Microalgae and Bacteria During Tertiary Wastewater Treatment,* Journal of Applied Microbiological Biotechnology, Vol.97, PP. 9847-9858.

- El-Gendy, N.Sh., and Nassar, H.N., 2015, *Kinetic Modeling of The Bioremediation of Diesel Oil Polluted Seawater Using Pseudomonas aeruginosa NH1.*, Journal of Energy Sources, part A: Recovery, Utilization, and Environmental Effects, Vol.37, PP.1147-1163.

- El-Naas, M.H., Al-Muhtaseb, S.A., and Makhlouf, S., 2009, *Biodegradation of Phenol by Pseudomonas Putida Immobilized in Polyvinyl Alcohol (PVA) Gel*, Journal of Hazardous Materials, Vol.164, PP. 720-725.

- El-Naas, M., Al-Zuhair, S., and Makhlouf, S., 2010, *Batch Degradation of Phenol in a Spouted Bed Bioreactor System,* Journal of Industrial and Engineering Chemistry, Vol.16, PP. 267–272.

- Karigar, C., Mahesh, A., Nagenahalli, M., and Yun, D.J., 2006, *Phenol Degradation by Immobilized Cells of Arthrobacter citreus,* Journal of Biodegradation, Vol.17, PP. 47–55.

- Kumar, D., Chauhan, P., Puri, N., and Gupta, N., 2014, *Production of Alkalin Thermostable Protease by Immobilized Cells of Alkalophilic Bacillus sp. NB 34*, International Journal of Current Microbiology & Applied Science, Vol.3, No.10, PP. 1063-1080.

- Kuyukina, M.S., Ivshina, I.B., Serebrennikova, M.K., Krivorutchko, A.B, Podorozhko, E.A., Ivanov, R.V., and Lozinsky, V.I., 2009, *Petroleum-Contaminated Water Treatment in Fluidized-Bed Bioreactor with Immobilized Rhosococcus Cells,* Journal of International Biodeterioration and Biodegradation, Vol.63, PP. 427-432.

- Loh, K.C., Chung, T.S., and Ang, W.F., 2000, *Immobilized-Cell Membrane Bioreactor for High Strength Phenol Wastewater,* Journal of Environmental engineering, January, PP. 75-79.

- Martins, S.C., Martins, C.M., and Fiuza, L.M., 2013, *Immobilization of microbial cells: a promising tool for treatment of toxic pollutants in industrial wastewater*, African Journal of Biotechnology, Vol.12, No.28, PP. 4412-4418.

- Michalowicz, J., and Duda, W., 2007, *Phenols – Sources and Toxicity*, Journal of Environmental Studies, Vol.16, No.3, PP. 347-362.

- Safont, B., Vitas, A.I., and Peñas, F.J., 2012, *Isolation and Characterization of Phenol Degrading Bacteria Immobilized onto Cyclodextrin-Hydrogel Particles within a Draft Tube Spouted Bed Bioreactor*, Journal of Biochemical Engineering, Vol.64, PP. 69-75.

- Stolarzewicz, I., Bialecka-Florjañczyk, E., Majewska, E., and Krzyczkowska, J., 2011, *Immobilization of Yeast on Polymeric Supports*, Journal of Chemical Biochemistry Engineering, Vol.25, PP. 135-144.

- Wang, Y., Tian, Y., Han, B., Zhaw, H., Bi, J., and Cai, B., 2007, *Biodegradation of Phenol by Free and Immobilized Acinetobacter sp. Strain PD12*, Journal of Environmental Science, Vol.19, PP. 222–225.

- Zhiguo, W., Lin, Y., Liu, H., Yia, Y., Shen, W., Hong, Q., Li, S., and Yao, H., 2012, *Characterization of The Nitrobenzene-degrading Strain Pseudomonas sp. a3 and use of its immobilized cells in the treatment of mixed aromatics wastewater*, Journal of Microbial Biotechnology, Vol.28, PP. 2679-2687.

NOMENCLATURE

AA: Agar-agar

CFU: Colony Forming-Unit

DW: Distilled water

FC: Free cells

GG: Guar gum

IC: Immobilized cells

IPM: Inoculum Production Medium

MSM: Mineral Salt Medium

PRW: Petroleum-Refinery Wastewater

PVA: Polyvinyl alcohol

rpm: revolution per minute

SBBR: Spouted bed bioreactor

VSS: Volatile Suspended Solids

Figure 1. Samples of the prepared beads.

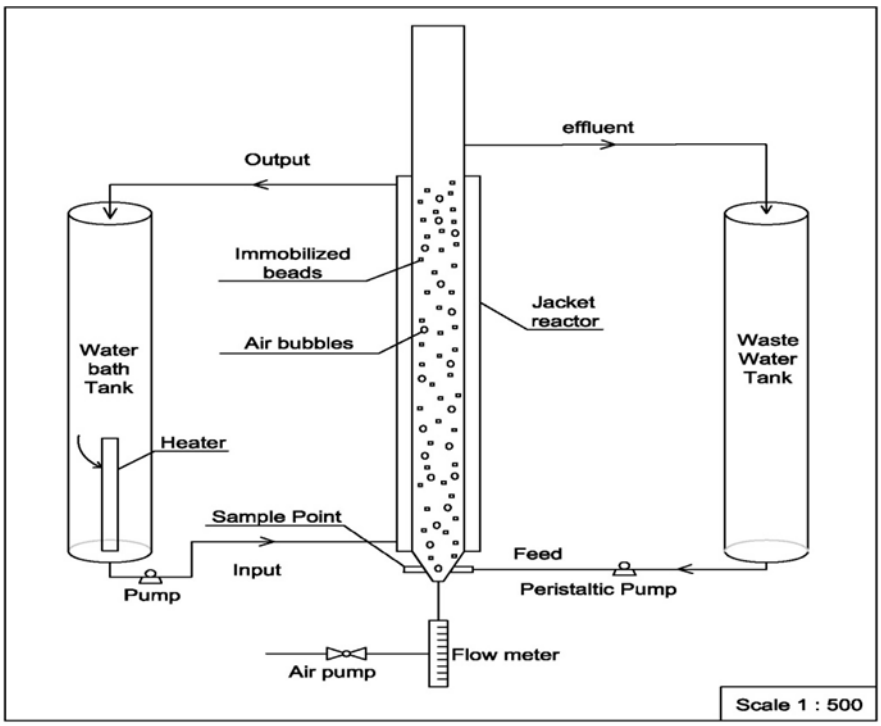

Figure 2. Schematic diagram of the lab-scale spouted bed bioreactor.

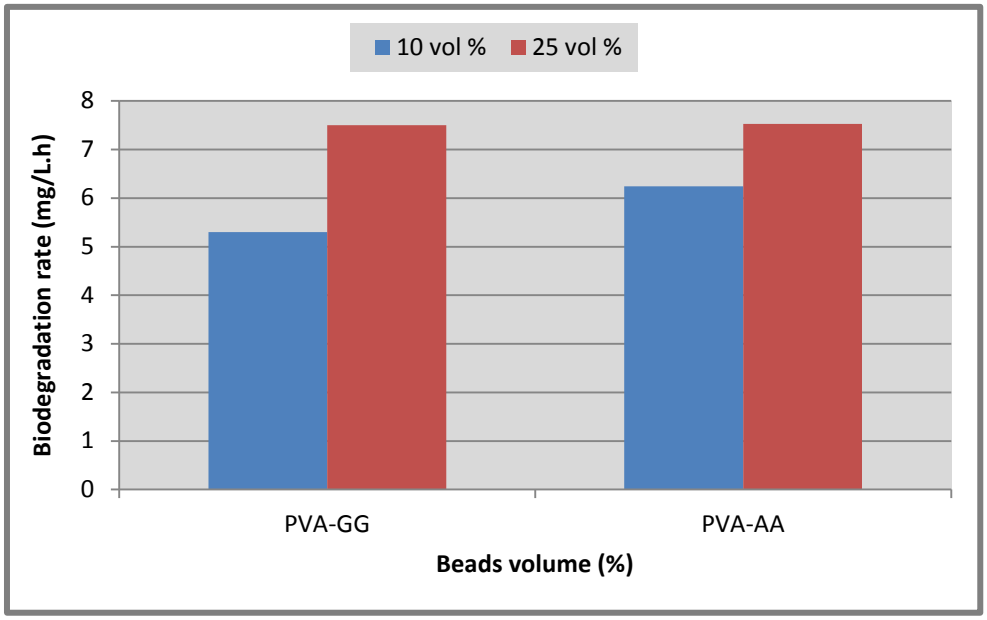

Figure 3. Biodegradation rate of phenol by Pseudomonas immobilized in two different bio-carriers using 20 mg/L initial phenol concentration .

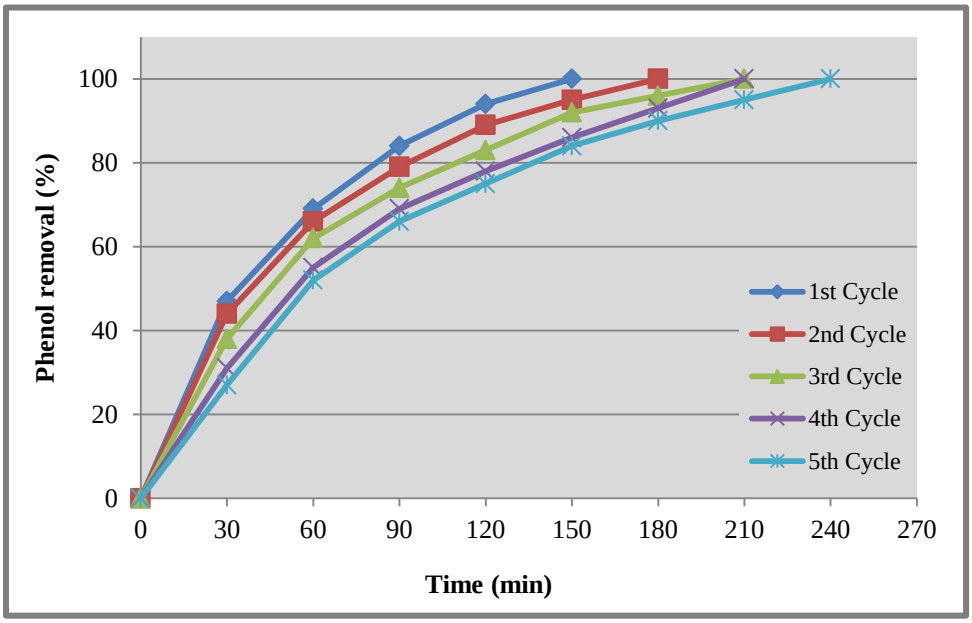

Figure 4. Profiles of phenol degradation by *Pseudomonas* cells immobilized in PVA-GG.

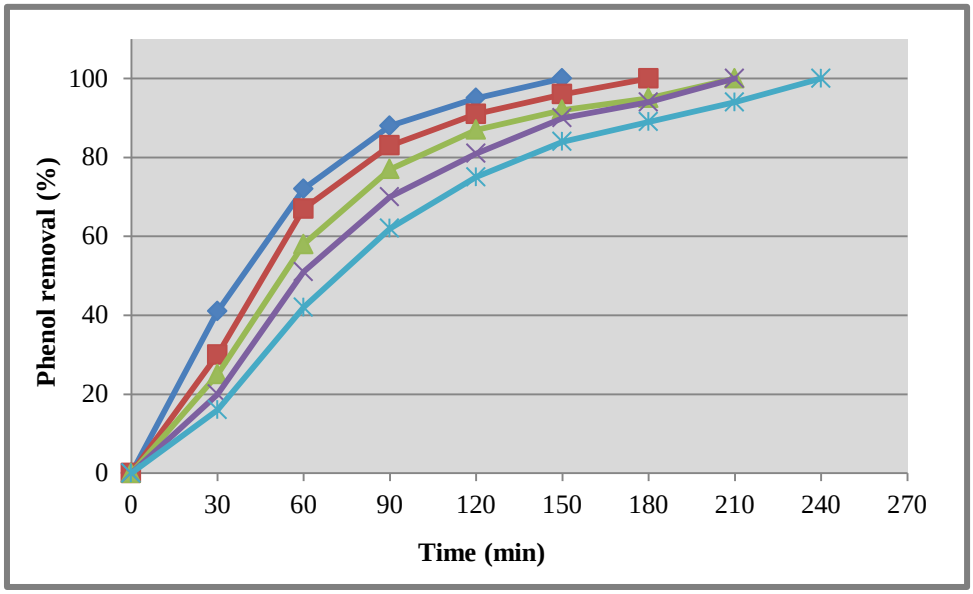

Figure 5. Profiles of phenol degradation by *Pseudomonas* cells immobilized in PVA-AA.

Table 1. Polymers used as bio-carriers in the study.

Name	Abbreviation	Chemical formula	Source	E. Code*
Polyvinyl alcohol	PVA	$(C_2H_4O)_n$	raw material of vinylon	———
Agar-Agar	AA	$(C_{12}H_{18}O_9)_n$	algal polysaccharides derivatives (Marine-Seaweed algae)	E406
Guar Gum	GG	$(C_6H_{10}O_5)_n$	Obtained from non-marine botanical resources	E412

*(E. Number): is a code for a substance that can be used as food additives within European Union & Switzerland.

Adding Cellulosic Ash to Composting Mix as a Soil Amendment

Asst. Prof. Jathwa Abd Alkareem Ibrahim
College of Engineering
Department of Environment Engineering
University of Baghdad
Email: Jathwa58@yahoo.com

Senior Eng. Omar Amer Hussein
Chemicals Division
Technical Department
Ministry of Environment
E mail:Omar_Amer85@yahoo.com

ABSTRACT

Solid waste generation and composition in Baghdad is typically affected by population growth, urbanization, improved economic conditions, changes in lifestyles and social and cultural habits.

A burning chamber was installed to burn cellulosic waste only. It was found that combustion reduced the original volume and weight of cellulosic waste by 97.4% and 85% respectively.

A batch composting study was performed to evaluate the feasibility of co-composting organic food waste with the cellulosic bottom ash in three different weight ratios (w/w) [95/5, 75/25, 50/50].

The composters were kept in controlled aerobic conditions for 7 days. Temperature, moisture, and pH were measured hourly as process successful indicators. Maximum temperature ranged between (41 to 53) ºC.

Results showed that the blend of M2 [OFMSW: BCA] [75:25] was the most beneficial to composting. It maintained the highest temperature for the longest duration for 9hrs. at (53) ºC, achieved the highest nitrogen content(1.65%) , a C/N ratio of (14.18 %), nitrification index(N-NH4/N-NO3) of (0.29),nitrogen, phosphorous and potassium(NPK)(1.65, 1.22, 1.73)% respectively, seed germination 80% indicating that the achieved compost is mature and stable.

Heavy metal contents (Cd, Cr, Cu, Mn, Ni, Pb and Zn) were detected in the above compost and all were lower than the regulation limits of the metal quality standards for compost and stabilized bio-waste.

Key words: cellulosic and organic waste, incineration, bottom ash, composting, seed germination

اضافة رماد المخلفات السليلوزية الصلبة الى المادة العضوية المتحللة كمحسن تربة

أ.م. جذوة عبد كريم ابراهيم
قسم هندسة البيئة
كلية الهندسة / جامعة بغداد

م.أ. عمر عامر حسين
قسم الكيمياويات
الدائرة الفنية / وزارة البيئة

الخلاصة

تتاثر معدلات تولد النفايات الصلبة ومكوناتها في مدينة بغداد بالنمو السكاني والمستوى الحضاري وتطور الحالة الاقتصادية والتغيير الحاصل في نمط الحياة واخيرا بالعادات الاجتماعية والثقافية.

وقد تم تصميم و صنع محرقة بمواد اولية محلية لغرض حرق 1 كغم من المخلفات السليلوزية حصرا وانتاج الرماد . بلغت نسبة نقصان الحجم 97.4% من الحجم الاصلي ونقصان الوزن 85% من الوزن الاصلي مما يؤكد فعالية عملية الحرق في تقليل الاوزان والاحجام للمخلفات السليلوزية.
تم اجراء عملية تحلل بايولوجي لثلاث خلطات مختلفة من مخلفات الطعام مع رماد المواد السليلوزية وبالنسب التالية (95:5 , 75:25 , 50:50).
استمرت عملية التحلل 7 ايام وتم تسجيل قراءات الحرارة ومحتوى الرطوبة ودرجة الحموضة على مدى ساعات التجربة و تعد هذه القراءات مؤشرات لنجاح عملية التحلل البيولوجي حيث تراوحت اعلى قيم درجات الحرارة للمفاعلات الثلاثة (41,53) م^0.
اثبتت النتائج النهائية ان افضل خلطة هي [75:25] M2 اذ انها احتفظت باعلى درجة حرارة 53 م^0 لمدة 9 ساعات ، واعلى نسبة من النتروجين (1.65%) , وكانت فحوصات% (NPK)(1.65, 1.22, 1.73) ومؤشر انضاج البذور % 80 والذي يعد مؤشر على الخصوبة وفق المحددات المعتمدة في البحث.
تم الكشف عن محتوى العناصر الثقيلة (Cd, Cr, Cu, Mn, Ni, Pb and Zn) في السماد العضوي للخلطة M2 اعلاه وقد كانت دون المحددات ومعايير النوعية لهذا النوع من الاسمدة الحيوية.

الكلمات الرئيسية : المخلفات السليلوزية والعضوية , الاحتراق , الرماد السفلي , السماد , انبات البذور

1. INTRODUCTION

Incineration is a common technique for treating waste, as it can reduce waste mass by 70% and volume by up to 90%, as well as providing recovery of energy from waste to generate electricity. Generally, municipal solid waste incineration (MSWI) produces several streams of ash: bottom ash and fly ash. Treatment processes may be applied to the combined ash or to individual streams, **Lam, et al, 2010**.

Such ash could better be used as a supplement to fertilizers as it contains a variety of micro nutrients and abound of potassium and calcium. Wood ash fertilization for example increases pH and concentration of dissolved organic carbon (DOC) in the soil solution and enhances the activity of soil microorganisms, **Jokinen, et al., 2006; Maljanen, et al., 2006; Bougnom,** and **Insam, 2009**.

Using the ash from MSW incinerators for environmentally sound application not only provides a low cost aggregate but further reduces the need for landfill capacity**, Huang, et al., 2011.**

In particular, incineration of waste containing heavy metals should be avoided to maintain suitable slag quality (however, ordinary household waste does contain small amounts of heavy metals)**, Song, et al., 2004.**

All waste disposal alternatives eventually decompose organic materials into simpler carbon molecules such as CO_2 (carbon dioxide) and CH_4 (methane), while incineration provides the best way to eliminate methane gas emissions and furthermore, energy obtained from waste incineration projects provides a substitute for fossil fuel combustion, **Lam, et al, 2010**.

If the organic waste is buried in pits under partially anaerobic conditions, it will be acted upon by anaerobic microorganisms with the release of methane and carbon dioxide; the organic residue left is good manure. This process is slower than aerobic composting and occurs naturally in landfills. However, thermophiles digestion leads to energy recovery through biogas generation, **Giusquiani, et al., 1988**.

The final product after this conversion is called compost (humus), which is of high agricultural value. It is used as fertilizer, and it is odorless with no pathogens.

Because of this composting process, volume of the waste can be brought down to 50–85% **, Tchobanoglous,** and **Kreith, 2002**.

Composting could be manual or mechanical. Manual composting is adopted in smaller urban centers while mechanical composting is adopted in big cities, **Zhou,** and **Wong , 2001.**

The recycling of the organic matter contained in municipal solid waste (MSW) as an amendment for agricultural soils after composting is a feasible option for conserving the organic matter levels in soil and also for improving soil quality and productivity, **Araújo, et al., 2010.**

Compost has been reported as having a great potential for retaining trace elements in non-available forms potentially reducing their overall bioavailability and toxicity due to several processes, including raising soil pH, complication, sorption, precipitation, or a combination of them, thus providing an effective soil remediation technique, **Brown, et al., 2003; Brown, et al., 2004.**

However, some drawbacks may happen with this technique, namely the potential mobilization of some elements in particular Cu associated to dissolved organic matter and the re-release of the immobilized elements after compost organic matter mineralization in the long term, **Zhou, and Wong , 2001.**

Therefore, the aim of this of this research is to produce a compost of high quality as a solid waste management approach by analyzing heavy metals content in cellulosic ash and applying the compost process as a treatment method to make food waste and paper ash mixture as a soil amendment meeting applicable regulations

2. EXPERIMENTAL WORK

The experimental work consisted of two stages. The first stage was to incinerate separated cellulosic waste, while the second stage was to prepare compost by composting food waste with previously prepared bottom ash in definite ratios.

2.1 Incineration of Separated Cellulosic Waste

A schematic diagram of the incineration chamber that was used in the experiment and work is shown in **Fig.1**. Only cellulosic waste was burned in manageable volumes so the fire does not get out of control.

2.1.1 The basis of the design of the combustion chamber

Combustion chamber was designed on the basis of burning of 1 kg of cellulosic waste, which equals to 0.015 m^3. The burning chamber was designed to be 0.025 m^3, where the excess size is 0.01 m^3 to provide enough space for air and for easy flipping for the sake of completion of combustion process.

2.1.2 Incinerator design

The burning chamber is normally 0.025 m^3 with a removable side, devices or features for higher burning temperatures, better mixing of air and suitable holding time, were affixed to the chamber. This chamber is made of heavy sheets of locally available materials 4 mm-ferrous alloy, with a side-covering lid to help in heat retention, suitable holding time inside the chamber, feed cellulosic materials, entering the combustion

flame, and flipping feed material during the burning process and provided with a chimney having a small slot for gas measuring that will be emitted during the process of burning.

A handmade waste distributer was used to turn burning material over and a handmade ash collector was used to collect totally burned waste.

A perforated steel plate was installed in the chamber, 10 cm a part from one end for ventilation to supply combustion air.

A pressure gage inlet air controlling gas and a compressor to pump air were provided for the combustion process.

Several burning test runs were held in order to optimize operational procedures and four runs were performed to collect bottom ash for analysis.

2.2 Composting Food Waste with Bottom Ash in Definite Ratios.

2.2.1 Materials and method

The preparation of the experimental samples was based on the representative components of MSW chosen from regular daily kitchen waste. The samples were mixed artificially according to definite ratios.

The composting system consisted of three plastic containers of 15 cm diameter and 30 cm height with screw covers as shown in **Fig.2**. The useful volume of each composter is 5.2 liter while the degree of initial filling is 75%. Approximately 2 kg of feed materials were introduced in each composter with different organic food municipal solid waste to bottom cellulosic ash (OFMSW: BCA) ratios according to definite C/N values.

C/N values were calculated using the following equation, **Tchobanoglous, et al., 1993**:

$$\frac{\text{C in 1 kg in OFMSW} + \text{C in x kg in BCA}}{\text{N in 1 kg in OFMSW} + \text{N in x kg in BCA}} = \text{C/N} \qquad (1)$$

Where:
C: Carbon percentage
N: Nitrogen percentage
OFMSW: Organic Food of Municipal Solid Waste in kg
BCA: Bottom Cellulosic ash in kg
X: weight of BCA in kg

Biodegradable (organic) waste was segregated at household level minced into pieces of <5 mm in diameter using a food processor (Brown, China), and mixed well with definite proportions of bottom cellulosic ash so as to achieve different C/N ratios. As leachate was formed during the composting process holes were made in the bottom of the composters for the release of this leachate. Temperature and moisture content were measured using sensors with platinum probe installed in the center inside each composter. Leaves were added as a bulking agent and as a source of nitrogen. Garden soil was also added to the mixture to provide more desired microorganisms, **Lin, et al., 2008**.Water was added as needed to facilitate the mixing and composting processes.

Experiments were carried out all together at one time to assess the effect of adding ash to the composting processes. Composting material was rolled every 12 h, for 5 min each time with open cover to ensure oxygen contact into the center of the composter and

regenerating heat. Composting is essentially completed when mixing no longer produces heat in the mixtures inside and temperature stands still, **Bass, et al., 1994 and Giannis, et al., 2012.**

2.3. Analytical Procedure

2.3.1 Characterization of the composting process

a. Temperature, pH and Moisture contents

The compost temperature, pH and moisture content were measured at regular time intervals throughout the composting period, using a digital thermometer. Measurements proceeded until the termination of the composting processes.

2.3.2 Characterization of the compost

a. Determination of organic matter and carbon

Organic matter was determined using combustion method, **ASAE, 2004**:

Two grams of sample were weighed and dried in an air oven at 105° C for 24 hr. The dried sample was weighed to determine dry weight (A). Then burned in afurnace at 550°C . After cooling,the sample was weighted to measure the ash weight (B).

The contents of organic matter and carbon are measured as follows**, Girovich, 1996**:

$$\% \text{ Organic matter} = (A-B)/A \times 100 \quad (2)$$

$$\% \text{ Carbon} = (\% \text{ organic matter}) / 1.8 \quad (3)$$

b. Determination of $N\text{-}NH_4$, $N\text{-}NO_3$ and Phosphorus

The content of nitrogen as ammonium and as nitrate and total phosphorous as P_2O_5 was determined by using Multi-Direct Photometer for multi-parameter analyses (lovibond) at Engineering Collage of Baghdad University / post graduate laboratories

c. pH

Ten grams of each sample were weighted and strewed into Erlenmeyer flasks with 100 ml of distilled water. The prepared sample was placed in an auto shaker for 30 min. pH of samples was measured by using a pH meter (Inolab WTW series)**, ASAE, 2004.**

d. Potassium and heavy metals concentrations

Potassium and heavy metals concentrations in BCA and in the final compost products were analyzed using Niton (XRF), Thermo scientific 900 heavy metals analyzer.

e. Germination Test

In order to employ the evaluated composts as plant growing media, the Germination Index (GI) was measured.

The germination test was performed for 48 h at 25°C in the dark with 20 radish seeds placed on a 9 cm filter paper (Whatman No. 1) soaked with 4 ml of compost extract and placed in a Petri dish, **Bertran, et al., 2004** as shown in **Fig. 3**.

The germination test was repeated with de-ionized water as a control, and repeated with extract of commercial compost.

The following equations were used to calculate the relative seed germination, relative root growth, and germination index (GI), **Zucconi, and Marco, 1997;Tiquia, et al., 1996** and **Marek, et al., 2003**:

$$\text{Relative seed germination (\%)} = \frac{\text{Number of seeds germinated in compost extract}}{\text{Number of seeds germinated in control}} \times 100 \quad (4)$$

$$\text{Relative rootgrowth(\%)} = \frac{\text{Mean root length in compost extract}}{\sqrt{\text{Mean root length in control}}} \times 100 \quad (5)$$

$$\text{GI (\%)} = \frac{\text{(Relative seed germination)x(Relative root growth)}}{100} \quad (6)$$

3. RESULTS AND DISCUSSION

3.1 Incineration of Separated Cellulosic Waste

3.1.1 Volume and weights percentage reduction

Table 1. represents volume and weight reduction of cellulosic waste due to the combustion process.

It can be noticed that combustion reduces the original volume and weight of the cellulosic waste by 97.4% and 85% respectively, still incineration is not very much practiced in Iraq.

3.2 Composting Food Waste With Bottom Ash in Definite Ratios.

3.2.1 C/N ratios

The C/N ratio was assumed to be 25 as a starting ratio using Eq. (1)**, Tchobanoglous, et al., 1993**:

(C/N) for mixing = 25: 1
(C/N) for OFMSW = 25.5:1
(C/N) for BCA = 20.5: 1
1. Moisture content of OFMSW= 60%
2. Moisture content of BCA = 8%
3. Nitrogen content of OFMSW = 2.6%
4. Nitrogen content of BCA= 0.5%

The percentage composition for OFMSW and BCA .

(a) For 1 kg of OFMSW
Water = 1 kg (0.60) = 0.60 kg
Dry matter = 1 kg - 0.60 kg = 0.40 kg
N = 0.40 kg (0.026) = 0.0104 kg
C = 25.5 (0.0104 kg) = 0.2652 kg

(b) For x kg of BCA:

Water = x kg (0.08) = 0.08 x kg

Dry matter = x kg - 0.08 x kg = 0.92 x kg

N = 0.92 x kg (0.005) = 0.0046 x kg

C = 20.5 (0.0046 x kg) = 0.0943 x kg

The amount of BCA to be added to 1 kg of OFMSW to achieve a C/N ratio of 25:

where x = weight of BCA required

$$\frac{0.2652\ \text{kg} + 0.0943\ (x)\ \text{kg}}{0.0104\ \text{kg} + 0.0046(x)\text{kg}} = 0.25\text{kg}$$

x = 0.25 kg BCA /1 kg OFMSW

Data are summarized in **Table 2.**

3.2.2 Physicochemical parameters of the composting process

a. Temperature

The temperature profile of the composting mixtures in each composter was measured at regular time intervals through the composting periods.

Fig. 4 shows the composting temperature variations as a function of composting time. The temperature follows a typical temperature profile for composting (mesophylic-thermophylic-mesophylic) phases. As seen, the temperature increased from ambient temperature to more than 40 °C, showing rapid initiation of the compost process. The substrates passed from an initial mesophylic phase (<30 °C) to the thermophylic phase after 18 hr. for mixture 1(M1), 15 hr. for mixture 2(M2), and 21 hr. for mixture 3(M3).

Comparing the mixtures it seems that higher temperature was achieved in the mixture of M2 (75% food waste:25% bottom cellulosic ash) by weight.

As the organic compounds were degraded, the mixture became richer in more stable compounds which were less accessible to the microorganisms. As a result corresponding temperature begun to decrease gradually reaching almost ambient temperature which represents a second mesophylic phase on the 36hr ofM1, the 42hr ofM2, and on the 30hr of M3.

Elevated temperatures (>50 °C) were maintained in one composter M2 for 9 hr. which is sufficient time for the sanitation of the substrate and to get rid of pathogenic microorganisms that exist in food waste. While lack of increasing in compost temperature of M1 and M3 may indicate low compost stability . Similar temperature profile was observed in related pilot scale composting experiments held locally by **Al-Zubaidi, 2013; Talib, 2014** and globally by **Tang, et al., 2007; Lu, et al., 2008; Elango, et al., 2009** and **Gao, et al., 2010**.

b. pH

Analysis of the pH curve on the basis of time in **Fig. 5** shows that the compost initial pH, was 9.0, 10.0 and 11.5 for M1, M2 , M3 respectively and declined over time and was moderated to the neutralization level.

The pH of the mature compost was near neutral (6.0–7.5) indicating a good quality compost and within the suggested range of (6–8.5) **(CCQC, 2001).**

This finding was closely related to **Sánchez-Mondero, et al., 2001; Huang, et al., 2011.**

c. Moisture content (Mc)

Moisture content is the most important factor that promotes and accelerates decomposition process.

The initial substrates were prepared to have relative high moisture content (75%, 72% and 80% for M1, M2 and M3 respectively). The moisture content was sustained at optimal levels around 50–70% to sustain the rmophylic phase.

At the final stage of composting water quantity was gradually decreased reaching at 54%, 39% and 59% at the final day of the process on the 7th, for M1, M2 and M3 respectively. Water, product of degradation, was expected to vaporize inside the composters and condensed on inner surface of containers and remained in the system. **Fig. 6** shows moisture content profiles.

d. Nitrogen content

Nitrogen content was measured at the end of each trial i.e. on the 7th day, it was found to be 1.5%, 1.65% and 1.04% for M1, M2 and M3 respectively as shown in **Table 3.**

During composting, nitrogen is metabolized mainly to ammonium while the non-soluble complexes of nitrogen decompose to soluble nitrogen forms that are readily available for metabolic activities. Gaseous nitrogen losses during composting occur mainly as ammonia but may also occur as nitrogen and nitrates oxides, **Eklind,** and **Kirchmann, 2000**.

On the other hand, in terms of dry weight, there is an increase in total nitrogen concentration due to the mineralization of organic matter and consequent loss of weight in the mass being composted through losses of CO_2 and H_2O, **Bane gas, et al., 2007** .

The initial substrate acquired 17.6, 21.2 and 31.0 C/N ratio, forM1, M2, and M3 respectively, while at the end of the process the C/N ratio had decreased to 14.13, 14.18 and 23.6 for M1, M2 and M3 respectively due to carbon consumption, which are qualified as good quality compost, **CCQC, 2001** and thus can be applied in agricultural land.

Researchers have suggested various ideal C/N ratios from more than 12 to lower than 25, **Brewer,** and **Sullivan, 2003; Rihani, et al., 2010** and **Al-zubaidi, 2013** depending on the initial feedstock. The ratios obtained in this survey for M1, M2 and M3 may be considered satisfactory**, CCQC, 2001**.

The degree of stability of the compost is also strictly related to the nitrification index N.I ($N\text{-}NH_4/N\text{-}NO_3$), and can be considered as an indicator of a high degree of compost stabilization**, Brinton, 2000; CCQC, 2001; Abouelwafa, et al., 2008** and **Huang, et al., 2011**.

In this survey, the acquired ratio was 0.2, 0.28 and 0.31, for M1, M2, and M3 respectively. ratios lower than 0.5 are the best mature compost**, Brinton, 2000** and **CCQC, 2001**.The nitrification index of 0.29 suggesting that M2 has the higher stability among the three mixtures as shown in **Table 4.**

e. Nitrogen, phosphorous and potassium (NPK)

Plants require more than a dozen different chemical elements. Nitrogen, phosphorus and potassium are the three main elements commonly supplied in fertilizers, while boron, copper, and manganese are sometimes also added in small quantities.

Ash is rich in two out of three of these main nutrients: phosphorous and potassium (nitrogen is lost during the combustion)**, Lam, 2010**. This means that ash can potentially supply P and K, replacing commercial fertilizers. Levels (NPK value) in the finished compost are important in determining the quality of compost, since those elements are essential nutrients for plant growth, **CCQC, 2001**.

Iyengar and Bhave in 2006 reported that the nitrogen, phosphorous and potassium (NPK) contents for compost should be more than 1% each.

The total N% was found to be 1.5%, 1.65% and 1.04% for M1, M2 and M3 respectively as previously mentioned in **Table 3**. The results shown in **Table 5** revealed that initial values of nutrient P as percentages decreased to 1.03, 1.22, and 0.87 for trials M1, M2, and M3 respectively. While the percentages of P in the original mixtures were 1.61 1.33, and 1.07 as percentages respectively . This reduction may be attributed to consumption of phosphoric compounds in cell growth .The amount of K values increased to 1.91, 1.73, and 1.89 as percentages for the three trials respectively. Accordingly the nutrients level of the end-product composts appeared to be sufficient for plant growth for all mixtures**,** **TMECC, 2002**.

f. Heavy metals

The concentration of heavy metals in BCA and in the end-product resulted from M1, M2 and M3 composting trials have been examined and presented in **Table 6**.The heavy metals concentrations in the composts were generally low and did not exceed the suggested limits by TMECC, Composting Council, 2002 as presented in **Table 6.**

High levels of aforementioned heavy metals in the composts represent an obvious concern if they are to be applied to food crops. Heavy metals do not degrade throughout the composting process, and frequently become more concentrated due to the microbial degradation and the loss of carbon and water from the compost, **Richard ,and Woodbury 1992.**

Compost produced from M1, M2 and M3 trials may be classified as first class compost based on the metal quality standards for compost, **Brinton, 2000** as shown in **Table 7**.

Total metal contents in compost are of concern when repeated applications to land occur. Field trials involving MSW compost application to soil have all reported an increase in soil and plant metal concentrations (e.g., Ni, Pb, Zn and Cu) **, Smith, 2009**.

g. Germination test

The compost obtained from M2, trial, after 7 days of composting of 72% moisture content and C/N ratio of 14.18 was used to carry out the germination test, to check the phytotoxic effect on plant growth**, Brinton, 2000**. .

The outcomes of the germination test are given in **Table 8** that shows 80% relative seed germination and 89 % root growth; the calculated value of germination index (GI) is 71.2 %, almost near to commercial compost extract outcomes having relative seed germination (70 %), root growth (76%) and GI (53.2%) as calculated below:

$$\text{Relative seed germintation } (\%) = \frac{8}{10} \text{ x } 100 = 80\%$$

$$\text{Relative } rootgrowth(\%) = \frac{0.89}{\sqrt{1}} \text{ x } 100 = 89\ \%$$

$$GI\ (\%) = \frac{(80)x(89)}{100} = 71.2\%$$

h. **Maturity assessment**

Compost is assigned a maturity rating of immature, mature, or very mature, pending the outcome of up to three parameters analyses. The compost C: N ratio is first evaluated: compost with a C: N ratio greater than 25:1 would be classified as immature compost; no further testing would be necessary needed for the maturity classification. If the C:N ratio is equal to or less than 25:1, then the compost must be evaluated for both stability and maturity using one of the indicators presented in **Table 9**, **TMECC, 2002.**

According to **Table 9** above M2 compost may be classified as mature compost.

4. CONCLUSIONS AND RECOMMENDATIONS.

4.1. Conclusions

1. Incineration proved to be a good cellulosic waste treatment. It can be noticed that combustion reduces the original volume and weight of cellulosic waste by 97.4% and 85% respectively.
2. Three different blend were suggested according to three C/N standard ratios to evaluate the feasibility of co-composting organic food waste with the cellulosic bottom ash [(M1) 95/5,(M2) 75/25,(M3) 50/50].
3. Results showed that the blend of M2 [OFMSW: BCA] [75:25] was most beneficial to composting. It maintained the highest temperature for the longest duration for 9 hrs. at (53) ºC, achieved the highest nitrogen content (1.65%) , a C/N ratio of (14.18 %), nitrification index (N-NH4/N-NO3) of (0.29), nitrogen, phosphorous and potassium (NPK)(1.65, 1.22, 1.73) %, Seed Germination 80 % indicating that the achieved compost is mature and stable according to regulations.
4. Heavy metal contents (Cd, Cr, Cu, Mn, Ni, Pb and Zn) were detected in the above compost and all were lower than the regulation limits of the metal quality standards for compost and stabilized bio-waste.

Finally the research proved a simple way of treating food solid waste with cellulosic bottom ash by turning these waste into useful biomass as soil amendment.

4.2 Recommendations

1. Government and its Ministries of Education, Health and Environment must collectively develop a plan that is recognized by all sectors of society to ensure the concept of environmental sustainability is understood and continues to be developed throughout society,

2. Encouraging recycling efforts, by giving incentives and tax exemptions where appropriate. Encourage public-private partnerships for instance giving licenses to private waste collectors.
3. Encouraging private sector to set up more recycling industries for recycling plastic and metallic solid waste. The private sector should also come up with strategies of reusing and conversion (composting) organic waste.

REFERENCES

- Abou el wafa, R., Ait Baddi, G., Souabi, S., Winterton, P., Cegarra, J., and Hafidi, M., 2008, *Aerobic Biodegradation of Sludge from the Effluent of a vegetable Oil Processing Plant Mixed with Household Waste: Physical–Chemical, Microbiological, and Spectroscopic Analysis*, Bio resource Technology, 99(18):8571-8577.

- Al-zubaidi, A. M., 2013, *Solid Wastes In-vessel Composting for Small Communities*, M.Sc. Thesis. University of Baghdad.

- Araújo, A.S., de Melo, W. J., and Singh, R. P., 2010, *Municipal Solid Waste Compost Amendment in Agricultural Soil: Changes in Soil Microbial Biomass*, Rev. Environ. Sci. Biotechnol, No.9, P:41–49.

- ASAE (2004). ASAE Standards, Food and processing Eng., ASAE, USA.

- Banegas, V, D., Moreno, J. L., Moreno, J. I., Garca, C.F., León, G.K., and Hernndez, T. I., 2007, *Composting Aanaerobic and Aerobic Sewage Sludge's Using Two Proportions of Sawdust*, Waste Management, 27, 1317–1327.

- Bass, L., *Extension Horticulture Specialist*, Bilder back T. E., *Extension Specialist, Nursery Crops* and Powell M. A., *Extension Horticulture Specialist*, 1994. A Guide to Managing Organic Yard Wastes.

- Bertran, E., Sort, X., Soliva, M., and Trillas, I., 2004, *Composting Winery Waste: Sludges and Grape Stalks*, Bio resource Technol. 95, 203–208.

- Bougnom , B. P., and Insam H., 2009, *Ash Additives to Compost Affect Soil Microbial Communities and Apple Seedling Growth*, AschezuschlagzuKompostbeeinflusst die mikrobielle Geme in schaft von BodensowieKeimung und Wachstum von Apfelsamlingen, Vol. 60, No. 2.

- Brewer, L.J.,and Sullivan, D.M., 2003, *Maturity and Stability Evaluation of Composted Yard Trimmings*, Compost Science and Utilization 11, 96–112.

- Brinton, W.F., 2000, *Compost Quality Standards and Guidelines*, an international view. Woods End Research Laboratory Inc., ME.

- Brown, S.L., Chaney R., Hallfrisch J., Ryan J.A., and Berti W.R., 2004, *In Situ Soil Treatments to Reduce the Phyto- and Bioavailability of Lead, Zinc, and Cadmium*, J. Environ. Qual., Vol. 33, P:522–531.

- Brown, S.L., Henry C.L. , Chaney R., Compton H., and DeVolder P.S., 2003, *Using Municipal Biosolids in Combination With Ether Residuals to Restore Metal-Contaminated Mining Areas*, Plant Soil, Vol. 249, P: 203–215.

- California Compost Quality Council (CCQC) Compost Maturity Index June 2001, *Compost Maturity Index*, California Compost Quality Council.

- Eklind, Y., and Kirchmann, H., 2000, *Composting and Storage of Organic Household Waste with Different Litter Amendments II: Nitrogen Turnover and Losses*, Bio resource Technology 74, 125–133.

- Elango, D., Thinakaran, N., Panneerselvam, P.,and Sivanesan, S., 2009, *Thermophilic Composting of Municipal Solid Waste*, Appl. Energy 865, 663–668.

- Gao, M., Li, B., Yu, A., Liang, F., Yang, L., and Sun, Y., 2010, *The Effect of Aeration Rate on Forced-Aeration Composting of Chicken Manure and Sawdust*, Bioresour.Technol. 101, 1899–1903.

- Giannis, A., Makripodis, G., Simantiraki, F., Somara, M. and Gidarakos, E., 2012, *Monitoring Operational and Leachate Characteristics of an Aerobic Simulated Landfill Bioreactor*, Waste Management 28 (8), 1346–1354.

- Girovich, M. J., 1996, *Biosolids Treatment and Management Processes for Beneficial Use*, Marcel Dekker, Inc.

- Giusquiani, P., Marucchinni C., and Businelli D., 1988, *Chemical Properties of Soil Amended with Compost of Urban Waste, Plant Soil*, Vol. 109, P: 73–78.

- Huang, G., Wang, X., and Han, L., 2011, *Rapid Estimation of Nutrients in Chicken Manure During Plant-Field Composting Using Physicochemical Properties*, Bioresour.Technol. 1022, 1455–1461.

- Iyengar, S.R., and Bhave, P.P., 2006, *In-vessel Composting of Household Wastes*, Waste Management 26, 1070–1080.

- Jokinen, H.K., Kiikkila O. and Fritze H., 2006, *Exploringthe Mechanisms Behind Elevated Microbial Activity After Wood Ash Application*, Soil Biol. Biochem, Vol. 38, PP:2285–2291.

- Lam , H. K., Alvin W. M. Ip, John P. Barford, and Gordon Mckay, 2010, *Use of Incineration MSW Ash: A Review*, Department of Chemical Engineering, Hong Kong University of Science and Technology, No. 2, P: 1943- 1968.

- Lin, Y.P., Huang, G.H. and Lu, H.W., 2008, *A simulation-Aided Factorial Analysis Approach for Characterizing Interactive Effects of System Factors on Composting Processe*, Science of the Total Environment 402 (2-3), 268–277.

- Lu, L.A., Kumar, M., Tsai, J.C., and Lin, J.G., 2008, *High-rate Composting of Dregs with Sewage Sludge in a pilot Scale Bioreactor*, Bio resource Technology 99, 2210–2217.

- Maljanen, M., Nykanen M., Moilanen and Martikinen P.J. , 2006, *Greenhouse Gas Fluxes of Coniferous Forest Floors as Affected by Wood Ash Addition*, Vol. 237, P: 143–149.

- Marek, S., Magdalena, J., and Roman, Z., 2003, *In-vessel Composting for Utilizing of Municipal Sewage Sludge*, Applied Energy 75, 249–256.

- Richard, T.L., and Woodbury, P.B., 1992, *The Impact of Separation on Heavy Metal Contaminants in Municipal Solid Waste Composts*, Biomass Bio energy. 3, 195–211.

- Rihani, M., DimitriMalamis, BouchraBihaoui, Samira Etahiri, Maria Loizidou, and Omar Assobhei, 2010, *In-vessel Treatment of Urban Primary Sludge by Aerobic Composting*,

- Sánchez-Mondero, M.A., Roig, A., Paredes, C., and Bernal, M.P., 2001, *Nitrogen Transformation During Organic Waste Composting by the Rutgers System and its Effects on pH, EC and Maturity of the Composting Mixtures*,Bio resource. Technol. 78, 301–308.

- Smith, S.R. , 2009, *A critical Review of the Bioavailability and Impacts of Heavy Metals in Municipal Solid Waste Composts Compared to Sewage Sludge*, Environ. Int., Vol. 35, P: 142–156.

- Song, G-J, Kim K-H, Seo Y-C, and Kim S-C., 2004, *Characteristics of Ashes from Different Locations at the MSW Incinerator Equipped with Various Air Pollution Control Devices*, Waste Management,Vol. 24, PP:99–106.

- Talib, R.A., 2014, *Biogas Recovery from Co-Anaerobic Digestion of Agro-Industrial Lingo Cellulosic Waste Materials for Clean Energy Production*, M.Sc. Thesis. University of Baghdad.

- Tang, J.-C., Shibata, A., Zhou, Q., and Katayama, A., 2007, *Effect of Temperature on Reaction Rate and Microbial Community in Composting of Cattle Manure with Rice Straw*, J. Bio sci. Bio Eng. 1044, 321–328.

- Tchobanoglous, G., and Kreith, F., 2002, *Handbook of Solid Waste Management*, McGraw-Hill, New York.

- Tchobanoglous, G., Thiesen, H. and Vigil, S. A. 1993, *Integrated Solid Waste Management*, p.134. McGraw Hill Book Co. New York, N.Y. U.S.A.

- Tiquia, S.M., Tam, N.F.Y., and Hodgkis, I.J., 1996, *Effect of Composting on Phytotoxicity of Spent Pig-Manure Sawdust Litter*, Environ. Pollute. 93, 249–256.

- TMECC, 2002, *Test Methods for the Examination of Composting and Compost*, USDA and US. Composting Council, Bethesda, MD.

- Zhou, L.X., and Wong J.W.C., 2001, *Effect of Dissolved Organic Matter From Sludge and Sludge Compost on Soil Copper Sorption*, J. Environ. Qual., Vol. 30 P: 878–883.

- Zucconi, F., and Marco, B., 1997, *Specifications for Solid Waste Compost*, BioCycle. 28(5):56-61.

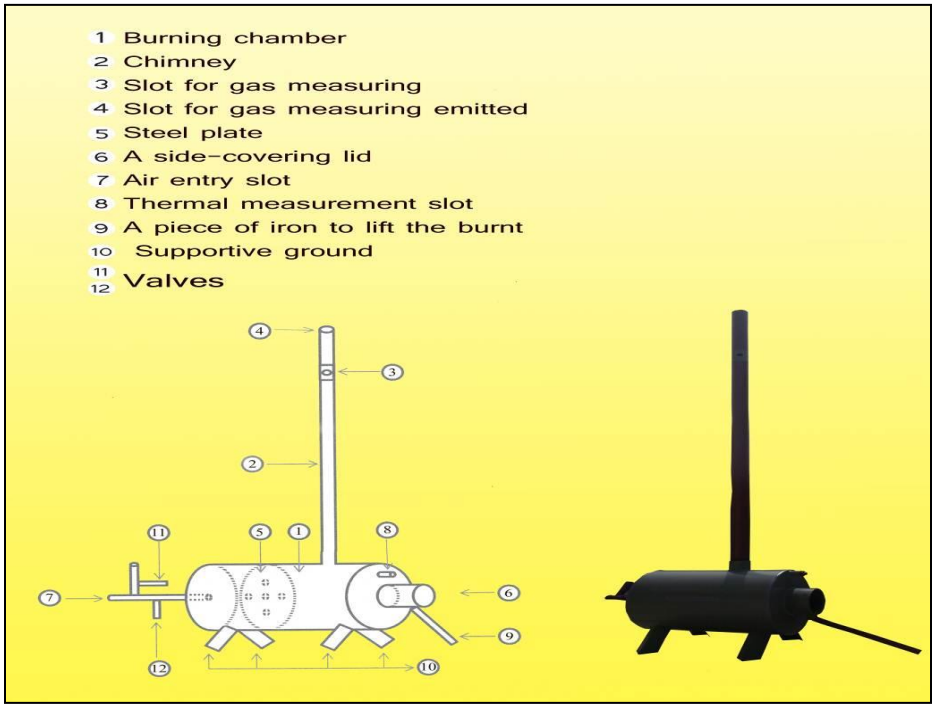

Figure 1. A schematic diagram of the incineration chamber .

Figure 2. Composters with three different OFMSW: BCA ratios.

Figure 3. Germination test with de-ionized water (1) and extract of commercial compost (3).

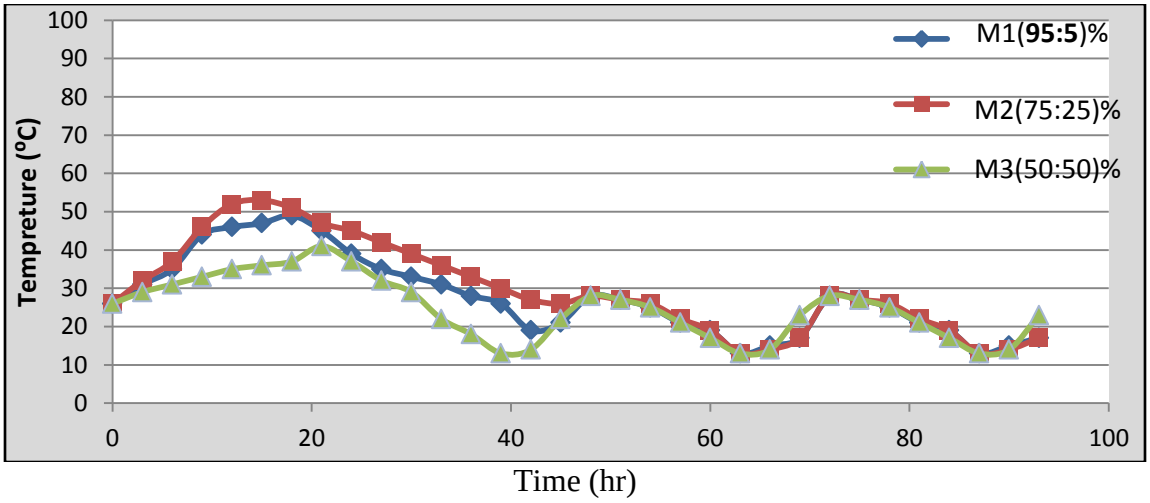

Figure 4. Temperature profile of M1, M2 and M3 as a function of time.

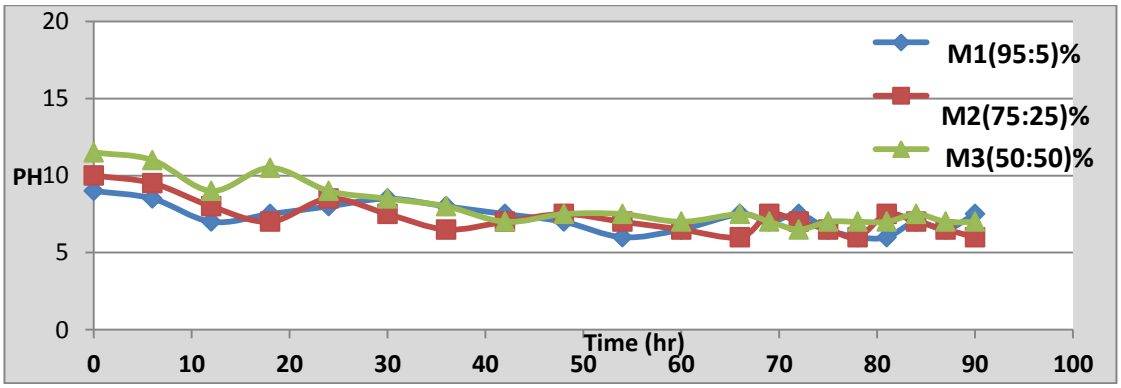

Figure 5. PH profile of M1, M2 and M3 as a function of time .

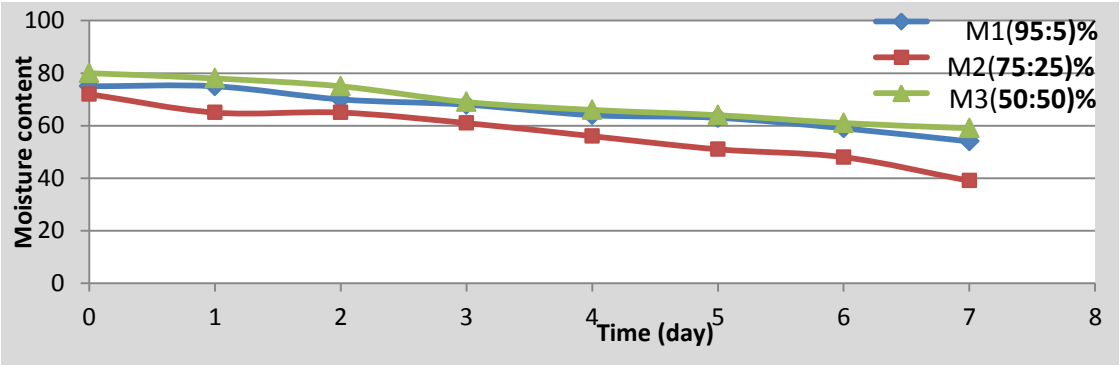

Figure 6 . Moisture profiles of M1, M2 and M3 as a function of time.

Table 1. Volume and weight reduction of cellulosic waste.

	Before combustion	After combustion	% reduction
Volume(m^3)	0.15	0.0039	97.4
Weight (kg)	10	1.5	85

Table 2. Percentage composition for food waste and ashes.

Mixture	OFMSW %	BCA%	OFMSW kg	BCA kg
M1	95	5	1.9	5
M2	75	25	1.5	0.5
M3	50	50	1	1

Table 3. Properties of initial and final compost .

	O.C.% INITIAL	O.C.% FINAL	N% INITIAL	N% FINAL	C/N INITIAL	C/N FINAL
M1 (95:5)	31.7	21.2	1.80	1.50	17.6	14.13
M2 (75:25)	35.8	23.4	1.69	1.65	21.2	14.18
M3 (50:50)	33.8	24.3	1.09	1.04	31.0	23.60

Table 4. Nitrification index for the concerned proportions .

mg/Kg	M1(95:5)	M2(75:25)	M3(50:50)
NH_4--N	267.90	312.40	399.40
NO_3+-N	848.30	1043.50	1150.80
NH_4--N/ NO_3+-N	0.31	0.29	0.34

Table 5. P and K levels in initial proportions and final composts .

	M1(95:5) Initial (final)	M2(75:25) Initial (final)	M3(50:50) Initial (final)	(TMECC, 2002)
P%	1.61 (1.03)	1.33 (1.22)	1.07 (0.87)	(0.56 -1.56)
K%	1.84 (1.91)	1.66 (1.73)	1.85 (1.89)	(0.62-1.22)

.

Table 6. Concentration of heavy metals in BCA and in compost end-product .

Metal mg/Kg	TMECC, 2002	BCA	M1 95:5	M2 25:75	M3 50:50
Cd	35	<LOD	<LOD	<LOD	<LOD
Cr	1200	<LOD	43	49	32
Cu	1500	114	55	12	44
Hg	7.8	<LOD	<LOD	<LOD	<LOD
Ni	420	<LOD	19	15	7
Pb	300	67	67	53	89
Zn	2800	173	188	154	96
As	41	<LOD	<LOD	<LOD	<LOD

LOD: Level of Detection

Table 7. Heavy metals concentration in M1, M2 and M3 compared to quality standards, **(Brinton, 2000)**.

Metal mg/Kg	Quality class A	M1	M2	M3
Cd	1.0	<LOD	<LOD	<LOD
Cr	50.0	43	49	32
Cu	60.0	55	12	44
Hg	0.3	<LOD	<LOD	<LOD
Ni	20.0	19	15	7
Pb	100.0	67	53	89
Zn	200.0	188	154	96
As	25.0	<LOD	<LOD	<LOD

Table 8. Outcomes of germination test.

Item/ parameter	Control test	Compost extract of M2	Compost extract of Commercial compost (beat moss)
Total seeds	10	10	10
Germinated seeds	10	8	7
Mean root length (cm)	1	0.89	0.76
Relative seed germination (%)	1	80	70
Relative root growth%	-	89	76
Germination index (%)	-	71.2	53.2

Table 9. Compost maturity indices **(TMECC, 2002) .**

Method	Units Rating		
	Very Mature	**Mature**	**Immature**
NH4- : NO3-N Ratio	< 0.5	0.5 - 3.0	> 3
Total NH3-N ppm	< 75	75 - 500	> 500
VOA ppm, dry basis	< 200	200 - 100	> 1,000
Seed Germination %	> 90	80 - 90	< 80
Plant Trials % of control	> 90	80 - 90	< 80
Nitrogen Draw-down	0	< 10%	> 25%

Numerical Study of Heat Transfer Enhancement in Heat Exchanger Using AL_2O_3 Nanofluids

Hussein Talal Dhaiban
Assist Lecturer
Refrigeration and Air-Conditioning Tech. - Dijlah University College
husseinayo@gmail.com

ABSTRACT

In this study, the flow and heat transfer characteristics of Al_2O_3-water nanofluids for a range of the Reynolds number of 3000, 4500, 6000 and 7500 with a range of volume concentration of 1%, 2%, 3% and 4% are studied numerically. The test rig consists of cold liquid loop, hot liquid loop and the test section which is counter flow double pipe heat exchanger with 1m length. The inner tube is made of smooth copper with diameter of 15mm. The outer tube is made of smooth copper with diameter of 50mm. The hot liquid flows through the outer tube and the cold liquid (or nanofluid) flow through the inner tube. The boundary condition of this study is thermally insulated the outer wall with uniform velocity at (0.2, 0.3, 0.4 and 0.5 m/s) at the cold loop and constant velocity at (0.5 m/s) at the hot loop.

The results show that the heat transfer coefficient and Nusselt number increased by increasing Reynolds number and particle concentration. Numerical results indicate that the maximum enhancement in Nusselt number and heat transfer coefficient were 9.5% and 13.5% respectively at Reynolds number of 7100 and particles volume fraction of 4%. Results of nanofluids also showed a good agreement with the available empirical correlation at particles volume fractions of 1%, 2% and 3%, but at volume fractions of 4% a slight deviation is obtained.

Keywords: heat transfer, heat exchanger, nanofluids.

دراسة عددية لتحسين انتقال الحرارة داخل مبادل حراري باستخدام نانو اوكسيد الالمنيوم-الماء

حسين طلال ذيبان
مدرس مساعد
هندسة تقنيات التبريد والتكييف - كلية دجلة الجامعة

الخلاصة

تمت عددياً دراسة خواص الجريان وانتقال الحرارة لمائع نانو اوكسيد الالمنيوم-الماء لمدى من عدد رينولدز 3000, 4500, 6000 و 7500 مع مدى من التركيز الحجمي لللدقائق من 1%, 2%, 3% و 4%. يتألف جهاز الاختبار من دورة باردة ودورة حارة مع جريان متعاكس للمائع داخل انبوب مزدوج متحد المركز بطول متر واحد. الانبوب الداخلي مصنوع من النحاس الاملس بقطر يعادل 15 مليمتر. والأنبوب الخارجي مصنوع من النحاس الاملس بقطر يعادل 50 مليمتر. جريان المائع الساخن خلال الانبوب الخارجي وجريان المائع البارد (او النانوي) خلال الانبوب الداخلي. الشروط الحدودية لهذه الدراسة هي السطح الخارجي معزول مع سرع متغيرة (0.2, 0.3 , 0.4 و 0.5)م\ثا للدورة الباردة وسرعة ثابتة (0.5)م\ثا للدورة الساخنة.

النتائج تبين ان معامل انتقال الحرارة وعدد نسيلت تزداد بزيادة عدد رينولد ومعامل التركيز الحجمي . والنتائج العددية تمثلت بأعلى نسبة تحسين لعدد نسلت ومعامل انتقال الحرارة ب 9.5% و 13.5% على التوالي عند عدد رينولد 7100 ومعامل التركيز الحجمي للجزيئات 4%.كذلك

النتائج بينت توافق جيد مع معادلة عددية عند معامل التركيزالحجمي للجزيئات 1%, 2% و 3% ولكن بمعامل الكسر الحجمي 4% حدث اختلاف بسيط .

1. INTRODUCTION

Rapid development in all sectors, which is infrastructure, industrial, transportation, defense, space; managing high thermal loads has become very critical. For that reason, several cooling technologies have been researched. However, the conventional technique of heat transfer by means of a flow system including fluids like water, ethylene glycol, mineral oils has always been popular and would always remain popular due to its simple nature. Conventional heat transfer systems used in applications like petrochemical, refining, and power generation are rather large and involve significant amount of heat transfer. However, in certain applications like electronics cooling in laptops and microprocessors, engine cooling in automobiles, cooling in power electronics used in military devices, cooling in space applications and many other areas, small heat transfer systems are required. These applications have a critical relationship between size of a mechanical system and the cost associated with manufacturing and operation. If improvements could be made in the existing heat transfer systems such as enhancing the performance of the heat transfer fluid, a lesser heat exchanger surface area and hence, a lesser space would be required to handle a specified amount of cooling load. The situation would lead to smaller heat transfer systems with lower capital costs and higher energy efficiencies. In this pursuit, numerous researchers have been investigating better techniques to enhance the thermal performance of heat transfer fluids. One of the methods used is to add nano-sized particles of highly thermally conductive materials like carbon, metal, metal oxides into the heat transfer fluid to improve the overall thermal conductivity of the fluid. The dispersion or suspension thus obtained is called nanofluid.

With the recent improvements in nanotechnology, the production of particles with sizes on the order of nanometers (nanoparticles) can be achieved with relative ease. Nanofluid (nanoparticles fluid suspensions) is the term coined by, **Choi,1995** to describe this new class of nanotechnology based heat transfer fluids that exhibit thermal properties superior to those of their host fluids or conventional particle fluid suspension. As a consequence, the idea of suspending these nanoparticles in a base liquid for improving thermal conductivity has been proposed recently,**Masuda, et al., 1993.**

2. HEAT TRANCFER ENHANCEMENT WITH NANOFLUIDS

A number of numerical and experimental studies were conducted to examine the effect of Al_2O_3-water nanofluids on heat exchanger enhancement under the laminar and turbulent regime. The configurations of heat transfer devices that were examined include concentric tube heat exchanger, some with twist and spiraled rod inserts, shell and tube heat exchanger, multichannel heat exchangers for electronic chip cooling.

Increase in the thermal conductivity of the working fluid improves the efficiency of the associated heat transfer process. When forced convection in tubes is considered, it is expected that heat transfer coefficient enhancement obtained by using a nanofluid is equal to the enhancement in thermal conductivity of the nanofluid, due to the definition of Nusselt number. However, research into the convective heat transfer of nanofluids indicates that the enhancement of heat transfer coefficient exceeds the thermal conductivity enhancement of nanofluids **,Hwang, 2009** and **Heris, 2006 and 2007.**

Pak and Cho, 1998, studied experimentally the heat transfer of Al_2O_3-water nanofluid at turbulent flow when detail of heat exchanger and the boundary conditions were circular pipe D=10.66 mm and length L=4.8 m at constant heat flux. At range of Reynolds number Re $=10^4 - 10^5$ and particle concentration (φ): 1.34%, 2.78% and 4.33% by volume. They found that the Nusselt number of the dispersed fluids for fully developed flow increased by increasing volume concentration as well as with Reynolds number. Also found that

maximum enhancement of heat transfer coefficient was 12% smallest than that in pure water at 3% particle concentration.

Fotukian and Esfahany, 2010, studied experimentally the turbulent flow of nanofluids with different volume concentrations (φ = 0.03%, 0.054%, 0.067% and 0.135% by volume) of nano particles flowing through shell and tube heat exchanger at constant wall temperature with range of Reynolds number from 6 x 10^4 to 3.1 x 10^4. Results had clearly showed a decrease in a the ratio of heat transfer coefficient of nanofluid with Reynolds number compared to that of pure water by 48% at φ = 0.054%.

Vasu et al., 2007, developed an empirical correlation for the thermal conductivity of Al_2O_3/water and Cu/water nanofluids, considering the effects of temperature, volume fraction and size of the nano particle. A correlation for the evaluation of Nusselt number was also developed, presented, and compared in graphical form. This enhanced thermo physical and heat transfer characteristics made fluids embedded with nano materials as excellent candidates for future applications.

Huminic and Huminic, 2011, used a three-dimensional analysis to study the heat transfer characteristics of a double-tube helical heat exchangers using nanofluids under laminar flow conditions. CuO and TiO_2 nanoparticles with diameters of (24 nm) dispersed in water with volume concentrations of (0.5–3 vol. %) were used as the working fluid. The mass flow rate of the nanofluid from the inner tube was kept and the mass flow rate of the water from the annulus was set at either half, full, or double the value. Effects of nanoparticles concentration level and of the Dean number on the heat transfer rates and heat transfer coefficients were presented. The results showed that for 2% CuO nanoparticles in water and same mass flow rate in inner tube and annulus, the heat transfer rate of the nanofluid is approximately (14%) greater than of pure water. The results also showed that the convective heat transfer coefficients of the nanofluids and water increases with increasing of the mass flow rate and with the Dean number.

Khalifa and Banwan, 2015, studied experimentally the effect of nanofluids with different volume concentrations (φ = 0.25%, 0.5%, 0.75% and 1% by volume) on heat transfer under turbulent regime in double concentric tube heat exchanger for four different volumetric flow rates of 150, 200, 250 and 300 L/h. Results showed the convective heat transfer increase by increasing particle concentration and flow rare. The maximum enhancement obtained in Nusselt number and heat transfer coefficient was 20 and 22.8% respectively, at Reynolds number6026 and particle concentration of 1%.

Nguyen et al., 2007, studied experimentally the investigation on turbulent heat transfer in closed system for cooling of microprocessors with Al_2O_3 nanofluids at particle concentration (φ) 1%, 3.1% and 6.8% by volume. The Reynolds numbers range that used in this study from 3 x 10^3 to 15 x 10^3. He concluded that the inclusion of nanoparticles into water produced a considerable enhancement of the cooling block convective heat transfer coefficient. Results showed the maximum enhancement in heat transfer coefficient was 40% at φ =6.8%.

Vajjha et al., 2010, investigated experimentally the heat transfer of Al_2O_3water nanofluid at turbulent flow. The detail of heat exchanger and the boundary conditions was circular pipe D=3.14 mm and length L=1.168 m at constant heat flux. The range of Reynolds number (Re) that used 3 x 10^3 – 1.6 x 10^4, the particle concentration 2%, 4%, 6%, 8% and 10% by volume. The results showed that by increasing the volume concentration, the wall shear stress and heat transfer rates increase also it showed the maximum enhancement of heat transfer coefficient was 81.74% at φ = 10% and Re = 7240.

The objectives of the study presented in this paper are to present the effect of heat transfer enhancement with and without Al_2O_3/water and comparison with other researches in a double-pipe heat exchanger.

3. HEAT EXCHANGER CONFIGURATION

The geometry consists of a three-dimensional counter flow double pipe heat exchanger with length equal to (l m). The outer diameter of the heat exchanger is equal to (50 mm) and the inner diameter of the heat exchanger is equal to (15 mm). The outer wall of heat exchanger is thermally insulated. The nanofluid enters the inner diameter (cold loop) with uniform velocity at (0.2, 0.3, 0.4 and 0.5 m/s) and temperature at (300 K). The velocity at hot loop of the outer diameter is constant at (0.5 m/s) with temperature at (350 K). The geometry is shown in **Fig. 1.**

4. THERMOPHYSICAL PRPPERTIES OF NANOFLUID

The calculation of nanofluid thermo physical properties is a crucial point since the results are strongly affected by them. As previously mentioned, the determination of nanofluids thermo physical properties is a very active area of research. The use of classical models is not certain for nanofluids, but, on the other hand, scarce experimental data on nanofluids are available to allow us to select a single model.

The physical properties of the nanofluid used in this work are calculated using the standard equations. **,Eastman, et al., 2001.**

The density (ρ_{nf}) in kg/m³is determined by the following equation

$$\rho_{nf} = \varphi \cdot \rho_p + (1-\varphi) \cdot \rho_{bf} \tag{1}$$

The specific heat $\left(C_{p_{nf}}\right)$in kJ/kg K is determined by the following equation

$$C_{p_{nf}} = (1-\varphi)Cp_{bf} + \varphi \cdot Cp_p \tag{2}$$

The following equation is used to calculate the viscosity ratio (μ_r)

$$\mu_r = \frac{\mu_{nf}}{\mu_{bf}} = 123\varphi^2 + 7.3\varphi + 1 \tag{3}$$

The thermal conductivity ratio (k_r) is calculated from

$$k_r = \frac{k_{nf}}{k_{bf}} = 4.97\varphi^2 + 2.27\varphi + 1 \tag{4}$$

Therefore, in our simulations the properties of nanofluids are temperature-dependent. Table 1.shows the properties of nanofluids at the inlet of internal pipe.

5. MATHEMATICAL CALCULATIONS

In the present study, the γ-Al_2O_3 nanoparticles dispersed in DI water were used to investigate the convective heat transfer coefficient and Nusselt number of the nanofluids. Thus, it can be calculated from the following equations:

The heat transfer rate into the cooling water $(Q_c)$is defined as:

$$Q_{bf} = \dot{m}_{bf} C_p \Delta T_{bf} \tag{5}$$

The heat transfer rate into the nanofluid$(Q_{nf})$is defined as:

$$Q_{nf} = \dot{m}_{nf} \cdot C_{p_{nf}} \Delta T_{nf} \quad (6)$$

The heat transfer coefficient (h) and the Nusselt number (Nu) of the cooling water are computed from the following equations:

$$h = \frac{Q_w}{A_S(T_W - T_f)} \quad (7)$$

$$Nu = \frac{hD}{k} \quad (8)$$

where $T_f = \frac{T_{in}+T_{out}}{2}$ (9)

The mathematical heat transfer coefficient $(h_{nf})$and Nusselt number of the nanofluid(Nu_{nf})are computed from the following equations:

$$h_{nf} = \frac{Q_{nf}}{A_s(T_w - T_{f,nf})} \quad (10)$$

$$Nu_{nf} = \frac{h_{nf} D}{k_{nf}} \quad (11)$$

The Reynolds number of cooling water (Re) and nanofluid (Re_{nf}) are obtained by the following equations:

$$Re = \frac{\rho_c \, v_c D_i}{\mu_w} \quad (12)$$

$$Re_{nf} = \frac{\rho_{nf} \, v_c D_i}{\mu_{nf}} \quad (13)$$

6. GOVERNING EGUATIONS

The basic equations that describe the flow and heat are conservation of mass, momentum and energy equations. These equations describe two-dimensional, turbulent and incompressible flow takes which the following forms, **Arnal, 1982.**

The assumptions that used for the instantaneous equation are:-

1- Steady, two-dimensional, incompressible flow, single phase flow, non-viscous, no slip, irrotational.
2- Cylindrical coordinate.
3- Thermal equilibrium between the nanoparticles and base fluid.

(i)*Conservation of Mass*

$$\frac{\partial}{\partial z}(\rho u) + \frac{1}{r}\frac{\partial}{\partial r}(\rho r v) = 0 \quad (14)$$

(ii) *Momentum Equations*

u-momentum (z-direction)

$$\frac{1}{r}[\frac{\partial}{\partial z}(\rho ruu)+\frac{\partial}{\partial r}(\rho ruv)]=-\frac{\partial p}{\partial z}+\frac{1}{r}[\frac{\partial}{\partial z}(r\mu_{eff}\frac{\partial u}{\partial z})+\frac{\partial}{\partial r}(r\mu_{eff}\frac{\partial u}{\partial r})]+S_u \quad (15)$$

vv-momentum (r-direction)

$$\frac{1}{r}[\frac{\partial}{\partial z}(\rho ruv)+\frac{\partial}{\partial r}(\rho rvv)]=-\frac{\partial p}{\partial r}+\frac{1}{r}[\frac{\partial}{\partial z}(r\mu_{eff}\frac{\partial v}{\partial z})+\frac{\partial}{\partial r}(r\mu_{eff}\frac{\partial v}{\partial r})-\Gamma^{v}\frac{v}{r^2}]+S_v \quad (16)$$

(iii) *Energy Equation*

$$\frac{1}{r}[\frac{\partial}{\partial z}(\rho ruT)+\frac{\partial}{\partial r}(\rho rvT)]=\frac{1}{r}[\frac{\partial}{\partial z}(r\Gamma_{eff}\frac{\partial T}{\partial z})+\frac{\partial}{\partial r}(r\Gamma_{eff}\frac{\partial T}{\partial r})] \quad (17)$$

The turbulence model utilized in this analysis is the two equation k-Epsilon model. This model is utilized for its proven accuracy in heat exchanger analysis and for its applicability to confined fluid flow. (k- ε) Turbulence Model is one of the most widely used turbulence models is the two-equation model of kinetic energy (k) and its dissipation rate (**ε**). The turbulence according to, **Launder and Spalding, 1972** is assumed to be characterized by its kinetic energy and dissipation rate (**ε**), where

(i) *Turbulence Energy, k*

$$\frac{1}{r}[\frac{\partial}{\partial z}(\rho ruk)+\frac{\partial}{\partial r}(\rho rvk)]=\frac{1}{r}[\frac{\partial}{\partial z}(r\Gamma^{k}\frac{\partial k}{\partial z})+\frac{\partial}{\partial r}(r\Gamma^{k}\frac{\partial k}{\partial r})]+G-\rho\varepsilon \quad (18)$$

(ii) *Energy Dissipation Rate, ε*

$$\frac{1}{r}[\frac{\partial}{\partial z}(\rho ru\varepsilon)+\frac{\partial}{\partial r}(\rho rv\varepsilon)]=\frac{1}{r}[\frac{\partial}{\partial z}(r\Gamma^{\varepsilon}\frac{\partial \varepsilon}{\partial z})+\frac{\partial}{\partial r}(r\Gamma^{\varepsilon}\frac{\partial \varepsilon}{\partial r})]+c_1\frac{\varepsilon}{k}G-c_2\rho\frac{\varepsilon^2}{k} \quad (19)$$

where

$$G=\mu_t\{2[(\frac{\partial u}{\partial z})^2+(\frac{\partial v}{\partial r})^2+(\frac{v}{r})^2]+(\frac{\partial u}{\partial z}+\frac{\partial v}{\partial r})^2\}+S_G \quad (20)$$

S_G given by**, Ideriah,1975**.

$$S_G=-\frac{2}{3}\mu_t\left[\frac{\partial u}{\partial z}+\frac{\partial v}{\partial r}\right]^2-\frac{2}{3}\rho k\left[\frac{\partial u}{\partial z}+\frac{\partial v}{\partial r}\right] \quad (21)$$

Also, $\mu_t=\rho c_\mu k^2/\varepsilon$ (22)

The values of the empirical constant used here are given in **Table 2**, **Launder and Spalding,1974.**

7. COMPUTATIONAL METHODOLOGY

Computational fluid dynamics (CFD) simulation is performed to analysis the heat transfer in heat exchanger. A commercially available CFD code**, Fluent 6.3.26, 2009,** was used to perform all simulations. Fluent is a pressure based flow solver that can be used with structured or unstructured grids. An unstructured grid was used for the study. Solutions were obtained by numerically solving the Navier-Stokes and energy equation through a control volume technique. All geometric construction and meshing were performed with (GAMBIT v2.4.6) program.

The meshing of the three-dimensional model starts with the completion of the geometric construction and assembly by using gambit program. During the building of these models it is critical to take into account the unique geometry and post-processing that will occur after a solution is obtained in fluent program, as this can significantly influence how a model is put together. Model construction, assembly and meshing require a trial and error approach that many times needs multiple iterations before a good geometry and mesh can be developed. Generally, the geometry is created from the ground up meaning that points are placed in the model with lines being drawn between points. Faces are made from lines and finally volumes emerge from the assembly of faces. **Fig. 2**shows the mesh of the test rigs of heat exchanger at tetrahedral cells.

Pressure and velocity were coupled with the Semi-Implicit Method for Pressure Linked Equations (SIMPLE) algorithm. SIMPLE uses a relationship between velocity and pressure corrections to obtain mass conservation and a pressure field.

Before starting any computations Fluent requires the flow to be initialized based on some condition within the model. This initialization process acts as an initial guess to the solution flow field. For all computational simulations the flow field is initialized by the inlet conditions of the cold water to start run the model.

Several times a solution could not be obtained due to the inability of the residual values to converge to an appropriate level. In cases where this issue is prevalent it is possible to adjust under-relaxation factors. The segregated solver uses under-relaxation to control the update of computed variables at iterations. Default values are generally set by Fluent to meet the demands of the widest range of flow scenarios. Unfortunately, these values do not always provide converged residual values for the models being investigated, so they are changed from their defaults values of 0.3, 0.7, 1.0, 0.8, 0.8 and 1.0 for pressure, momentum, energy, turbulent kinetic energy, turbulent dissipation rate and viscosity, respectively, to 0.2, 0.5, 0.8, 0.5, 0.5 and 0.9.

Solution convergence means that the results are essentially constant from iteration to iteration, and verifying this is a critical step to achieving accurate results. Convergence is declared on the basis of the following strict criteria: (i) global mass and energy imbalances drop below 0.01%; (ii) the flow field is unchanging, based on observation of profiles of velocity, pressure, temperature, and turbulence quantities in critical areas. There is no exact rule for determining when a solution is complete.

Fluent has defaults values of convergence set to (10^{-3}) for all quantities except energy, which is set to (10^{-6}). During this study the residuals were required to drop to values of (10^{-4}), with the exception of energy, which was required to reach (10^{-7}). **Fig. 3**shows scaled residuals of continuity, momentum, energy, k and ε as the solution progresses to convergence around 2500 iterations to reach the specified convergence levels.

8. RESULTS AND DISCUSSION

The nanopowder γ-Al_2O_3 with a base fluid of DI water with four different particles volume fractions of 1%, 2%, 3% and 4% and four different velocities of 0.2, 0.3, 0.4 and 0.5 (m/s) under turbulent flow regime were investigated in concentric counter flow heat exchanger to study the heat transfer enhancement due to nanofluids.

Before initiating systematic numerical on nanofluids, the reliability and accuracy of numerical measurements, were tested using DI water alone. Numerical results were compared with the prediction of Dittus-Boelter correlation, **Incropera and DeWitt, 2009,** shown below.

$$\left.\begin{array}{l} Nu = 0.023 Re^{0.8} Pr^{n} \\ \text{for } 1.5 \le Pr \le 500;\ 10^{4} \le Re \le 10^{6} \\ \text{where } n = 0.4 \text{ for heating.} \end{array}\right\} \quad (23)$$

Fig. 4 displays the calculated Nusselt number for pure water at various Reynolds numbers that compared with the equation given by Dittus–Boelter and found bad agreement because the high Reynolds number that deals with this correlation above 10^4. (The conditions in present study resemble at the conditions in the equation 23), but when compared with Gnielinski equation, **Bejan, 1993.**

$$\left.\begin{array}{l} Nu = 0.012\,(Re^{0.87} - 280)\,Pr^{0.4} \\ \text{for } 7 \le Pr \le 500;\ 3*10^3 \le Re \le 10^6 \end{array}\right\} \quad (24)$$

As it is shown an excellent agreement is observed with maximum deviation and average deviation of computed values from theoretical equation being 9 and 2%, respectively, over the range of the Reynolds numbers studied. This correlation given by Gnielinski equation over the traditional Dittus–Boelter equation, because the errors are usually limited to about ±10%. Also the last point in fluent shows higher than in Gnielinski, equation over 7000 Reynolds numbers because the higher separation flow at the velocity exit.

Fig. 5 indicates the comparison between the Nusselt number of nanofluids at four different particles volume fractions and four different volume flow rates at Reynolds number in the range 3000 and 7500 with that of DI water. The numerical results indicate that the Nusselt number of nanofluid is increased by increasing both the Reynolds number and particles volume fraction.

At 1% volume fraction, the Nusselt number is increased from 19.6 to 64.32 by increasing Reynolds number from 3000 to 7500, which are higher than those obtained for DI water alone by 1% and 10.5% respectively. At 2% volume fraction, the Nusselt number is increased from 19.65 to 65.2 by increasing the Reynolds number from 3000 to 7500, which are higher than those obtained for DI water alone by about 3% and 12.3%. For 3% volume fraction the Nusselt number increased from 20.576 to 66.2 by increasing Reynolds number from 3000 to 7000, these values are higher than the values of DI water by 5% and 15.3% respectively. At particles volume fraction of 4% the Nusselt number increased from 20.63 to 67.3 by increasing Reynolds number from 2800 to 7100, these values are higher than the values of DI water by 8.5% and 23.5% respectively.

Fig.6 indicates the contours of temperature distribution along the inner tube of cold flow at Reynolds number 6000 of pure water. This figure shows increasing in temperatures when the fluid moved toward the exit to record higher temperatures at the end tube (cold exit) when the hot flow input at high temperature.

Fig.7 illustrates the dimensionless Nu that presented by calculating the ratio (Nu_{nf}/Nu_w) at different volume fraction that increased from 1% to 4%, and different Reynolds numbers. The dimensionless Nu is at φ = 1% is found to increase from 1.0125 to 1.09 by increasing the Reynolds number from 3000 to 7500. For φ = 2% the dimensionless Nu value is 1.02 to 1.1 at Reynolds number of 3000 and 7500 respectively. Also at φ = 3%, the dimensionless Nu value is increased from 1.033 to 1.105 at Reynolds numbers of 3000 and 7500 respectively. At the highest particle volume fraction used of 4%, the dimensionless Nu is increased from 1.045 to 1.125 when the Reynolds number is increased from 3000 to 7500.

Fig.8 displays the comparison between heat transfer coefficient of DI water and nanofluid for four different particle volume fractions at varies Reynolds numbers. The fluent results indicate that the heat transfer coefficient is increased by increasing both the Reynolds number and particles volume fraction. The heat transfer coefficient (HTC) at φ = 1% is found to increase from 801.5 to 2645.3 by increasing the Reynolds number from 3000 to 7500. For φ = 2% the HTC value are 830.4 and 2723 at Reynolds number of 3000 and 7500 respectively. At φ = 3%, the HTC values are 896.77 and 2847.7 at Reynolds numbers of 3000 and 7500 respectively. At the highest particle volume fraction used of 4%, the HTC is increased from 912.6 to 2990 when the Reynolds number is increased from 3000 to 7500. Therefore, a better heat transfer is achieved and hence the relative gain in heat transfer is higher at lower Reynolds number for a fixed concentration.

The numerical values of Nusselt number with different particle volume fractions and Reynolds numbers are compared with empirical correlation, **Vajjha, et al., 2010,** that presented in **Fig.9.** The boundary conditions, Reynolds number range, base fluid and particles material for the correlation used in the comparison are given in **Table 3**.

$$Nu_{nf} = 0.065\left(Re_{nf}^{0.65} - 60.22\right)(1 + 0.0169\,\varphi^{0.15})Pr_{nf}^{0.542} \quad (25)$$

Fig.9 shows the comparison in particle volume fractions of 1%, 2%, 3% and 4% respectively. The numerical results show a good agreement with, **Vajjha et al., 2010,** correlation at volume fractions of 1%, 2% and 3% as shown in **Fig.9**. The deviation is found to increase with increasing Reynolds number. However, at volume fractions of 4%, the deviation is increased, which may be caused by several effects such as different in configuration of the test section and boundary condition.

9. CONCLUSION

In this study, the flow and heat transfer characteristics of Al_2O_3-water nanofluids for a range of the Reynolds number (3000 to 7500) with a range of volume concentration (1 to 4%) are studied numerically.

- The results show that both the Nusselt number and the heat transfer coefficient of nanofluid are strongly dependent on nanoparticles and increase by increasing of the volume concentration of nanoparticles.
- A good agreement is obtained between the numerical data for water and the results obtained from Gnielinski correlation with a maximum deviation of about 3%.
- The heat transfer coefficient and Nusselt number are increased by increasing Reynolds number.
- Numerical results indicate that the minimum enhancement in Nusselt number and heat transfer coefficient are 1.5% and 4% respectively at Reynolds number of 3000 and particles volume fraction of 1%.
- Numerical results indicate that the maximum enhancement in Nusselt number and heat transfer coefficient are 9.5% and 13.5% respectively at Reynolds number of 7500 and particles volume fraction of 4%.
- These results are in good agreement with correlation of, **Vajjha et al., 2010.**

REFERENCES

- Arnal, M.P., 1982, *A General Computer Program for Two-Dimensional, Turbulent, Re-Circulating Flows*, report No.Fm-83-2.
- Bejan, 1993, Heat Transfer, text book, John Wiley & Sons, New Jersey.
- Choi, S. U. S.,1995, *Enhancing Thermal Conductivity of Fluids with Nanoparticles*, Developments and Applications of Non-Newtonian Flows, The American Society of Mechanical Engineers, New York, FED-Vol. 231 / MD-Vol.66, pp. 99-105.
- Eastman, J. A., Choi, S., Li, S., Yu, W., and Thompson, L. J., 2001, *Anomalously Increased Effective Thermal Conductivities of Ethylene Glycol-Based Nanofluids Containing Copper Nanoparticles*, Appl. Phys. Lett.,Vol. 78(6), pp. 718-720.
- Fotukian, S. M., and Esfahany, M. N., 2010, *Experimental Investigation of Turbulent Convective Heat Transfer of Dilute γ-Al_2O_3/water Nanofluids Inside a Circular Tube*, International Journal of Heat and Fluid Flow; Vol. 31, pp. 606–612.

- Fluent Inc., 2009, *Fluent User's Guide, Version 6.3.26*.
- Hwang, K. S., Jang, S. P., and Choi, S. U. S.2009, *Flow and Convective Heat Transfer Characteristics of Water-Based Al_2O_3Nanofluids in Fully Developed Laminar Flow Regime*, Int. J. Heat Mass Tran., Vol. 52(1-2), pp. 193-199.
- Heris, S. Z., Etemad, S., and Esfahany, M. N., 2006, *Experimental Investigation of Oxide Nanofluids Laminar Flow Convective Heat Transfer*, Int. Commun. Heat Mass, Vol. 33(4), pp. 529-535.
- Heris, S. Z., Esfahany, M. N., and Etemad, S.,2007,*Experimental Investigation of Convective Heat Transfer of Al_2O_3/Water Nanofluid in Circular Tube*, Int. J. Heat Fluid Fl., Vol. 28(2), pp. 203-210.
- Huminic, G., and Huminic, A., 2011,*Heat Transfer Characteristics in Double Tube Helical Heat Exchangers Using Nanofluids*, Int. J. Heat Mass Tran., Vol. 54, pp. 4280–4287.
- Ideriah, F. J. K., 1975, *Review of Equation Solved in TEACH*, private communication.
- Incropera, F.P., and DeWitt, D.P., 2009, *Fundamentals of Heat and Mass Transfer*, text book, Springer.
- Khalifa, A. J. N, and Banwan, M. A., 2015, *Effect of Volume Fraction of γ-Al_2O_3Nanofluid on Heat Transfer Enhancement in a Concentric Tube Heat Exchanger*, Taylor and Francis group, heat transfer engineering, Vol. 36(16), pp. 1387-1396.
- Launder, B.E. and Spalding, D.B., 1972, *Mathematical models of turbulence*, text book, Academic press, London.
- Masuda, H., Ebata, A., Teramae, K., and Hishinuma, N., 1993, *Alteration of Thermal Conductivity and Viscosity of Liquid by Dispersing Ultra-Fine Particles (Dispersion of γ-$Al_2O_{3_3}$, SiO_2, and TiO_2Ultra-Fine Particles)*,NetsuBussei, Vol. 4(4), pp. 227-233.
- Nguyen, C. T., Roy, G., Gauthier, C., and Galanis, N.,2007, *Heat Transfer Enhancement Using Al_2O_3 –Water Nanofluid, for an Electronic Liquid /cooling System*, Applied Thermal Engineering, Vol. 27, pp. 1501-1506.
- Pak, B. C., and Cho, Y. I., 1998, *Hydrodynamic and Heat Transfer Study of Dispersed Fluids with Submicron Metallic Oxide Particles*, Exp. Heat Transfer, Vol. 11(2), pp. 151-170.
- Vajjha, RS., Das, DK., and Kulkarni, DP., 2010, *Development of New Correlations for Convective Heat Transfer and Friction Factor In Turbulent Regime for Nanofluids*, Int. J. Heat Mass Tran., Vol. 53, pp. 4607–4618.
- Vasu, V., Krishna K., and Kumar A.C.S., 2007, *Analytical Prediction of Forced Convective Heat Transfer of Fluids Embedded with Nano Structured Materials (Nanofluids)*, Vol. 69, pp. 411-421.

NOMENCLATURE

Symbol	*Description*	Dimension
A	Area	m^2
As	circumference area ($A_s = \pi DL$)	m^2
C_P	spesific heat at constant pressure	kJ/kg.K
P	pressure	Pa
Re	Reynolds number ($Re=\rho UD/\mu$)	
Nu	Nusselt number (hd/k)	
T	temperature	˚C
u ,v	velocity component in r, z respectively	m/s
Pr	Prandtl number	
$\dot{m}$	mass flow rate	kg/s
μ_r	viscosity ratio	
K	thermal conductivity	W/m.K
Q	heat transfer rate	W
Γ	diffusion coefficient	N.s / m^2
U_h	velocity at hot loop	m/s
U_c	velocity at cold loop	m/s
T_g	temperature of hot gases	˚C
T_c	temperature at cold loop	˚C
T_h	temperature at hot loop	˚C
r,z	cylindrical coordinate	
L	Length	M
D	diameter	M
Greek Letters		
Φ	particles volume fraction	
ρ	density	kg/m^3
ε	rate of dissipation of kinetic energy	m^2/s^{-3}
μ	viscosity	$N.m/s^2$
Subscript		
nf	Nanofluid	
bf	base fluid (water)	
c	cold flow	
h	hot flow	
f	Film	
w	Wall	
Abbreviation		
DI	de ionized	
HTC	heat transfer coefficient	
SIMPLE	semi-implicit method for pressure linked equation	

Table1. Properties of nanofluids at the inlet of the inner pipe.

Type of fluid	φ(%)	ρ(kg/m3)	μ(Pa.s)*10^{-3}	Cp(J/kg.K)	K_{eff}(W/m.K)	Pr
Pure water	0	998.2	1	4182	0.6	6.5
Al_2O_3/water	1	1027.4	1.02	4046.96	0.617	6.7
Al_2O_3/water	2	1057.2	1.13	3922.46	0.635	7
Al_2O_3/water	3	1086.9	1.26	3804.78	0.653	7.3
Al_2O_3/water	4	1116.6	1.41	3693.36	0.671	7.8

Table2. Values of constants in the (k-ε) model, **Launder and Spalding, 1972.**

C_μ	C_D	C_1	C_2	σ_k	σ_ε
0.09	1.0	1.44	1.92	1.0	1.3

Table3. Nanofluids, boundary conditions and Reynolds range for the correlation used in the comparison, **Vajjha et al., 2010**.

Author	Nanofluids	Conditions	Re range
Vajjha et al.	Cu,SiO_2, Al_2O_3	Turbulent	3000-16000

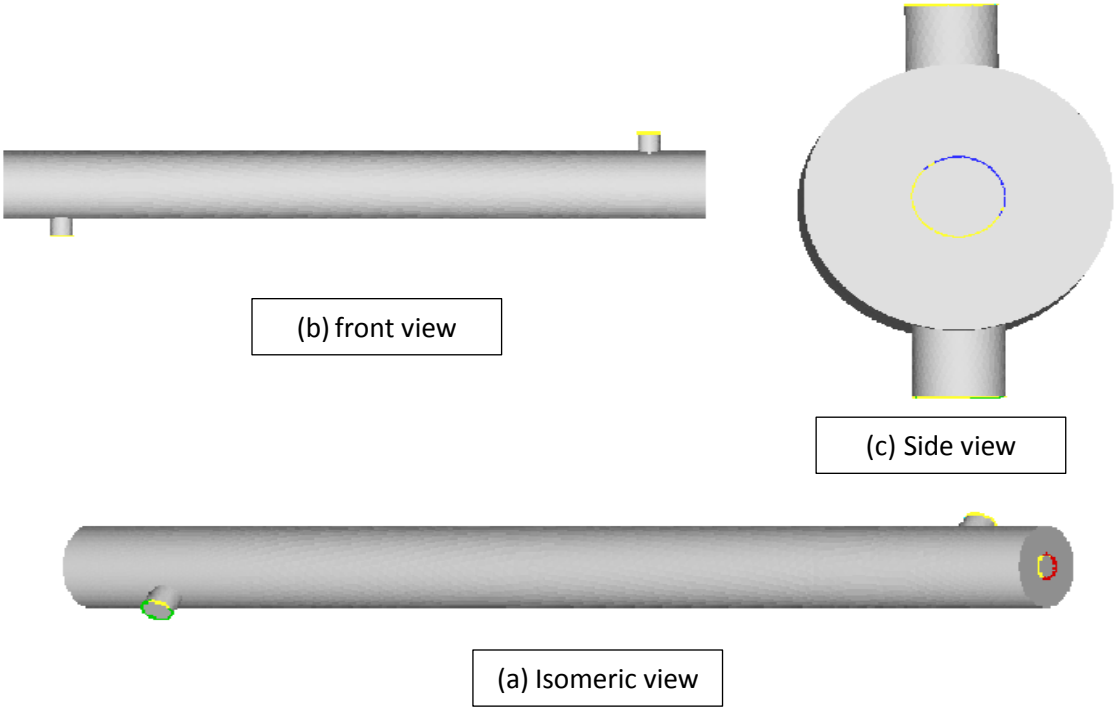

Figure 1. Heat exchanger geometry.

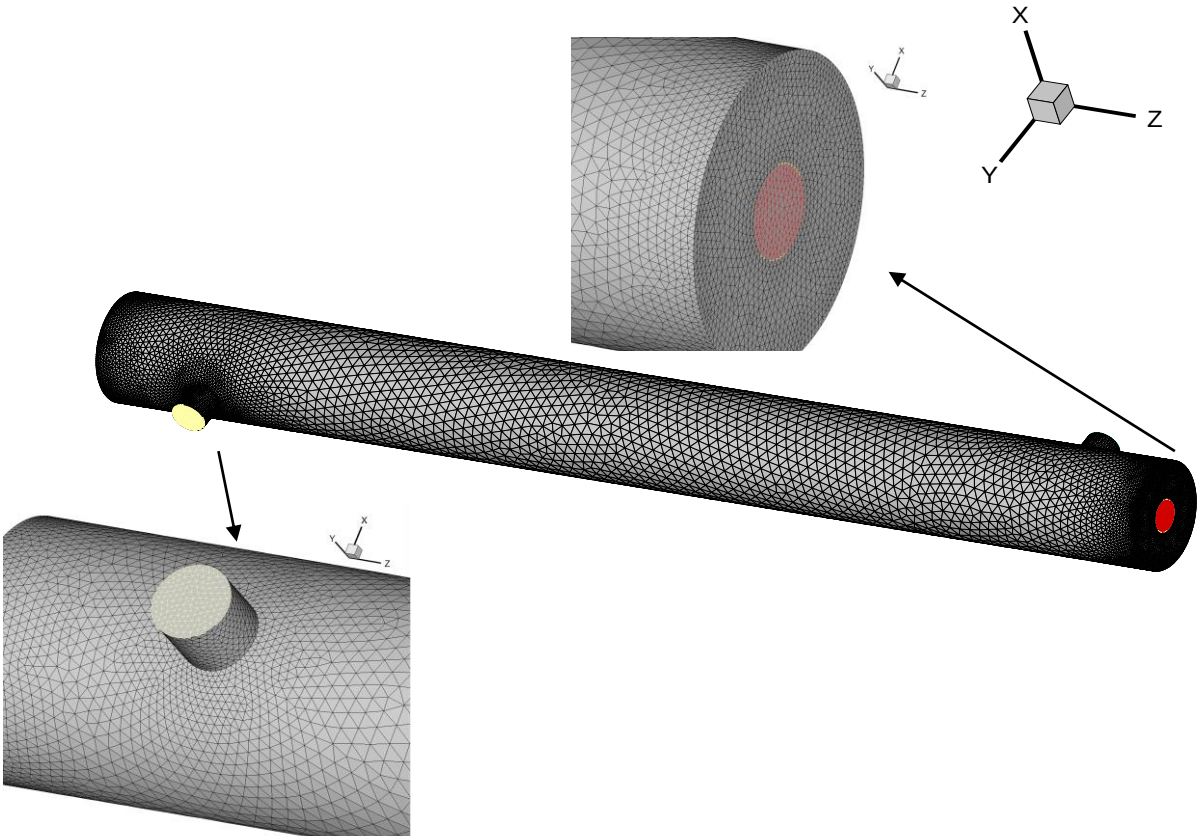

Figure 2. Heat exchanger mesh with tetrahedral cell.

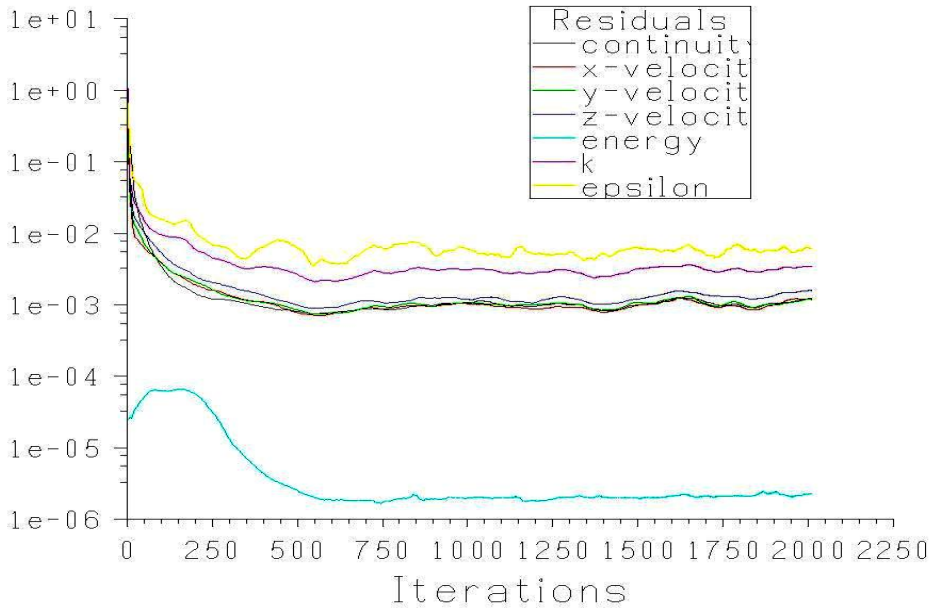

Figure 3. Typical residual convergence for heat exchanger model at Re=6000.

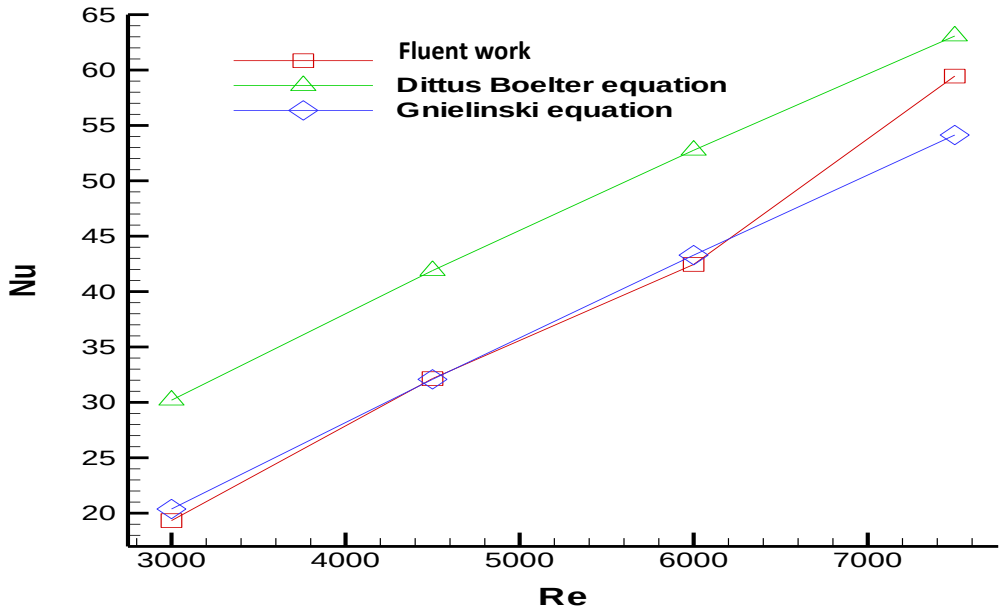

Figure 4. Comparison between the computed values of the Nusselt numbers and the equations given by Gnielinski and Dlttus -Boelterfor water.

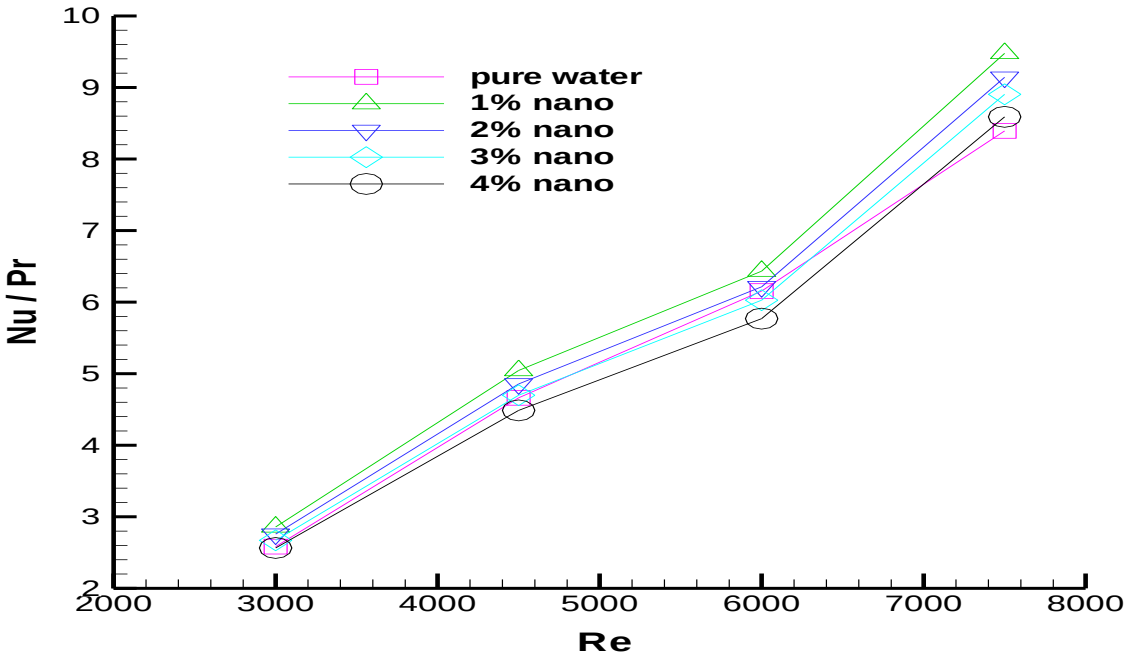

Figure 5. Comparison between dimensionless Nusselt/Prandtl numbers of nanofluids and DI water.

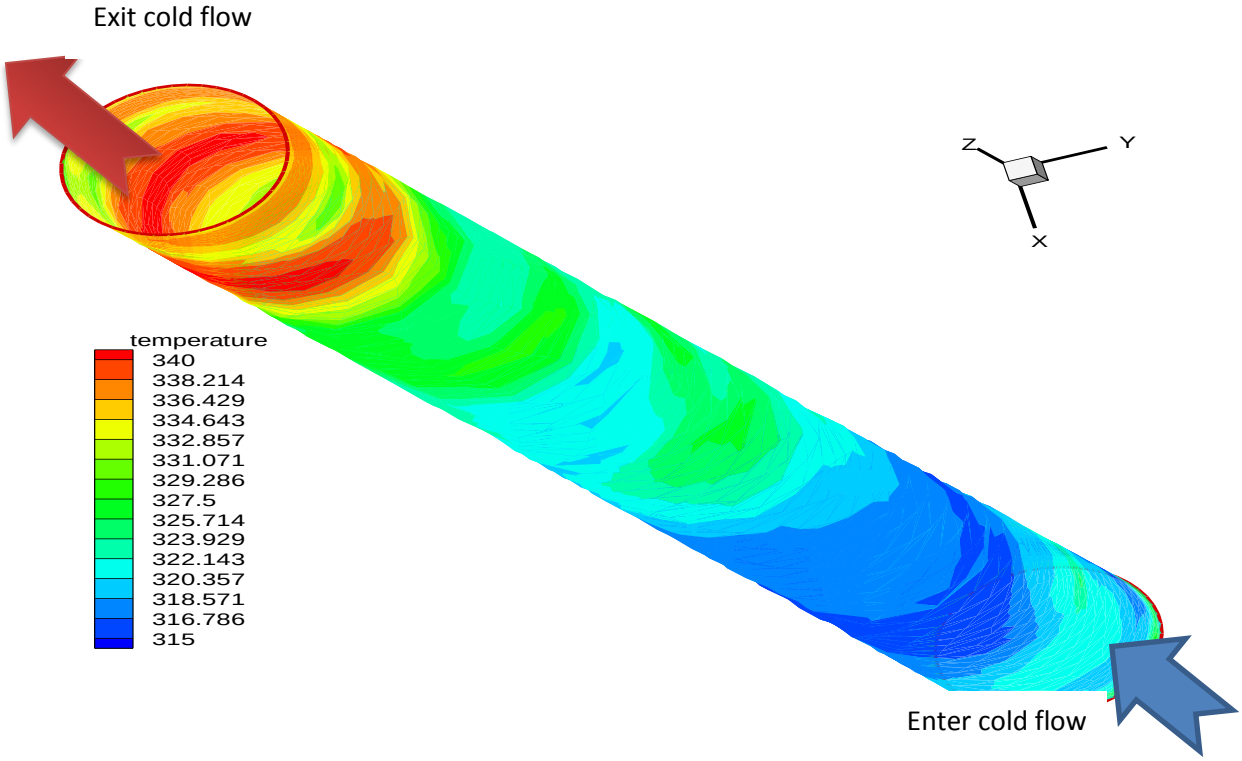

Figure 6. Contours of temperature distribution along the inner tube at Re=6000 of pure water.

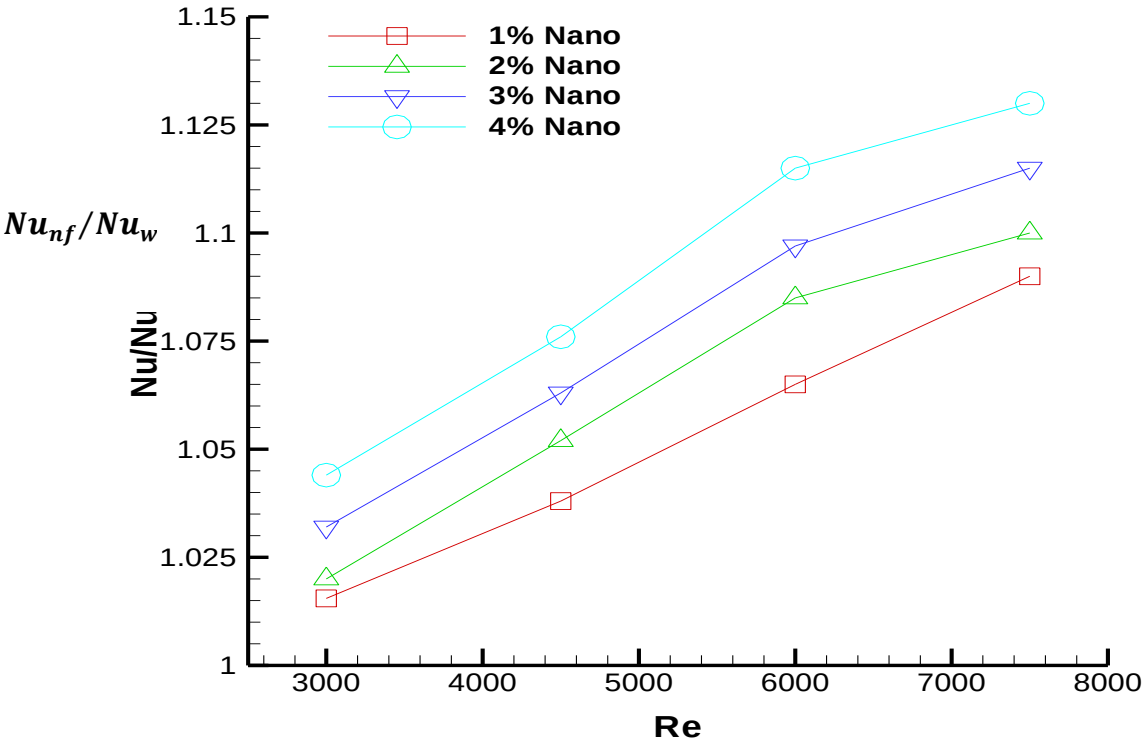

Figure 7. The ratio of (Nu_{nf}/Nu_w) at various Reynolds numbers and particles volume fractions.

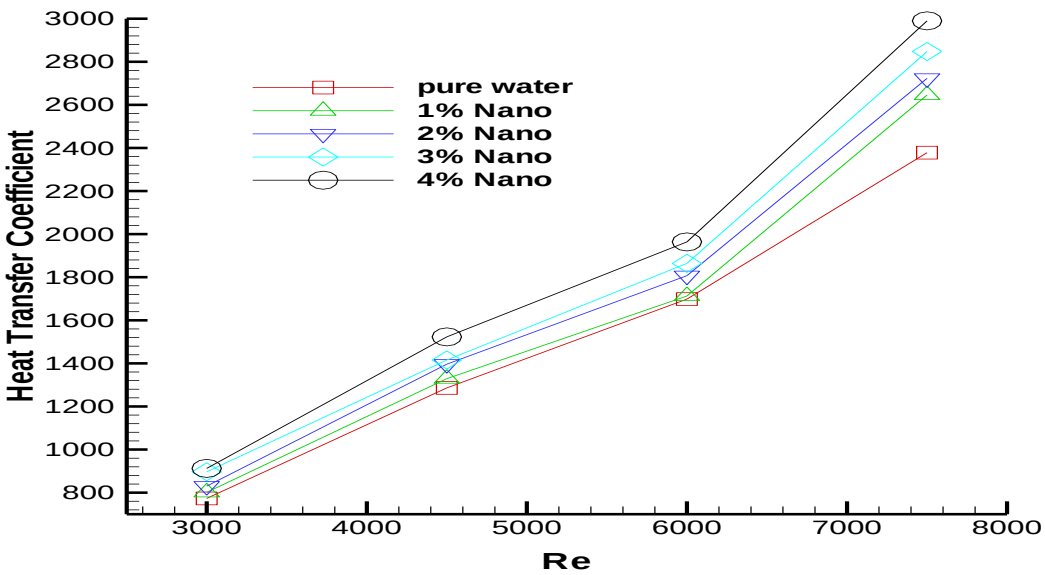

Figure 8. Heat transfer coefficient of nanofluids an DI water at various particles volume fractions and Reynolds numbers.

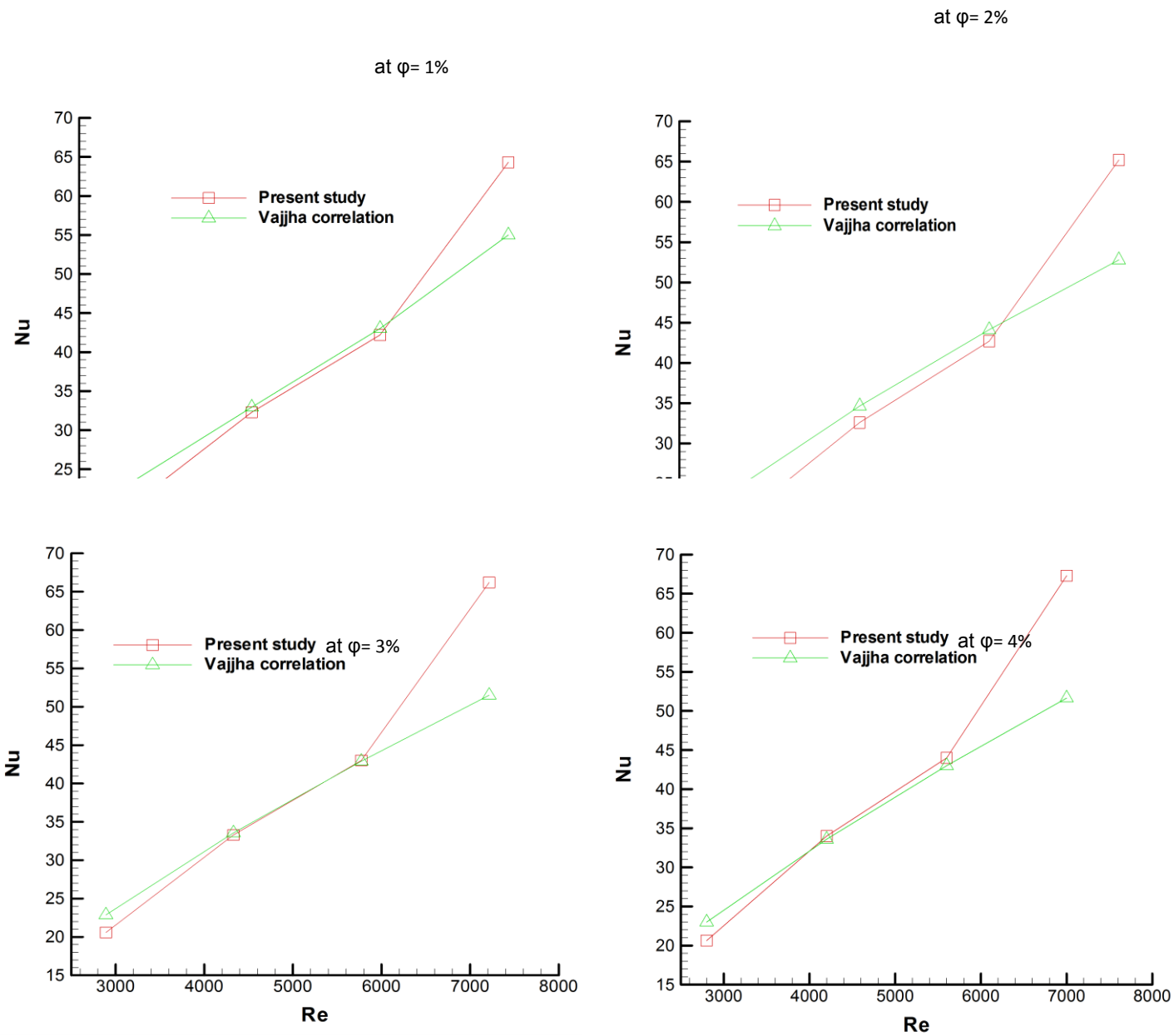

Figure 9. Comparison between present study and empirical correlation forVajjha et al. at volume concentrations 1%, 2%, 3% and 4% of nanofluids.

Preparation and Study of morphological properties of ZnO nano Powder

Mohammed Salab Hamza
Assistant Professor
Department of material science engineering, University of Technology
E-mail: Dr. msh2013@yahoo.com

Suaad Salim Shaker
Assistant Lecturer
Research Centre of Nanotechnology and Advanced Materials
University of Technology
E-mail: Suaad.salim @yahoo.com

khitam Salim Shaker
Assistant Lecturer
Research Centre of Nanotechnology and Advanced Materials
University of Technology
E-mail:khitam.Salim @yahoo.com

ABSTRACT

In this work, ZnO nanostructures for powder ZnO were synthesized by Hydrothermal Method. Size and shape of ZnO nanostructureas can be controlled by change ammonia concentration. In the preparation of ZnO nanostructure, zinc nitrate hexahydrate [$Zn(NO_3)_2 \cdot 6H2O$] was used as a precursor. The structure and morphology of ZnO nanostructure have been characterized by scanning electron microscopy (SEM), atomic force microscopy (AFM), X-ray diffraction (XRD). The synthesized ZnO nanostructures have a hexagonal wurtzite structure. Also using Zeta potential and Particle Size Analyzers and size distribution of the ZnO powder

Keywords: Hydrothermal method, ZnO, nanostructure.

تحضير ودراسه لخصائص التركيبيه والطوبوغرافيه لباودر اوكسيد الخارصين النانوي

محمد صلاب حمزة
أستاذ مساعد
قسم هندسة المواد /الجامعة التكنولوجية

سعاد سالم شاكر
مدرس مساعد
مركز بحوث النانوتكنولوجي والمواد المتقدمة
الجامعة التكنولوجية

ختام سالم شاكر
مدرس مساعد
مركز بحوث النانوتكنولوجي والمواد المتقدمة
الجامعة التكنولوجية

الخلاصه

في هذا العمل، حضرت تراكيب نانويه لباودر اوكسيد الخارصين بطريقه الهيدرو-حراري ,شكل وحجم التراكيب النانويه لاوكسيد الخارصين يمكن السيطره عليها بواسطه تغير تركيز الامونيا . في تحضير التراكيب النانويه تستخدم نترات الخارصين هيكسايدرات كمحفزات . شخصت البنيه ومورفولوجيه التراكيب نانويه لاوكسيد الخارصين بواسطه المجهر الالكتروني الماسح ومجهر القوى الذريه وحيود الاشعه السينيه للتراكيب نانويه لاوكسيد الخارصين المحضره تمتلك تراكيب سداسيه ,وباستخدام كل من جهازجهد زيتا و جهاز تحليل الحجم الحبيبي لمعرفه تحليل الحجم الحبيبي والتوزيع الحجمي لباودر اوكسيد الخارصين المحضر .

الكلمات الرئيسيه : الطريقة الهيدرو-حراري, اوكسيد الزنك, البنية النانوية.

1. INTRODUCTION

Nano particles have been attracted increasing attention in recent years and their different types have been used in concrete mixtures in order to improve both the mechanical and physical properties of the concrete , **Sahereh, 2013**.

Zinx oxid nanostructure always in the center of attention due to their fascinating properties ,**Donya, et al., 2013**. It has a unique material because it has exhibits semiconducting and piezoelectric dual properties on optical, semiconducting, piezoelectric, and magnetic and gas sensing properties. It exhibits interesting properties including, high exciton binding energy (60 mV), high chemical stability, high catalytic efficiency, strong adsorption ability and low growth temperature makes it an excellent candidate for room temperature UV lasing application, **Rizwan, et al. 2009**, **Radu 2011**.

Due to its vast industrial applications, ZnO powder has attracting considerable attention ,it has been used in the rubber manufacture and cigarettes (used as a filter), and it has used as a coating agent various paints and as an additive in the manufacture of concrete and ,**Matei1 et al., 2014** , **Manish and Shakti 2010**. Ceramic, cement, glass, and adhesive, sealants, lubricants, pigments, fire retardants, pigments and , ZnO has used for concrete manufacturing, improves the processing time and the resistance of concrete against water ,**Vigneshkumar, 2014**.

Furthermore, ZnO has an environmentally friendly material, which has desirable especially for bio-applications such as bio-imaging and cancer detection ,**Munusamy, et al., 2013**. It has extensive applications in water purification ,**Gnanasangeetha, and Sarala, 2013**. It is also used as an additive in food products such as breakfast cereal. It has used in a host of other creams and ointments that are used to treat skin diseases ,**Manish, and Shakti, 2010**.

Fernandez, et al., 2001. demonstrated that ZnO has huge impact on setting time (ST) and retards the ST with respect to that of the cement. They also measured unconfined compressive strength (UCS) and showed that the UCS of the final product decreases at short ages in presence of ZnO.

The efficiency of ZnO as a photocatalyst increases with the increase of surface to volume ratio compared with bulk ZnO materials. The main advantage of ZnO is relative ease of preparation of phoptocatalytic nanostructures.

Number of simple as well as complex forms of ZnO nanostructures was reported in literature including, nanorods, nanobelts, nanotubes, nanorings and hierarchical structures ,**Yang ,2010**.

On the other hand some of the above reported structures show superhy drophobicity due to high surface roughness. ZnO nanorod was relatively easily show high activity due to high surface area compared to ZnO nanoparticles mostly due to their high purity and crystalline ,**Elias, et al., 2008, Yu., et al., 2007**.

In this paper, different shapes of ZnO nanopartical and nanorod were synthesized with a single precursor at relatively low temperature by employing simple solution method. ZnO nanostructure was synthesized by variation of ammonia concentration in the preparation of ZnO nanoparticles. The results indicated that addition of high amount of ammonia to aqueous solution of Zn $(NO_3)_2 \cdot 6H_2O$ could greatly affect the morphology and size of ZnO. We suggest a procedure of preparation of ZnO nanorod and nanopartical powder, to add to concrete activity to the material.

2. EXPERIMENTAL WORK

2.1 Materials

Chemical materials zinc nitrate [Zn $(NO_3)_2 \cdot 6H_2O$], ammonia solution (2%) (NH_3), 1,4- butanediol ($C_6H_{12}O$) were supplied by Fluke Company (Germany).

2.2 Preparation of ZnO Nanopowder

The preparation of zinc oxide nanostructure described as: (1.20 g) zinc nitrate hexahydrate [Zn $(NO_3)_2 \cdot 6H_2O$] was dissolved into 50 ml of distilled water. Then, 5ml of NH_3 aqueous solution (2%) for solution (A) and 10 ml of NH_3 aqueous solution (2%) for solution (b) was added drop by drop to an aqueous solution of zinc nitrate. This results rising of solution pH to 9.7 for sample (A) and 12 for (B). Resulted $Zn(OH)_2$ precipitate was separated by centrifugation at 2800 rpm for 5 min and then dispersed in 50 ml of 1,4-butanediol. The solution with the dispersed Zn $(OH)_2$ was heated at 105°C for 10 h in a closed glass bottle. Then separate the obtained particle from the solution and centrifuged at 3000 rpm for10 min and washed several time with methanol to remove the remaining ions in the final product, and finally, the precipitate was dried at 80°C for 6h.

2.3. CHARACTERIZATION TECHNIQUES

The crystalline structure of the powder has been determined by using x-ray diffraction (Philips PW 1050 X-ray diffract meter of 1.5^{o}A from Cu-Kα. Additionally, the surface morphology and optical properties were examined using: Scanning Electron Microscopy (SEM,the VEGA easy probe), also by Atomic Force Microscopy (AFM) (Digital Instruments Nanoscope II) and Scanning Probe Microscope (AA3000). Zeta potential and Particle Size Analyzers and size distribution of the ZnO powder were analyzed using (NanoBrook 90Plus Particle Size Analyzer).

3. RESULT AND DISCASSION

Fig.1 shows the SEM images of the products with different amount of ammonia concentration. The surface morphology of the sample is showed in **Fig**.**1a.**

A different shape of nano sphere ZnO have been shown the obtained size of full array of a nano spheres structure with diluted ammonia was 50 ml of NH_3 which includes some nanorods forming. As amount of ammonia concentration increase nanorods forming the crystalline as shown in **Fig 1.b**. It was found that the addition of ammoni has affected on structure and morphology ZnO.

Fig. 2 shows AFM image of ZnO powder deposition on glass substrate by sputtering methods. Also the three dimensional AFM pictures of ZnO films are shown in right side on the same figure. From this image, it can be seen that the dispersion of ZnO nanoparticles is relatively uniform with the average diameter with root mean square (RMS) surface roughness is about 140 nm and 5.3nm respectively. As concentration of NH_3 aqueous solution increases, the RMS roughness of the films and the grain size dropped to about 62 nm and 2.68 nm respectively as shown in **Table1**.

Phase composition and phase purity of the obtained products were identified by XRD as shown in **Fig.3 a,b**. Relatively strong and sharp peaks in the XRD pattern confirm that the products are ZnO .Hexagonal phase with a wurtzite structure, no diffraction peaks of Zn or other impurities were observed in the spectrum, which indicates excellent crystal quality of the products. The particle size histograms of ZnO nanoparticles (illustrated in **Fig. 4a**) ZnO nanostructures with pH=12 the particles range in size from 10 to 50 nm and the particles range in size from 60 nm to150 respectively ,with mean diameter of 60nm when concentration of NH_3 decreased at pH equal to 9.7 the particles increased with range in size from 26.8 to 93 nm and the

particles range in size from102 nm to388.2 respectively ,with mean diameter of 162.3nm as shown in **Fig.4b**.

ZnO nanopowder was determined at pH 9.7 with zeta potential values -156.93 mV and a mean particle size of 162.3.nm. As the pH increased to 12, the zeta potential dropped to -165.65 mV and consequently decreases an mean particle size of 60nm

The ZnO NPs were found to partially disaggregate due to surface charge repulsion. (**Li, et al., 2013, Ma, et al., 2013, Omar, et al., 2014**) as shown in **Fig.5**

4. CONCOLUTION

1. The synthesis of ZnO nano powder is demonstrated by hydrothermal methods
2. XRD pattern show that all the diffraction peaks in the pattern can be easily indexed as the pure hexagonal phase of ZnO with a wurtzite structure.
3. The SEM images of nanospherers and nanorods with increase pH depends on the concentration of ammonia .
4. Zeta potential and particle size analyzer surely zeta potential values -156.93mV and an average particle size of 162.3.nm for pH 9.7. As the pH was increased, to 12, the zeta potential dropped to -165.65 mV and consequently decreases an average particle size of 60nm.

REFERENCES

- -A. Matei1, V. Tucureanu and I. Dumitrescu, 2014, *Aspects Regarding Synthesis and Applications of ZnO Nanomaterials*, Bulletin of the Transilvania University of Braşov , Series I: Engineering Sciences, . No. 2, 56.
- -Donya R., Mohd Z.B. H. and Yun H. T ., 2013, *Hydrothermal Synthesis of Zinc Oxide Nanoparticles using Rice as Soft Biotemplate*, Ramimoghadam et al. Chemistry Central Journal ,Vol. 7, PP.136.
- -F. M. Omar, H. A.l Aziz, and S. Stoll, 2014, *Aggregation and Disaggregation of ZnO Nanoparticles: Influence of pH and Adsorption of Suwannee River Holmic Acid*, Science of the Total Environment,Vol.468-469, PP.195-201.

- -Fernández O., Chacon E., and Irabien A., 2001, *Influence of lead, Zinc, Iron (III) and Chromium(III) Oxides on the Setting Time and Strength Development of Portland Cement,* Cement and Concrete Research, Vol.31,pp.1213-1219 .
- -Gnanasangeetha D. and Sarala T. D., 2013, *One Pot Synthesis of Zinc Oxide Nanoparticles via Chemical and Green Method,* Research Journal of Material Sciences, Vol. 1(7), PP.1-8.
- -Jamil E., Ramon T. Z., Guillaume-Y. W. and Claude L. C., 2008, *Conversion of ZnO Nanowires into Nanotubes with Tailored dimensions,* Chem. Mater, Vol.20, PP .6633–6637.
- -Li M., Lin D., and Zhu L., 2013, *Effects of Water Chemistry on the Dissolution of ZnO Nanoparticles and Their Toxicity to Escherichia Coli*, Environ Pollut, Vol.173, PP.97–102.
- Lili Y., 2010, *Synthesis and Characterization of ZnO Nanostructures*, Ph.D. Thesis, Department of Physical Electronic Division, Linköping University, SE-601 74 ,Norrköping, Sweden.
- -Ma PPH., Williams P., and Diamond S., 2013, *Ecotoxicity of Manufactured ZnO Nanoparticles Areview,* Environ Pollut, Vol.172, PP.76–85.
- -Manish K. and Shakti S. S.,2010, *Zinc Oxide Nanostructures Synthesized by Oxidization of Zinc,* Thesis Submitted in Partial Fulfillment of the Requirements for the Degree of Bachelor of Technology in Metallurgical & Materials Engineering.
- -Munusamy T., Kai-L. H. and Jiunn-F.L., 2013, *Preparation and Morphology Studies of Nano Zinc Oxide Obtained Using Native and Modified Chitosans*, Materials, Vol. 6, PP. 4198-4212.
- -Q. J. Yu, W. Y. Fu, C. L. Yu, H. B. Yang, R. H. Wei, M. H. Li, S. K. Liu,Y. M.Sui, Z. L. Liu, M. X. Yuan, G. T. Zou，G. R. Wang, C. L. Shao, and Y. C. Liu, 2007, *Fabrication and Optical Properties of Large-Scale ZnO Nanotube Bundles Via a Simple Solution Rout,* J. Phys. Chem. C, Vol.111 ,PP.17521-17526.
- -Radu O., 2011, *Nanomaterial and Nanotechnology in Civil Engineering*, Buletinul Institutului Politehinic Diniasi, Publicat de Universitatea Tecnica,

Gheorghe Asachi" din Iasi, Tonul LIV (LVIII), Fasc. 4, Sectia, Constructii ,Arhitectura.

- -Rizwan W.,Young-Soon K. and Hyung-Shik S., 2009, *Synthesis, Characterization and Effect of pH Variation on Zinc Oxide Nanostructures*, Materials Transactions, Vol. 50, PP. 2092 – 2097.
- -Sahereh M., 2013, *Nanotechnology Applications in Construction Industry*, Journal of Basic and Applied Scientific Research, Vol.3, PP. 391-396.
- -Vigneshkumar C., 2014, *Study on Nanomaterials and Application of Nanotechnology and Its Impacts in Construction*, Discovery, Vol., No. 23(75), PP.8-12

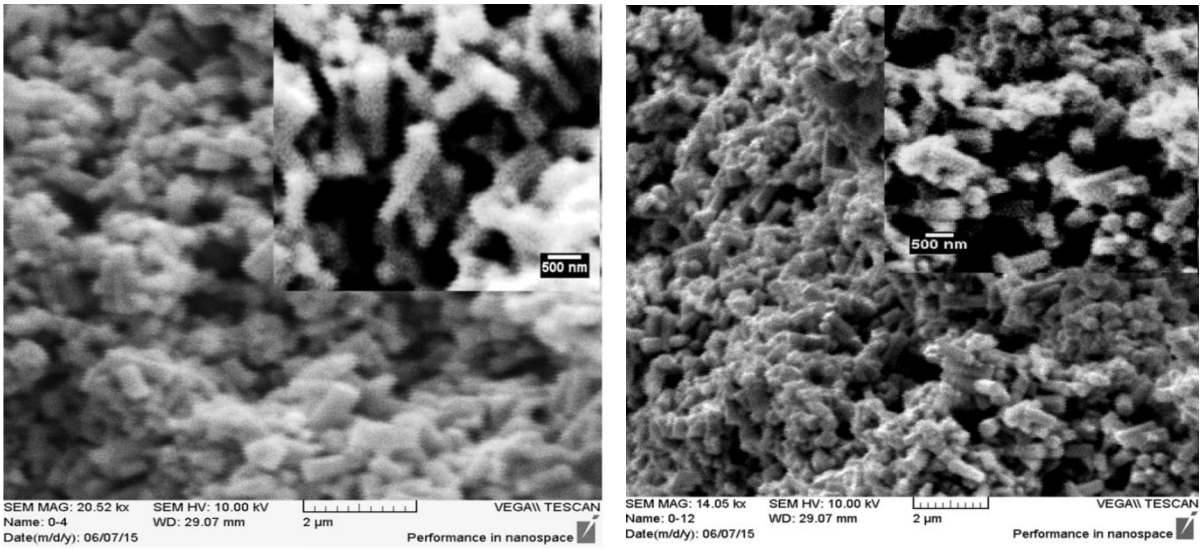

b **a**

Figure 1. SEM image of ZnO nanostructure at different concentration at pH=9.7 (a) pH=12(b).

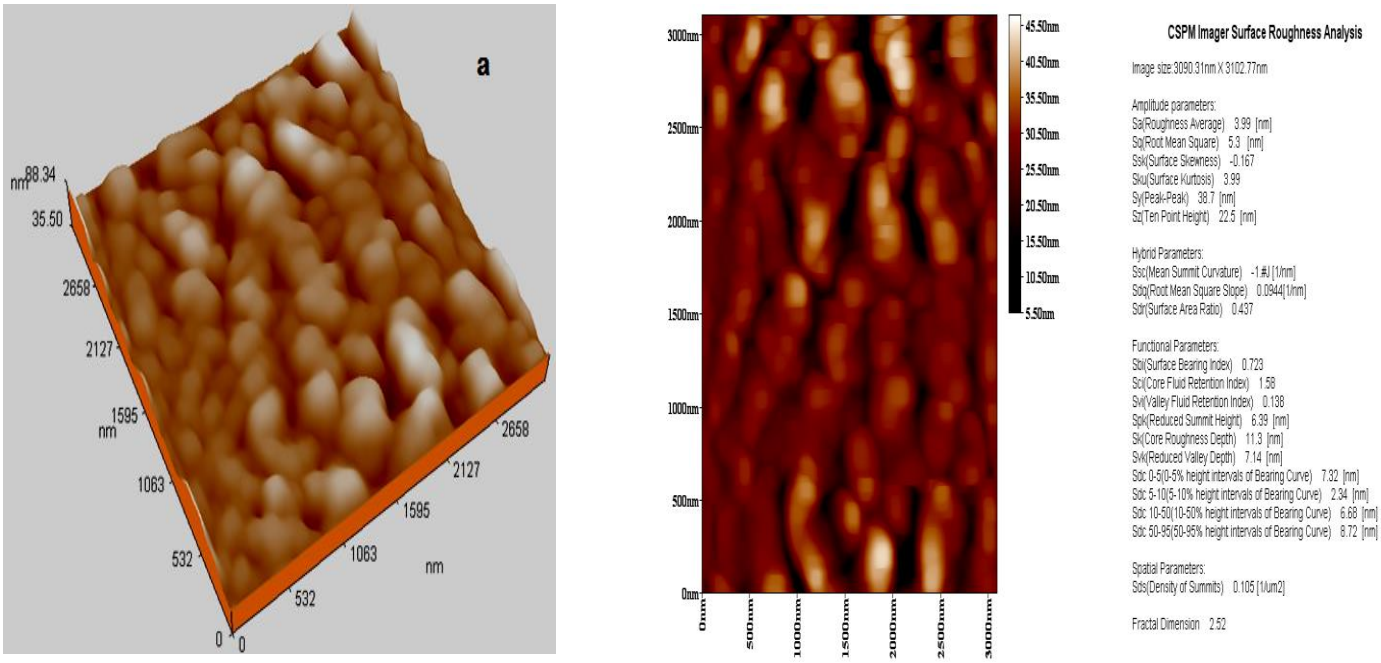

(A)

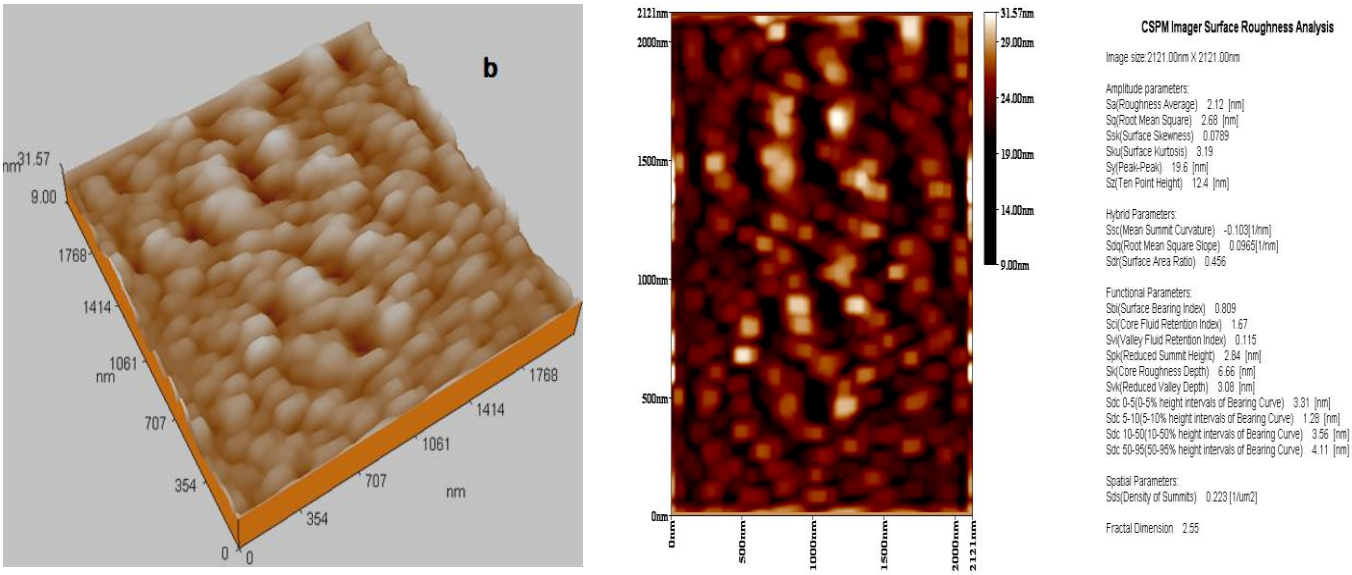

(B)

Figure 2. AFM images of the ZnO powder at different concentration a) pH=9.7 ,b)pH= 12.

.

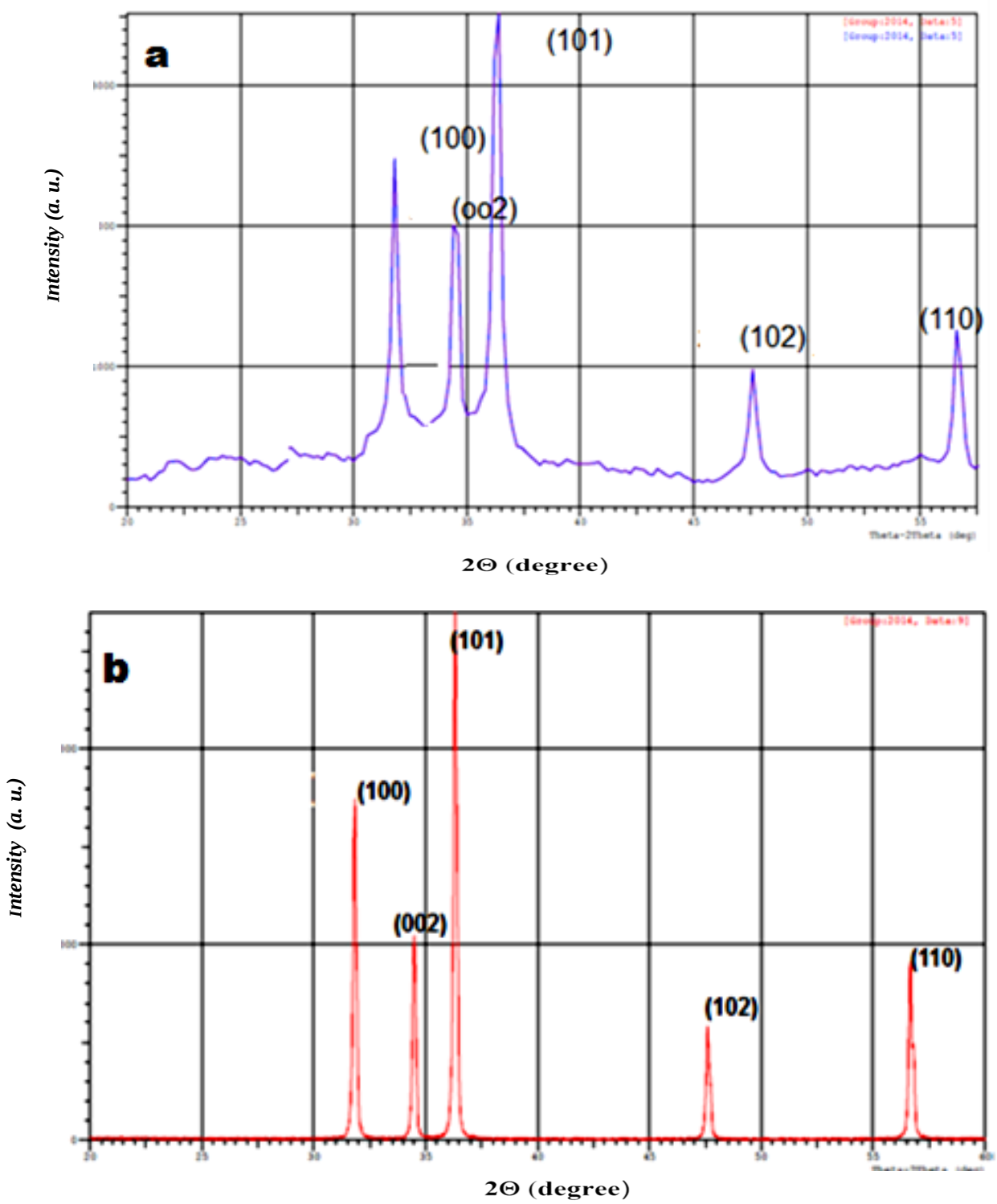

Figure 3. XRD patterns of ZnO nanostructures changed with different amount of ammonia (a) 5 ml solution of ammonia with pH=9.7, (b) 10 ml solution of ammonia with pH=12.

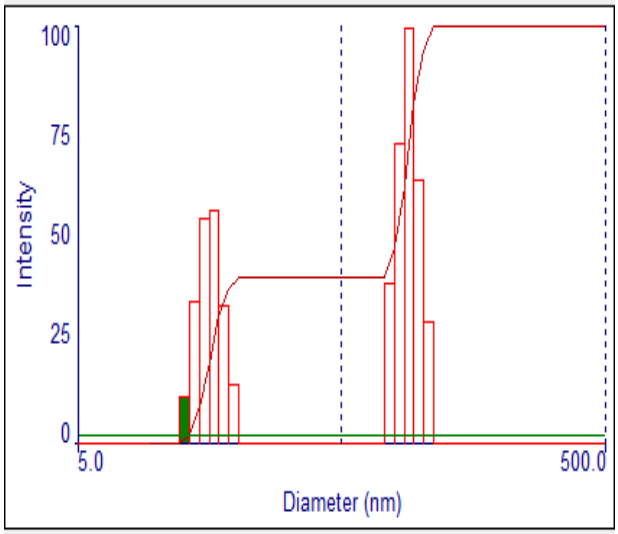

d(nm)	G(d)	C(d)	d(nm)	G(d)	C(d)	d(nm)	G(d)	C(d)
9.9	0	0	25.1	0	40	63.9	0	40
10.7	0	0	27.3	0	40	69.5	0	40
11.7	0	0	29.8	0	40	75.7	38	48
12.7	11	2	32.4	0	40	82.4	72	62
13.9	34	9	35.3	0	40	89.7	100	82
15.1	54	20	38.4	0	40	97.6	63	94
16.4	56	31	41.8	0	40	106.3	29	100
17.9	33	37	45.5	0	40	115.7	0	100
19.5	14	40	49.5	0	40	126.0	0	100
21.2	0	40	53.9	0	40	137.1	0	100
23.1	0	40	58.7	0	40	149.3	0	100

a)ZnO nanostructures with pH=12

size distribution using the software of (PSA),for sample(a)

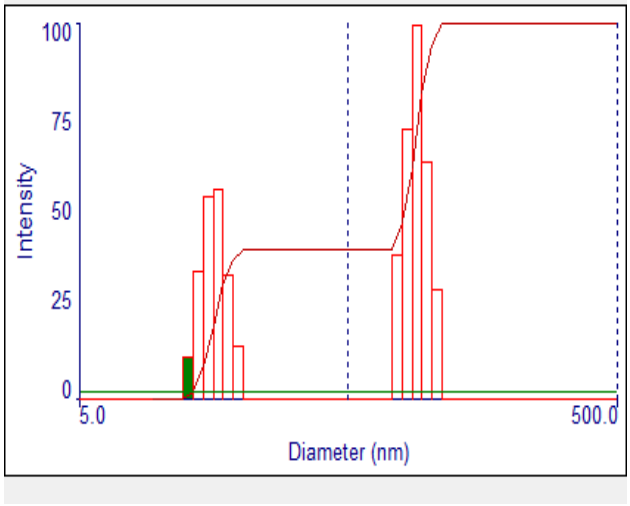

d(nm)	G(d)	C(d)	d(nm)	G(d)	C(d)	d(nm)	G(d)	C(d)
26.8	0	0	67.2	0	44	168.4	0	44
29.2	0	0	73.1	0	44	183.1	0	44
31.7	0	0	79.4	0	44	199.0	6	45
34.4	0	0	86.3	0	44	216.4	39	52
37.5	22	4	93.9	0	44	235.2	78	66
40.7	53	13	102.0	0	44	255.7	100	83
44.3	82	28	110.9	0	44	278.0	66	95
48.1	61	39	120.6	0	44	302.2	28	100
52.3	29	44	131.1	0	44	328.5	0	100
56.9	0	44	142.5	0	44	357.1	0	100
61.8	0	44	154.9	0	44	388.2	0	100

b) **ZnO nanostructures with pH=9.7**

size distribution using the software of (PSA),for sample(a)

Figure 4. Show the result of PSA of ZnO nanostructures different pH concentration.

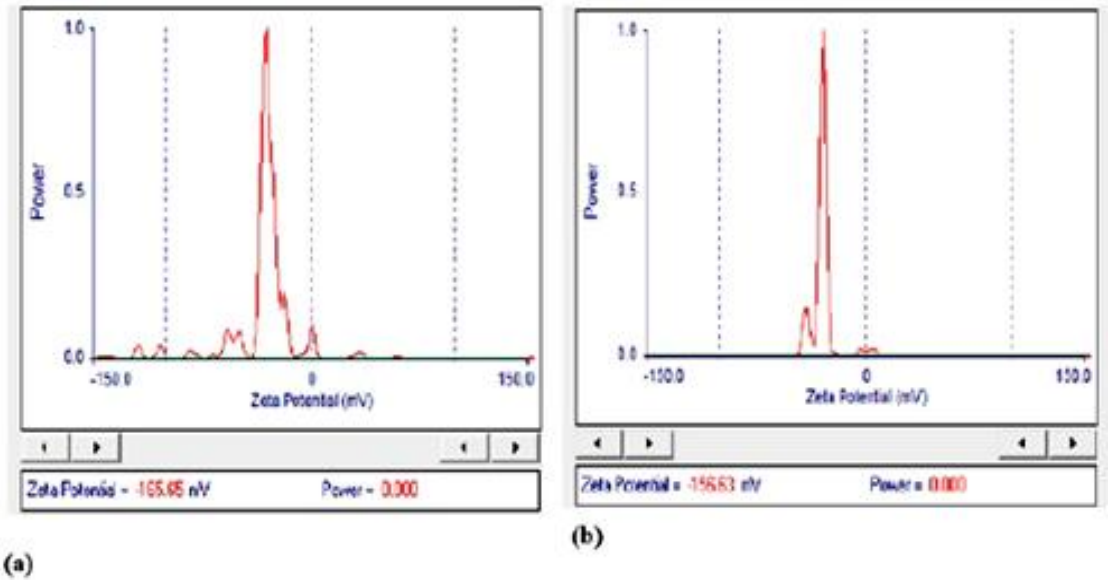

Figure 5. Show the zeta potential of ZnO nanostructures different concentration a) ZnO nanostructures with pH=12 b)ZnO nanostructures with pH=9.7

Table 1. The grain size,zeta potential and root mean square of the ZnO different concentration for solution.

Sample	Grain size in AFM(nm)	Grain size in PSA(nm)	Root Mean Square (RMS) (nm)	Zeta potential (mV)
pH=9.7	**140**	**162.3**	**5.3**	**-156.6**
pH=12	**62**	**60**	**2.68**	**-165.63**

Absorber Diameter Effect on the Thermal Performance of Solar Steam Generator

Prof. Dr. Karima Esmael Amori
Department of Mechanical Engineering
College of Engineering
University of Baghdad
Email: drkarimaa63@gmail.com

Rand Ahmed Adeeb
Department of Energy Engineering
College of Engineering
University of Baghdad
Email: a.rand82@yahoo.com

ABSTRACT

In this work, a convex lens concentrating solar collector is designed and manufactured locally by using 10 convex lenses (concentrator) of a diameter 10cm and one Copper absorber tube of a diameter 12.5mm and 1mm in thickness 1m length. Two axes manual Tracking system also constructed to track the sun continuously in two directions. The experiments are made on 17th of May 2015 in climatic conditions of Baghdad. The experimental data are fed to a computer program to solve the thermal performing equation, to find efficiency and actual useful energy. Then this data is used in numerical CFD software for three different absorber diameters (12.5 mm, 18.75 mm and 25 mm). From the results that obtained the maximum thermal efficiency for the collector of diameter 12.5mm equal to 82.3% is higher than that for the collector of 18.75 mm and 25 mm diameter. The maximum outlet temperature is found equal to (105°C, 93.9°C and 83.5°C) for collector absorber diameter equal to (12.5 mm, 18.75mm and 25 mm) respectively. The maximum mass flow rate 0.53 kg/hr when the solar radiation intensity equal to 899 W/m^2. The all-day collector efficiency varies with diameter and reaches to maximum value of (77.9%, 61.4% and 52.8) for collector diameter equal to (12.5 mm, 18.75mm and 25 mm) respectively.
Keywords: Steam Generator, Solar, Thermal Performance.

تاثير قطر الانبوب الماص على الاداء الحراري لمولد بخار شمسي

أ.د.كريمه اسماعيل عموري
قسم الهندسة الميكانيكية
كلية الهندسة / جامعة بغداد

رند احمد اديب
قسم هندسة الطاقه
كلية الهندسة / جامعة بغداد

الخلاصه

في هذا العمل تم تصنيع المركز الشمسي محليا باستخدام (10) عدسات محدبه, قطر الواحده منها يساوي (10 سم) , وانبوب من النحاس قطره (12.5 سم) وطوله (1 م) وسُمكه (1 ملم) كمستلم للاشعاع الشمسي المركزبواسطه العدسات. كما تم استخدام نظام تتبع ثنائي المحور لتتبع الشمس يدويا بصوره مستمره خلال فتره القياس. سُجلت النتائج العمليه في اليوم السابع عشر من شهر نيسان , في الظروف الجويه لمدينة بغداد. تم ادخال القيم العمليه الى الحاسبه بواسطه (CFD software)لحل المعادلات وايجاد الايداء الحراري لاقطار مختلفه للانبوب المستلم تساو (25ملم , 18.75 ملم ,12.5 ملم) ,حيث تم حساب كل

من الكفاءه, و الطاقه الحقيقه المفيده الكليه. من خلال النتائج تبين ان الكفاءه العظمى للمركز الشمسي ذو نصف القطر الذي يساوي 12.5 ملم تساوي 82.3% حيث كانت اعلى من الكفائه للحالتين ذات القطر الذي يساوي 18.75 ملم وكذلك 25 ملم. سجلت اعلى درجة حراره للماء بمقدار (105˚C, 93.9˚C, 83.5˚C). وكان اعظم معدل لتدفق المائع يساوي 0.53 kg/hr عند اشعاع شمسي مقداره 899 W/m^2. وجد ان اعلى معدل للكفاءه الكليه لليوم الواحد تساوي (52.8% and 61.4% , 77.9%,)بتغيير القطر للمستلم للشعاع بمقدار (25ملم , 18.75 ملم ,12.5 ملم) على التوالي.

الكلمات الرئسيه: مولد بخار, شمسي, اداء حراري

1. INTRODUCTION

With the increase of fossil fuel demand, the environmental pollution caused by burning of fossil fuels has been considered as an international problem. The stratospheric ozone depletion, the acid precipitation and the global warming are examples of environmental pollution. Renewable energies including, solar energy, wind energy, biomass, hydropower, geothermal energy are suggested to resolve the global warming problem and alleviate the potential of energy crisis, **Tyagi et al., 2009**. Solar energy is a large source of energy. The power from the sun intercept by the earth is approximately 1.8×10^{17} W. Solar energy could supply all the present and future energy needs of the world on a continuing basis. This makes it one of the most promising of the unconventional energy sources**, Aung** an**d Li, 2014**.

The first study about two-phase thermosyphon loop was done by, **McDonald, et al., 1977.** They studied the effect of changing the tilt angle of the loop and the temperature difference between the evaporator and the condenser in a single rectangular loop with R-11 and R-113 as working fluids. They found that the highest performance is achieved when the loop is horizontally oriented because the condenser is flooded with no dry out. **El-Ouederni, et al., 2008** studied experimentally the parabolic solar concentrator. They used an experimental device consist of a dish of 2.2 m opening diameter. The experimental results show that the temperature in the center of the disc is near to 400°C. **Gupta, et al., 2014** investigated experimentally the performance of convex lens concentrating solar power collector prototype in water heating applications. They found that the maximum efficiency obtained was 72% and 78%. They concluded that the convex lenses panels' prototype was more efficient than conventional panels.

The objective of this work is to directly produce steam using convex lenses to concentrate the solar radiation into a small area at the absorber surface. An estimation of the effect of change of inlet water temperature and effect of solar radiation on the production of the steam for two absorber fill ratios 0.75 and 1 will be accomplished. A mathematical model based on heat balance principle for different parts of the system is developed and then solved numerically to evaluate the fluid flow and thermal characteristics of the system under different conditions.

2. EXPERIMENTAL SETUP

The components of the experimental rig consists of convex lenses (Concentrator part) with receiver. It is also consists of supply tank and connecting pipes, shown in **Fig.1a** and **Fig.1b.** The concentrating part is used as presented in **Fig.2**. 10 pieces of Magnifying Glass lenses fixed in aluminum rectangular frame, and the specifications of the lenses are given in **Table 1.**

A copper tube acts as an absorber with diameter of (12.5 mm), and length of (1 m), black mat painted as shown in **Fig.1**.The absorber is covered by glass tube of (50 mm) in diameter, closed with cups from spherical rubber to isolate the absorber from the ambient condition and to reduce the thermal losses.

The water is fed to the absorber tube by one vertical cylindrical tank made of plastic shell of (2 mm) thickness. The tank has diameter of (29 cm), length of (34 cm) and capacity of (17.5 liter). Inlet water enter the tank from top hole with floating used to control the water level, and the bottom outlet point feeds the absorber with water shown in **Fig.3**. The external surface is well insulated by glass wool insulator of (2 cm) in thickness. Plastic pipes of (12.5 mm) diameter are used as connecting pipes between the components of the system. They covered by glass wool insulator and connect the supply tank, receiver and condenser with each other as closed loop. Fittings such as elbows, valve and bends are used as connecting parts.

The frame of the lenses is manufactured locally from two aluminum slides with length of (1 m) connected together and the lenses fixed between them as illustrated in **Fig.4**. The frame of the lenses is located at the top of another frame manufactured locally from aluminum with dimensions of (0.4m x 0.4m x 0.5m) black painted.

2.1 Measurements

In order to measure the absorber surface temperature and inlet and outlet temperatures of water, 10 thermocouples J (Iron - constant) type are used, for measuring the glass cover and ambient temperature one kind of thermocouple is used type-K . Thermocouples are attached near the focal point to measure the surface temperature of the absorber. Thermocouple is placed for the inlet and outlet water of the absorber shown in **Fig.5**. These thermocouples are joined to a selector switch in series with a digital reader **Fig6a**. Pro'sKit 3PK-6500 thermometer reader is used for type-K thermocouple with measuring range: (-50ºC ~ 750ºC) shown in **Fig.6b**. One thermocouple is used to measure the glass cover temperature. Solar radiation data is taken from the meteorological station in Baghdad for the test days. Wind data are gained from the meteorological station in Baghdad for the test days

3. DATA PROCESSING

The local useful energy is calculated at each focal point by the following equation:

$$Q_{useful(x)} = Q_{abs(x)} - Q_{loss(x)} \tag{1}$$

$$Q_{abs(x)} = (\tau\alpha) I_T A_a \tag{2}$$

$$Q_{loss(x)} = \pi\, D_g\, x\ \left[h_w\left(T_g - T_a\right) + \varepsilon_g\, \sigma\left(T_g^4 - T_{sky}^4\right)\right] \tag{3}$$

T_{sky} is the effective sky temperature calculated by the equation suggested by, **Beckman** and **Duffie, 2005.**

$$T_{sky} = 0.0552\ (T_a)^{\ 1.5} \tag{4}$$

h_w Is the natural convective heat transfer coefficient from the outer surface of the glass tube to ambient air is calculated by the equation suggested by, **Mullick** and **Nanda, 1989**.

$$h_w = 4 V_w^{0.58} D_g^{-0.42} \tag{5}$$

The total useful energy is calculated by the sum of all the local useful energy.

$$Q_{useful(T)} = \sum_{1}^{10} Q_{useful(x)}$$

The mass flow rate of the system is calculated by:

$$\dot{m} = \frac{Q_{useful(T)}}{C_p \Delta T} \quad (6)$$

$$\Delta T = T_{out} - T_{in}$$

The local actual useful heat gain is calculated as:

$$Q_{u(x)} = A_a F_{R(x)} \left[I_T(\tau\alpha) - \frac{U_{L(x)}(T_{in} - T_a)}{C} \right] \quad (7)$$

where C is the concentration ratio calculated as:

$$C = \frac{Aperture\ area\ (A_a)}{surface\ area\ of\ the\ absorber\ (A_{abs})} \quad (8)$$

The aperture area is calculated as shown in **Fig.7a**:

No. of lens = 10
Diameter of lens = 10 cm
Height of the triangle = 4.4656 cm Shown in **Fig.7b**
Base of the triangle = 4.465 cm

No. of shaded area = (no. of lenses × 2) + 2
= 22

Area of sector $= \frac{1}{2}\theta r^2$

$\theta = in\ rad$

$\theta = 2 \times \tan^{-1} \frac{2.2325}{4.4656}$

= 53°

= 0.9271 rad

Area of the sector = $\frac{1}{2} \times 0.9271 \times 5^2$

= 11.5898 cm^2

Area of the triangle = $\frac{1}{2} \times 4.465 \times 4.4656$

= 9.9694 cm^2

Shaded area = 11.5898 – 9.9694

= 1.6203 cm^2

Area of all lenses = area of one lens * 10

$= \frac{\pi\, 10^2}{4} \times 10$
$= 785\ cm^2$

Total Actual area of lenses = 785 – (1.6203 × 22)
= 749.3523 cm^2
= 0.0749 m^2

Surface area of the absorber tube is calculated as:

$$A_{abs} = \pi D_{abs} L$$

a- For absorber tube with diameter (D_{abs} = 1.25 cm):

$A_{abs} = 0.0125\, \pi\, m^2$
$C = 2$

b- For absorber tube with diameter (D_{abs} = 1.875 cm):

$A_{abs} = 0.01875\, \pi\, m^2$
$C = 1.3$

c- For absorber tube with diameter (D_{abs} = 2.5 cm):

$A_{abs} = 0.025\, \pi\, m^2$
$C = 1$

The value of the local heat loss coefficient $U_{L(x)}$ is calculated by the equation suggested by, **Beckman** and **Duffie, 2005:**

$$U_{L_{(x)}} = \left(\frac{A_{abs}}{(h_w + h_{r,g-s})\, A_g} + \frac{1}{h_{r,abs-g_{(x)}}}\right)^{-1} \quad (9)$$

The radiation coefficient can be calculated from equation suggested by, **Beckman** and **Duffie, 2005.**

$$h_{r,g-s} = \varepsilon_g\, \sigma(\bar{T}^3) \quad (10)$$

The local radiation coefficient $h_{r,abs-g_{(x)}}$ between the absorber and glass cover is calculated as:

$$h_{r,abs-g_{(x)}} = \frac{\sigma(T_{abs(x)} + T_g)(T_{abs(x)}^2 + T_g^2)}{\frac{1-\varepsilon_p}{\varepsilon_p} + 1 + \frac{1-\varepsilon_g}{\varepsilon_g}\left(\frac{A_{abs}}{A_g}\right)} \quad (11)$$

The local heat loss coefficient based on the outside receiver tube diameter between the surrounding and the fluid is suggested by, **Beckman** and **Duffie, 2005**.

$$U_{\circ(x)} = \left[\frac{1}{U_{L_{(x)}}} + \frac{D_{abs,o}}{h_{i(x)}\, D_{abs,i}} + \frac{D_{abs,o} \ln(D_{abs,o}/D_{abs,i})}{2k_{abs}}\right]^{-1} \quad (12)$$

The local collector efficiency factor is calculated as:

$$F'_{(x)} = \frac{U_{\circ(x)}}{U_{L(x)}} \tag{13}$$

a – For single phase region: ($h_i = h_1$)

$Nu_{(x)}$ Depends on the length of the heated surface, and the Grashof number defined by, **Ishi and Kataoka, 1984.**

$$Gr = \frac{g\beta\left(T_{abs,x} - T_f\right)x^3}{\left(\mu_l/\rho_l\right)^2} \tag{14}$$

$$Nu_{(x)} = 0.3(Gr\mathrm{Pr}_l)^{0.3}\left(\frac{D_{abs}}{x}\right) \tag{15}$$

$$h_{1(x)} = \frac{Nu_{(x)}\, k_l}{D_{abs}}$$

$$F''_{1(x)} = \frac{F_{R1(x)}}{F'_{1(x)}} = \frac{\dot{m}\, C_p}{A_a U_{L1(x)} F'_{1(x)}}\left[1 - e^{-\left(A_a U_{L1(x)} F'_{1(x)}/\dot{m}\, C_p\right)}\right] \tag{16}$$

$$F_{R1(x)} = F'_{1(x)} \times F''_{1(x)}$$

$$Q_{u1(x)} = A_a F_{R1(x)}\left[I_T(\tau\alpha) - \frac{U_{L1(x)}(T_i - T_a)}{C}\right] \tag{17}$$

b- For two phase region: ($h_i = h_b$)

$h_{b(x)}$ is the convection heat transfer coefficient for the fluid inside the absorber tube is assumed to be homogeneous pool boiling, and calculated by the equation proposed by, **Roshenow, 1952.**

$$h_{b(x)} = \frac{q_{b(x)}}{T_{abs(x)} - T_{sat}} \tag{18}$$

$$q_{b(x)} = \mu_l\, h_{fg}\left[\frac{g(\rho_l - \rho_v)}{\in}\right]^{\frac{1}{2}}\left[\frac{C_{pl}\,(T_{abs(x)} - T_{sat})}{0.01\, h_{fg}\, Pr^{1.7}}\right]^{1.8} \tag{19}$$

$$F''_{b(x)} = \frac{F_{Rb(x)}}{F'_{b(x)}} = \frac{\dot{m}\, C_p}{A_a U_{Lb(x)} F'_{b(x)}}\left[1 - e^{-\left(A_a U_{Lb(x)} F'_{b(x)}/\dot{m}\, C_p\right)}\right] \tag{20}$$

$$F_{Rb(x)} = F'_{b(x)} \times F''_{b(x)}$$

$$Q_{ub(x)} = A_a F_{Rb(x)}\left[I_T(\tau\alpha) - \frac{U_{Lb(x)}(T_i - T_a)}{C}\right] \tag{21}$$

The efficiency of the collector is calculated as:

$$Q_{u(Total)} = \sum Q_{u1(x)} + \sum Q_{ub(x)} \tag{22}$$

$$\eta = \frac{Q_{u(Total)}}{I_T A_a \times 10} \tag{23}$$

4. ERROR ANALYSIS

Thermal efficiency (η) is a function of different variables according to Eq. (24).

$$\eta = \eta(\Delta T, I_T, \dot{m}) \tag{24}$$

Based on the error analysis presented in, **Holman, 1989**. The percentage error of the collector efficiency is calculated as:

$$w_R = \left[\left(\frac{\partial R}{\partial x_1} w_1\right)^2 + \left(\frac{\partial R}{\partial x_2} w_2\right)^2 + \cdots + \left(\frac{\partial R}{\partial x_n} w_n\right)^2\right]^{1/2} \tag{25}$$

$$w_\eta = \left[\left(\frac{\partial \eta}{\partial \Delta T} w_{\Delta T}\right)^2 + \left(\frac{\partial \eta}{\partial I_T} w_{I_T}\right)^2 + \left(\frac{\partial \eta}{\partial \dot{m}} w_{\dot{m}}\right)^2\right]^{1/2}$$

where w_R is the uncertainty in the result and w_1, w_2, ... w_n are the uncertainty in the independent variables.

$$\frac{\partial \eta}{\partial \Delta T} = \frac{\dot{m} C_p}{I_T A_a} = \frac{1.95 * 10^{-04} * 4175}{945 * 0.0749} = 0.0110$$

$$\frac{\partial \eta}{\partial I_T} = -\frac{\dot{m} C_p \Delta T}{{I_T}^2 A_a} = -\frac{1.95 * 10^{-04} * 4175 * 73}{945^2 * 0.0749} = -8.4734 * 10^{-4}$$

$$\frac{\partial \eta}{\partial \dot{m}} = \frac{C_p \Delta T}{I_T A_a} = \frac{4175 * 73}{945 * 0.0749} = 4108.4$$

$$w_\eta = 0.0420$$

$$\frac{w_\eta}{\eta} = \frac{0.0420}{0.8007} = 5.24\%$$

5. NUMARICAL MODEL.

5.1 Mathematical Model

5.1.1 Geometry.

The geometry of the physical model shown in **Fig.9** is created in GAMBET, version (2.4.6). The model consists of circular absorber of 1m length, (12.5 mm, 18.75 mm and 25 mm) in diameter.

5.1.2 Mathematical assumptions.

1- The absorber properties do not changed with temperature.

2- The emissivity of the glass cover and absorber were assumed to be constant with temperature.

3- The flow within the collector absorber is considered to be unsteady, three-dimensional laminar natural convection.

4- In energy equation the viscous dissipation is neglected.

5- The Boussineq approximation is invoked for the fluid properties to relate density change to temperature change, and to couple in this way the temperature field to the flow field.

5.2 GOVERNING EQUATIONS.

The software (FLUENT 2.3.26) was used to solve the governing continuity, momentum and energy equations. The steady state solution has been obtained by numerically solving the three-dimensional form of the governing equations, these equations being written in terms of dimensional variables for the defined geometry and associated boundary conditions. The domain was defined in the global coordinate frame in which the solver carries out the calculations. **White, 1991.**

5.2.1 The continuity equation

$$\frac{1}{r}\cdot\frac{d}{dr}\left(\rho_w\ r\ V_r\right)+\frac{1}{r}\cdot\frac{d}{d\emptyset}\left(\rho_w V_\emptyset\right)+\frac{d}{dz}\left(\rho_{ref} V_z\right)=0 \qquad (26)$$

where: ρ_{ref} = water density at the reference temperature.

$V_r, V_\emptyset$ and V_z are the flow velocities components in the r,∅ and z direction respectively.

5.2.2 The momentum equation

r-component

$$\rho_{ref}\left(V_r\frac{dV_r}{dr}+\frac{V_\emptyset}{r}\frac{dV_r}{d\emptyset}+V_z\frac{dV_r}{dz}-\frac{V_\emptyset^2}{r}\right)$$
$$=\frac{-dp}{dr}+\mu\left[\left(\frac{d}{dr}\left(\frac{1}{r}\frac{d}{dr}(rV_r)\right)\right)+\frac{1}{r^2}\frac{d^2\ V_r}{d\emptyset^2}+\frac{d^2\ V_r}{dz^2}+\frac{2}{r^2}\ \frac{dV_\emptyset}{d\emptyset}\right]\rho g_r \qquad (27a)$$

where : gr is radial gravitational acceleration and calculated as $g\ cos\emptyset\ cos\theta$

∅-component

$$\rho_{ref}\left(V_r\frac{dV_\emptyset}{dr}+\frac{V_\emptyset}{r}\frac{dV_\emptyset}{d\emptyset}+v_z\frac{dV_\emptyset}{dz}-\frac{V_rV_\emptyset}{r}\right)=\frac{-dp}{d\emptyset}+\mu\left[\left(\frac{d}{dr}\left(\frac{1}{r}\frac{d}{dr}(rV_\emptyset)\right)\right)+\frac{1}{r^2}\frac{d^2\ V_\emptyset}{d\emptyset^2}+\frac{d^2\ V_\emptyset}{dz^2}+\frac{2}{r^2}\ \frac{dV_\emptyset}{d\emptyset}\right]+\rho g_\emptyset \qquad (27b)$$

where: $g_\emptyset$ is the circumferential gravitational acceleration, its determined as $g\ sin\emptyset\ cos\theta$

z-component

$$\rho_{ref}\left(V_r\frac{dV_z}{dr}+\frac{V_\emptyset}{r}\frac{dV_z}{d\emptyset}+V_z\frac{dV_z}{dz}-\frac{V_z\ dV_z}{dz}\right)$$
$$=\frac{-dp}{dz}+\mu\left[\left(\frac{d}{dr}\left(\frac{1}{r}\frac{d}{dr}\left(\frac{dV_z}{dr}\right)\right)\right)+\frac{1}{r^2}\frac{d^2\ V_z}{d\emptyset^2}+\frac{d^2\ V_z}{dz^2}\right]\ +\rho g_z \qquad (27c)$$

where: gz is gravitational acceleration in z direction it is evaluated as $g\ sin\theta$

5.2.3 The energy equation

$$\rho_{ref}\, C_p \left(V_r \frac{dT}{dr} + \frac{V_\emptyset}{r}\frac{dT}{d\emptyset} + V_z \frac{dT}{dz}\right) = k\left[\frac{1}{r}\frac{d}{dr}\left(r\frac{dT}{dr}\right) + \frac{1}{r^2}\frac{d^2T}{d\emptyset^2} + \frac{d^2T}{dz^2}\right] \quad (28)$$

$$\rho = \rho_{ref}\left[1 - \beta\left(T - T_{ref}\right)\right] \quad (29)$$

5.2 Boundary Conditions and Modeling Specifications.

The boundary conditions are assigned for inlet velocity, inlet temperature, wall's heat flux and outlet pressure. The inlet velocity assumed to be equal to 10^{-5} m/s just to run the program. Inlet temperature data and wall heat flux are listed in **Table 2**. Pressure outlet boundary conditions required the specification of the static (gage) pressure at the outlet boundary. The value of static pressure assumed to be uniform atmospheric pressure since the pipe is open to ambient conditions.

5.3 Fluent Code

In this work FLUENT version 6.3.26 is used. FLUENT is a computational fluid dynamics (CFD) software package to simulate fluid flow and heat transfer problems. It uses the finite volume method to solve the partial differential equations of fluid flow and heat transfer. It provide the capability to use different physical models such as incompressible or compressible, in viscid or viscous, laminar or turbulent flow, and thermal or adiabatic heat transfer.

A mesh is used to reach to the correct converged solution that captures all the key parameters of the simulation. For the current simulation, enough nodes are needed to be placed near the boundaries to capture boundary layer flow, as well as the temperature gradient. Using too many nodes in the system may increases the computational resources and execution time without providing additional resolution. The details of the adopted mesh are: Interval Size of (Wall, inlet, outlet) Edges = 0.0004 cm, Growth Rate = 1.2 and Maximum Size = 0.001 cm. The mesh of the system is shown in **Fig.8**.

6. RESULTS AND DISCUSSION

Fig.10 shows that the efficiency of the system increases with the decreasing of the absorber diameter on 17th of May 2015. [I.e. the efficiency for the case of diameter equal to (12.5mm) was 12.1% higher than that for absorber with diameter of (18.75mm) and 30.3% higher than that for absorber of diameter equal to (25 mm).

Fig.11 shows that the useful energy of the system increases with the decreasing of the absorber diameter on 17th of May 2015. The useful energy for the case of diameter equal to (12.5mm) was 17.7% higher than that for absorber with diameter of (18.75mm) and 32.3% higher than that for absorber of diameter equal to (25 mm), due to the higher heat fluxes.

Fig.12 illustrates that the outlet temperature of the absorber (with diameter of 12.5, 18.75, and 25mm) increases from the first hour of the day to reach maximum value of (105 , 93.9, and 83.5°C) respectively at solar noon then decreased after that. This figure also shows that the outlet temperature increases with the decreasing of the absorber diameter.

Fig.13 Shows that the heat flux decreasing with the increasing of absorber size, because of the increasing of the surface area that the useful energy divided by it. The heat flux for the absorber diameter of (12.5 mm) was 33.2% higher than that for absorber with diameter of (18.75 mm) and 50% higher than for absorber with diameter of (25 mm) mm.

Fig.14 reports the mass flow rate for all three cases of (12.5, 18.75, and 25mm) increasing from the beginning of the day to reach maximum value of (0.53, 0.51 and 0.5 kg\hr) respectively at solar noon then decreased after that, due to large amount of evaporation in the system with the case of small diameter.

Fig.15 presents the daily efficiency for three different cases of absorber diameter of (12.5, 18.75, and 25 mm). It is increases with the decreasing of absorber diameter as (82.5, 70.2, and 58%) respectively.

Fig.16 shows the variation of outlet temperature with solar radiation for three different absorber sizes. It can be noticed that the outlet temperature in the case of (12.5mm) diameter was 10.45% higher than in case of (18.75mm) and 20.47% in case of (25mm) for the same solar radiation due to the smaller surface area produced larger heat flux.

Fig.17 illustrates the effects of absorber size variation on the useful energy, for same solar radiation. the useful energy at 13:00 PM was (48.19 , 39.66 and 32.78 W) for absorber diameters of (12.5, 18.75 and 25 mm) respectively for same amount of solar radiation equal to 899 W/m^2, because of the differences between inlet and outlet temperature and mass flow rate in case of the small diameter was higher than that for cases of large diameter.

Fig.18 shows the effect of the variation of the absorber diameter on the value of heat flux, for same solar radiation the heat flux increases with the decreasing of the absorber diameter. The heat flux at 13:00 PM was (1477.7, 986.13, and 738.8 W/m^2) for absorber diameter of (12.5, 18.75 and 25 mm) respectively for same amount of solar radiation equal to 899W/m^2.

7. CONCLUSIONS

The conclusions extracted from this work are:

1. Outlet temperature of the system increased about 10.45% and 20.47% with the decreasing of absorber size from (18.75 mm) and (25 mm) to (12.5 mm) for the same amount of solar radiation and useful energy.
2. The maximum value of outlet temperature for absorber tube with diameters equal to (12.5 mm, 18.75mm and 25 mm) were (105°C, 93.9°C and 83.5°C) respectively on 17th of May 2015.
3. The mass flow rate decreased with increasing of absorber diameter. The maximum value of mass flow rate reported was about (0.53 kg/hr.) at solar noon for collector with absorber diameter equal to (12.5mm).
4. The calculated heat flux subjected on the absorber surface increases with decreasing its diameter for same amount of incident solar radiation. For three different absorber diameters of (12.5, 18.75, and 25 mm) the maximum heat flux were (1477, 986, and 738 W\m^2) respectively for the same amount of incident solar radiation of 899W/m^2.

5. For two axes manual tracking system the average efficiency reached during the day was about (77.9, 61.4, and 52.8%) for collector diameter equal to (12.5, 18.75 and 25 mm) respectively.

REFERENCES.

- -Aung N. Z., and Li S., 2013, *Numerical Investigation on Effect of Riser Diameter and Inclination of System Parameters in a Two-Phase Close Loop Thermosyphon Solar Water Heater*, Energy Conversion and Management, Vol.75, pp. 25-35.

- -Beckman W. A, and Duffie J.A., 2005, *Solar Engineering of Thermal Process*, Wiley Interscience Publications, John Wiley & Sons, New York.

- -El-Ouederni A. R., Dahmani A. W., Askri F., Salah M. B, Nasrallah S. B., 2008 , *Experimental Study of a Parabolic Solar Concentrator*, Renewable Energies proceedings CICME' 08 source, pp. 193-199.

- -Gupta A. K., Gehlot D., Gujrathi A. S., 2014, *Experimental Investigation of Convex Lens Concentrating Solar Power Collector Prototype Performance*, International Journal of innovation in Engineering Research and Management, Vol.1, Issue.2, pp.193-199.

- -Grald E. W., Kuehn T. H., 1989, *Performance Analysis of a Parabolic Trough Solar Collector with a Porous Absorber Receiver*, Solar Energy, Vol. 42, pp. 281-292.

- -Howell J. R., Bannerot R.B., Vliet G.C., 1983, *Solar Thermal Energy System and Design*, McGraw-Hill Book Company, New York.

- -Holman J.P., 1989, *Heat Transfer*, fifth edition McGraw-Hill.

- -Ishii M., Kataoka I., 1984, *Scaling Laws for Thermal-Hydraulic System Under Single-Phase and Two-Phase Natural Circulation*, Nuclear Engineering and Design, Vol. 81, pp.411-425.

- -Joudi K. A., Al-tabbakh A. A., 1999, *Computer Simulation of a Two Phase Thermosyphon Solar Domestic Hot Water Heating System*, Energy conversion and management, Vol.40, pp. 775-793.

- -Lin M., Sumathy K., Dai Y. J., Zhao X. K., 2014, *Performance Investigation on a Linear Fresnel Lens Solar Collector Using Cavity Receiver*, Solar Energy, Vol.107, pp.50-62.

- -McDonald T. W., Huang K. S., Diciccio R., 1977, *Thermosyphon Loop Performance Characteristics Part 1*, Experimental study, ASHRAE Trans., Vol. 83, pp. 250-259.

- -Mullick S.C., and Nanda S.K., 1989, *An Improved Technique for Computing the Heat Loss Factor of a Tubular Absorber*, Solar Energy, Vol. 42, Issue 1, pp. 1-7.

- -Mohamad A., Orfi J., Alansary H, 2014, *Heat Losses From Parabolic Trough Solar Collectors*, International Journal of Energy and Research, Vol.38, pp. 20-28.
- -Rohsenow W. M., 1952, *A Method of Correlating Heat Transfer Data for Surface Boiling Liquids*, Trans. ASME, Vol.74, pp. 969-976.
- -Shuai Y., Xia X. L., Tan H. P., 2008, *Radiation Performance of Dish/Cavity Receiver Systems*, Solar Energy, Vol.82, pp.13-21.
- -Tyagi H., Phelan P., Prasher R., 2009, *Predicted Efficiency of a Low-Temperature Nanofluid–Based Direct Absorption Solar Collector*, Journal of Solar Energy Eng. 131, 041004.
- -Vincent C. C. J, and Kok J. B. W., 1992, *Investigation of the Overall Transient Performance of the Industrial Two-Phase Closed Loop Thermosyphon*, International Journal Heat Mass Transfer, Vol.35, No.6, pp.1419-1426.
- -White F.M., 1991, *Viscous Fluid Flow*, second edition, McGraw-Hill, Inc.

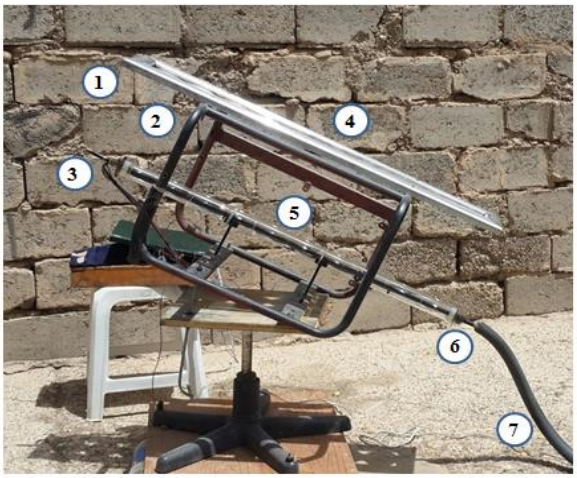

Figure 1a. Photograph for the outdoor testing set up.
1. Frame structure of the lenses.
2. Frame structure of the collector.
3. Outlet point.
4. Concentrating part.
5. Receiver (copper tube + glass cover).
6. Inlet point.
7. Connecting pipe.

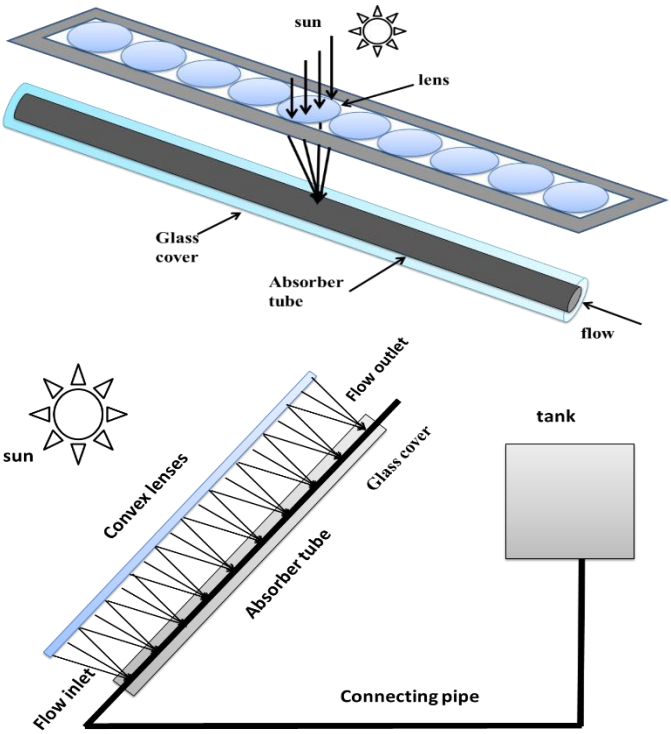

Figure 1b: Schematic diagram for the natural circulation concentrated solar collector.

Figure 2. Concentrating part (convex lenses).

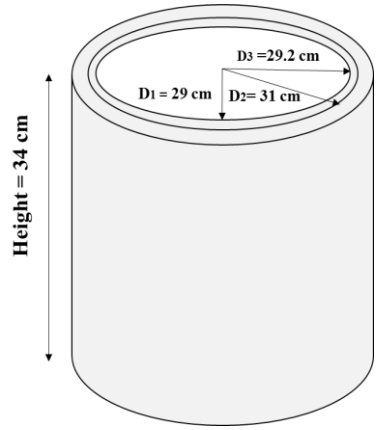

Figure 3. Schematic diagram for the supply tank.

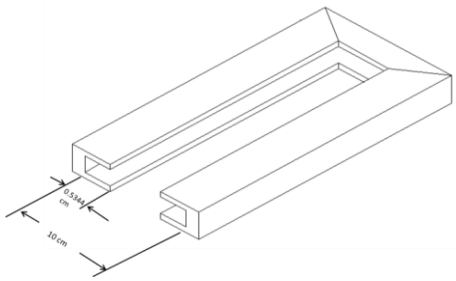

Figure 4. Schematic diagram of the frame of the lenses

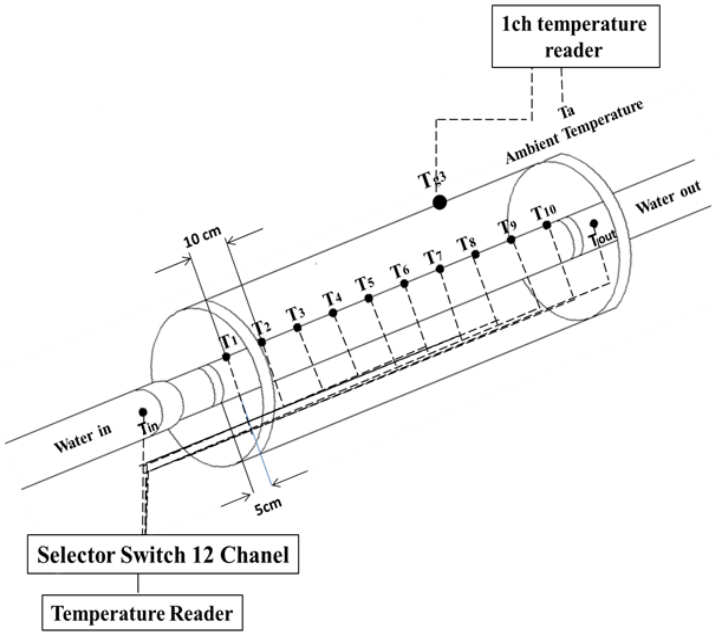

Figure 5. Schematic diagram of thermocouples locations.

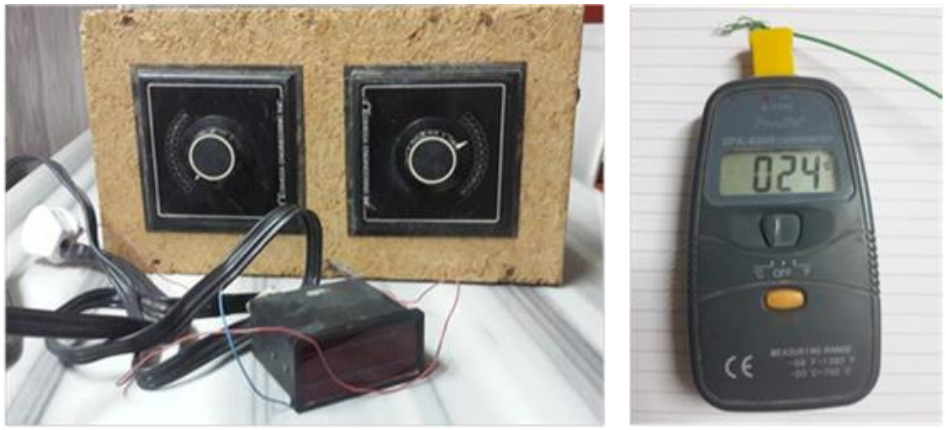

(a) (b)

Figure 6. (a)-Selector switch and the temperature reader.
(b)- Pro'sKit 3PK-6500thermometer reader.

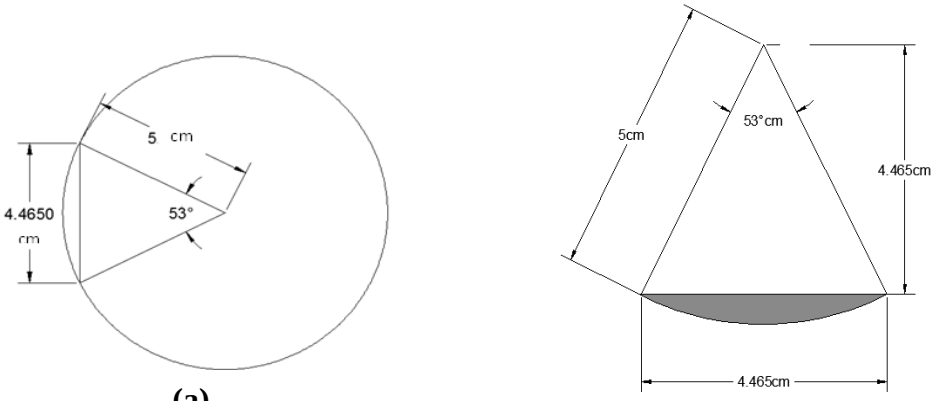

(a) (b)

Figure 7. Schematic diagram of (a) lens (b) sector from the lens.

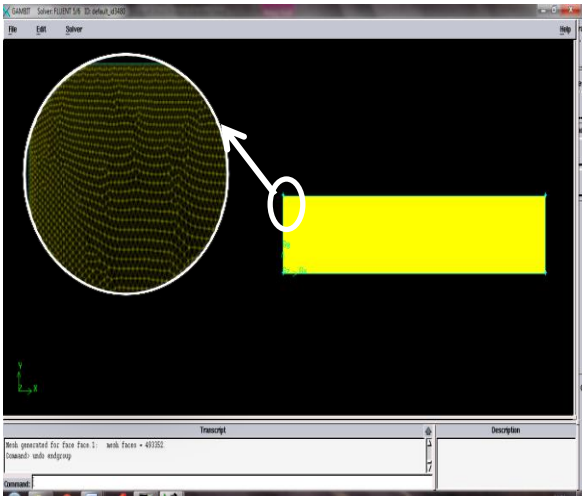

Figure 8. The geometry under the computational mesh.

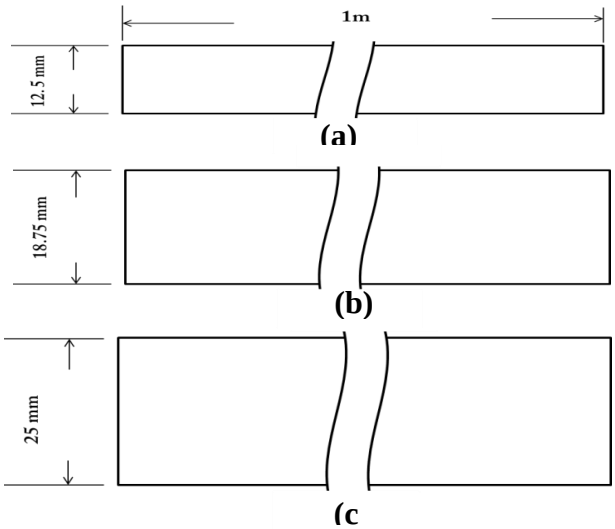

Figure 9. Physical geometry of absorber with diameter of (a) 12.5 mm, (b) 18.75 mm, (c) 25 mm.

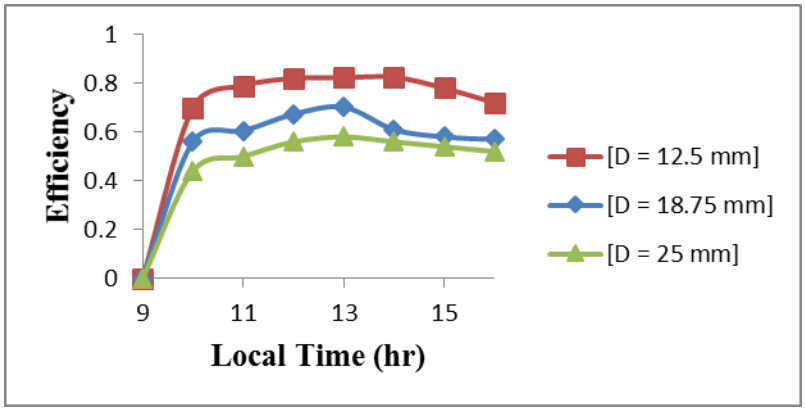

Figure 10. Variation of efficiency with local time for three different absorber diameters.

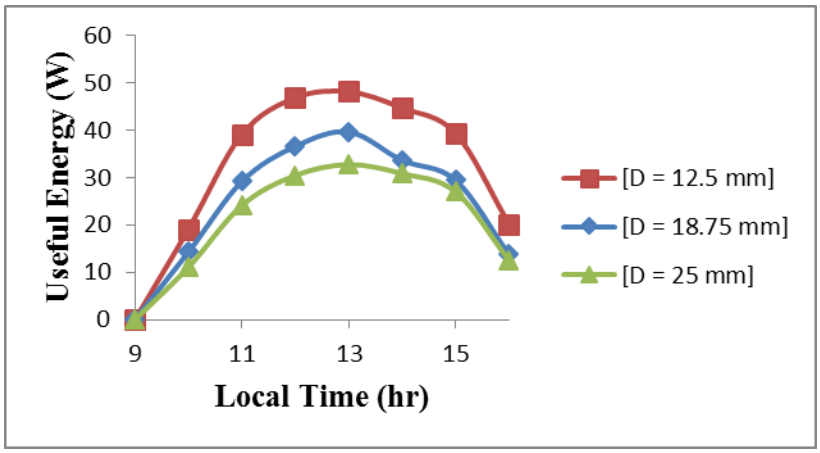

Figure 11. Variation of useful energy with local time for three different absorber diameters.

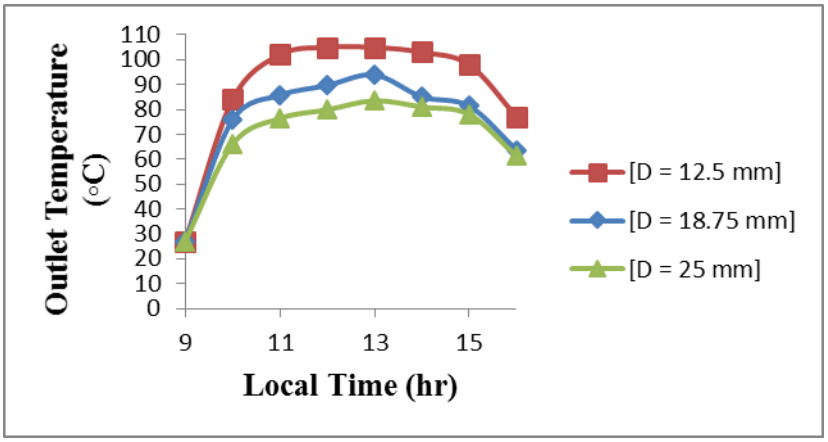

Figure 12. Variation of outlet temperature with local time for three different absorber diameters.

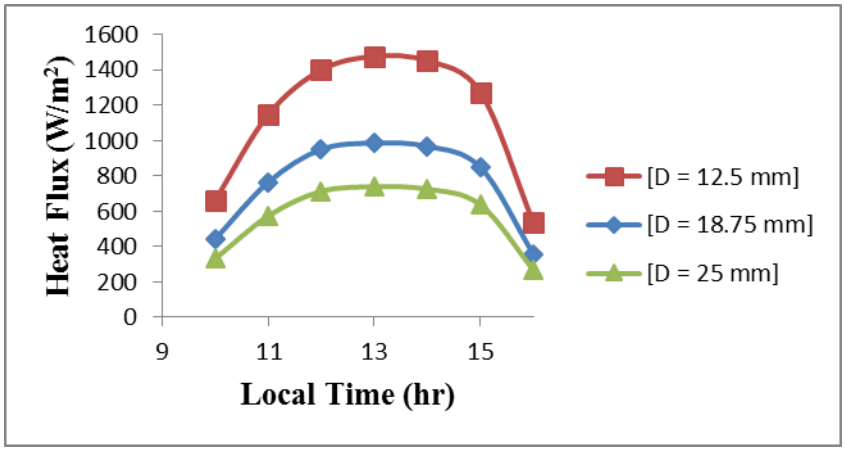

Figure 13. Variation of heat flux with local time for three different absorber diameters.

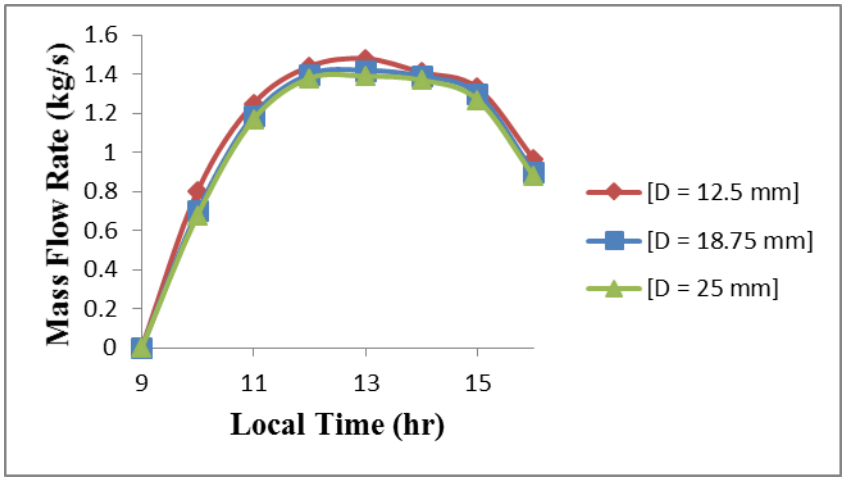

Figure 14. Variation of mass flow rate with local time for three different absorber diameters.

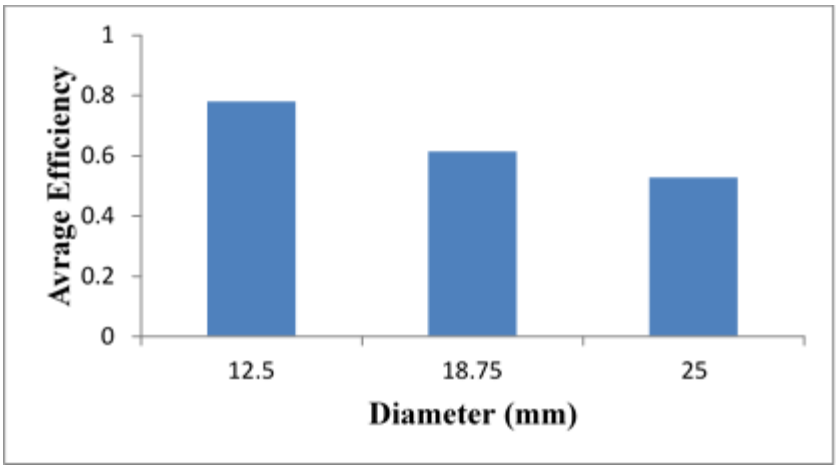

Figure 15. Variation of daily efficiency with absorber diameters on 17th of May 2015.

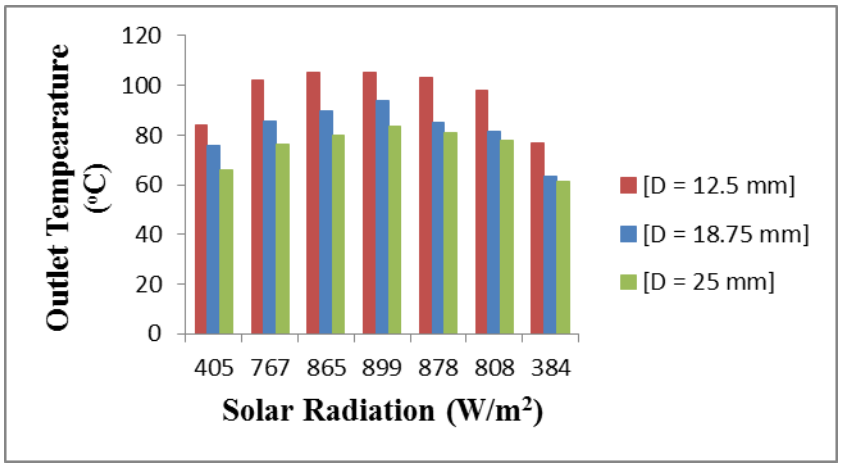

Figure 16. Variation of outlet temperature with solar radiation for three different absorber diameters.

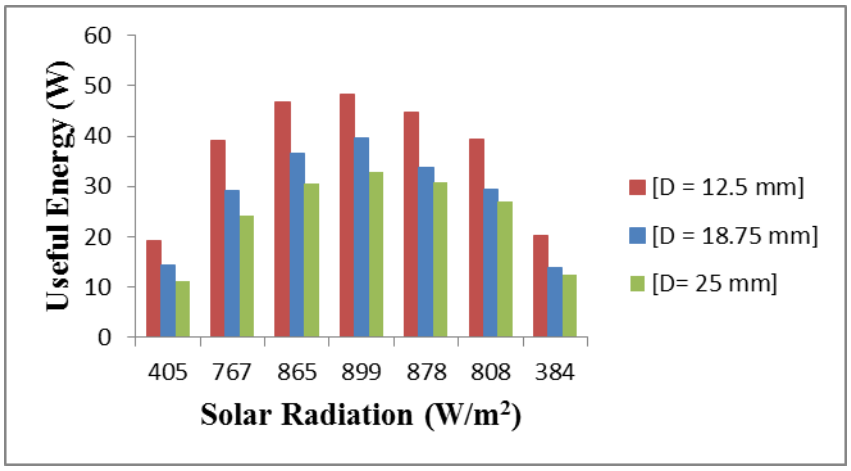

Figure 17. Variation of useful energy with solar radiation for three different absorber diameters.

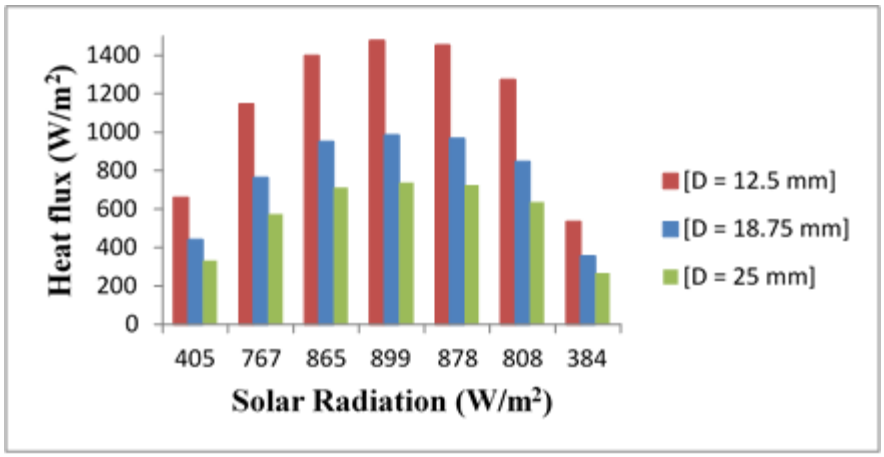

Figure 18. Variation of heat flux with solar radiation for three different absorber diameters.

Table 1. Description of the lens.

Lenses	Description
Appearance	Circle
Diameter size	100 mm
Thickness	5 mm
Focal length	300 mm

Table 2. Boundary conditions of inlet temperature and wall heat flux.

Time (hr)	Inlet Temperature (˚C)	Heat Flux (W/m^2) D=12.5 mm	Heat Flux (W/m^2) D=18.75 mm	Heat Flux (W/m^2) D=25 mm
10:00 AM	27	662	441.6	331.2
11:00 AM	27	1146	764.33	573.24
12:00 PM	27	1400	951	713.3
13:00 PM	27	1478	986.13	738.8
14:00 PM	27	1452	968.26	726.11
15:00 PM	27	1274	849.2	636.9
16:00 PM	27	535	356.68	267.5

NOMENCLATURES

Latin Symbols

Symbol	Description	Symbol	Description
A	area (m^2)	q_b	pool boiling heat transfer (W/m^2)
Cp	specific heat (J/kg. K)	Q_{loss}	heat loss (W)
C	concentration ratio	Q_{useful}	useful heat (W)
D	diameter (m)	Q_{abs}	absorbed heat (W)
F'	collector efficiency factor	Q_u	actual useful heat gain (W)
F''	collector geometry factor	t	time (s)
F_R	collector heat removal factor	T	temperature (K)
$F.R$	fill ratio	$\overline{T}$	average temperature between ambient and sky (K)
Gr	Grashof number	ΔT	temperature difference (K)
g	Gravitational acceleration (m/s^2)	T_a	ambient temperature (K)
h	heat transfer coefficient (W/$m^2.K$)	U_L	overall heat loss coefficient (W/m^2.K)
h_{fg}	latent heat of vaporization (W/$m^2.K$)	U_o	heat loss coefficient based on the outside diameter of the absorber (W/m^2.K)
I_T	solar radiation intensity (W/m^2)	V_w	wind speed (m/s)
k	thermal conductivity (W/m. K)	V_r	flow velocity at r direction (m/s)
L	length of the collector (m)	$V_\emptyset$	flow velocity at $\emptyset$ direction (m/s)
$\dot{m}$	mass flow rate (kg/s)	V_z	flow velocity at z direction (m/s)
Nu	Nusselt number	x	distance along the collector (m)
Pr	Prandtl number		

Greek Symbols

Symbol	Description
$\tau\alpha$	transmittance-absorptance product
ρ	density (kg/m^3)
ϵ	surface tension (N/m)
β	thermal expansion coefficient (K^{-1})
ε_g	emissivity of the glass cover
ε_g	emissivity of the Absorber
μ	dynamic viscosity of the working fluid (Kg/m. s)
σ	Stefan-Boltzmann constant (W/m^2.K^4)
η	efficiency

Subscript

Symbol	Description
1	single-phase region
a	aperture
abs	absorber
abs, cs	absorber cross-sectional
air	air
b	pool boiling region
f	working fluid
g	glass cover
i	inside side
in	inlet
l	liquid-phase
out	outlet
o	outside side
$r, abs - g$	radiation between absorber and glass cover
ref	reference
$r, g - s$	radiation from glass cover to the ambient
sky	sky
sat	saturated
T	total
v	vapor-phase
w	wind
x	local

Satellite Images Classification in Rural Areas Based on Fractal Dimension

Mohammed Sahib Mahdi
Assistant Professor
Department of Computer Science
College of Science
Alnahrain University
email: altaeimohamed@gmail.com

Aqeel Abboud Abdul Hassan
Assistant Instructor
Department of Surveying Engineering
College of Engineering
University of Baghdad
email: al_hammashi87@yahoo.com

ABSTRACT

Fractal geometry is receiving increase attention as a quantitative and qualitative model for natural phenomena description, which can establish an active classification technique when applied on satellite images. In this paper, a satellite image is used which was taken by Quick Bird that contains different visible classes. After pre-processing, this image passes through two stages: segmentation and classification. The segmentation carried out by hybrid two methods used to produce effective results; the two methods are Quadtree method that operated inside Horizontal-Vertical method. The hybrid method is segmented the image into two rectangular blocks, either horizontally or vertically depending on spectral uniformity criterion; otherwise the block is segmented by the quadtree. Then, supervised classification is carried out by means the Fractal Dimension. For each block in the image, the Fractal Dimension was determined and used to classify the target part of image. The supervised classification process delivered five deferent classes were clearly appeared in the target part of image. The supervised classification produced about 97% classification score, which ensures that the adopted fractal feature was able to recognize different classes found in the image with high accuracy level.

Key words: quadtree, box counting, fractal dimension, supervised classification.

تصنيف الصور الفضائية في المناطق الريفية بالإعتماد على البعد الكسوري

أ.م. محمد صاحب مهدي
استاذ مساعد
قسم علوم الحاسوب
كلية العلوم / جامعة النهرين

عقيل عبود عبد الحسن
مدرس مساعد
قسم هندسة المساحة
كلية الهندسة / جامعة بغداد

الخلاصة

حصلت الهندسة الكسورية على اهتمام كبير كونها توفر نموذج نوعي وكمي لوصف الظواهر الطبيعية, حيث بإمكانها إنشاء تقنية تصنيف فعالة للصور الفضائية. في هذا البحث, الصورة الفضائية المستخدمة ملتقطة بواسطة القمر الصناعي الطائر السريع حيث تحتوي على اصناف مختلفة. بعد إجراء المعالجة الأولية للصورة الفضائية, إنها تمر خلال مرحلتين: التقطيع والتصنيف. يتم تنفيذ طريقة التقطيع بإستخدام أسلوب هجين من طريقتين للحصول على نتائج جيدة. هاتان الطريقتان هما طريقة الشجرة التربيعية التي تنفذ داخل الطريقة الأفقية-الشاقولية. الطريقة الهجينة تجزأ الصورة الى مستطيلين أما أفقياً أو شاقولياً إعتماداً على معيار الأنتظامية الطيفية, أو يتم تجزأة الصورة بإستخدام طريقة الشجرة التربيعية. بعد عملية التقطيع تجري عملية التصنيف المراقب بإستخدام البعد الكسوري. حيث يتم حساب البعد الكسوري لكل جزء من الصورة ناتج من عملية التقطيع لكي يستخدم ذلك البعد الكسوري نوعية التفاصيل التي تغطيها الصورة الفضائية. عملية التصنيف أنتجت خمسة أصناف مختلفة تظهر بوضوح على الصورة المستخدمة . أثبت دقة التصنيف التي تم الحصول عليها والتي تصل الى 97% إن الصفة الكسورية المعتمدة قادرة على تمييز الأصناف المختلفة التي تظهر في الصور الفضائية وبدقة عالية.

الكلمات الرئيسية: الشجرة التربيعية, عدّ الصناديق, البعد الكسوري, التصنيف المراقب.

1. INTRODUCTION

Remote sensing is the use of satellite imagery to collect a specific data from the earth about object or phenomenon without physical contact, **Asrar, 1989**. Aerial sensor technologies are used to detect and classify objects on the earth by propagated signals (i.e. electromagnetic radiation). Remotely sensed data are contributed with information from ecosystem models to offer opportunity for predicting and understanding the behavior of the earth's ecosystem reference. High spatio-temporal resolutions of sensors make the observation of precise spatial and temporal structures more accessible in dynamic scenes. Spectral and spatial dimensions combined with temporal components give a valuable information source. Such information helps to detect complex and important patterns by means applications deal with environmental monitoring and analysis of land-cover dynamics. Satellite imagery is sometimes supplemented with aerial photography for achieving an integral form about the target area. Aerial photography has higher resolution, it used for specific applications since it is more expensive than satellite imagery. Satellite imagery is sometimes contributed with vector or raster data in GIS (Geographic Information System) when the imagery needs to be spatially rectified, **Matzler, 2008**. Multi-spectral satellite imagery is an economical, precise and appropriate method of obtaining information on land use and land cover since they provide data at regular intervals and is economical when compared to the other traditional methods of ground survey and aerial photography, **Prasad, 2011**.

Many applications based on using satellite imagery in a quantitative fashion require classification of image regions into a number of relevant categories or distinguishable classes. Satellite image classification is a clustering method based on image features, the classification results are represented by visualization techniques, **Antoni and Nuno, 2005**.

Fractal geometry is the branch of mathematics which studies the properties and behavior of fractals. It describes many situations which cannot be explained easily by classical geometry. Fractal geometry provides a suitable textural image classification framework by studying the nature irregularity shapes in the image, since it allows to easily describing such fractal images. The fractal geometry can recognize small image segment that characterized by its spectral uniformity, this necessitate first to segment the image before the classification. The main characteristics of fractal images are that they are continuous but not differentiable that allows showing the fine details at any arbitrarily small scale, **Iodice, et al., 1995**.

Fractal models have been used in a variety of image processing and pattern recognition applications. Several researchers have applied fractal techniques to describe image textures and segment various types of images; Kasparis et al. in 1995 demonstrated the fractal dimension for texture segmentation. The fractal dimension was not sufficiently describing enough textural characteristics, additional features are needed. They combined the fractal dimension with a simple textural energy measure. A significant performance improvement was achieved compared to using each feature alone. The textural energy is easily computed using convolutional masks. The natural textures were segmented and classified with considering the effect of additive noise, **Kasparis, et al., 1995**, while Al-Ani in 2007 introduced a supervised classification for TM-multi-spectral satellite images. The traditional quadtree segmentation method was applied, then for each segmented block; the fractal features are computed and then used as maximum likelihood classifiers. The used fractal features are fractal dimension and lacunarity. The result showed that the fractal dimension do not have the ability to classify the image blocks whereas the lacunarity showed good classification results. It was found that the fractal geometry can assign efficient parameters for describing images, **Al-Ani, 2007**, and **Mahmood et al. in 2009** proposed a new algorithm for recognizing text object images by using fractal geometry. The fractal dimension was used to recognize text objects within images. Box-counting method was

used to estimate the fractal dimension for image contents. In order to determine a threshold value for the textual objects within image, the fractal dimension was computed for a number of gray scale textual images. The fractal number of each pixel was calculated, and then the mean values of all these fractal values were computed. The threshold value was used in recognizing and retrieving the textual objects within image. The proposed algorithm has performed extremely well with recognition rates 91.5%. It is a promising technique for optical character recognition system, **Mahmood, et al., 2009**.

2. AIM OF RESEARCH

The present work aims to utilize concepts of fractal geometry to classify satellite images in rural areas. This requires analyzing remote sensing imageries to prove that the fractal models exhibit textural features of satellite images, and it offers a significant potential for improving the measurement and analysis of spatially and spectrally complex remotely sensed images.

3. AREA OF STUDY

Fig.1 shows the selected area from the overall image. This area was clipped and saved in new image file of type bitmap 24*bit/pixel*. The memory size of this file was about 12*MB* with spatial resolution of 2048×2048*pixels*. This image resolution covered a land area of about 1.25×1.25*km*, and contained a variety image features. Actually, the geographical region demonstrated in the image of training area was visited to determine the types of the landcover found in the study area. It was found that there are five distinct classes: river, bare land, vegetation and housing. The ensured training sites of were pointed on whole satellite image to be compared with the classification results. It should be mentioned that just the clipping process is done by using ArcGIS 9.3 software.

4. PROPOSED CLASSIFICATION METHOD

The concept of multi-stage query processing and features extraction has been used to model the proposed method. It is claimed that these stages can beneficially be combined and that, through the combination, a significant fast and efficient satellite image classification can be achieved. The generic structure of the proposed satellite image classification method is shown in **Fig.2**. It is shown that the proposed method is designed to be consisted of two phases: the training and recognition. The training is an offline phase, it is responsible on collecting sample image classes to be stored as comparable models in database. Whereas the recognition is an online phase, which is responsible on verifying the test image blocks in comparison with the trained models found in the database. Both phases are composed of three stages include: image preprocessing, image partitioning, and features extraction. Features extraction attempts to estimate the fractal dimension (D) and spectral power (P) for all test image blocks. Last stage is a comparison based on fractal feature between the image blocks and training classes found in the database, the result of the comparison will determine the similarity measure between the considered image blocks and then help to make the classification decision. More details about each stage are given in the following sections:

4.1. Image Preprocessing

This stage involves two stages: multiband image enhancement and conversion multiband image to grey scale image. Image enhancement is a preprocessing stage seeks to improve the visual appearance of the image under consideration that was shown in **Fig. 3**. This stage is relied on the intensity of pixels with no effect the correlation of adjacent pixels. Such enhancement

leads to improve the distinguishing between image features, which can be achieved by applying the Eq. (1) on the image, **El Hassan, 2007**:

$$I_e(x,y) = round[(\frac{I_o(x,y)-l}{h-l})\times 255] \quad (1)$$

Where, $I_e(x,y)$ represent the new enhanced image, $I_o(x,y)$ is the original image, x, and y are indices of the pixel in the image, l represent the bottom 1% of all pixel values of original image, and h represent the top 1% of all pixel values of original image. Then, the three enhanced band components (R_e, G_e, and B_e) were concatenated together to get new one enhanced image ($I(x,y)$) using Eq. (2) as shown in **Fig. 4**, **Richards and Jia, 1999**:

$$I(x,y) = 0.2989R_e(x,y) + 0.5870G_e(x,y) + 0.1140B_e(x,y) \quad (2)$$

4.2. Image Segmentation

Hybrid method was suggested to carry out segmentation process, in which the horizontal-vertical method is operated inside the quadtree method. The two methods are contributed with each other to produce high quality results. The implementation of such hybrid partitioning method requires to set some values are related the control of the partitioning process, they called control parameters. These control parameters are, **Al-Aboudy, 2002**:

a. Maximum block size.
b. Minimum block size.
c. Mean factor: represents the multiplication factor; when it is multiplied by the global mean of image it will define the value of the extended mean.
d. Inclusion factor: represents the multiple factor, when it is multiplied by the global standard deviation it will define the value of the extended standard deviation.
e. Acceptance ratio: represents the ratio of the number of pixels whose values differ from the block mean by a distance more than the expected extended standard deviation.

Fig. 5 shows the segmented image using hybrid method.

4.3. Features Extracton

The search for the fractal features in the literatures shows that there are many available fractal features can be used to describe fractal objects such as satellite images. There is an important note was noticed, which state that all the fractal features are related to fractal dimension, implies that the use of fractal dimension substitutes on using other fractal features. Therefore, it was decided to employ just the fractal dimension for satellite image classification. Fractal dimension is a fraction number restricted in between the range 2-3 for two dimensional images, which may give interfered values belonging to different classes, and leads to confuse the classification results. Such that, the researchers goes to adapt the fractal dimension to be compatible with the study case.

The next step after completing image segmentation process is the computation of fractal dimension of each block. The procedure that was used to compute the fractal dimension may be considered a novel box-counting method that was produced according to experiments to develop and eliminate the limitation of the traditional method and other methods came later.

In the present work, the novel effort is adapting the boundary conditional values of the fractal dimension estimated by the box counting method to achieve intended results. The fractal dimension computation is applied on each image block resulted from the segmentation stage.

4.4. Training Based Classes

The stage of determining image classes is based on specifying a range of fractal dimension for each phenomenon that appearing in the used image. The field visit to the study area shows that there are five distinct classes can be found. Also, this make sure by reliance other information about covered area, such as, recently aerial images and thematic maps, reconnoitering zone or any earlier information about study area. Therefore, a specific range of fractal dimension for each class should be determined and stored in database to be used for classification of training area firstly, and then classify other adjacent areas in the same image later on. Table 1 denotes the range of fractal dimension used for each class.

4.5. Image Classification

According to the five similarity measures of each block, the block assigned to the class that gives highest similarity measure. When this procedure is applied on all the image blocks, a specific color is needed for coloring each block according to its ownership class. Also, there is a color legend should be fixed to explain the meaning of colors appear in the classification results. Then, the classification results should be compared to the actual classification information delivered from manual process based on field view in order to evaluate the classification process. After ensuring the classification results of the training area, other areas in the image can be classified with high creditability.

5. RESULTS

Throughout the classification of the training area, the fractal dimension delivers encouraging supervised classification outcomes, where each class of image has a relatively different range of fractal dimension (D_F). **Fig. 6** displays the classification result of the training area; such result should be evaluated before classifying other areas in the test image. Actually, the acceptable classification results of training area encourage completing the classification by taking other areas found in the test image. **Figs. 7** and **8** show the classification results of different selected area. It is noticeable that the classification is carried out with efficient performance, where the classification percentages reach to 97%.

6. CONCLUSIONS

Throughout the implementation of the presented work, a number of conclusions have been achieved based on the practical results. The following statements summarize the most important ones:

1. The high classification results prove that the fractal geometry exhibit the description of satellite images.
2. The normal distribution of the fractal dimension of multi conglomerates with narrow width refers to high discriminant power of fractal dimension for image classification.
3. Higher accuracy of fractal dimension estimation is achieved by allowing the height of the box at the top of each grid block to be adaptable to the maximum gray-scale of that block and the method is applicable to blocks with arbitrary sizes and shapes.

4. The uniformity of blocks' characteristics which produced by the suggested segmentation method leads to get independent range of D_F for each class. This has increased the accuracy of the classification.
5. The convergence in D_F for different phenomena and the smallness of the range of it caused to decrease the efficiency of classification.

REFERENCES

- Al Ani, L. A., 2007, *Satellite Images Classification Based Fractal Features*, Journal of Al-Nahrain University, vol. 10, no. 1, pp. 79-83.
- Al Aboudy, B. K., 2002, *Color Image Data Compression Using Multilevel Block Truncation Coding Technique*, PhD. Thesis, Baghdad University, College of Science, Department of Astronomy & Space.
- Antoni, B. and Nuno, V., 2005, *Probabilistic Kennels for the Classification of Auto Regressive Visual Processing*, IEEE, Conference on computer Vision and Pattern recognition, San Diago.
- Asrar, G., 1989, *Theory and Applications of Optical Remote Sensing*, New York, Wiley.
- El Hassan, I. M., 2007, *Digital Image Processing in Remote Sensing*, Research Center, College of Engineering, King Saud Univ-ersity.
- Iodice, A., Migliaccio, M., and Riccio, D., 1995, *SAR Imagery Classification: the Fractal Approach*, Proceeding, Europto Series, vol. 936, pp. 539-551.
- Kasparis, T., Tzannes, N. S., Bassiouni, M. and Chen, Q., 1995, *Texture Description Based on Fractal and Energy Features*, Comput. Elect. Eng., vol. 21, no. 1, pp. 21–32.
- Mahmood, H. F., Sultan, E. A. and Najim, O. A., 2009, *Recognizing Text Objects within Images by Uses Fractal Dimension*, J. Education and Science, vol. 22, no. 2, pp. 167–177.
- Matzler, C., 2008, *Physical Principles of Remote Sensing*, University of Bern, Switzerland.
- Prasad, S. V. S., Savitri, T. S. and Krishna, I.V. M., 2011, *Classification of Multispectral Satellite Images Using Clustering with SVM Classifier*, International Journal of Computer Applications, vol. 35, no.5, pp. 32−44.
- Richards, J. A. and X. Jia, 1999, *Remote Sensing Digital Image Analysis*, Springer Verlag, Berlin, Germany.

NOMENCLATURE

I_e= new enhanced image, dimensionless.
I_o= original image, dimensionless.
x , y= indices of the pixel in the image, dimensionless.

l= the bottom 1% of all pixel values of original image, dimensionless.
h= the top 1% of all pixel values of original image, dimensionless.
I= grey enhanced image, dimensionless.
R_e= red color components of enhanced image, dimensionless.
G_e= green color components of enhanced image, dimensionless.
B_e= blue color components of enhanced image, dimensionless.

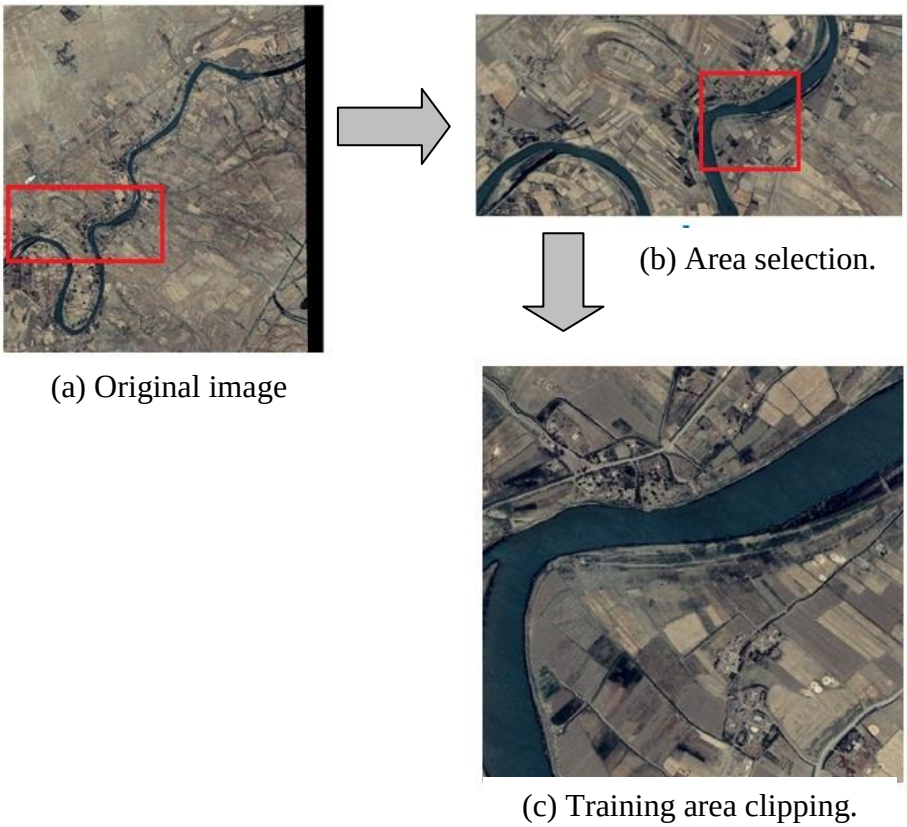

Figure 1. Training area selection**.**

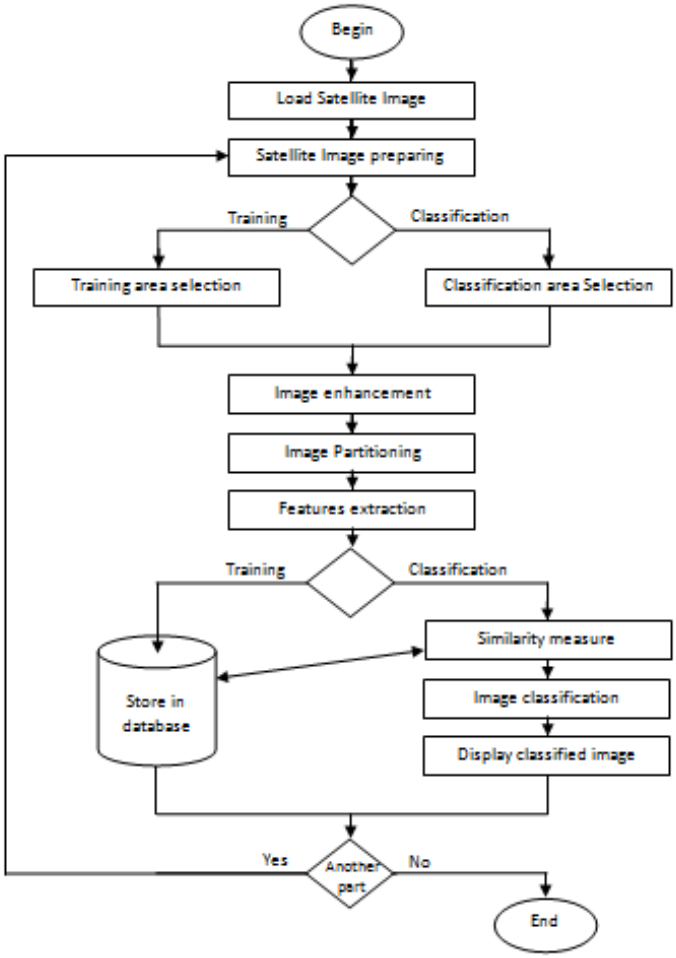

Figure 2. Block diagram of the proposed satellite image classification method.

Figure 3. Original image.

Figure 4. Grey enhanced image.

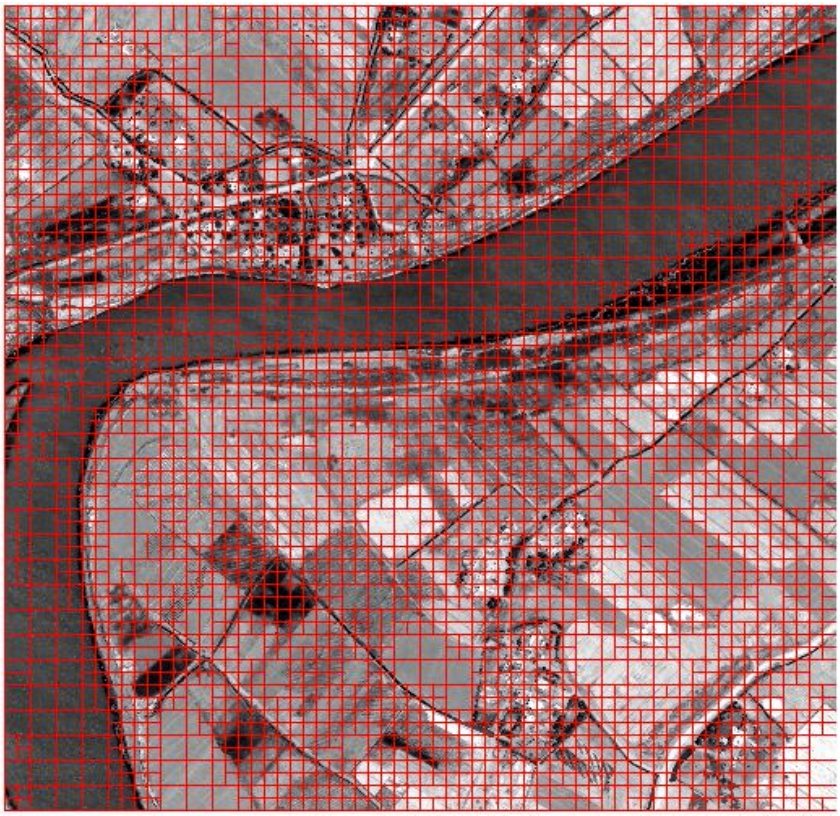

Figure 5. Partitioned image

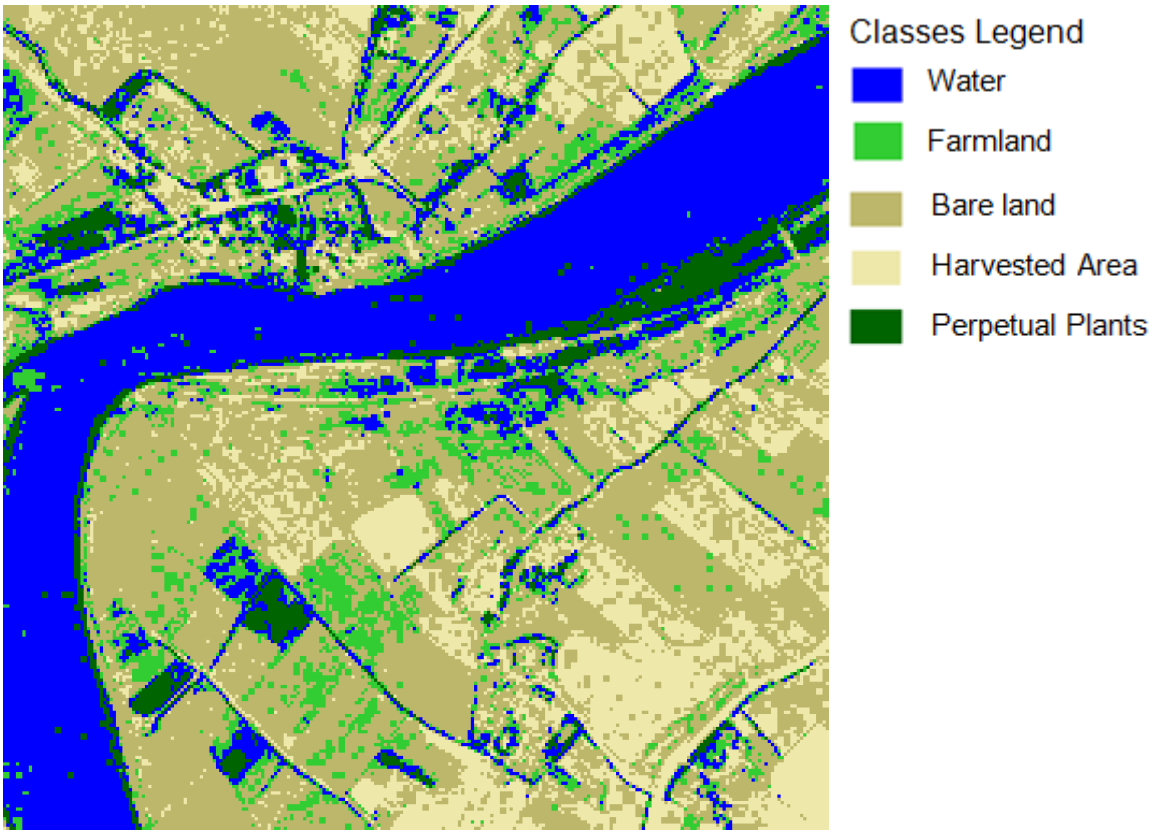

Figure 6. Classification result of the testing area.

Figure 7. Second case study.

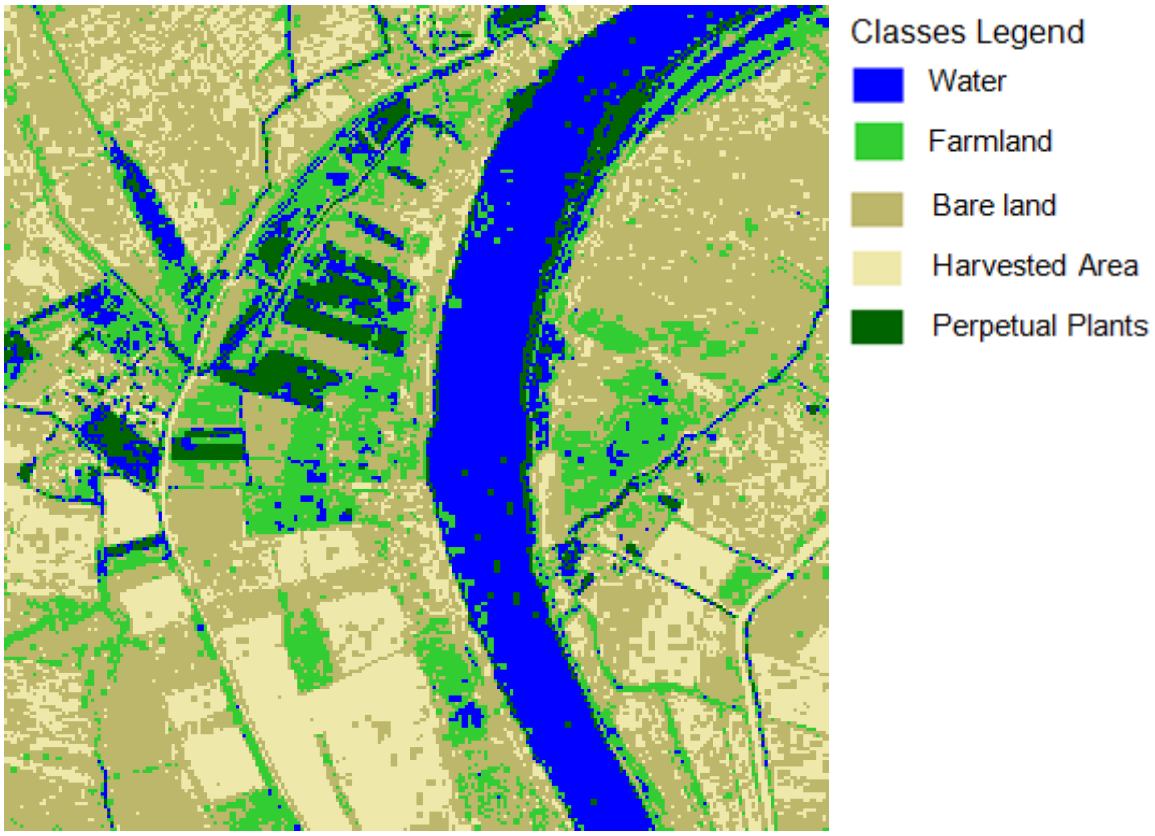

Figure 8. Classification result of second case study.

Table 1. Range of fractal dimension for each class

Class	Fractal Dimension	
	Min.	**Max.**
Perpetual plants	1.9107	2.335
Water	2.335	2.5
Farmlands	2.5	2.588
Bare lands	2.588	2.73
Harvested areas	2.73	3.13

Estimation of Mass Transfer Coefficient for Copper Electrowinning Process

Dr. Sarmad Talib Najim

Chemical Engineering. Department. /Collage of Engineering/Al-Nahrain University

E-mail: dr_sarmadalani@yahoo.com

ABSTRACT

Mass transfer was examined at a stationary rectangular copper electrode (cathode) by using the reduction of cupric ions as the electrochemical reaction. The influence of electrolyte temperature (25, 45, and 65 ^{o}C), and cupric ions concentration (4, 8, and 12 mM) on mass transfer coefficient were investigated by using limiting current technique. The mass transfer coefficient and hence the Sherwood number was correlated as $Sh = 4.25 \times 10^{-3}(Gr\ Sc)^{0.486}$

Key words: Mass transfer coefficient, copper electrowinning, limiting current, dimension less group.

حساب معامل انتقال الكتلة لعملية استخلاص النحاس

د. سرمد طالب نجم

قسم الهندسة الكيمياوية/كلية الهندسة/جامعة النهرين

الخلاصة

تم اختبار انتقال الكتلة على قطب النحاس الساكن (كاثود) باستخدام الاختزال الكهروكيمياوي لأيونات النحاس الثنائية. ومن ثم التحري عن تأثير درجة حرارة المحلول الالكتروليتي (25، 45،و 65 م^{o}) اضافة الى تركيز ايونات النحاس الثنائية (4، 8، و12 ملي مولاري) على معامل انتقال الكتلة باستخدام تقنية التيار المحدد. تم الحصول على علاقة تربط بين (Sherwood number) وكل من (Grashof number) و (Schmidt number).

الكلمات الرئيسيه: معامل انتقال الكتلة، استخلاص النحاس، التيار المحدد.

1. INTODUCTION

An increase world population with growing industrial demands has led to the situation where the protection of the environment has become a major issue and crucial factor for the future development of industrial processes, which will have to meet the requirements of sustainable development**, Juttner K. et al., 2000**. There are increasing economic, social, legal, and environmental pressures to utilize "the best available technology" not entailing excessive cost and to aspire to "performance without pollution", i.e., "zero pollution processing". Electrochemical technology has an important role to play as part of an integrated approach to:

- The avoidance of pollution reagents in materials synthesis
- Monitoring of pollution and reagent levels in the gas and liquid phase
- The removal of environmental contaminants, such as metal ions and organics from industrial process streams
- Cleaner processing involved the clean conversion of chemical to electrochemical energy using fuel cell and photovoltaic devices, and modern techniques for electrical energy storage and conversion, **Walsh F.C., 2001.**

The removal (recovery) of metals from aqueous solutions by electrolytic means has been a major factor in extractive technology during the last decades. The source of metal can be an ore as well as waste residue (scrap metals, dusts, sludge's collected from metallurgical operations, etc.), **Soliman H. et al., 2011.** Copper is the most widely mined mineral in many countries though a few other minerals such as gold, cobalt, and silver are also exploited. Copper producing companies have acknowledged the importance of producing high quality copper in order to satisfy the market demands and requirements. There are two methods of electrochemical for production copper: electrorefining is one method that produces high quality copper from 98% to 99.98% copper while electrowinning is used for the recovery of copper from dilute solutions, **Ntengwe F.W, 2008, Fogarasi S. et al. 2015**. One of the aims in studying metal electrowinning is to gain better understanding of the metal electrodeposition. The electrodeposition of copper on foreign substrates is widely used in electronic industry for interconnects, manufacturing printed-circuit boards, as well as making protective and decorative coatings, **Majidi M.R. et al., 2009**.

The objective of the present work is to design and construct a copper electrowinning cell in order to study the effect of different operating parameters (electrolyte temperature and cupric ions concentration) on the mass transfer coefficient.

2. THEORY

Electrochemistry deals with the study of mutual conversion of chemical and electrical forms of energy. It deals with reactions that proceed at the expense of electrical energy. The application of external voltage is the key factor in the electrodeposition of metal from the anode to the cathode or from solution to the cathode as the case may be. The mass transfer through migration, convection, and diffusion in electrochemical reactors is the result of the applied overvoltage, **Ntengwe F.W, 2008**. The main advantages of the electrochemical technology are:

- Electrons are clean reagents, this strategy include both the treatment of effluents and waste and development of new processes or products with less harmful effects.
- Effective control of the electron transfer rate (current density)
- Measurement of reaction conditions (current density and electrode potential).
- The process can be turn on and off via the current.
- Ambient conditions of temperature and pressure can be used, **Walsh F.C., 2001**.

Electrolytic cell solutions used for an electrowinning studies always contains a certain concentration of an electroactive species (Cu^{+2}) and large concentration of an inert electrolyte such as H_2SO_4 to supply high solution conductivity and a large number of ions that act as the actual current carriers within the electrolytic solution. Therefore, the transfer of Cu^{+2} to the cathode surface by migration is eliminated, so it transferred by diffusion and free convection. When a small potential difference is applied across electrodes, the ions move within the solution toward the oppositely charged electrodes and accumulate near the respective electrodes, current suffer a sudden jump due to exchange of electrons between electrodes and the electroactive ions. Eq. (1) expresses the reduction of Cu^{+2}, **Zaki M.M., 2000**:

$$Cu^{+2} + 2e^{-} \longrightarrow Cu \qquad E^{o} = 0.337V \tag{1}$$

Due to the discharge of some Cu^{+2} ions, the concentration of Cu^{+2} ions in the immediate vicinity of the cathode is decreased to C_i accordingly, the interfacial solution density decreased from ρ_b to ρ_i and this density difference gives rise to a buoyancy force, g Δρ, which causes upward solution flow at the electrode surface. This flow enhances the transfer of Cu^{+2} from bulk solution to the edge of the diffusion layer, **Grigin A.P. et al., 2000**. If the cell voltage is sufficiently increased, a state is reached where interfacial concentration becomes zero and the rate of mass transfer becomes maximum. Under this condition, the current reaches a constant value known as the limiting current (I_{Lim}). In the meantime, the cathode potential increases to a high value where hydrogen gas starts to evolve simultaneously with copper deposition according to the reaction shown in Eq. (2):

$$2H^{+} + 2e \longrightarrow H_2 \qquad E^{o} = 0.0\ V \tag{2}$$

The flux of Cu^{+2} ions ($N_{Cu^{+2}}$) may be obtained from Eq. (3), **Wiebe S., 2015, Thomas B. D., 1978**:

$$N_{Cu^{+2}} = \frac{I_{Lim}}{Z\,A\,F} = \frac{D\,\Delta C}{\delta} = k_m\,(C_b - C_i) \tag{3}$$

$$\frac{I_{Lim}}{Z\,F} = k_m\,A\,C_b \text{ (when } C_i = 0 \text{ at Limiting current)} \tag{4}$$

Or $k_m = \frac{I_{Lim}}{Z\,F\,A\,C_b}$

For the electrolysis of Cu^{+2} in an electrolyte that contains H_2SO_4, under free convection it was found that Sherwood number based on the Grashof number and Schmid number is given in Eq.(5).

$$Sh = \alpha\,(Gr\,Sc)^{\beta} \quad (5)$$

The Grashoof number is given by the following equation since the free convection in the ion transfer is caused by density differences due to concentration change between bulk solution and electrode surface, **Mizushina, T. et al., 1971**:

$$Gr = \frac{g\,d^3\,(\rho_b - \rho_i)}{\mu^2} \quad (6)$$

3. EXPERIMENTAL

3.1 Materials

Annular grade sulfuric acid (1 M H_2SO_4) (purity > 98.5 wt%) and copper sulfate ($CuSO_4$) was used as redox system to give various concentrations of cupric ions 4, 8, and 12mM.

3.2 Electrowinning Cell and Circuit

The experimental apparatus which were used for performing the present work is shown in **Fig. 1**.

The cell consisted of beaker with capacity 1.5 liter, the anode was a square graphite sheet($5cm\ height \times 5cm\ width$), the cathode was a square copper sheet ($5cm\ height \times 5cm\ width$), the distance between electrodes is 2cm. The back of the cathode was coated with epoxy. The electrical circuit consisted of 5V DC power supply was connected in a series with cell and ammeter. A voltmeter was connected in a parallel with the reference electrode and cathode.

The potentiostat technique was used for obtaining the polarization curves at different conditions. The polarization curve (overpotential versus log i) was drawn and the limiting current was measured. The mass transfer coefficient k_m calculated from the obtained limiting current.

4. RESULTS and DISCUSSION

The limiting current I_{Lim} is obtained from polarization curves (from the clear constant current region which almost start at -100 mV) under the following conditions: cupric ions concentration 4, 8, and 12 mM and electrolyte temperatures 25, 45, and 65 ℃ in order to determine mass transfer coefficient k_m.

Figure 2 shows the polarization curve for electrolyte containing 1 M H_2SO_4 only at various electrolyte temperatures, while **Figs. 3 to 5** show the polarization curves for copper

electrodeposition from electrolyte containing 1 M H_2SO_4 and different concentrations of cupric ions at different electrolyte temperatures. From these figures it is clear that the limiting current is increased with increasing cupric ions concentration, and electrolyte temperature, and this can be attributed to the fact that increasing the reactant concentration will increase the reaction rate(I_{Lim}), while increasing the temperature will increase the diffusivity of reactant species and decrease the viscosity of electrolyte.

It can be observed from **Fig 6** that increasing cupric ions concentration leads to an increase in the limiting current and hence k_m. This is a consequence to increase the electrical conductivity of solution i.e. decrease the solution resistivity to the flow of the current between electrodes, **Majidi M.R. et al., 2009**. It is clear from **Figs 7 and 8** that as the temperature increases k_m increases. This is due to the fact that increasing temperature will increase the rate of copper diffusion to the metal surface and decrease the viscosity of electrolyte which will aid the copper diffusion, **Uhlig H.H., 1985, Theordore L., 2010**.

Figure 9 shows log Sh against log Gr Sc (the values of dimensionless groups are listed in table 2), straight lines were obtained with a slope equal to the constant β while the intercept gives the other constant α. And finally the average mass transfer coefficient for a free convection of cupric ions reduction in acidic media was correlated as in the following equation:

$$Sh = 4.25 \times 10^{-3}(Gr\ Sc)^{0.486} \quad (7)$$

Within an average deviation of ± 4.5% for the following region

$$2.97 \times 10^{12} < Gr\ Sc < 6.1 \times 10^{12}$$

This proves that the cupric ions reaction results in a movement of ions in the bulk solution guiding to laminar natural convection flow.

5. CONCLUSIONS

- The reduction of Cu^{+2} ion in acidic media starts at about -100 mV vs. SCE and reaches the maximum at approximately -280 mV vs. SCE.
- Electrolyte temperature is the most significant operating parameters that affects the mass transfer coefficient.
- The electrowinning process of copper is under mass control in the cathodic region (-280 to -550) mV vs. SCE.
- The copper electrowinning process is under laminar natural convection for a stagnant electrolyte.

REFERENCES

- Fogarasi, S., Lucaci, F., Egedy, A., Lucaci, A.I., and IIea, P., 2015, *Eco- friendly copper recovery process from waste printed circuit boards using Fe^{+3}/Fe^{+2} redox system*, waste management, vol. 40, PP. 136-143.

- Grigin, A.P. and Davydov, A.D., 2000, *Limiting Current of electrochemical deposition of copper from copper sulfate and sulfuric acid solution on a vertical electrode under conditions of Natural convection*, Journal of electroanaltical chemistry, vol. 493, PP. 15-19.
- Juttner, K., Galla, U., and Schmieder, H., 2000, *Electrochmical approaches to environmental problems in the process industry*, Electrochimica Acta, vol. 45, PP. 2575-2594.
- Majidi, M.R., Asadpour-Zeynali, K. and Hafezi, B., 2009, *Reaction and nucleation mechanisms of copper electrodeposition on disposable pencil graphite electrode*, Electrochimica Acta, vol. 54, PP. 1119-1126.
- Mizushina, T., Irvine, T.F., Jr. and Hatnett, J.P., 1971, *Advances in Heat Transfer*, Academic press, Inc., vol.7.
- Ntengwe, F.W., 2008, *The Effect of Impurities, Smootheners and other Factors on the recovery of copper from solutions*, M.Sc. Thesis, South Africa University.
- Soliman, H. and Abd El- Moneim, A., 2011, *Electrowinning of copper using Rotating Cylinder Electrode utilizing lead anode*, Engineering, vol. 3, PP. 340-358.
- Theordore, L., Ricci, F., 2010, *Mass Transfer Operations For the practicing Engineering*, John Wiley & Sons, Inc.
- Thomas, B. D., 1978, *Advances in Chemical Engineering*, Academic Press, Inc., vol. 10.
- Uhlig, H.H., 1985 *Corrosion and Corrosion Control*, 3rd Edition, Wiley-Interscience publication, New Yourk, . PP. 100.
- Walsh, F.C., 2001, *Electrochemical technology for environmental treatment and clean energy conversion*, IUPAC, Pure Appl. Chem., vol. 3, No. 12, PP. 1819-1837.
- Wiebe, S., 2015, *Modeling and Fault Detection of an industrial copper electrowinning process*, M.Sc. Thesis, Laurentian University.
- Zaki, M.M., Nirdosh, I., Sedahmed, G.H. and Baird, M.H.I., 2000, *Low – cost Experiments in Mass Transfer Part 7. Natural convection mass transfer on a vertical cylinder with sealed ends*, CHE Division of ASEE.

NOMENCLATURE

A = Cathode area, cm^2

C_b = bulk concentration of cupric ions, mol/cm^3

C_i = interfacial concentration of cupric ions, mol/cm^3

D = diffusion coefficient, cm^2/s

F = Faraday's constant (96487)

g = acceleration due to gravity, cm/s^2

Gr = Grashof number, $\frac{g\, l^3\, (\rho_b - \rho_i)}{\mu^2}$

I_{Lim} = limiting current, A

i_{Lim} = limiting current density, A/m^2

k_m = mass transfer coefficient, cm/s

l = characteristic length dimension in Sherwood and Grashog numbers, cm

$N_{Cu^{+2}}$ = diffusional flux of electroactive species, $mol/s.cm^2$

Sh = Sherwood number, $k_m\, l/D$

Sc = Schmidt number, v/D

T = temperature, ℃

Z = number of electrons involved in the reaction

α = constant used in equation 5

β = constant used in equation 5

ΔC = concentration difference between bulk concentration and interfacial concentration, mol/cm^3

Δρ = density difference between bulk concentration and interfacial concentration, g/cm^3

μ= dynamic viscosity of cupric ions, g/cm.s

v = kinematic viscosity of cupric ions, cm^2/s

ρ_b = bulk density of cupric ions, g/cm^3

ρ_i = interfacial density of cupric ions, g/cm^3

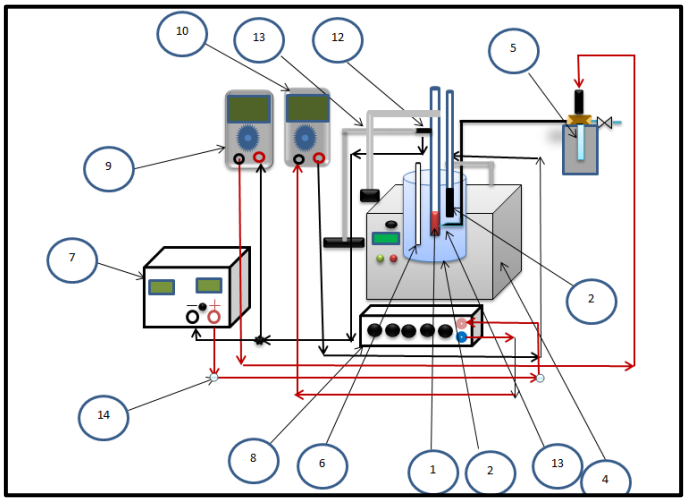

Figure 1. Schematic view of equipment setup.

Table 1. Experimental Apparatus.

NO.	Item Name	NO.	Item Name
1	Cathode	8	Resistance box
2	Graphite electrode (anode)	9	Voltmeter
3	Beaker	10	Ammeter
4	Water bath	11	Luggin capillary tip
5	Reference electrode (SCE)	12	Brush
6	Thermometer	13	Stand
7	Power supply	14	Electrical wires

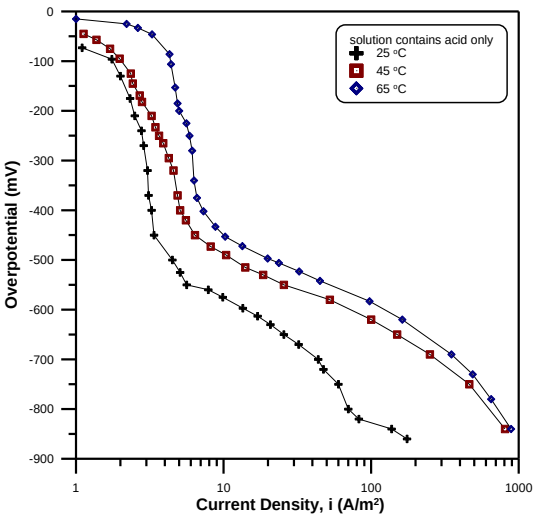

Figure 2. Effect of temperature on polarization curves for acid only (1 M H_2SO_4).

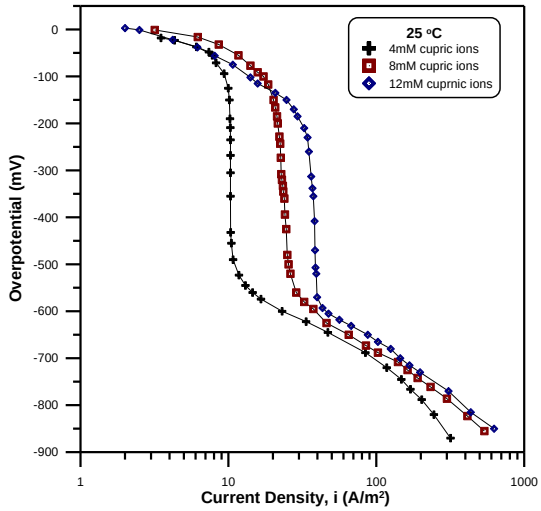

Figure 3. Effect of cupric ions concentration on polarization curves of electrolyte solution at 25 ^{o}C.

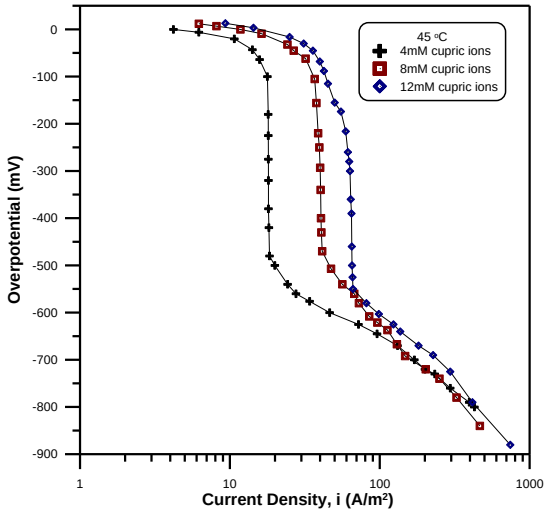

Figure 4. Effect of cupric ions concentration on polarization curves of electrolyte solution at 45 ^{o}C.

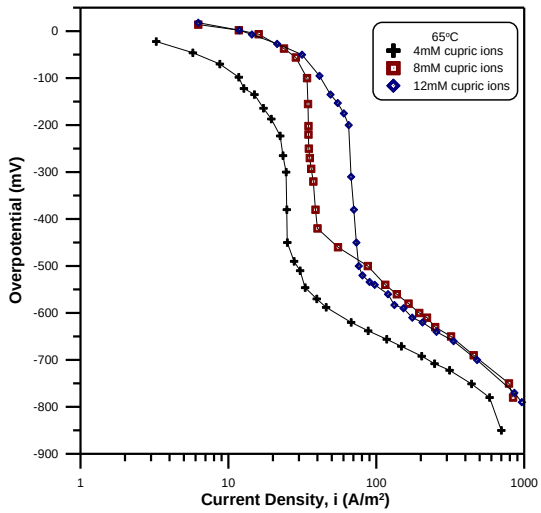

Figure 5. Effect of cupric ions concentration on polarization curves of electrolyte solution at 65 ^{o}C.

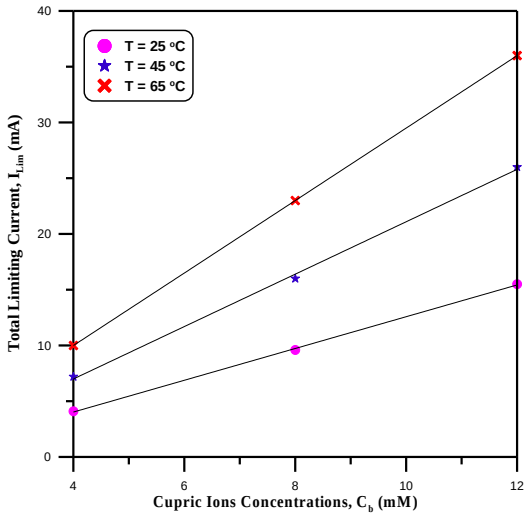

Figure 6. Effect of cupric ions concentration on the Limiting current at different temperatures.

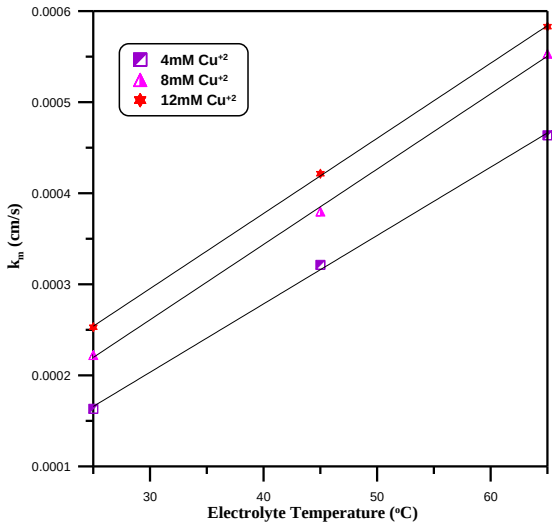

Figure 7. Mass Transfer coefficients vs. electrolyte temperatures at different cupric ions concentrations.

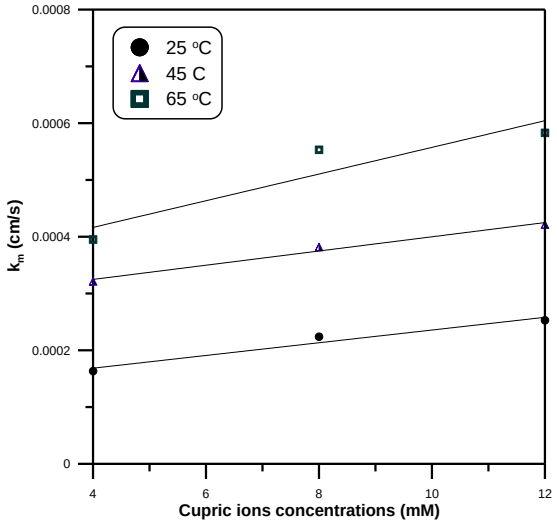

Figure 8. Mass Transfer coefficient vs. cupric ions concentrations at different Temperatures.

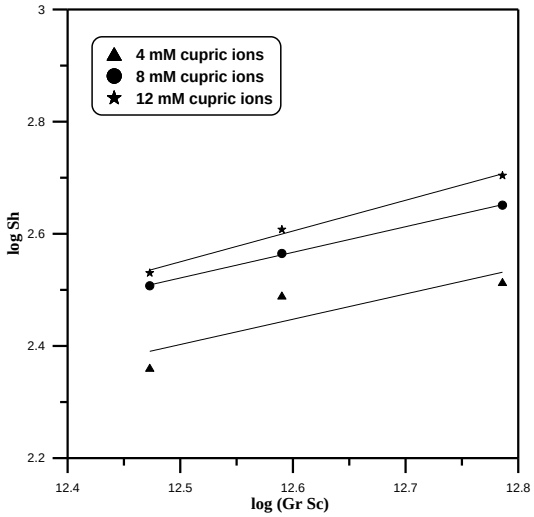

Figure 9. The relationship between Sh vs. Gr*Sc.

Table 2. Values of dimensionless group (Sh, Gr, and Sc) at different operating conditions.

T ℃	Cu^{+2} Conc. mM	Sh	Gr $\times 10^{-9}$	Sc
25	4	326.6844	1.9	3212
	8	447.8738		
	12	505.8339		
45	4	309.0531	3.33	1166
	8	367.3173		
	12	405.3156		
65	4	229.7574	5.32	559
	8	321.6603		
	12	339.0198		

برنامج تطبيق قواعد السلامة في المشاريع الهندسية

م.د. انتصار كاظم رشيد
قسم الهندسة المدنية
كلية الهندسة / جامعة بغداد

الخلاصة

عندما بدأ عصر النهضة الصناعية والانشائية في العالم الحديث كان الاهتمام الأكبر يتجه نحو الآلات والمعدات على اساس انها الوسيلة الاولى للانتاج، وبعد ان استقرت الصناعة بدأت الأنظار تتجه الى القوى العاملة التي يعتمد عليها الانتاج وثبت بأنها تمثل الجزء الأساسي في جميع العمليات وكانت وقاية هؤلاء الافراد من اخطار المعدات والصناعة وحوادثها من اولى الامور التي خضعت للأبحاث العديدة حتى تبلورت في مبادئ عامة لكل الصناعات واخرى تهتم بكل صناعة على حدة.

تعتبر السلامة المهنية المانع الذي يهدف الى الحفاظ على المقومات البشرية والمادية وكذلك الى رفع انتاجية هذه المقومات في اطار السلامة والصحة وتوفير الجو المناسب الصحي للعامل فيشعر بالامان والثقة والاستقرار النفسي وهذا سوف يؤدي الى زيادة الانتاج وبغية المحافظة على الايدي العاملة من مخاطر العمل وتمكيناً لها في اداء دورها بصورة افضل لزيادة الانتاج وتحسين نوعيته والمحافظة على الآلة ودعم الاقتصاد الوطني ومواكبة للتطورات الصناعية والتكنلوجية فقد جاءت فكرة البحث في التركيز على اهمية دراسة موضوع السلامة المهنية وذلك بإجراء المسح الميداني للإطلاع على واقع السلامة المهنية في الدوائر المعنية ومواقع العمل ومن خلال إجراء استبيان حول هذا الموضوع وإجراء المقابلات الشخصية مع المعنيين في هذا المجال والتوصل الى إعداد برنامج لتطبيق قواعد السلامة المهنية لكل الموارد (العمالة، الآليات، المواد، المال) في المواقع الانشائية والدوائر المعنية.

A Program Applying Professional Safety Basics in Construction Projects

Lecturer Dr. Entisar Kadhim Rasheed
Department of Civil Engineering
College of Engineering
Baghdad University
E-mail:int.pros_62@yahoo.com

ABSTRACT

When industrial and constructional renaissance started in the world, the great interest was going on towards the equipment's, which was the first mean for production. After industry was settled the interest was going on towards the men ship which manpower on which the production depends. It was approved that it represents the basic part in all of the processes and the protection of those individuals against dangers of these equipment's, industry and its accidents was the basic things which was studied in many researches until it crystallized in general principles for all industries and other take care in each industry.

The professional safety is concerned as restrict which aims to take care of humanitarian and material principles also to raise the production of these principles, in the aspect of safety, health and providing the suitable healthy condition to the worker so he can feel safety, confidence and sociological settle, this will increase the production. So In order to maintain the manpower of business risks and to enable them to fulfill their role better to increase production and improve the quality and maintain the machine and supporting the national economy and keep pace with

industrial developments and technological came the idea of research to focus on the importance of studying the subject of occupational safety by conducting a field survey to see the reality of professional safety in the relevant departments and work sites and through a questionnaire on the subject and conduct personal interviews with those concerned in this area and to prepare a program for the application of professional safety for each resource (labor, machines, materials, money) in construction sites and departments concerned.

1. المقدمة:

ان اي عمل مهما كان يقترن بالمخاطر وتسمى هذه المخاطر بالمخاطر المهنية وستبقى هذه المخاطر محيطة بالعمل مادام الانسان يعمل ويدير عملية الانتاج ولكن هذه المخاطر يمكن السطرة عليها وتقليلها الى الحد الادنى وخلق بيئة صحية وأمينة للعاملين.

ان الحوادث ليست حتمية الوقوع بل هي كأي ظاهرة في العالم لهل مسبباتها وطرق معالجتها وتفاديها ومن هنا اصبح موضوع الصحة والسلامة المهنية موضوعاً اساسياً في الدراسات والبحوث وذلك من أجل كسب الفني والمهندس وكل العاملين في المنشآت الخبرة الكافية للوقاية من الحوادث ويحقق الاستفادة من الاساليب الفنية للأمان واستعمال وسائل ومعدات الأمان المتاحة والاعتناء بها بحيث تكون صالحة وفعالة في وقت الحاجة لها.

وبما ان القوى العاملة المدربة تعتبر أهم مقومات الانتاج وزيادة الدخل القومي لذا وجب إعداد هذه العملية ورفع مستواها الثقافي في هذا المجال من خلال فتح الدورات التدريبية نظرياً وعملياً لغرض تنفيذ البرنامج الذي يحقق زيادة الدخل، وكما حمل القائمون على الصناعة مسؤولية إعداد هذه العمالة فهم اليوم يحملون مسؤولية المحافظة على المقومات الأساسية للانتاج والانتاجية وهي الانسان، الآلة، المواد وذلك باتحاذ الوسائل الكفيلة بمنع وقوع الحوادث والاصابات والتعرض للأمراض المهنية التي تؤثر على الثروة الاقتصادية والتي لم يعد هناك شك في انها خسارة يمكن تلافيها لما تضيفه من أعباء على نفقات الانتاج.

هدف البحث :

ان مشكلة الحوادث والاصابات تعتبر من المشاكل الرئيسية التي تواجه المسؤولين على كافة المستويات في العالم والمنشآت وبالتالي تنعكس على الاقتصاد الوطني. من هنا جاءت فكرة البحث ليكون هدفه الرئيسي إلقاء نظرة على واقع السلامة المهنية في الدوائر المعنية بقطاع التشييد والمواقع الانشائية ومعرفة المشاكل في هذا المجال بغية التوصل الى قواعد السلامة المهنية ووضع برنامج في كيفية تطبيق هذه القواعد.

منهجية البحث :

لقد تضمن البحث جانبين هما:

الاول : الجانب النظري، حيث تم الاطلاع على الادبيات والكتب والبحوث السابقة التي تناولت موضوع السلامة المهنية من اجل الوقوف على المفهوم النظري للسلامة المهنية وهدفها وأهميتها ومعرفة ماتوصل اليه الباحثون في هذا المضمار.

الثاني : الجانب العملي، فقد تم التركيز على المسح الميداني وجمع المعلومات من المعنيين في الدوائر والمواقع الانشائية من خلال استبيانهم وكذلك إجراء المقابلات الشخصية معهم لغرض إغناء البحث بمعلومات تفيد في التوصل الى استنتاجات لتحسين واقع السلامة المهنية في قطاع التشييد في القطر.

(الجانب النظري)

أولاً : السلامة المهنية:

1-1 مفهوم السلامة المهنية (المشهداني، 1988):

ان المقصود بالسلامة المهنية هو تقديم خدمات وقائية واحتياطات كفيلة لحماية ووقاية عناصر الانتاج وهي:

1-1-1 القوى البشرية

1-1-2 الآلات والمعدات والأبنية

1-1-3 المواد الأولية والمصنعة

حيث تحمي القوى البشرية من مخاطر العمل والتي تشمل اصابات العمل والامراض المهنية اليومية لغرض المحافظة عليها لأطول فترة بالطاقة الانتاجية الكمية والنوعية اضافة لذلك حماية المواد عن طريق الخزن والنقل السليم كما تهدف السلامة المهنية الى حماية اموال الدولة.

لقد عرفت منظمة العمل الدولية(عبد الكريم، 2000) السلامة المهنية على انها جميع الانشطة الهادفة الى حماية القوى العاملة والمكائن من التعرض للحوادث الناجمة عن ظروف العمل والأداء السيء.

1-2 هدف السلامة المهنية (المشهداني، 1988):

تهدف السلامة المهنية الى:

1-2-1 حماية العاملين من الاصابات اثناء العمل وذلك بعدم تعرضهم الى الحوادث والاصابات والامراض المهنية.

1-2-2 تخفيف كلفة الانتاج وذلك عن طريق رفع الكفاءة الانتاجية للعامل.

1-2-3 المحافظة على المكائن والآلات من التلف والاستهلاك.

1-2-4 تدريب العاملين على طرق العمل الفنية الصحيحة والاشراف عليها.

1-2-5 التفتيش الدوري المستمر على مسائل العمل والاجهزة المستعملة والمطبقة اضافة الى الادوات.

1-2-6 دراسة اسباب الحوادث والاصابات داخل المنشأة ووضع الحلول المناسبة لتأمين عدم تكرارها ثانيةً.

1-2-7 تهيئة بيئة للعمل صحيحة وسليمة دون اي ضرر (التهوية، الاضاءة، الرطوبة، الاشعاعات، الضوضاء، الاهتزازات).

1-2-8 اختبار اجهزة الوقاية المناسبة.

ثانياً : نسبة اتباع وسائل السلامة المهنية في ادارة المشاريع الهندسية :(الجار الله وآخرون، 1984)

تعتبر السلامة المهنية المانع الذي يهدف الى الحفاظ على المقومات البشرية والمادية وكذلك الى رفع انتاجية هذه المقومات في اطار السلامة والصحة وتوفير الجو الصحي المناسب للعامل فيشعر بالأمان والثقة والإستقرار النفسي وبالتالي يؤدي هذا الى زيادة الانتاج وتعود الفائدة عليه وعلى البلد.

يتسبب وقوع الحوادث اثناء العمل في ضياع الارواح والاموال والاجهزة والمعدات كما يتسبب في تعطيل الاعمال واضافة اعباء مادية ومعنوية على كاهل المقاول هو في غنى عنها، ومهما كان حجم الحادثة فهي تؤثر على المصاب وعلى سير العمل بالاضافة الى ما تسببه من تكاليف باهظة تبلغ اضعاف ما يلزم إنفاقه لتوفير وسائل السلامة من تلك الحوادث، كما ان بعض المقاولين يستكثر النفقات التي يجب صرفها في سبيل اتباع اصول وقواعد السلامة.

لقد وجد من تحليل احصائيات الحوادث في المشاريع الانشائية بأن توزيع تلك الحوادث هو كما يلي (الجار الله وآخرون، 1984):

2-1	السقوط والتعثر والانزلاق	22%
2-2	الاجهزة والآلات والمكائن	20%
2-3	سقوط المواد والادوات	20%
2-4	الآليات والادوات الاحتياطية	13%
2-5	المسامير والأدوات الحادة	12%
2-6	ما يسببه القطع والبرم واللوي	7%
2-7	اسباب اخرى متنوعة	6%

أما بالنسبة الى مخاطر السلامة المهنية في العمل فقد تم تصنيفها كما يلي (عبد الكريم، 2000):

2-1 المخاطر الكيمياوية

2-2 المخاطر الميكانيكية

2-3 المخاطر الكهربائية

2-4 المخاطر الفيزياوية

2-5 المخاطر الصحية والبايولوجية

2-6 المخاطر النفسية

تؤدي هذه المخاطر الى الحوادث والاصابات في حالة تجاوز الحدود المسموح بها. وهناك عدة عوامل تؤدي الى حدوث الحوادث (الشيخلي، 1997) و (مقابلة مع مسؤول، 2003) منها إطالة العمل والسرعة وكذلك ظروف العمل غير الجدية كالحرارة والرطوبة والاضاءة غير المناسبة وكذلك نقص خبرة العامل وعدم التزامه بالتعليمات المطلوبة. ان واجبات ادارة المشروع يمثلها مدير المشروع ويساعده جميع المهندسين والمراقبين وعليه ان يضع قواعد السلامة الاساسية التي تتلائم ونوع العمل الذي يشرف عليه.

ثالثاً : الاحصائيات والسلامة :

تلعب الاحصائيات الخاصة بحوادث واصابات العمل والامراض المهنية دوراً هاماً في هذا المجال باعتبارها مصدراً مهماً للمعلومات المستخدمة في التقييم والتخطيط والمتابعة وبالتالي فهي تساهم في تطوير وتوجيه عمل المؤسسات الوطنية ذات الصلة بحوادث واصابات العمل والامراض المهنية وتقدير الحاجة لتطوير الخدمات التي تقدمها كما تساهم على مستمى الشركة في تطوير الخدمات المتعلقة بصحة وسلامة العاملين. تشير الاحصائيات العالمية الحديثة الى وقوع (250) مليون اصابة عمل سنوياً في العالم بين اصابة عمل وحادثة ووفاة، واستناداً لدراسة لعشرات الآلاف من الحوادث والاصابات وجد ان (88%) من الحوادث والاصابات سببها الاشخاص وان (10%) سببها الاشياء المحيطة بالعمل (الثويني، 1991).

تقسم احصائيات اصابات العمل الى الانواع التالية (علي، 1991):

3-1 احصائية عدد ونتيجة الاصابات

3-2 احصائية اسباب الاصابات وتشمل:

3-2-1 الاسباب الاجمالية لاصابات

3-2-2 الاسباب التفصيلية للاصابات

3-3 احصائية انواع الحوادث

3-4 احصائية وقت وقوع الحوادث

3-5 احصائية موضوع الاصابة في الجسم

3-6 احصائية الاصابة (واسطة الاصابو ونوعها)

3-7 معدلات التكرار أو الشدة

3-8 نسبة المصابين الى المعرضين للاصابة

عادة ما تقترن احصائيات اصابة العمل برسوم بيانية تبين الاصابات كما في الاشكال (1-5) (علي، 1991).

رابعاً : الاسعافات الأولية :(الثويني، 1991)

هي التدابير والخطوات التي يقوم بها المعالج أو المسعف الى المصابين بالحوادث الطارئة قبل وصولهم الى المراكز الطبية أو المستشفيات. تعتبر الاسعافات الأولية في مواقع العمل خط الدفاع لعلاج اصابات العمل سواء البسيطة أو المعقدة أو المرض المفاجئ لحظة وقوعه من قبل المسعف الصحي المهني.

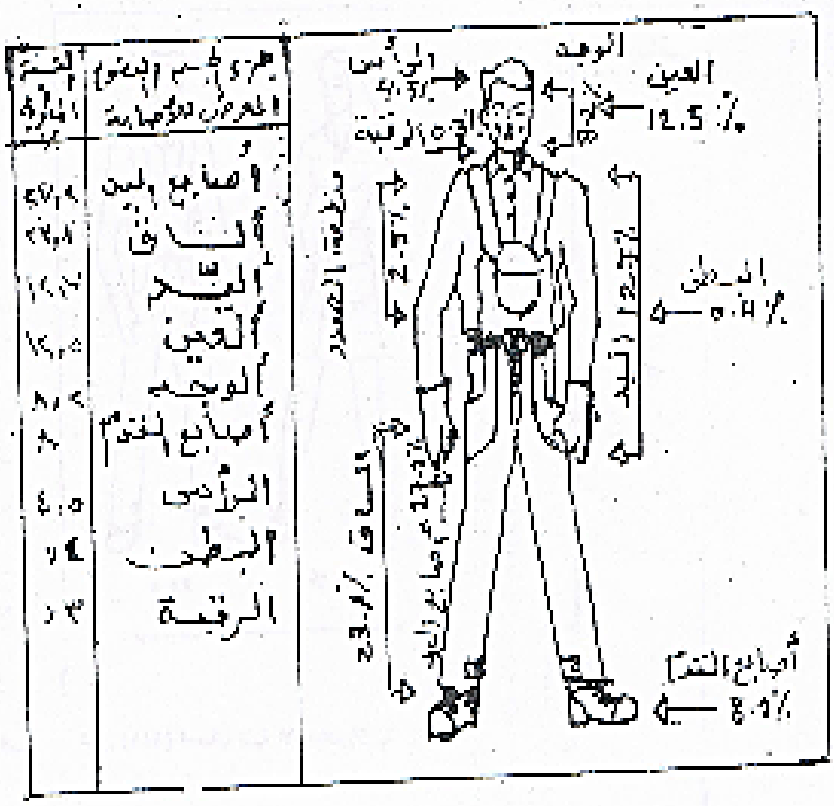

شكل رقم (1): يبين النسبة المؤية لاجزاء الجسم المعرضة للاصابة

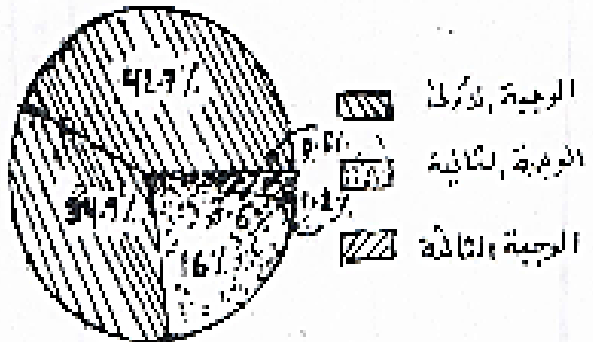

شكل رقم (2): يبين احصائية لاصابات العمل بالنسبة لوقت العمل وواجبات العمل (شفتات) حيث يظهر بأن نسبة عدم الحوادث في الوجبة الاولى 77.6 % (من الساعة 6–10 صباحاً ومن الساعة 10–14 ظهراً) ونسبة عدد الحوادث للوجة الثانية 20.6 % والثالثة 1.8 %.

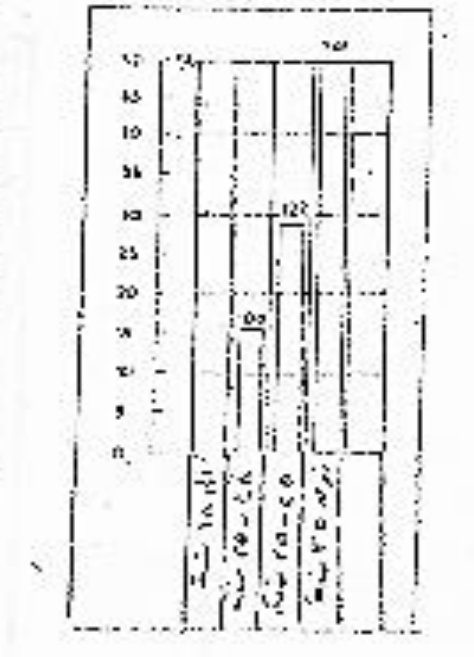

شكل رقم (3):احصائية نسبة الاصابات بالنسبة للعمر

شكل رقم (4):احصائية نسبة الاصابات بالنسبة للجنس

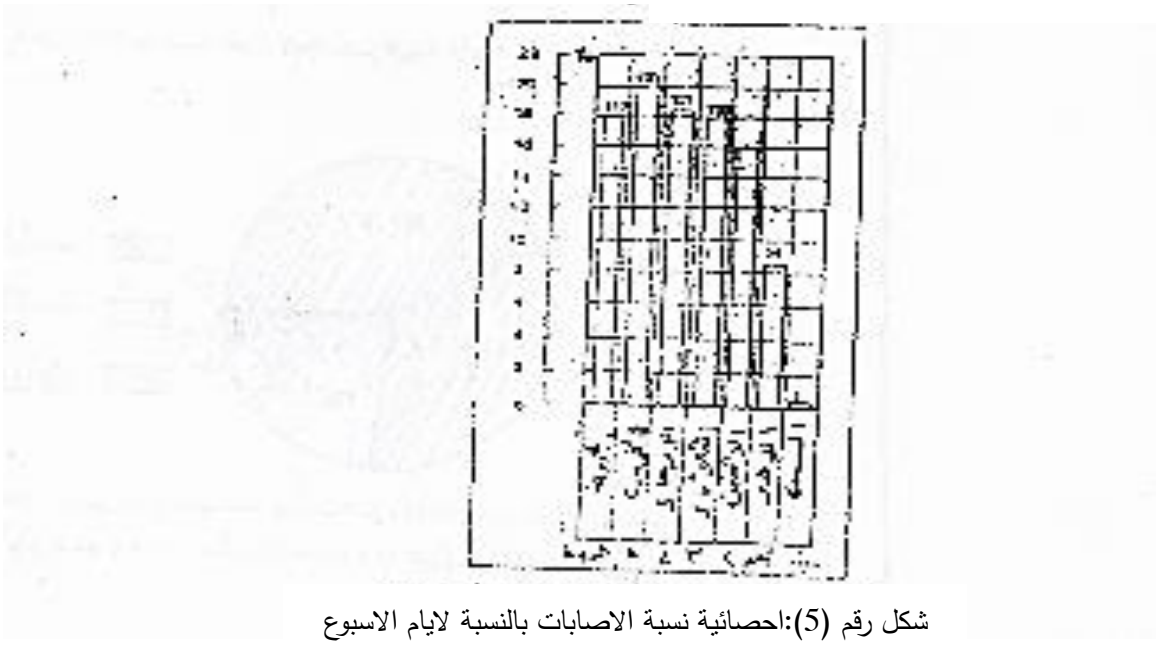

شكل رقم (5):احصائية نسبة الاصابات بالنسبة لايام الاسبوع

(الجانب العملي)

اجراء الإستبيان

1- حجم العينة :

لما كان من الصعب استبيان كل مجتمع المعنيين بموضوع السلامة المهنية لذا تم أخذ عينة من هذا المجتمع ممثلاً بـ (38) مستبيناً بموجب المواصفة الأمريكية (ASTM – E – 122 -79)، لقد كانوا من المهندسين والفنيين ومسؤولي السلامة من ذوي الخبرة الطويلة (اكثر من 10 سنوات).

2- تصميم استمارة الاستبيان :

من خلال مراجعة المصادر والبحوث المذكورة في الجانب النظري ومن خلال المقابلات الشخصية التي اجريت مع عدد من المسؤولين عن السلامة المهنية في دوائر الدولة والمشاريع الانشائية تم استخلاص اسئلة معينة تضمنتها استمارة الاستبيان والموضح نموذجاً منها في الملحق رقم (1). لقد تم جمع الاستمارات وتفريغ الاجابات في الجدول في الملحق رقم(2).

3- جمع الاجابات وتحليلها :

لقد تم احتساب التكرار للاجابات ومن ثم احتساب النسبة المئوية كأسلوب بسيط وشائع في الدراسات الاحصائية (ابو صالح وآخرون، 1983). لقد لوحظ ان اجابة اكثر المستبينين على عدد كبير من الاسئلة بالإجابة (كلا) مقارنة بالإجابة (نعم) وهذا يؤكد عدم توفر التعليمات الخاصة بموضوع السلامة في اغلب دوائر قطاع التشييد ومواقع العمل الانشائية والى عدم وجود قواعد رئيسية واجبة التطبيق في هذا الموضوع ولقلة عدد المسؤولين عن السلامة المهنية.

خامساً : البرنامج المقترح لتطبيق قواعد السلامة المهنية :

من اجل تحقيق الهدف الرئيسي وهوسلامة العاملين والمعدات والأبنية وبعد الاطلاع على نتائج تحليل اجابات الاستبيان والمقابلات الشخصية وإعتماداً على الدراسات والبحوث حول موضوع السلامة المهنية تم التوصل الى اقتراح برنامج لتطبيق قواعد السلامة المهنية وبالمحاور التالية:

المحور الأول : وضع السياسة العليا للسلامة المهنية :

وضع السياسة العليا للسلامة المهنية يجب ان يبدأ من الجهات العليا في الدولة ونزولاً الى االمؤسسات والدوائر الاخرى على ان تكون هنالك جهة مركزية تأخذ على عاتقها عملية التطبيق وتكون لها صلاحيات ملزمة وكما يلي:

1- مهام الادارات العليا عند وضع سياسة السلامة المهنية :

1-1 ان قسم السلامة المهنية يجب ان يرتبط مباشرة بمدير عام الشركة للاسباب التالية:

1-1-1 ان قسم السلامة المهنية يعد من الاقسام المهمة جداً بسبب سعيه المستمر لمنع وقوع الحوادث والاصابات ومن ثم تقليل الخسائر البشرية والمادية.

1-1-2 ان الاجراءات التي يتخذها قسم السلامة من حيث عدم ملائمة محل العمل أو معاقبة المخالفين أو اية قرارات اخرى تخص تطبيق السلامة لايمكن ان تتحقق اذا كان ارتباط هذا القسم بغير مدير عام الشركة.

1-1-3 ان قرارات قسم السلامة سيكون لها اثراً واقعاً ملموساً وبأقرب فرصة مقارنةً بما لو كان ارتباط القسم مع غير المدير العام.

1-2 يجب ان يكون للادارة العليا دور فعال وجدي واجب التحقيق بخصوص تأمين سلامة وصحة جميع العاملين.

1-3 تكون المسؤولية تضامنية تشترك فيها جميع المديريات والاقسام لتحقيق مستلزمات الصحة والسلامة المهنية.

1-4 عدم اهمال السلامة المهنية أو جعل مهامها مشاعة غير محددة المفهوم ولا واضحة الأهداف أو فكرة مسؤوليتها عبئاً ثقيلاً على مسؤول السلامة أو لجنة السلامة بل يجب تحديد هذه المسؤوليات وتحديد المعنيين بها.

1-5 تحمل المسؤوليات التي قد تظهر في الظروف غير الاعتيادية ومايتبعها ومعالجتها منها:

1-5-1 مخاطر تتصل بالحروب.

1-5-2 مخاطر تتصل بتأمين أماكن العمل.

1-5-3 مخاطر تتصل بحسن اختيار مقومات الانتاج البشرية والمادية.

1-5-4 مخاطر تتصل بتدريب ونوعية العاملين.

1-5-5 مخاطر تتصل بتنظيم الاجهزة الفنية المعاونة كأجهزة السلامة والصحة المهنية والدفاع المدني وغيرها.

1-5-6 خاطر تتصل بمستوى العلاقات الانسانية بين مختلف مستويات العاملين.

1-5-7 مخاطر تتصل بتخطيط برامج السلامة ومتابعة التنفيذ وتقديم النتائج.

1-5-8 مخاطر تتصل بتنظيم العمل وعدم تحديد المسؤوليات.

2- مسؤوليات الادارة العليا :

2-1 مسؤوليات تتصل بتخطيط الشركة أو التوسع فيها.

2-2 مسؤليات تتصل بسياسة الشركة في تنفيذ التزاماتها ومتابعة التفيذ.

2-3 مسؤوليات تتصل بتنظيم العمل وتحديد العلاقات بين مختلف الوحدات.

2-4 مسؤوليات اتخاذ الاجراءات اللازمة التي تضمن حماية العاملين اضافة الى الاجراءات المتعلقة بتنظيم خدمات الصحة والسلامة المهنية كالقوانين والنظم واللوائح ذات اعلاقة.

3- دور الادارة في منع الحوادث بالتركيز على مايلي :

3-1 توجيه اقسام السلامة والاطفاء وتحديد مسؤولية كل قسم منها.

3-2 الاشراف الفعلي على تدريب المنتسبين بما يخص السلامة.

3-3 اختيار منتسبي اقسام السلامة والاطفاء.

3-4 الاشراف على تطبيق قوانين وانظمة السلامة.

3-5 رفع مستوى الوعي الوقائي للعاملين.

3-6 تشكيل لجان السلامة والصحة المهنية وتحديد مهامها وواجباتها.

3-7 تشجيع المقترحات واعمال اللجان والأخذ بها ومناقشة المقترحات والأعمال التي يتم رفضها قبل اتخاذ قرار الرفض لكي تكون اللجنة على علم بذلك ولكي تتجاوز تلك المقترحات في حالة كونها لاتخدم الشركة أو العاملين.

المحور الثاني : المهام الرئيسية للسلامة :

1- قواعد السلامة التي يجب تطبيقها من قبل كل مسؤول في موقع العمل :

1-1 شرح اسباب الحوادث لكافة العاملين في موقع العمل ثم إعطائهم التعليمات والتدريبات اللازمة على كيفية انجاز العمل بأمان.

2-1 يجب ان يهيئ كافة العاملين في موقع العمل بحيث يتمكنوا من رؤية كافة المخاطر المحتملة، كما يشجعون على تقديم التقارير عن حدوث الخلل أو الأخطاء والعيوب.

3-1 المنع الشديد مع شرح الاسباب لعدم الاعتناء والاهمال.

4-1 ايصال التعليمات الجديدة وقواعد السلامة الى كافة الأفراد العاملين في موقع العمل كلما سنحت الفرصة.

2- مهام مهندس السلامة :

1-2 مراجعة طرق التصميم والتنفيذ وتطوير مواصفات السلامة ايتم تضمينها في وثائق عقود الانشاء.

2-2 وضع خطة السلامة التي تتناسب مع متطلبات المشروع.

3-2 مراجعة برنامج المقاول الخاص بالسلامة على ضوء خطة الانشاء للسلامة والحصول على موافقة المالك على خطة السلامة الخاصة بالمشروع.

4-2 تخطيط نظم التقيد بالخطة من قبل موظف السلامة والمفتشين ومنسقي الانشاء للمناطق المختلفة بالمشروع.

5-2 تنظيم لجنة سلامة المشروع.

6-2 عقد اجتماع لموضوع السلامة مع رؤساء العمال وحضور اجتماعات لمناقشة السلامة.

7-2 مراقبة نظام تقارير الحوادث ووضع التوصيات الخاصة بتحسين برنامج السلامة.

8-2 تأمين خدمات المستشفى والإسعاف.

9-2 تامين الحماية من الحريق وخدمات الأمن.

3- مهام مسؤول السلامة :

1-3 تجهيز وسائل أمينة للوصول الى نقاط الأعمال مع اوضاع أمينة للعمل مبنية على نظام متكامل للعمل في جو السلامة.

2-3 تجهيز وصيانة الاجهزة والمكائن والآليات الأمينة للعمل.

3-3 جعل موقع العمل مرتباً منظماً نظيفاً بصورة دائمة.

4-3 التفكير قبل القيام بأي عمل في معرفة اسباب الحوادث مع توقع المخاطر واتخاذ الاحتياطات لمنعها.

5-3 اختيار الطريقة الأكثر سلامة واماناً عند اتخاذ قرار القيام بعملية معينة.

6-3 عدم التسرع في استغلال الفرص المحفوفة بالمخاطر وفي حالة ملاحظة شئ غير أمين يجب اتخاذ الاجراءات الفورية لإزالة الخطر.

7-3 إسداء النصح الى كافة العاملين في الموقع عن اسباب الحوادث وإعطائهم الارشادات والتعليمات بوضوح ثم التأكد من تنفيذها.

8-3 المحافظة على أرضية الممرات آمنة ضد التزلق وخالية من العوارض المؤدية الى التعثر.

3-9 التأكيد على كافة العاملين في الموقع بالنظر الى الأمام والى ماحولهم عند المشي.

3-10 يجب ان يكون مسؤول السلامة وبقية المهندسين أسوة يقتدى بهم في تطبيق قواعد وأصول السلامة.

المحور الثالث : المتطلبات الفنية لتطبيق انظمة السلامة :

1- الإيعاز بشراء مستلزمات السلامة الخاصة.

2- رفع الأنقاض.

3- وضع العلامات الدالة والإرشادية والتحذيرية وتعليمات السلامة والبوسترات .

4- صيانة التأسيسات الكهربائية في مكاتب المهندسين وغرف العاملين.

5- صيانة منظومات التهوية والساحبات الهوائية والإضاءة.

6- توفير معدات الوقاية الفردية العامة والمتخصصة ووفق جدول الإعمار.

7- إقامة دورة متخصصة في السلامة لمدة يوم في الشهر.

8- ايقاف عمل الماكنة في حالة عدم صدور أو وجود شهادات السلامة بالمنظومات والكرينات الجسرية.

9- الفحص الطبي الدوري للعاملين.

10- تطبيق تعليمات السلامة العامة والخاصة.

11- متابعة سجل الكشف اليومي قبل التشغيل من قبل السلامة.

12- متابعة التجاوزات في الطاقات أو الهدر بها وكما يلي:

- الطاقة الخزنية داخل المخزن.
- طاقات الخدمات الفنية (الكهرباء، الماء، الوقود) والادوات الاحتياطية.
- ساعات العمل وفترات استراحة العاملين المحددة.
- عدد العاملين لكل فترة عمل.

13- متابعة إدامة الآليات بعد انتهاء وجبة العمل.

14- مدى توفر معدات وادوات المناقلة والرفع المناسبة.

15- التأكيد على مايلي:

- تعريف العاملين بمواقع الخطر ومسببات الخطورة في عملهم.
- توفر صيدلية للاسعافات الأولية وديمومة المحتويات.
- عدم البدء بتشغيل الآلية بعد صيانتها الا بتأييد مسؤول السلامة.
- إدامةالمواقع الخدمية للعاملين (الحمامات والمغاسل).
- تحقيق متطلبات التعبئة والتغليف الجيد.
- نظافة شبكات المجاري من المخلفات وتأمين الأغطية للمانهولات والشبكات المفتوحة.
- تأمين حاويات لجمع المخلفات وتأمين التأريث الأرضي ذات الجهد العالي.
- وضع ملصقات التحذير المناسبة.
- عدم عمل العاملين بدون الوقاية الشخصية المحددة.

16- السعي لتوفير اذاعة داخلية مع موسيقى تساعد العاملين على تجاوز الملل والكآبة.

17- ان تطبيق ومتابعة الانظمة الفنية يتطلب التوثيق وفق مراحل للانجاز لإزالة الملاحظات لدى مسؤول نشاط السلامة.

المحور الرابع : المتطلبات الادارية لتطبيق انظمة السلامة :

1- تكليف ممثلي السلامة من حملة شهادة الدبلوم أو الاعدادية ومن لديهم خبرة جيدة في السلامة لغرض تطبيق المهام والواجبات اليومية الخاصة بعمل السلامة.

2- على الشركات ان تحقق الأعداد المطلوبة لممثلي السلامة وحسب كادر كل شركة أو موقع عمل.

3- العمل ضمن الهيكلية الادارية لكل شركة من حيث ارتباط نشاط السلامة ارتباطاً مباشراً بمدير عام الشركة.

4- تأمين تغطية مستلزمات انشطة السلامة واعطاء الاهتمام الكبير لها.

5- منح مدير السلامة بعض الصلاحيات الادارية والمالية من قبل ادارة الشركة.

6- تكليف مسؤولي السلامة بفتح السجلات الخاصة لغرض التوثيق والكشف اليومي ويؤخذ بالحسبان بأن هذه السجلات خاضعة للتفتيش والكشف عليها من خلال فرق السلامة للشركة الرئيسية.

7- يتم رفع موقف شهري من قبل مسؤولي السلامة في المواقع الى مدير عام الشركة ومن المدراء الى المسؤول الأعلى في الوزارة.

8- يطبق مبدأ الثواب والعقاب للمتميزين والمهملين من مسؤولي السلامة في تطبيقات اجراءات السلامة فصلياً.

9- يعاقب ممثل السلامة في حالة ثبوت استغلاله للصلاخيات الممنوحة له على ان تكون العقوبة من مجلس ادارة الشركة.

المحور الخامس : دور الاحصائيات في السلامة المهنية :

أولاً : تحديد اهداف ووظائف احصائيات حوادث العمل والامراض المهنية :

1- على المستوى الوطني :

1-1 تحديد مصادر الخطورة في كل نشاط اقتصادي أو قطاع مهني.

1-2 تقدير الاحتياجات التقنية والعلمية للتحكم بمخاطر العمل ومعالجة نتائجه.

1-3 تقدير الحاجة الى تطوير عمل الدوائر الحكومية المسؤولة عن تطبيق معايير حماية وحفظ صحة العاملين وسلامتهم.

1-4 مراجعة وتطوير الجداول الخاصة بحدود التعرض وداول الامراض المهنية.

2- على مستوى الشركة :

2-1 التقييم الاولي لفعالية قسم السلامة المهنية وتقدير احتياجات تطويره.

2-2 التحديد الدقيق لأسباب الحوادث والامراض المهنية التي تقع نتيجة لظروف العمل وسبل معالجتها ومنع تكرارها.

2-3 المساهمة في الكشف عن مصادر خطورة غير محددة أو معروفة.

2-4 تحديد حجم الخسائر البشرية والاقتصادية الناجمة عن الاصابات والحوادث.

2-5 تقدير الحاجة لتقديم أو تطوير خدمات اضافية (صحية أو تدريبية) تساهم في مجال حماية العاملين والمحافظة على صحتهم.

ثانياً : تغطية احصائيات الحوادث والامراض المهنية في مختلف قطاعات العمل لمل يلي:

2-1 جميع الحوادث المهنية سواء أدت الى اصابات أم لم تؤدي الى ذلك.

2-2 جميع الاصابات التي تؤدي الى غياب المصاب عن العمل لمدة يوم واحد على الأقل.

2-3 جميع الاصابات المهنية التي تؤدي الى الوفاة.

2-4 جميع الاصابات الناتجة عن حوادث الطريق من والى موقع العمل.

2-5 اصابات العاملين من الأحداث.

يجب اعتماد مبدأ الإبلاغ عن الاصابات بملئ استمارات تتضمن المعلومات التي تساعد في اجراء احصائيات الحوادث وكنماذج لها في الملحق رقم (3) وهي:

- معلومات عن الشركة أو صاحب العمل.
- معلومات عن المصاب.
- صفات الحادث.
- كيفية وقوع الحادث.

يجب الاستفادة من جمع وتحليل البيانات الخاصة بحوادث واصابات العمل والامراض المهنية في :

1- تحديد الانشطة الاقتصادية والمهنية التي تقع فيها الحوادث والامراض المهنية مع بيان درجة خطورتها وطرق وقوعها بغية وضع قاعدة للاجراءات الوقائية.

2- استكشاف التغيرات في نمط الحوادث والاصابات المهنية ومعدلات وقوعها.

3- تحديد الأولويات في مجال الوقاية من المخاطر ومتطلبات التدخل والمعالجة.

4- تقدير الخسائر الاقتصادية وكلفة الاصابات المهنية وأهمها ايام العمل المفقودة.

5- توفير قاعدة بيانات من اجل تصميم أو إعادة النظر في برامج السلامة.

6- إطلاع الإدارات واصحاب العمل والعاملين ومنظماتهم على المخاطر المرتبطة بعملهم.

7- توفير قاعدة بيانات موثوقة لإجراء بحوث مستقبلية في مجال الوقاية.

8- إعداد تقرير سنوي أو نصف سنوي عن احصائيات اصابات العمل والامراض المهنية.

سادساً : الاستنتاجات:

يمكن تلخيص ماتم التوصل اليه بما يلي :

1- تفتقر أغلب دوائر قطاع التشييد ومواقعها الانشائية الى انظمة وقواعد السلامة.

2- عدم الالتزام الصحيح بتعليمات السلامة المهنية في حالة توفرها، أو ضعف شديد في تطبيقها.

3- عدم وجود قسم خاص وبالعدد الكافي من المنتسبين المعنيين بأمور السلامة.

4- عدم إعطاء الصلاحيات المناسبة والكافية لمسؤوسم السلامة المهنية في حالة وجود هكذا قسم.

5- عدم اهتمام الادارات العليا بشكل جدي بموضوع السلامة المهنية مع استكثار النفقات التي يجب صرفها على اتباع اصول وقواعد السلامة وعدم تقديرها للتكاليف وخسائر الحوادث التي تهبط المعنويات وتزرع الخوف والفوضى وتزيد من تبذير المواد وتؤدي الى عطب الآليات والاجهزة وتؤخر سير العمل وتزيد تكاليف البناء والتشغيل والصيانة اضافة الى التكاليف غير المباشرة.

6- ضرورة ان يبدأ الاهتمام بالسلامة المهنية من الجهات العليا للدولة ونزولاً الى المؤسسات والدوائر الاخرى على ان تكون هنالك جهة مركزية تأخذ على عاتقها عملية التطبيق وتكون لها صلاحيات ملزمة.

7- تم التوصل الى برنامج لتطبيق قواعد السلامة في دوائر قطاع التشييد وقد شمل البرنامج خمسة محاور لضمن سلامة العاملين والمواد والآليات والمال.

المصـــادرالعربية:

- المشهداني، أزهر عبد الرحمن، " الصحة والسلامة المهنية "، بغداد، دار الحرية للطباعة، 1988.
- عبد الكريم، عبد المنعم، " السلامة المهنية في مواقع العمل " ، الجمعية العراقية للحة والسلامة المهنية، الدورة الاساسية للعمل في اقسام السلامة والصحة المهنية، للفترة 2/26 – 2000/3/9.
- الجار الله، د. محمد ابراهيم ونوارة، د. جمال محمد، " ادارة المشاريع الهندسية" ، المملكة العربية السعودية، الناشر جامعة الملك سعود، مطبعة جون وايلي وأولاده، نيويورك، 1984.
- الشيخلي، د. سامي، " صحة العامل " مديرية البيئة البشرية العامة ، مديرية الصحة المهنية، دار الحرية للطباعة والنشر، بغداد، 1979.
- مقابلة شخصية مع مسؤول السلامة المهنية، شركة الفاو الهندسية للمقاولات، آذار 2003
- الثويني، د. هلال جاسم، " احصاء حوادث واصابات العمل والامراض المهنية "، محاضرة الجمعية العراقية للصحة والسلامة المهنية، بغداد، 1991.
- علي، رحيم تركي، " المبادئ الاساسية للسلامة المهنية "، بغداد، هيئة المعاهد الفنية، 1991.
- الثويني، د. هلال جاسم، " الاسعافات الاولية في مواقع العمل "، محاضرة الجمعية العراقية للصجة والسلامة المهنية، بغداد، 1991
- ابو صالح، محمد صبحي وعوض، عدنان محمد، " مبادئ الإحصاء "، جامعة اليرموك، إربد، الأردن، الناشر : جون وايلي وأولاده، نيويورك 1983.

المصادر الاجنبية:

- ASTM – E122 – 79, “Standard Recommended Practice for choice of Sample Size to Estimate the Average Quality of a Lot or Process “.

ملحق رقم (1)

نموذج استمارة الاستبيان

اسم الدائرة :

نوع اعمال الدائرة :

تأريخ تأسيس الدائرة :

يرجى وضع اشارة (√) أمام الجواب الذي تختاره:

ت	السؤال	نعم	كلا
1-	هل يوجد قسم للسلامة ؟		
2-	في حالة وجود قسم للسلامة، متى تأسس.		
3-	هل يوجد مهندس للسلامة ؟		
4-	هل يوجد مسؤول للسلامة ؟		
5-	هل يتم استعمال معدات الوقاية الشخصية أدناه ؟		
	- واقيات الوجه والعيون		
	- واقيات السمع		
	- واقيات اليد والذراع		
	- واقيات الرأس		
	- واقيات القدم والساق		
	- واقيات الجسم		
	- واقيات مخاطر السوق		
	- واقيات الجهاز التنفسي		
6-	هل يتم احتساب معدل وقوع الاصابة كمقياس مقارنة لوقوع الحوادث بين المواقع المتماثلة وكما يلي: معدل الوقوع = عدد الاصابات خلال الفترة الزمنية / العدد الاجمالي للعاملين خلال نفس الفترة * 1000		
7-	هل يتم احتساب تكرار وقوع الاصابات كمقياس مقارنة مع عدد ساعات العمل الفعلية وكما يلي : معدل تكرار الاصابات = عدد الاصابات خلال الفترة الزمنية / عدد العاملين * عدد الايام الفعلية خلال الفترة الزمنية * عدد ساعات العمل اليومي * 1000000		
8-	هل يتم احتساب شدة خطورة الاصابات الناجمة عن حوادث العمل وكما يلي: معدل الخطورة= عدد ايام العمل المفقودة نتيجة للاصابات خلال فترة معينة / عدد العاملين*عدد ايام العمل الفعلية خلال الفترة الزمنية * عدد ساعات العمل اليومي * 1000000		
9-	هل يتضمن نموذج الابلاغ عن اصابات العمل البيانات التالية:		
	- معلومات عن الشركة او صاحب العمل		
	- اسم وعنوان الشركة / موقع العمل		

		- النشاط الاقتصادي	
		- فعاليات العمل	
	10-	هل تسجل المعلومات أدناه على المصاب:	
		-الاسم – العمر – الجنس – العنوان – الوضع المهني – موظف – عامل – أجير بعقد – المهنة – مدة الخدمة – خبرة التدريب	
	11-	هل يتم وصف الاحداث :	
		- حادث مميت	
		- حادث أدى الى عجز دائم أو مؤقت	
		- طبيعة الإصابة	
		- مكان الإصابة	
	12-	هل يتم وصف كيفية وقوع الحادث :	
		- مكان وقوع الحادث	
		- زمن / تأريخ وقوع الحادث	
		- العمل / النشاط الذي أدى الى الحادث	
		- نوع الحادث	
		- العامل المادي المسبب	
		- العوامل الاخرى	
	13-	هل تتوفر خدمات الاسعاف الأولي أدنا في مواقع العمل :	
		- توفر المسعف الصحي المهني لحين قدوم الطبيب أو لنقل المصاب	
		- تأمين صندوق الإسعاف الأولي بكل مواده لإجراءات الإسعاف الأولي	
	14-	هل يتم تطبيق الواجبات والمهام أدناه للسلامة والصحة المهنية :	
		- وضع وإعتماد برنامج للسلامة بحيث ينسجم والطموحات	
		- جمع البيانات والإحصائيات عن الحوادث والإصابات وتنظيم استمارات الإصابات وتصنيفها وترصيدها ورفعها بمواقف فعلية الى المسؤولين	
		- تحقيق في الحوادث والاصابات ومعرفة اسبابها وتثبيتها في سجل خاص واقتراح الإجراءات الكفيلة بمنع تكرارها	
		- مراقبة ومتابعة تنفيذ التشريعات القانونية والتعليمات والأوامر الصادرة من الجهات المختصة والسلامة المهنية	
		- نشر الوعي الوقائي لكافة العاملين من خلال اصدار النشرات ووسائل الإيضاح وفتح الدورات التدريبية للعاملين	
		- المشاركة في دراسة المشاريع في مرحلة التخطيط والإشراف على التنفيذ لضمان مراعاة قواعد الصحة والسلامة المهنية	
		- التنسيق والتعاون مع الدوائر المختصة في مجال الصحة المهنية كالمركز القومي للصحة والسلامة المهنية، حماية البيئة، الدفاع المدني، مركز البحوث وغيرها	
		- متابعة التأمين على العاملين ضد الحوادث والاصابات واستحصال التعويضات للمتضررين بما يضمن حقوقهم	
		- متابعة اجراء الفحوصات الدورية للعاملين وحسب طبيعة عمل كل شركة وفتح سجلات خاصة بذلك	
		- متابعة الفحوصات الدورية للعاملين والمعدات ومتابعة تطبيق نظم الصيانة الوقائية المبرمجة لمنع وقوع الحوادث والاصابات	
		- متابعة نظافة المكائن والآلات والاقسام الفنية بصورة مستمرة وكذلك مرافق الشركة	
		- متابعة التأمين على المكائن والمعدات ضد اخطار الانفجار والحريق والكوارث الطبيعية	

	– العمل على توفير المعدات الشخصية لحماية العاملين من اخطار العمل وحسب المواصفات العالمية ومتابعة استخدامها		
	– العمل على اتخاذ كافة احتياطات السلامة للمكائن والمعدات الخاصة فيما يتعلق بالحواجز الواقية للأجزاء المتحركة والأغطية		
	– مراقبة الاعمال العرضية ذات الصلة مثل تفريغ الحمولات الثقيلة خاصة الخطرة منها لتلافي حدوث الحرائق والانفجارت واصابة العاملين		
	– المشاركة في اللجان التحقيقية في الحوادث الخطرة مثل التسمم، الحرائق، الاصابة بالامراض المهنية		
	– متابعة اعمال الطبابة في الشركة ومواقع العمل التابعة لها والتأكد من تقديمها الخدمات الطبية وتوفير كافة المستلزمات الطبية والبشرية		

ملحق رقم(2)

جدول تحليل اجابات المستبينين

ت	السؤال	نعم %	كلا %
1-	هل يوجد قسم للسلامة ؟	60	40
2-	في حالة وجود قسم للسلامة، متى تأسس.		
3-	هل يوجد مهندس للسلامة ؟	54	45
4-	هل يوجد مسؤول للسلامة ؟	58	42
5-	هل يتم استعمال معدات الوقاية الشخصية أدناه ؟		
	– واقيات الوجه والعيون	30	70
	– واقيات السمع	33	67
	– واقيات اليد والذراع	20	80
	– واقيات الرأس	60	40
	– واقيات القدم والساق	38	62
	– واقيات الجسم	35	65
	– واقيات مخاطر السوق	30	70
	– واقيات الجهاز التنفسي	22	78
6-	هل يتم احتساب معدل وقوع الاصابة كمقياس مقارنة لوقوع الحوادث بين المواقع المتماثلة وكما يلي: معدل الوقوع = عدد الاصابات خلال الفترة الزمنية / العدد الاجمالي للعاملين خلال نفس الفترة * 1000	32	68
7-	هل يتم احتساب تكرار وقوع الاصابات كمقياس مقارنة مع عدد ساعات العمل الفعلية وكما يلي : معدل تكرار الاصابات = عدد الاصابات خلال الفترة الزمنية / عدد العاملين * عدد الايام الفعلية خلال الفترة الزمنية * عدد ساعات العمل اليومي * 1000000	30	70

8-	هل يتم احتساب شدة خطورة الاصابات الناجمة عن حوادث العمل وكما يلي: عدد ايام العمل المفقودة نتيجة للاصابات خلال فترة معينة معدل الخطورة=ـــ* 1000000 عدد العاملين*عدد ايام العمل الفعلية خلال الفترة الزمنية * عدد ساعات العمل اليومي	25	75
9-	هل يتضمن نموذج الابلاغ عن اصابات العمل البيانات التالية:		
	– معلومات عن الشركة او صاحب العمل	60	40
	– اسم وعنوان الشركة / موقع العمل	55	45
	– النشاط الاقتصادي	25	75
	– فعاليات العمل	65	35
10-	هل تسجل المعلومات أدناه على المصاب:		
	–الاسم – العمر – الجنس – العنوان – الوضع المهني – موظف – عامل – أجير بعقد – المهنة – مدة الخدمة – خبرة التدريب	67 72 40 57	33 28 60 43
11-	هل يتم وصف الاحداث :		
	– حادث مميت	34	66
	– حادث أدى الى عجز دائم أو مؤقت	41	59
	– طبيعة الإصابة	30	70
	– مكان الإصابة	39	61
12-	هل يتم وصف كيفية وقوع الحادث :		
	– مكان وقوع الحادث	36	64
	– زمن / تأريخ وقوع الحادث	45	55
	– العمل / النشاط الذي أدى الى الحادث	28	72
	– نوع الحادث	37	63
	– العامل المادي المسبب	20	80
	– العوامل الاخرى	22	78
13-	هل تتوفر خدمات الاسعاف الأولي أدنا في مواقع العمل :		
	– توفر المسعف الصحي المهني لحين قدوم الطبيب أو لنقل المصاب	70	30
	– تأمين صندوق الإسعاف الأولي بكل مواده لإجراءات الإسعاف الأولي	64	38
14-	هل يتم تطبيق الواجبات والمهام أدناه للسلامة والصحة المهنية :		
	– وضع وإعتماد برنامج للسلامة بحيث ينسجم والطموحات	40	60
	– جمع البيانات والإحصائيات عن الحوادث والإصابات وتنظيم استمارات الإصابات وتصنيفها وترصيدها ورفعها بمواقف فعلية الى المسؤولي	37	63
	– تحقيق في الحوادث والاصابات ومعرفة اسبابها وتثبيتها في سجل خاص واقتراح الإجراءات الكفيلة بمنع تكرارها	30	70
	– مراقبة ومتابعة تنفيذ التشريعات القانونية والتعليمات والأوامر الصادرة من الجهات المختصة والسلامة المهنية	34	66
	– نشر الوعي الوقائي لكافة العاملين من خلال اصدار النشرات ووسائل الإيضاح وفتح الدورات التدريبية للعاملين	27	73
	– المشاركة في دراسة المشاريع في مرحلة التخطيط والإشراف على التنفيذ لضمان مراعاة قواعد الصحة والسلامة	75	25

	المهنية		
	– التنسيق والتعاون مع الدوائر المختصة في مجال الصحة المهنية كالمركز القومي للصحة والسلامة المهنية، حماية البيئة، الدفاع المدني، مركز البحوث وغيرها	35	65
	– متابعة التأمين على العاملين ضد الحوادث والاصابات واستحصال التعويضات للمتضررين بما يضمن حقوقهم	60	40
	– متابعة اجراء الفحوصات الدورية للعاملين وحسب طبيعة عمل كل شركة وفتح سجلات خاصة بذلك	30	70
	– متابعة الفحوصات الدورية للعاملين والمعدات ومتابعة تطبيق نظم الصيانة الوقائية المبرمجة لمنع وقوع الحوادث والاصابات	37	63
	– متابعة نظافة المكائن والآلات والاقسام الفنية بصورة مستمرة وكذلك مرافق الشركة	41	59
	– متابعة التأمين على المكائن والمعدات ضد اخطار الانفجار والحريق والكوارث الطبيعية	30	70
	– العمل على توفير المعدات الشخصية لحماية العاملين من اخطار العمل وحسب المواصفات العالمية ومتابعة استخدامها	34	66
	– العمل على اتخاذ كافة احتياطات السلامة للمكائن والمعدات الخاصة فيما يتعلق بالحواجز الواقية للأجزاء المتحركة والأغطية	31	69
	– مراقبة الاعمال العرضية ذات الصلة مثل تفريغ الحمولات الثقيلة خاصة الخطرة منها لتلافي حدوث الحرائق والانفجارت واصابة العاملين	30	70
	– المشاركة في اللجان التحقيقية في الحوادث الخطرة مثل التسمم، الحرائق، الاصابة بالامراض المهنية	40	60
	– متابعة اعمال الطبابة في الشركة ومواقع العمل التابعة لها والتأكد من تقديمها الخدمات الطبية وتوفير كافة المستلزمات الطبية والبشرية	20	80

ملحق رقم (3)

نماذج استمارات معلومات احصائيات الحوادث

نموذج – أ – بيانات اصابات العاملين

ت	اسم المصاب	العمر	المهنة	تأريخ الاصابة	الاصابة			الاجازة الممنوحة	الخسائر المادية	التعويضات المالية	الحالة الاجتماعية	عدد الاطفال	موقع العمل
					موقعها	تسببها	أدت الى						
المجموع													

نموذج – ب– ادخال بيانات اصابات العمل والامراض المهنية

اسم الشركة :	**مقدار التعويض من التأمين**	
موقع العمل :	**مقدار التعويض من الوزارة**	
اسم المنتسب :	**مقدار التعويض من الشركة**	
العمر :	**مقدار التعويض من صندوق دعم الموظفين :**	
المهنة :	**الخسائر المادية لتوقف الانتاج للمصاب :**	
سبب الاصابة :	**الخسائر المادية العلاجات الطبية :**	
	الخسائر المادية للمكائن والمعدات والابنية :	
	الحالة الاجتماعية :	**عدد الاطفال :**
عدد ايام الاجازة المرضية :	**موقع السكن :**	
الاصابات ادت الى :	**موقع الاصابة بالشركة :**	
موقع الاصابة من الجسم		

نموذج – جـ – بيانات حوادث الحريق

ت	**اسم الشخص الذي قام بالعمل**	**وظيفة الشخص الذي قام بالعمل**	**اليوم والساعة**	**التأريخ**	**موقع الحريق**	**اسباب الحريق**	**المسؤولين عن الحريق**	**نوع الحريق**	**الاجراءات المتخذة**	**الخسائر المادية**	**الخسائر البشرية**	**مدة استغراق الحريق**	**المواد المستخدمة في الاطفاء**	**الجهة الساندة في اخماد الحريق**
الدروس المستنبطة من الحريق								التدابير الاحترازية المتخذة						
الدروس المستنبطة من الحريق								التدابير الاحترازية المتخذة						
الدروس المستنبطة من الحريق								التدابير الاحترازية المتخذة						

نموذج – د – ادخال بيانات حوادث الحريق في الشركات

اسم الشركة :	اليوم والساعة :	التأريخ :
موقع الحريق :	سبب الحريق :	نوع الحريق :
خسائر مالية :	خسائر بشرية :	
مدة استغراق الحريق :	المسؤولين عن الحريق :	
المواد المستخدمة في الاطفاء :	اسم الشخص الذي قام بالاطفاء :	
وظيفة الشخص الذي قام بالاطفاء :	الجهة الساندة في عملية اخماد الحريق :	
التدابير الاحترازية :	الدروس المستنبطة من الحريق :	